ECCOMAS Thematic Conference

AGH

XXIX Conference on Computer Methods in Materials Technology

KOMPLASTECH 2025

PROGRAMME

Conference Programme

March 2–5, 2025, Krynica-Zdrój, Poland

International Scientific Committee

Tudor BALAN	Ecole Nationale Supérieure d'Arts et Métiers, Paris, France
Markus BAMBACH	ETH D-MAVT Zurich, Switzerland
Thierry BARRIERE	FEMTO-ST Institute, Besancon, France
Wolfgang BLECK	RWTH Aachen University, Germany
Dominik BRANDS	University of Duisburg-Essen, Germany
Ryszard BUCZKOWSKI	West Pomeranian University of Technology in Szczecin, Poland
Tadeusz BURCZYŃSKI	IPPT PAN, Warszawa, Poland
Witold CECOT	Cracow University of Technology, Poland
Jose Cesar de SA	University of Porto, Portugal
Francesco CHINESTA	Ecole Centrale of Nantes, France
Zbigniew GRONOSTAJSKI	Wrocław University of Technology, Poland
Ernst KOZESCHNIK	TU Wien, Austria
Jan KUSIAK	AGH University of Krakow, Poland
Wacław KUŚ	Silesian University of Technology, Gliwice, Poland
Jari LARKIOLA	University of Oulu, Finland
Maciej PASZYŃSKI	AGH University of Krakow, Poland
Ulrich PRAHL	TU-Bergakademie Freiberg, Germany
Stefanie REESE	RWTH Aachen University, Germany
Jerzy ROJEK	IPPT PAN, Warszawa, Poland
Jan SLADEK	Slovak Academy of Sciences, Bratislava, Slovakia
Christof SOMMITSCH	Graz University of Technology, Austria
Bartek WIERZBA	Lukasiewicz Research Network – Institute of Organic Industry, Warszawa, Poland
Bradley WYNNE	University of Strathclyde, Glasgow, UK

Steering Committee

Maciej PIETRZYK	AGH University of Krakow, Poland

Conference Chairs

Danuta SZELIGA
Łukasz RAUCH
AGH University of Krakow, Poland

Conference Secretary

Anna SMYK
AGH University of Krakow, Poland

Local Organizer

ACADEMICA

Partner

AGH

Department of Applied Computer Science and Modelling
Faculty of Metals Engineering and Industrial Computer Science
AGH UNIVERSITY OF KRAKOW

Supporting Organisations

ECCOMAS Thematic Conference

European Community on Computational Methods
in Applied Sciences
ECCOMAS

PAN
POLISH ACADEMY OF SCIENCES

Metal Technological Processes,
The Materials Engineering and Metallurgy Committee
POLISH ACADEMY OF SCIENCES

pacm

Polish Association for Computational Mechanics

isim

Department of Applied Computer Science and Modelling
Faculty of Metals Engineering and Industrial Computer Science
AGH University of Krakow

Venue

Hotel Belmonte *****
https://www.belmonte.com.pl/en/
ul. Piękna 23
33-380 Krynica-Zdrój
Poland

Journals

COMPUTER METHODS IN MATERIALS SCIENCE

http://www.cmms.agh.edu.pl/

Taylor & Francis
Taylor & Francis Group

Philosophical Magazine Letters
https://www.tandfonline.com/journals/tphl20

The project is co-financed by funds from the state budget,
granted by the Minister of Science and Higher Education as part of the Excellent Science II Program,
project no. KONF/SP/0109/2024/02, subsidy amount 67 870 PLN

Doskonała Nauka II

Ministry of Science and Higher Education
Republic of Poland

Republic of Poland

Sunday, 2nd March

16:00–19:00 Registration, *Main Hall*
18:00–20:00 Casual Buffet Dinner, *Restaurant*

Monday, 3th March

8:55 Opening Ceremony
9:00–9:40 Plenary lecture, *Pieno room*
9:40–10:00 Industrial lecture, *Pieno room*
10:00–12:00 Morning lectures in two rooms:
Modelling of processes and materials, *Pieno room*
Artificial intelligence and machine learning, *Luna room*
12:00–12:05 Conference Participants photo in front of the hotel
12:05–13:00 Lunch, *Restaurant*
13:00–13:40 Plenary lecture, *Pieno room*
13:40–14:00 Industrial lecture, *Pieno room*
14:00–16:00 I Afternoon lectures in two rooms:
Advanced modelling of rolling processes, *Pieno room*
Atomic and micro scale simulations, *Luna room*
16:00–16:20 Coffee break
16:00–18:00 II Afternoon lectures in two rooms:
Application of numerical methods in medicine, *Pieno room*
Physical Informed Neural Networks, *Luna room*
19:20–19:30 Transfer to regional restaurant
19:30–22:00 Regional evening

Tuesday, 4th March

9:00–13:00 Morning Winter sports
13:00–14:00 Lunch, *Restaurant*
14:00–15:20 Plenary lectures, *Pieno room*
15:20–15:40 Coffee break
15:40–17:00 Afternoon lectures in two rooms:
Numerical modeling of modern materials, *Pieno room*
Digital Twins and Big Data applications, *Luna room*
19:30–22:00 Formal Banquet, *Hotel Restaurant*

Wednesday, 5th March

9:20–10:00 Plenary lecture, *Pieno room*
10:00–10:20 Industrial lecture, *Pieno room*
10:20–10:40 Coffee break
10:40–12:00 Morning lectures in two rooms:
Advanced numerical models and techniques, *Pieno room*
Discrete and coupled modelling, *Luna room*
12:00–13:00 Lunch, *Restaurant*
13:00 Transfer to Krakow

Plenary speakers

Nirupam Chakraborti, Faculty of Mechanical Engineering, Czech Technical University in Prague

Professor Nirupam Chakraborti was educated in India and in the USA, receiving his B.Met.E from Jadavpur University followed by an MS from New Mexico Tech, USA and subsequently PhC and PhD degrees from University of Washington, Seattle, USA. He lectured and conducted research in numerous universities worldwide. He is a former Docent of Åbo Akademi, Finland, former long term Visiting Professors of Florida International University, Miami, USA and POSTECH, Korea, and he also taught and conducted research at several other academic institutions in Austria, Brazil, Finland, Germany, Italy and the US. He was a Higher Academic Grade Professor at Indian Institute of Technology, Kharagpur and since 2022, after superannuating in India, he is working as a Visiting Professor of Czech Technical University in Prague. He is a Co-Editor of the prestigious journal Philosophical Magazine Letters published by Taylor and Francis. Internationally known for his pioneering work on evolutionary computation in the area of Metallurgy and Materials, Professor Chakraborti has been continuously rated among the top 2% highly cited world researchers in the Materials area, as per the reports published from Stanford University in the USA. Beside numerous journal articles, he is also author of a comprehensive book Data-driven Evolutionary Algorithms in Materials Technology published by CRC Press, USA/UK. His Plenary Lecture at KomPlasTech 2025 will involve a detailed description of the Evolutionary deep learning and optimization algorithm EvoDN2 developed in his group, along with several examples of its application in the material design and manufacturing domain as currently pursued by him and his students.

Bartosz Iżowski, Rzeszów University of Technology, Poland

Bartosz Iżowski, PhD, is a Senior Materials and Stress Engineer in the Research and Development Department of one of the leading aerospace companies and an independent entrepreneur. With a career spanning over a decade, he specializes in leveraging advanced numerical methods to optimize manufacturing processes such as heat treatment, forging, and machining. Dr. Iżowski holds a B.Sc. and M.Sc. in Materials Science and Engineering from Warsaw University of Technology and a postgraduate diploma in Engineering of Casting and Metal Forming Processes from the Silesian University of Technology. He earned his PhD from the Faculty of Mechanical Engineering and Aeronautics at Rzeszów University of Technology, where his doctoral research focused on modeling quenching distortion during high-pressure gas quenching of gears made of Pyrowear 53 steel, designed for aerospace transmission applications. In his professional role, Dr. Iżowski has led projects addressing critical industry challenges, such as enhancing the durability of aerospace components, reducing material waste in forging operations, and optimizing heat treatment cycles for high-performance steels. He has successfully developed customized material and process models, implemented predictive tools for distortion and residual stress control, and contributed to the adoption of novel alloys and heat treatment methods for aerospace applications. Dr. Iżowski is a trusted consultant for companies seeking to improve operational

workflows through numerical analysis, simulation-driven process optimizations, and tailored engineering solutions. His efforts have been instrumental in improving production efficiency, material performance, and product quality across various manufacturing sectors.

Cristian Ciobanu, Department of Mechanical Engineering and in the Materials Science Program at Colorado School of Mines, US

Cristian V. Ciobanu is a Professor in the Department of Mechanical Engineering and in the Materials Science Program at Colorado School of Mines. Prior to joining the School of Mines in 2004, he was a postdoctoral fellow in the Division of Engineering at Brown University (2001-2004). He holds degrees in Physics from University of Bucharest (B. Sc., 1995) and Ohio State University (M.S., 1998 and Ph.D., 2001). His research interests are in computational materials science and mechanics, specifically in structure-property relationships, nanoscale/nanomaterials problems, two-dimensional materials, materials for renewable energy applications, developments of evolutionary algorithms for computational materials design and optimization of atomic structures, self-organized nano and bio structures on crystal surfaces, among others. His research work in these areas has led to over 100 journal articles, two patents, and a book. Prof. Ciobanu is the current Chair of the Rocky Mountain Chapter of the American Vacuum Society, Fellow of the Royal Society of Chemistry, Fellow of the Institute of Physics; he is also a lifetime member of the American Physical Society (APS) and The Mineral, Metals and Materials Society (TMS). In addition to his teaching and research, Dr. Ciobanu carries out significant professional service in various editorial capacities for several journals (Materials Letters, Chinese Journal of Physics, Metals, Philosophical Magazine Letters, Materials Research Express), as well as technical paper and proposal reviewer and session chair/organizer for certain professional conferences.

Sebastian Pfaller, Institute of Applied Mechanics, Friedrich-Alexander-Universität Erlangen-Nürnberg, Germany

Sebastian Pfaller is a university lecturer at Friedrich-Alexander-Universität Erlangen-Nürnberg (FAU). He achieved is doctorate (degree Dr.-Ing.) in 2015 with the doctoral thesis entitled „Multiscale Simulation of Polymers". He habilitated on „Discrete and Continuous Methods for Modelling and Simulation of Polymeric Materials" in 2021 and is head of the Capriccio group, which he established at the Institute of Applied Mechanics at FAU. His research interests comprise interdisciplinary and scale bridging simulations and their applications. This includes particle-based descriptions at atomistic and molecular resolution, material characterisation and development of continuum mechanical constitutive laws, which forms the basis for multiscale description of deformation and failure processes in various kinds of amorphous materials like polymers and inorganic glasses as well as the understanding of interphases and interfaces in composites. He has acquired various third-party funding, among others for projects in the interdisciplinary research training group "Fracture across Scales" and in the collaborative international research project "BIO ART" on bio-sourced polymers. Following his strong interdisciplinary interests, he has collaborations with national and international experts from chemistry, physics, mathematics, materials science,

and engineering science, is (co-)organiser of various (mini)symposia at international conferences, and is active as reviewer for international funding agencies as well as scientific journals. Sebastian Pfaller will present current research results on fracture simulations of amorphous materials like inorganic glasses and polymers. In this context, he will introduce the Capriccio method as a concurrent technique to couple a continuum to particle-based regions, which has been designed for amorphous thermoplastics and is also applied to thermosetting polymers and silica glasses. He will discuss current achievements with regard to its capabilities for quantitative predictions of fracture mechanical quantities as well as challenges in view of length and time scales involved in such simulations.

Sergio Rojas Hernandez,
School of Mathematics, Monash University

Dr. Sergio Rojas is a Senior Lecturer in the Applied and Computational Mathematics section of the School of Mathematics at Monash University, Australia. His research focuses on numerical analysis, scientific computing, and mathematical modeling, with emphasis on developing and analyzing residual minimization-based numerical methods for solving complex Partial Differential Equations. These methodologies integrate state-of-the-art approaches such as Finite Element, Discontinuous Galerkin, Hybridizable Discontinuous Galerkin, Minimum-Residual, and Variational Physics-Informed Neural Networks methods. Before joining Monash, Dr. Rojas was a Lecturer at Pontificia Universidad Católica de Valparaíso (PUCV), Chile, and a Research Associate at Curtin University, Australia. He earned his PhD and MSc in Engineering Sciences from Pontificia Universidad Católica de Chile, where he specialized in analytical and semi-analytical methods for electromagnetic problems. Additionally, he holds a Master's in Mathematics from the University of Pavia, Italy, and a Bachelor's in Mathematics from PUCV.

In early 2024, we introduced RVPINNs, a robust extension of the Variational Physics-Informed Neural Networks (VPINNs) method. In RVPINNs, the loss functional is formulated using a Petrov-Galerkin-type variational approach, where the trial space consists of a (Deep) Neural Network and the test space is a finite-dimensional vector space. Unlike standard VPINNs, RVPINNs minimise a loss based on the discrete dual norm of the residual, providing a reliable estimator of the approximation error in the energy norm under the assumption of a local Fortin operator. This ensures more accurate approximations of the partial differential equations governing experimental data. However, a key challenge of RVPINNs is the need to invert a Gram matrix at each Neural Network nonlinear solver step, making the method computationally expensive if the variational formulation and discrete test space are not carefully selected.

In this talk, we will present recent advances in RVPINNs, focusing on adaptive strategies for test space selection and variational formulations that enable the construction of block-diagonal Gram-matrices, significantly accelerating training while maintaining accuracy. We will also demonstrate the effectiveness and robustness of our approach through tailored numerical experiments, confirming theoretical error estimates and highlighting substantial improvements in computational efficiency.

Plenary lectures

Monday, *Pieno room*

9:00 Numerical predictions of fracture in amorphous materials: Current achievements and challenges
Sebastian Pfaller

13:00 Recent Advances in Robust Variational Physics-Informed Neural Networks
Sergio Rojas Hernandez

Tuesday, *Pieno room*

14:00 Forays in Functional High-Entropy Ceramic Materials
Cristian Ciobanu

14:40 Data-Driven Deep Learning Evolutionary Algorithm EvoDN2: Development and Applications
Nirupam Chakraborti

Wednesday, *Pieno room*

9:20 Modeling and Numerical Simulation of the Gas Quenching Process of Pyrowear 53 Steel Gears
Bartosz Izowski

QR codes lead to pdf files containing extended abstracts. Applications capable to read QR codes can be found in Google Play (for Android) or Apple App Store (for IOS).

Industrial lectures

Monday, *Pieno room*

9:40 The simulation-driven automated process design for forging, rolling and extrusion
Nikolay Biba, Micas Simulations Limited trading as QForm UK

13:40 Virtual Experimentation in Continuous Casting Using ‚MAGMA CC for Steel' Simulation Tool
Ryszard Skoczylas, KomOdlew

Wednesday, *Pieno room*

10:00 Development of nondestructive online investigation system with software controlling high frequency induction welding machine on the basis of an analysis of linear weld mechanical properties *
Robert Chrzan, Stalprodukt

* This activity has received funding from the European Union from the European Regional Development Fund under the Intelligent Development Operational Program, the National Centre for Research and Development: POIR.01.02.00-00-0091/19.

Modelling of processes and materials

Monday morning, *Pieno room*

10:00 Development of advanced Zn–Al–Mg coatings using thermodynamic calculations and physical simulation
Roman Kuziak, Krzysztof Radwański, Krzysztof Oleś, Krzysztof Kwapisz

10:20 The design of thermomechanical processing of non-eqiatomic FeMnNiCoMo high entropy alloy for critical applications based on CALPHAD and ab-inito calculations
Krzysztof Muszka, Kamil Cichocki, Paulina Lisiecka-Graca, Piotr Bala, Lutz Krüger, Sebastian Henschel

10:40 Rheological Characterization of Heterogeneous Materials After Severe Plastic Deformation
Marcin Kwiecień, Krzysztof Bzowski, Bartłomiej Pabich, Szymon Bajda, Janusz Majta

11:00 Enhanced metal flow control through targeted surface treatment of additively manufactured metal forming dies
Artem Alimov, Alexander Sviridov, Sergej Dubinin, Felix Jensch, Sebastian Härtel

11:20 Multiscale numerical approach for cold levelling process based on digital material representation
Konrad Perzyński, Kamil Pyżyński, Sebastian Świerczyński, Janusz Kliś, Krzysztof Radwański, Roman Kuziak, Łukasz Madej

11:40 Design and Implementation of a digital Infrastructure for autonomous Open-Die Forging
Roy Rechenberg, Grzegorz Korpala, Magdalena Jabłońska, Marek Wojtaszek, Krystian Zyguła, Marek Tkocz, Iwona Bednarczyk, Karolina Kowalczyk, Ulrich Prahl

Artificial intelligence and machine learnings

Monday morning, *Luna room*

10:00 Deep Learning-Based Analysis of High-Temperature Microstructure Dynamics with Experimental Soap Bubble Models
Grzegorz Korpala, Krzysztof Bzowski, Łukasz Rauch, Ulrich Prah

10:20 The Role of Machine Learning in Metal Forming Technology: Microstructure Evolution, Heat Transfer Coefficient Determination and Flow Stress Modelling
Nikolay Biba, Olga Bylya, Denis Tretyakov, Artur Gartvig, Andrey Shitikov, Abhilash Puthanveettil Madathil, Aleksey Reshetov, Andrew Sherlock, Sergey Stebunov

10:40 Multi-Aspect modeling in bainite microstructure recognition on steel products images based on supervising unsupervised learning
Tomasz Jażdżewski, Filip Hallo, Grzegorz Korpała, Krzysztof Regulski

11:00 Explainable Artificial Intelligence (XAI) methods and their practical use in the heavy industry sector *
Wojciech Jędrysik, Piotr Hajder, Lukasz Rauch

11:20 Industry 4.0 technologies in designing of monitoring systems **
Jakub Michalik, Marcin Hojny, Danuta Szeliga

11:40 Development of a prediction model for the phases fraction in the microstructure of compacted graphite iron (CGI) using machine learning techniques
Sandra Gajoch, Łukasz Marcjan, Michał Zmarły, Dorota Wilk-Kołodziejczyk, Grzegorz Gumienny

(*, **) This activity has received funding from the European Union from the European Regional Development Fund under the Intelligent Development Operational Program, the National Centre for Research and Development:
* POIR.01.01.01-00-0996/19, ** POIR.01.01.01-00-0031/21.

Advanced modelling of rolling processes

Monday afternoon I, *Pieno room*

14:00 Investigating Alligator and Edge Crack Formation in High-Silicon Grain-Oriented Electrical Steel During Cold Rolling
Vipul Jain, Abhijit Ghosh, Chandan Halder

14:20 Influence of last deformations during thermo-mechanical rolling on the impact toughness of flat bars
Natalia Wolańska, Michał Piwowarczyk, Roman Kuziak, Valery Pidvysots'kyy, Łukasz Poloczek, Krzysztof Rodwański

14:40 Thermomechanical simulations of a hot rolling process of DP600 steel
Tomasz Kaźmierski, Kamil Cichocki, Janusz Krawczyk, Łukasz Frocisz

15:00 Applying numerical methods to analyse the problem of rolling TRB strips
Bartosz Sułek, Janusz Krawczyk

15:20 Microstructure formation during hot rolling of high-silicon steels for the manufacture of grain oriented electrical sheets
Kamila Ścibisz, Janusz Krawczyk, Piotr Matusiewicz, Karolina Wójciak

15:40 Strengthening response to changes in the microstructure of β titanium alloy
Janusz Krawczyk, Łukasz Frocisz

Atomic and micro scale simulations

Monday afternoon I, *Luna room*

14:00 Modeling of particles pushing and engulfment by solidification front using a cellular automaton model
Andriy Burbelko, Ewa Olejnik, Pawel Kurtyka

14:20 Investigation of Nitrogen-Doped Amorphous Carbon Nanofilms on Magnesium Alloys: A Study of Chemical Characteristics, Microstructural Analysis, Corrosion Behavior, and Biocompatibility
Adarsh Rai, Michal Krzyzanowski, Szymon Bajda

14:40 Atomistic Simulation of Grain Boundary Segregation and its Migration in Aluminium-Magnesium Alloy
Ranesh Kumar Saha, Amlan Dutta

15:00 Electronic, Optical and Water-splitting Properties of Rare Earth Single-atom Catalysts Supported on g-C3N¬4 Monolayer: A DFT study
Tarun Kumar Kundu, Ranjini Sarkar

15:20 Boron-phosphorus dual doped hard carbon anode for sodium-ion battery
Sanchayan Mahato, Koushik Biswas

15:40 The effect of composition on local structure formation in BMGs
Debopriyo Banerjee, Amlan Dutta

Application of numerical methods in medicine

Monday afternoon II, *Pieno room*

16:20 Blood Flow Simulations by Lattice Boltzmann Method
Robert Straka

16:40 Design of minimally invasive implatological kit for thoratic defects using advanced computational approach
Alicja Turek-Kozik, Bartosz Czarnecki, Laura Gołąbek, Jerzy Dybich, Wojciech Korlacki, Joanna Sulej-Chojnacka, Daniel Andrzejewski, Agata Kuliberda, Andrij Milenin, Piotr Kustra, Marek Paćko, Konrad Perzyński, Mateusz Sitko, Marcin Kwiecień, Piotr Bała, Łukasz Madej, Krzysztof Muszka

17:00 Effect of a New Dieless Drawing Process on the Properties of Biodegradable Zn-Mg Alloy Surgical Wire
Marcin Kapusta, Piotr Kustra, Anna Osyczka, Andrij Milenin

17:20 An MCDM Framework for Occupational Safety and Health Management in the Sugarcane Farming
Sumit Kumar, Millie Pant

17:40 Numerical modelling of thin-layer PLD sputtering using the COMSOL Multiphysics numerical package
Bartłomiej Kopecki, Konrad Perzyński, Łukasz Madej

18:00 An attempt of application of Bayesian Optimization approach to modelling of materials processing
Jan Kusiak

Physical Informed Neural Networks

Monday afternoon II, *Luna room*

16:20 Modelling of dynamic processes using Artificial Neural Networks
Łukasz Sztangret, Paweł Maczuga, Danuta Szeliga, Maciej Paszyński

16:40 Fast simulations using exponential integrators and finite difference method
Magdalena Pabisz, Askold Vilkha, Maciej Paszyński

17:00 Application of the Robust Variational Physics-Informed Neural Networks augmented with the Collocation Method for stationary Stokes equations
Marcin Łoś, Tomasz Służalec, Paweł Maczuga, Askold Vilkha, Carlos Uriarte, Maciej Paszyński

17:20 Speeding up the Robust Variational Physics Informed Neural Networks with the Collocation Method
Marcin Łoś, Tomasz Służalec, Paweł Maczuga, Askold Vilkha, Danuta Szeliga, Maciej Paszyński

17:40 CO2 sequestration problem implementation in the IGA-ADS software
Askold Vilkha, Maciej Paszyński, Marcin Łoś

18:00 Technological challenges in developing a self-forming thread design for electric car components
Tomasz Lorenc, Paweł Paćko, Łukasz Rauch, Marek Paćko, Stanisław Węglarczyk

Numerical modeling of modern materials

Tuesday afternoon, *Pieno room*

15:40 Modelling of temperature change during dynamic deformation of TWIP steel
Zbigniew Gronostajski, Katarzyna Jasiak, Michał Kostka, Mateusz Wesołowski, Magdalena Barbara Jabłońska

16:00 Numerical simulation of precipitates evolution during solidification and ageing of Super 304H steel
Roman Kuziak, Adam Zieliński, Hanna Purzyńska, Łukasz Poloczek

16:20 Defect-Influenced Plasticity and Deformation Mechanisms in Ni-Based High Entropy Alloys under Nanoindentations
Francisco Dominguez Gutierrez, Edyta Wyszkowska, Gordana Markovic, Marie Landeiro Dos Reis, Amil Aligayev, Damian Kalita, Krzysztof Muszka, Lukasz Kurpaska

16:40 Corrosion Behaviour of Silicon Steel Prepared with Recycled Steel Scrap After 24-Hour Immersion in 3.5 wt.% NaCl Solution
Adarsh Rai, Mirosław Karbowniczek, Pradeep Padhamnath

Digital Twins and Big Data applications

Tuesday afternoon, *Luna room*

15:40 Digital Twin for temperature prediction in the laser hardening process of NC10 steel
Piotr Lacki, Anna Derlatka, Michał Lacki, Kuba Lachs

16:00 Challenges in Processing of High Integrity Aerospace Alloys
Brad Wynne, Salah Rahimi

16:20 Cyber Physical System in welding industry – data management and analysis challenges *
Krzysztof Bzowski, Krzysztof Regulski, Monika Pernach, Lukasz Rauch

16:40 The Kalman Filter as a state estimation method based on measurement data from hardware sensors
Andrzej Opaliński, Maciej Urbański, Kacper Bielak

* This activity has received funding from the European Union from the European Regional Development Fund under the Intelligent Development Operational Program, the National Centre for Research and Development: POIR.01.02.00-00-0091/19.

Advanced numerical models and techniques

Wednesday morning, *Pieno room*

10:40 The Impact of FPV Drone Frame Materials on Motor Thermal Conditions: Experimental and Numerical Analysis
Andrij Milenin

11:00 Efficient Aerodynamic Wing Load Discretization for Static Structural Testing Using Optimization and Machine Learning
Javed Arshad Butt, Florian Dexl, Johannes Markmiller

11:20 Application of the SSRVE method to evaluate the uncertainty of microstructure properties of steels after cooling
Krzysztof Bzowski, Danuta Szeliga, Łukasz Rauch, Maciej Pietrzyk, Roman Kuziak, Władysław Zalecki

Discrete and coupled modelling

Wednesday morning, *Luna room*

10:40 Discrete element model for coupled thermal and electrical phenomena in spark plasma sintering
Fatima Nisar, Jerzy Rojek, Szymon Nosewicz, Marcin Chmielewski, Kamil Kaszyca

11:00 A DEM model to analyse granular material compaction process
Hanna Sadłowska, Andrzej Kochański, Joanna Wiącek, Rafał Kobyłka, Robert Biernacki, Artur Soroczyński

11:20 Influence of the pseudo-random number generators on the determination of grain growth driving force in full-field discrete modelling approach
Mateusz Sitko, Łukasz Madej

11:40 Evaluation of deformation inhomogeneity in multilayered steel-titanium systems
Bartłomiej Pabich, Bartłomiej Żurowski, Janusz Majta, Łukasz Madej

Development of advanced Zn–Al–Mg coatings using thermodynamic calculations and physical simulation

Roman Kuziak[1], Krysztof Radwański[1], Krzysztof Oleś[2], Krzysztof Kwapisz[2],
[1] Sieć Badawcza Łukasiewicz Górnośląski Instytut Technologiczny
K. Miarki 12-14, 44-100 Gliwice, Poland
[2] ArcelorMittal Poland S.A. Metalowców 5, 41-600 Świętochłowice, Poland
romankuziak@git.lukasiewicz.gov.pl,
krzysztof.radwanski@git.lukasiewicz.gov.pl,
Krzysztof.Oles@arcelormittal.com,
Krzysztof.Kwapisz@arcelormittal.com

A growing applicability of galvanized products has increased the demand for improved corrosion-resistant coatings to counter severe environments conditions. Among these, Zn–Mg–Al ternary alloys coatings have excellent corrosion resistance, resulting in their commercialization and substantial industrial demand. However, to increase the performance of the coatings, their composition and Hot Dip Galvanizing (HDG) parameters should be optimised. For enhancing the coatings properties, the analysis of the solidification process was performed using the thermodynamic calculations. The calculations were performed with ThermoCalc software that is an integrated computational tool based on the CALPHAD method [1]. Studies on the corrosion resistance of the Zn--Al-Mg coatings show that already at 0.5% Mg, the corrosion resistance of the zinc-based coating increases significantly as compared to the zinc-only coating [2]. Therefore, it was assumed that the content of this element in experimental coatings will be close to 0.5%. In addition, according to the literature, it was assumed that the formation of the eutectic FCC_A1 + HCP_ZN + LAVES_C1 in the coating will have a positive effect on the corrosion resistance [3].

Example of the performed calculations is shown in Figure1 in which the section (isopleth) of the phase diagram is presented showing the effect of temperature and Al content on the occurrence of different phases in Zn-Al-0.5%Mg system.

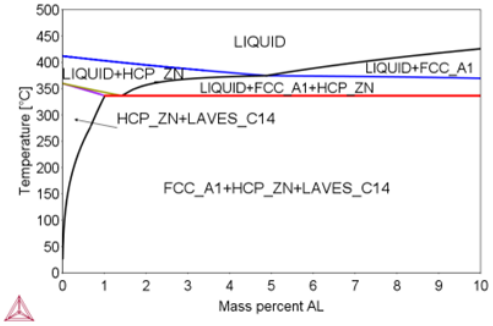

Figure 1. Calculated isopleth for the metastable equilibrium system Zn-Al-0.5%Mg

The project is co-financed by funds from the state budget, granted by the Minister of Science as part of the Excellent Science II Program, project no. KONF/SP/0109/2024/02, subsidy amount 67 870 PLN.

Figure 1 shows that when setting the Al content in the system at approximately 5 wt.% and the content of Mg at 0.5%, crystals of Al(FCC_A1) and Zn(HCP) initially separate from the liquid phase, and then the eutectic transition occurs, and as a result the triple eutectic Al(FCC_A1)/Zn(HCP)/$MgZn_2$(Laves_C14) is formed.

As a result of the thermodynamics calculations, the following ranges of the Al were defined:

- 0.5%Mg – 6.5%Al – Zn;
- 0.5%Mg – 3.0%Al – Zn.

The physical simulations of the HDG process were performed in the simulator designed at Łukasiewicz Upper Silesian Institute of Technology (Figure 2). An example of the coating's microstructure is presented in Figure 3.

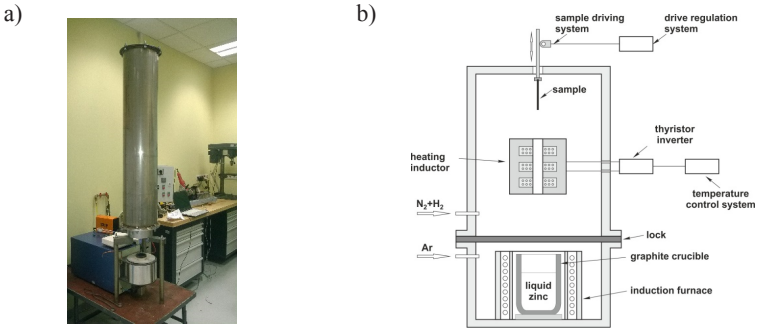

Figure 2. Simulator of HDG process: a) general view; b) schematic drawing

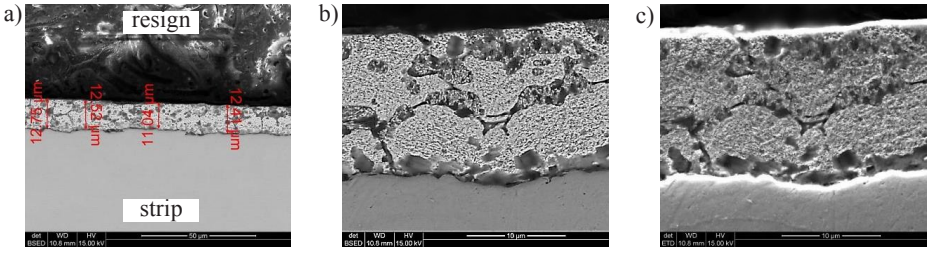

Figure 3. Example of the coating microstructure obtained in the course of the simulation of HDG process; strip and bath temperature during immersion was, respectively, 460°C and 440°C. a) thickness, b) BSE, c) SE

The microstructure investigation revealed that the coating microstructure is composed of Zn (HCP), Al(FCC), and $MgZn_2$ (Laves_C14).

The results of the investigations were implemented in the production line of ArcelorMittal Poland, Branch in Świętochłowice.

References

1. *The SGTE Casebook Thermodynamics at Work*, ed. K. Hack, The Institute of Materials, 1996.
2. S.K. Shukla, M.Depa, S. Kumar; *Effect of Mg addition (in Zinc Bath) on Galvanized Sheet Quality*, Int. Journ. Of Mat. Engineering, 2(6), 2012, 105-111.

Acknowledgements. The presented results were obtained in the course POIR.01.02.00-00-0176/16 project, entitled „Development of innovative Zn-Mg-Al coating used in the production of HDG strips" co-financed by National Centre for Research and Development.

The design of thermomechanical processing of non-eqiatomic FeMnNiCoMo high entropy alloy for critical applications based on CALPHAD and ab-inito calculations

Krzysztof Muszka[1], Kamil Cichocki[1], Paulina Lisiecka-Graca[1], Piotr Bała[1],
Lutz Krüger[2], Sebastian Henschel[2], Javier Dominguez[3]

[1] AGH University of Krakow, Faculty of Metals Engineering and Industrial Computer Science,
30 Mickiewicza Ave., 30-059 Kraków, Poland
[2] TU Bergakademie Freiberg, Institute of Materials Engineering,
Gustav-Zeuner-Str. 5, 095999 Freiberg, Sachsen, Germany
[3] National Center for Nuclear Research,
Andrzeja Sołtana St., 05-400 Otwock-Świerk. Poland
muszka@agh.edu.pl, cichocki@agh.edu.pl, graca@agh.edu.pl,
pbala@agh.edu.pl, Krueger@ww.tu-freiberg.de,
Sebastian.Henschel@iwt.tu-freiberg.de,
Javier.Dominguez@ncbj.gov.pl

Keywords: High Entropy Alloy, Ab-initio Modelling, CALPHAD Method,
Molecular Dynamics, Mechanical Response

1. Introduction

Structural materials with high impact fracture toughness, enabled by twinning mechanisms, are of significant interest for extreme-environment applications at low temperatures, such as transportation and storage of liquefied gases, cryogenic technologies, and structural components in space vehicles.

Besides the already well-known, the new class of metallic high entropy alloys (HEAs) offer new potentials for possible applications up to extreme loading conditions [1-2]. High-entropy effects, including the „cocktail effect" and sluggish diffusion, offer additional potential advantages i.e. excellent combination of strength and ductility. In the present work, the numerical tools were employed to design (FeMnNiCo)1-xMox alloy where x=<0-10>. The special focus was put on assessment of the effect of Mo addition on the Stacking Fault Energy (SFE), strength and susceptibility to twinning at room and cryogenic temperatures.

2. Materials and procedures

The development of a stable (FeMnNiCo)1-xMox high entropy alloy (HEA) with a Face-Centered-Cubic (FCC) solid solution was investigated using a combination of basic parameter calculations, CALPHAD, Density Functional Theory (DFT), and Molecular Dynamics (MD) simulations to explore plastic deformation in the studied systems. This methodology is valuable for predicting the properties of new alloys or modifying existing ones.

To achieve a single-phase solid solution, multicomponent alloys must satisfy specific criteria. A critical requirement is achieving a sufficiently high mixing entropy, greater than 1.5R (where R is the gas constant). Other important parameters include mixing enthalpy and the Valence Electron

The project is co-financed by funds from the state budget, granted by the Minister of Science as part of the Excellent Science II Program, project no. KONF/SP/0109/2024/02, subsidy amount 67 870 PLN.

Doskonała Nauka II
Ministry of Science and Higher Education
Republic of Poland
Republic of Poland

Concentration (VEC). This study examines these parameters in detail, using them to determine the phase composition of the studied HEAs in the initial design phase. Model alloys from the $(FeMnNiCo)_{100-90}(Mo)_{0-10}$ system were produced using an arc furnace, and phase composition was analysed through microstructural and X-ray diffraction (XRD) techniques. The (FeMnNiCo)90Mo10 alloy was found to contain molybdenum-rich μ-phase precipitates, while the other alloys exhibited stable solid solutions in the RSC lattice. The alloys were hot rolled, followed by microstructural analysis, and tensile and compressive test specimens were prepared for mechanical property evaluation. Basic parameter-based design proved insufficient for establishing clear correlations between thermodynamic functions and material structure. Therefore, the CALPHAD method was employed, with thermodynamic calculations performed using Thermo-Calc software and the TCHEA-5.4 database for high entropy alloys. However, results were imprecise, particularly regarding the identification and extent of precipitates. To refine phase stability predictions, DFT calculations were employed, enabling insights into phase stability as a function of temperature, without experimental data. DFT also predicted mechanical properties such as elasticity tensor, Young's modulus, shear modulus, and thermodynamic properties like specific heat, offering valuable insights into material behaviour before production [3]. Molecular dynamics simulations were conducted using Lennard-Jones potentials, as no existing potentials for these alloys were available. While simple potentials like Lennard-Jones provide a general understanding of material properties, more sophisticated potentials are required for accurate property predictions. In this work, Embedded Atom Model (EAM) potentials, enhanced with Ziegler-Biersack--Littmark (ZBL) corrections, were used in LAMMPS software. These simulations revealed that molybdenum addition reduces stacking fault energy (SFE), promoting deformation via twinning, which was a key objective of the study.

Experimental studies on plastic deformation followed, including compression tests at hot plastic working temperatures using an ASP thermomechanical simulator. These results were used to design hot-forming processes by analysing stress-strain curves and dynamic recrystallization kinetics. Further tests on cold-rolled alloys with varying degrees of deformation were conducted, including microstructural and texture evolution analysis, which showed strain twinning and characteristic texture formation. The final phase involved evaluating mechanical properties at room temperature and liquid nitrogen temperatures, with compression tests conducted at various strain rates, from quasi-static to dynamic. Microstructural, texture, and XRD analyses confirmed that molybdenum enhances the material's tendency to deform via twinning.

This study provides valuable insights into the FeMnNiCoMo high entropy alloy system's potential in modern materials engineering. The computational and experimental results offer a deeper understanding of the thermodynamics, microstructure, and mechanical properties of high--entropy alloys, highlighting the challenges in HEA design. The addition of molybdenum improves strength properties with minimal impact on ductility and promotes twinning deformation. Cryogenic strength tests indicate that these Mo alloys are suitable for low-temperature applications, even under dynamic loading conditions.

References

1. Grässel O.; Krüger L.; Frommeyer G.; Meyer L. W.: *High strength Fe-Mn-(Al, Si) TRIP/TWIP steels development – properties – application*, International Journal of Plasticity, 16, 2000, 1391–1409.
2. Cantor B., Chang I.T.H., Knight P., Vincent A.J.B., *Microstructural development in equiatomic multicomponent alloys*, Materials Science & Engineering A, 375–377, 2004, 213–18.
3. Cichocki, K., Bała, P., Koziel, T. et al., *Effect of Mo on Phase Stability and Properties in FeMnNiCo High-Entropy Alloys*, Metallurgical and Materials Transactions A, 53, 2022, 1749–1760.

Acknowledgements. The authors acknowledge the research project supported by the program "Excellence initiative—research university" for the AGH University of Science and Technology.

Rheological Characterization of Heterogeneous Materials After Severe Plastic Deformation

Marcin Kwiecień, Krzysztof Bzowski, Bartłomiej Pabich,
Szymon Bajda, Janusz Majta
AGH University of Krakow al. Adama Mickiewicza 30
30-059 Kraków, Poland
mkwiecie@agh.edu.pl, kbzowski@agh.edu.pl, bpabich@agh.edu.pl,
bajda@agh.edu.pl Janusz.majta@gmail.com

Keywords: heterostructured materials, multilayered composite, multi-stage wire drawing, numerical simulation

1. Abstract

Metal-to-metal composite systems are gaining popularity due to their ability to achieve an optimal balance between strength and ductility. Their main advantages lie in two key aspects:

a) Properties Synergy – These composites integrate the distinct mechanical and physical properties of their individual metal components, resulting in a material with enhanced performance tailored to specific engineering needs;
b) Efficient Implementation – A deep understanding of their mechanical behavior reduces the need for extensive testing and preliminary studies before industrial application. This is particularly beneficial for structural components where safety is a critical factor, as it accelerates the adoption of new materials while maintaining reliability [1,2].

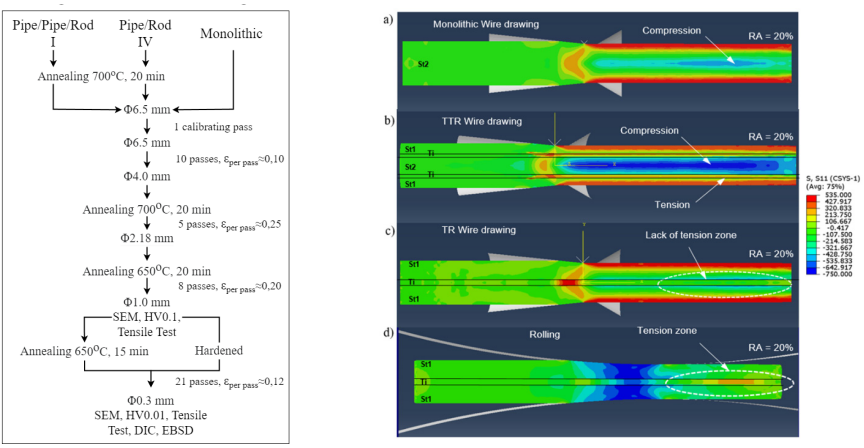

Figure 1. An example of numerical simulation results of wire drawing for the Pipe/Pipe/Rod specimen, using data from Abaqus and data from inverse analysis. a, b) Stress intensity; c, d) Stress in the X direction; e, f) Strain intensity

The project is co-financed by funds from the state budget, granted by the Minister of Science as part of the Excellent Science II Program, project no. KONF/SP/0109/2024/02, subsidy amount 67 870 PLN.

Doskonała Nauka II
Ministry of Science and Higher Education
Republic of Poland
Republic of Poland

The rheological behavior of heterogeneous materials subjected to Severe Plastic Deformation (SPD) is crucial for understanding their mechanical response and potential industrial applications. This study investigates the effect of SPD on the flow properties, microstructural evolution, and strain-induced mechanisms in heterogeneous metallic and composite systems. The results reveal significant grain refinement, enhanced strain hardening, and improved ductility, contributing to superior mechanical performance. Additionally, the study highlights the role of phase distribution and interfacial interactions in governing the flow characteristics of these materials. The findings provide insights into optimizing SPD-processed heterogeneous materials for advanced structural and functional applications.

In this work, the heterostructure materials, after undergoing caliber rolling and wire drawing processes, were subjected to mechanical property analysis based on the uniaxial tensile test. The history of the applied deformation process is presented in Figure 1.

2. Inverse analysis

The presented study focuses on a methodology for identifying material parameters based on the inverse method, using a uniaxial tensile test. A method for converting experimental data from a force-displacement relationship to a true stress-strain relationship is presented, accounting for corrections resulting from changes in the specimen's cross-section during the test. Particular attention is given to the process of approximating the parameters of the Hollomon constitutive equation, which is widely used in numerical simulations of plastic forming processes. The developed procedure includes the automation of the strengthening curve fitting process using the non-linear regression method, allowing for precise determination of the strengthening coefficient K and the strengthening exponent n. A method for validating the obtained parameters by comparing the numerical simulation results with experimental data is also presented. The proposed approach enables efficient identification of material parameters necessary for reliable numerical simulations. Based on the obtained stress-strain curves the anaylsis of the multi-stage drawing process of multilayered systems was performed. The results are presentd in the Figure 2.

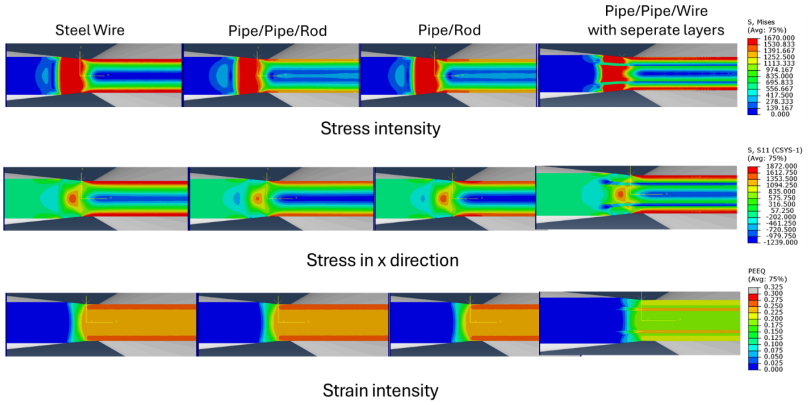

Figure 2. An example of numerical simulation results of the longitudinal stress distribution during the processes of wire drawing of Steel Wire, Pipe/Pie/Rod, Pipe/Rod system based on inverse analysis

The results obtained from the application of stress-strain curves derived using the inverse method show that the strain and stress distributions in the wires after the drawing process vary depending on the system. In the case of the Pipe/Pipe/Rod system, tension occurs in the Ti pipe in

the initial material, while in the Pipe/Rod system, only compression is observed in the Ti rod. The situation changes when the materials acquire new rheological properties after microstructure development. Based on these observations, it can be assumed that the Pipe/Pipe/Rod system behaves similarly to the rolling process, offering the potential to achieve the expected fragmentation of Ti layers, but only in the initial stages of wire drawing.

References

1. Wu X.L., Zhu Y.T., "*Heterogeneous materials: a new class of materials with unprecedented mechanical properties*". Mater Res Lett. 5, 2017, 527–532.
2. Majta J., Kwiecień M., Lisiecka-Graca P., Bloniarz R., Kopytek E., Muszka K., *Precipitation -based Strengthening Mechanisms in Ultrafine-grained and Nano-Structures in Microalloyed Steel Wires*, 11th International Conference on Advanced Computational Engineering and Experimenting ACE-X, Vienna, 2017.

Acknowledgements. OPUS.: The research was funded in whole by National Science Centre, Poland Grant number: 2022/45/B/ST8/01383.

Enhanced metal flow control through targeted surface treatment of additively manufactured metal forming dies

Artem Alimov, Alexander Sviridov, Sergej Dubinin,
Felix Jensch, Sebastian Härtel
[1] Chair of Hybrid Manufacturing, Brandenburg University of Technology Cottbus-Senftenberg, Cottbus, Germany
alimov@b-tu.de, sviridov@b-tu.de, dubinser@b-tu.de, jensch@b-tu.de, sebastian.haertel@b-tu.de

Keywords: metal forming, metal flow control, targeted surface treatment, additively manufactured dies, simulation

1. Introduction

Metal flow during metal forming has a great influence on the quality of produced parts. In bulk forging, improper metal flow causes defects like folds or laps, may lead to underfilling of the die cavities [1], and also reduces the mechanical properties due to the formation of specific unfavorable grain flow patterns. Proper metal flow is also important in sheet metal forming to produce defect--free parts. For example, incorrect die or blank geometry, blank holder pressure, lubricant or process parameters can lead to wrinkling, unacceptable thinning, or even tearing of the workpiece [2].

Friction is one of the most effective tools to control the metal flow. For example, in bulk forming, using a lubricant can significantly reduce friction on the active die surfaces and ensure that deep die cavities are properly filled [3]. On the other hand, higher friction at the flash land, due to its design (Figure 1), increases the resistance of the metal flow from the die cavity and promotes the completion of hard-to-fill cavities [4]. In sheet metal forming, localized braking grooves are widely used for metal flow control to increase the resistance to metal flow targeted and to prevent defect formation. Therefore, controlling the friction between the workpiece and the die surface can effectively control the metal flow.

Figure 1. Die flash design

One of the promising trends in die making is the additive manufacturing of sheet metal [5] and hot bulk forming dies [6], which enables the production of high-quality die inserts requiring minimal post-machining in the shortest time. For example, previously we have produced and successfully proven (Figure 2) lightweight die inserts with internal lattice structure made of 17-4PH maraging steel [7], [8] as well as die inserts made of Inconel 718 nickel alloy (pending publication) for turbine blade forging.

The project is co-financed by funds from the state budget, granted by the Minister of Science as part of the Excellent Science II Program, project no. KONF/SP/0109/2024/02, subsidy amount 67 870 PLN.

Doskonała Nauka II
Ministry of Science and Higher Education Republic of Poland
Republic of Poland

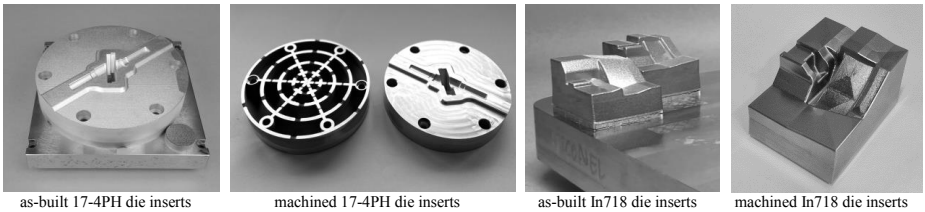

as-built 17-4PH die inserts | machined 17-4PH die inserts | as-built In718 die inserts | machined In718 die inserts

Figure 2. Additive-manufactured hot metal forming die inserts

One of the disadvantages of the additive manufacturing of metals is the low surface quality, which also depends on the surface inclination to the deposition direction, deposition strategy itself and process parameters. However, post-processing techniques, such as sandblasting and chemical or electrochemical treatment, can significantly improve surface quality. Applying these methods targeted, metal flow can be controlled by localized changes in friction.

The work aims to develop the enhanced metal flow control approach through targeted surface treatment of additively manufactured metal forming dies. The paper numerically analyses the effect of post-processing treatment on the roughness and friction conditions of the dies produced with laser powder bed fusion technology. A modified approach based on the spike test [9] allows the evaluation of not only the surface roughness and lubrication effect on metal flow and friction but also allows for the analysis of the influence of flash design and locally tailored tool surface conditions. A model considering anisotropic friction is developed and implemented in FEM Code QForm UK using a user subroutine.

2. Effect of the post-processing treatment on surface roughness and friction conditions

To investigate the effect of post-processing on surface roughness and waviness after additive manufacturing using the LPBF method, flat test dies were produced for the subsequent cold ring compression testing of D12×d6×h4 samples from EN AW 6060 with Molykote BR2 plus lubricant using a Gleeble 3500 thermomechanical simulator. The results of the investigation are presented in Figure 3. Thus, the post-processing die surface treatment allows the control of the friction and, thus, the metal flow.

Surface condition	As-built	Machined	Sandblasted	Chemically polished
Test die surface	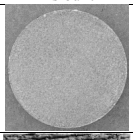	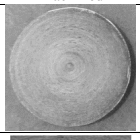	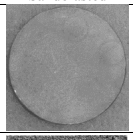	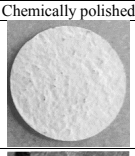
Surface topography	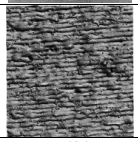	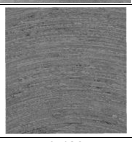	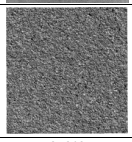	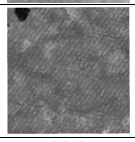
Average roughness R_a, µm	7,424	0,489	2,649	0,352
Average waviness W_a, µm	14,667	0,269	1,963	3,638
Shear friction factor m	0,61	0,19	0,63	0,32

Figure 3. Effect of surface post-processing of LPBF-manufactured dies

3. Modified spike-test

A modified approach based on the spike test, which allows us to assess not only the surface roughness and lubrication effect on metal flow and friction but also allows analyzing the influence of flash design and locally tailored tool surface conditions, has been developed. The tool geometry has been modified better to represent the metal flow pattern during closed-die forging. According to Figure 1, different flash designs could be used for the analysis. A preliminary assessment involving only critical friction factor values, as shown in Figure 4, clearly demonstrates that targeted friction tailoring can significantly change the metal flow pattern and improve the filling of deep die cavities.

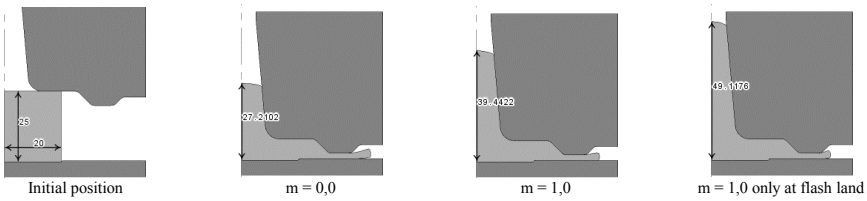

Figure 4. Simulation of the modified spike-test with different friction conditions

4. Numerical evaluation of metal flow control capabilities using targeted surface treatment in bulk and sheet forming

Metal flow control capabilities in bulk forming using a targeted surface treatment will be evaluated with modified spike test. In addition to the influence of different local surface post-processing of the metal flow, the possibility of replacing the traditional metal flow control with local flash design and size variations, as well as using braking grooves, will also be analyzed.

The potential of targeted die surface treatment to prevent defect formation and improve formability in sheet metal forming will be analyzed.

References

1. S.-W. Lee, J.-W. Jo, M.-S. Joun, and J.-M. Lee, "*Effect of Friction conditions on Material Flow in FE Analysis of Al Piston Forging Process*," Int. J. Precis. Eng. Manuf., vol. 20, no. 10, pp. 1643–1652, Oct. 2019, doi: 10.1007/s12541-019-00189-8.
2. A. Fallahiarezoodar, "*Prediction And Reduction Of Defects In Sheet Metal Forming*," PhD Thesis, The Ohio State University, 2018.
3. E. Felder and J. L. Montagu, "*Friction and wear during the hot forging of steels*," Tribology International, vol. 13, no. 2, pp. 61–68, Apr. 1980, doi: 10.1016/0301-679X(80)90011-0.
4. J. Langner, M. Stonis, and B.-A. Behrens, "*Investigation of a moveable flash gap in hot forging*," Journal of Materials Processing Technology, vol. 231, pp. 199–208, May 2016, doi: 10.1016/j.jmatprotec.2015.12.019.
5. D. Chantzis et al., "*Review on additive manufacturing of tooling for hot stamping*," Int J Adv Manuf Technol, vol. 109, no. 1–2, Art. no. 1–2, Jul. 2020, doi: 10.1007/s00170-020-05622-1.
6. D. Junker, O. Hentschel, R. Schramme, M. Schmidt, and M. Merklein, "*Performance of hot forging tools built by laser metal deposition of hot work tool steel X37CrMoV5-1,*" in Proceedings of the laser in manufacturing conference, 2017.
7. A. Alimov, A. Sviridov, B. Sydow, F. Jensch, and S. Härtel, "*Additive manufacturing of hot-forming dies using laser powder bed fusion and wire arc direct energy deposition technologies*," Metals, vol. 13, no. 11, p. 1842, 2023.

8. A. Alimov, “Fatigue life analysis of hot forming dies produced by the L-PBF and WA-DED additive technologies,” presented at the Material Forming, May 2024, pp. 2154–2163. doi: 10.21741/9781644903131-237.
9. F. Bleyl, M. Liewald, and T. Schiemann, “Spike-Test für Tribologieversuche*,” wt, vol. 102, no. 11–12, pp. 769–776, 2012, doi: 10.37544/1436-4980-2012-11-12-769.

Multiscale numerical approach for cold levelling process based on digital material representation

Konrad Perzyński[1,2], Kamil Pyżyński[2],
Sebastian Świerczyński[2], Janusz Kliś[2], Krzysztof Radwański[3],
Roman Kuziak[3], Łukasz Madej[1,2]

[1] AGH University of Krakow, Faculty of Metals Engineering and Industrial Computer Science
Mickiewicza 30 av., 30-059, Kraków, Polanda
[2] ArcelorMittal Distribution Solutions Poland Sp. z o.o.,
ul. Łowińskiego 15, 31-752 Kraków, Poland
[3] Łukasiewicz Research Network-Institute for Ferrous Metallurgy,
K. Miarki 12-14 st., 44-100 Gliwice, Poland
kperzyns@agh.edu.pl, kamil.pyzynski@arcelormittal.com,
sebastian.swierczynski@arcelormittal.com,
janusz.klis@arcelormittal.com,
Krzysztof.Radwanski@imz.pl,
roman.kuziak@git.lukasiewicz.gov.pl,
lmadej@agh.edu.pl

Keywords: levelling, RVE, FEM, Barkhausen method, multiscale modeling

1. Introduction

The ever-growing quality requirements imposed by the modern automotive, machinery, and railroad industries are compelling manufacturers to deliver components with high geometric accuracy. Precise metal forming equipment is essential to produce such components, followed by machining, plasma cutting, laser cutting, etc.

However, a significant challenge, particularly in the sheet metal forming sector, lies in the spring-back effect [1] caused by residual stresses within the deformed components. This issue poses technical complications and threatens equipment integrity, resulting in costly production line downtime. Consequently, the timely fulfilment of orders is compromised, and material as well as labour costs increase. Therefore, ensuring the quality of the initial sheet material after rolling, intended for subsequent processing operations like bending and stamping, is crucial.

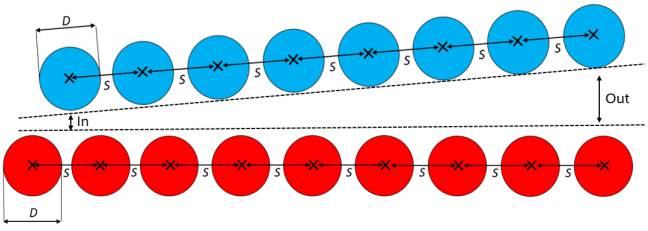

Figure 1. Concept of the work rolls setup in the leveller

The project is co-financed by funds from the state budget, granted by the Minister of Science as part of the Excellent Science II Program, project no. KONF/SP/0109/2024/02, subsidy amount 67 870 PLN.

Doskonała Nauka II
Ministry of Science and Higher Education
Republic of Poland
Republic of Poland

The usual solution to improve the sheet quality before further processing is the use of roller levelling systems [2]. The concept is based on a series of cyclic deformations induced by a set of work rolls with specific diameter D and roll spacing S (Figure 1). However, creating an optimal alignment of roller configuration to achieve flat and low residual stress sheets requires a series of industrial experiments that are expensive and time-consuming.

Therefore, providing computational support for developing technology for levelling high--strength steel sheets using a multiscale numerical modeling approach is described within the present work.

2. Multiscale levelling simulations

In the first part of the work, a user-friendly plug-in was implemented using Python for the Abaqus application to fully automate the generation of the levelling process FE models with various setups. With this approach, it was possible to execute a series of simulations to determine the range of input parameters for the leveller and identify the optimal leveller setup for a wide range of steel grades. In the next step, micro-scale digital material representation models based on the representative volume element (RVE) concept [3] were developed with the purpose of detailed analysis of the microstructure state during levelling accounting for the role of local heterogeneities. As a result, an industrial levelling process was simulated at macro and micro scales at the same time. This approach facilitates the validation of the levelling configuration's accuracy while considering the material's microscopic stress state. The concept of the simulations is presented in Figure 2.

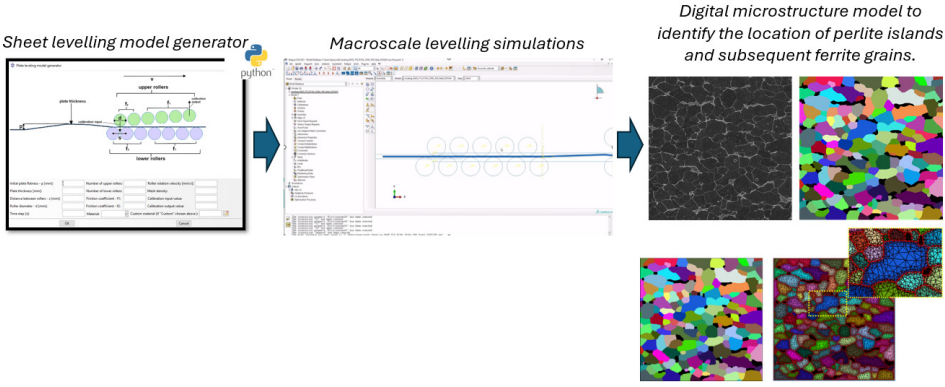

Figure 2. Concept of the multiscale simulations of the levelling process

3. Results

The exemplary results from the macro and micro scales presented in Figure 3 were additionally supplemented by residual stress measurements with the Barkhausen method [4], executed under industrial conditions.

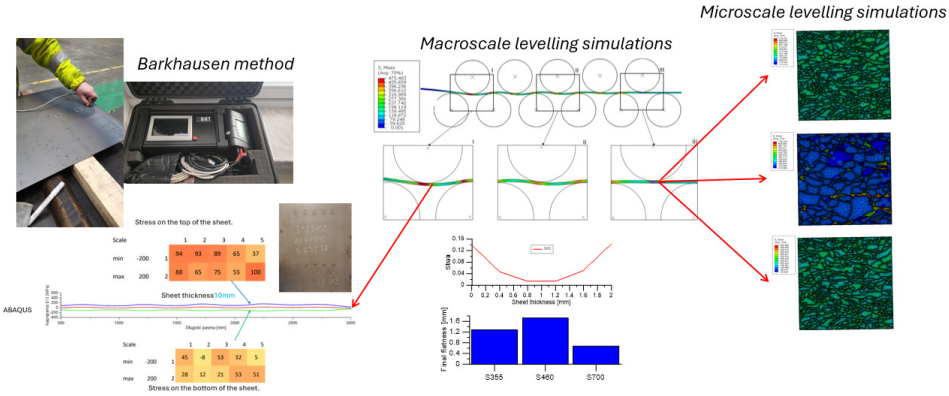

Figure 3. Exemplary results presenting multiscale levelling process simulations

References

1. Wagoner R.H., Lim H., Lee M-G., *Advanced issues in springback*. International Journal of Plasticity, 45, 2013. p. 3–20.
2. Smith R.P,, *The effect of the number of leveling rolls on the straightening process*, Iron Steel Technology, 4, 2007 p. 57–68.
3. Madej L., Cybulka P., Perzynski K., Rauch L., *Numerical analysis of strain inhomogeneities during deformation on the basis of the three dimensional digital material representation*, Computer Methods in Materials Science, 11, 2011, p. 375.
4. Frederick C.O., Armstrong P.J. *A mathematical representation of the multiaxial Bauschinger effect*. Materials at High Temperatures, 24, 2007, p. 1–26.

Acknowledgements. This research was conducted within the collaborative framework of the NCBiR project POIR.01.01.01–00-0786/18 “Innovative hybrid technology for levelling hot rolled sheets”.

Design and Implementation of a digital Infrastructure for autonomous Open-Die Forging

Roy Rechenberg[1], Grzegorz Korpala[1], Magdalena Jabłońska[2], Marek Wojtaszek[3], Krystian Zyguła[3], Marek Tkocz[4], Iwona Bednarczyk[4], Karolina Kowalczyk[5], Ulrich Prahl[1]

[1] TU Bergakademie Freiberg, Akademiestraße 6, 09599 Freiberg, Germany,
[2] Lukasiewicz Research Network – Institute of Non-Ferrous Metals, ul. Sowińskiego 5, 44-100 Gliwice, Poland,
[3] AGH University of Krakow, al. Adama Mickiewicza 30, 30-059 Kraków, Poland
[4] Silesian University of Technology, ul. Akademicka 2A, 44-100 Gliwice, Poland
[5] University of Silesia, ul. Bankowa 12, 40-007 Katowice, Poland
Roy.Rechenberg@imf.tu-freiberg.de, Grzegorz.Korpala@imf.tu-freiberg.de, magdalena.jablonska@imn.lukasiewicz.gov.pl, mwojtasz@metal.agh.edu.pl, kzygula@agh.edu.pl, marek.tkocz@polsl.pl, iwona.bednarczyk@polsl.pl, karolinakowalczyk992@gmail.com, Ulrich.Prahl@imf.tu-freiberg.de

Keywords: Automation, Forging, Open die forging

1. Introduction

Open die forging, one of the oldest metal forming technologies, remains crucial for manufacturing large components such as generator shafts and crankshafts for ship engines. Although it is mainly applied to single pieces or small production batches, the process still heavily relies on manual labour and the expertise of skilled operators. Traditional automation is impractical due to the high variability and low production volumes, which results in long manufacturing times, frequent adjustments to production plans, and challenges in maintaining consistent quality. In recent decades, there have been some attempts to automate the process using industrial robots, showcasing promising potential for innovation [1].

The process typically involves multiple reheating stages and extended production cycles, which can last days or even weeks. The quality of industrial open die forging is still highly dependent on the operator experience. Retirement of experienced staff and shift work, which is a common industrial working method, introduces variability into the complex production process. These factors make it particularly difficult to achieve consistent process stability, reproducibility, and quality - requirements that are crucial in modern manufacturing, especially with advanced materials technologies.

To address these challenges, a novel concept for autonomous forging has been developed and tested at the Institute of Metal Forming at the Technical University of Freiberg. This system integrates traditional components, such as a furnace and a forging press, with modern technologies. An industrial robot is responsible for handling workpieces, while a custom-designed 3D scanning system captures geometric data to create a digital twin of the workpiece. Thermal imaging cameras provide monitoring of the temperature profile.

The project is co-financed by funds from the state budget, granted by the Minister of Science as part of the Excellent Science II Program, project no. KONF/SP/0109/2024/02, subsidy amount 67 870 PLN.

Doskonała Nauka II
Ministry of Science and Higher Education Republic of Poland
Republic of Poland

A forging robot cell was developed to meet the basic hardware requirements for autonomous forging. The main challenge in this system was the design of a digital infrastructure to facilitate effective communication between components. In addition, modular process control software was implemented to seamlessly coordinate and operate these components, thereby replacing the role of a human operator.

The robot cell operates as a distributed system, with multiple nodes connected via a local area network (LAN). Key hardware components include a main computer as the human-machine interface, the KUKA Robot Control 2 system for controlling the manipulator, and a position sensor integrated as a web server. The press control system and three blue light line laser scanners are also configured as web servers. Three thermal imaging cameras measure temperatures between 450°C and 1800°C, with the data being accessible via USB interfaces. This combination establishes the foundation for precise, efficient, and autonomous forging operations.

The software architecture follows a modular design to ensure maintainability, facilitate error diagnostics, and enable the replacement or enhancement of individual subsystems. This flexibility is essential for adapting to different manufacturing plants with specific requirements or integrating new technologies in the future. Within the modular software architecture, multiple nodes are implemented according to the logical steps of the forging process. The basic tasks are: workpiece positioning, measuring, heating, deformation, and process planning.

To integrate the KUKA robot as a manipulator into the software architecture and make it accessible for custom process control, a third-party software called RoboDK is used. This software enables offline programming of industrial robots for path planning and process planning. Compared to conventional offline programming software, which only allows the export of programs via a postprocessor, RoboDK provides a software interface for online interaction with the robot. An additional software component was installed on the KUKA robot control system, which works as a web server and enables the exchange of system variables between the robot and the RoboDK client. This software also provides a programming interface for easy integration into custom projects, such as the forging cell. In the current automation setup, a digital twin of the forging cell is created within RoboDK, and transportation paths and programs between each component are set up and tested within this software. Due to the API and the connection to the robot control system, these transportation programs or custom motions, such as linear or joint movements, can also be executed directly from custom software.

The geometry and temperature measurement are achieved through a custom scanning system consisting of three blue light laser scanners and three thermal imaging cameras. Each sensor type is mounted in a vertical plane to measure a part of the crosssection of the workpiece, resulting in a two-dimensional dataset. To generate a three-dimensional digital twin of the workpiece, multiple cross-sectional scans along the longitudinal axis of the workpiece are taken. The scanning system is mounted on a linear actuator, which provides a measurement range of 700 mm. An additional position sensor was added to determine the current position of the scanning system and link it with the geometry and temperature data. This position monitoring is also implemented as a web server, which can be accessed by each sensor individually. The raw geometry and temperature data of the workpiece are stored on the main computer for access by the process planning tool and other use cases.

The process planning itself is designed as an independent tool that uses the geometry and temperature data to calculate a pass sequence. The output includes instructions for positioning the workpiece between the dies of the forging press or in the furnace (rotation and translation), small correction movements to compensate for any tilted gripping of the workpiece, and instructions for the press movement (dimensions). This pass sequence planning can easily be exchanged with custom pass sequence calculation algorithms, depending on the applications, production conditions or goals [2].

In the automation concept at the IMF, the forging press does not provide a native interface for

external control, and enhancing it is not straightforward. Therefore, an electromechanical device was created to interact with the human-machine interface of the forging press. This device is also designed as a web server and can provide the current position of the press or based on an instruction, the press is set to a defined gap between the dies. This device enables only displacement-controlled use of the press.

To minimize dependencies between the software modules, a Core-module has been implemented to coordinate the interaction of all software components and subsystems. This approach simplifies the process of exchanging or extending the robot cell or individual subsystems, ensuring that no other subsystems are directly impacted. In the case of a change, only the Core-module needs to be updated to accommodate the new setup, thus maintaining system flexibility and reducing the need for widespread modifications. The overall software architecture, as depicted in Figure 1, illustrates the structure and interaction of the various components within the system.

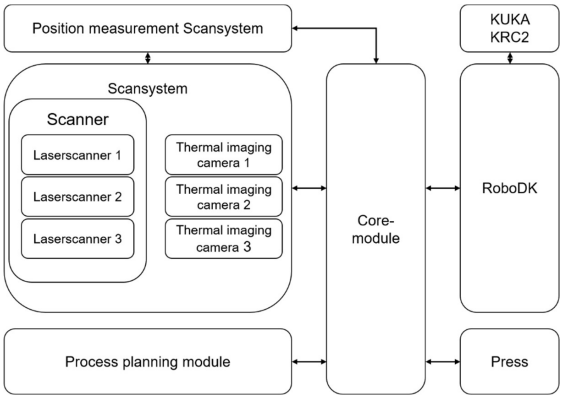

Figure 1. Software architecture of the autonomous forging concept

This approach offers a promising platform for implementing customized open die forging process controls, thereby enhancing flexibility in production. By integrating advanced technologies, it aims to improve process control, stability, and quality while addressing challenges such as workforce shortages and the increasing demands of modern material concepts. However, it is important to note that the system is still in the early stages of development. Initial trials show promising results, but further adjustments and testing are required to fully realize its potential. As development continues, the system will be refined to meet the specific needs of modern manufacturing and achieve sustainable improvements in forging operations, particularly in the context of advanced material technologies.

References

1. W. Liu, „*Adaptive control for intelligent open die forging,*“ in Proceedings of International Mechanical Engineering Congress and Exposition, Anaheim, California USA, 2004.
2. R. Rechenberg, M. Pulawski, M. Zapf, K. Grzegorz und U. Prahl, „*Adaptive calculation of pass sequences for open die forging*,“ in 29. Sächsische Fachtagung Umformtechnik. Dresden, Dresden, 2023.

Deep Learning-Based Analysis of High-Temperature Microstructure Dynamics with Experimental Soap Bubble Models

Grzegorz Korpala[1,2], Krzysztof Bzowski[3], Łukasz Rauch[3], Ulrich Prahl[1]

[1] TU Bergakademie Freiberg, Akademiestraße 6, 09599 Freiberg, Germany
[2] MiViA GmbH, Halsbrückerstraße 34, 09599 Freiberg, Germany
[3] AGH University of Krakow, al. Adama Mickiewicza 30, 30-059 Kraków, Poland
Grzegorz.Korpala@imf.tu-freiberg.de,
kbzowski@agh.edu.pl, lrauch@agh.edu.pl,
Ulrich.Prahl@imf.tu-freiberg.de

Keywords: U-Net, Microstructure, Evolution, Soap

1. Introduction

For decades, neural networks have evolved in dependence on the available computing capacity. In most cases, computations have become increasingly complex and energy-intensive. However, with the technique of transfer learning, training neural networks has become easier and faster.

Models with a large number of parameters, designed for classification or semantic segmentation (e.g., U-Net with 50 million parameters [1]), are often used to generate applications that solve relatively simple problems. In research, where such models are applied, the number of parameters is often irrelevant. However, in everyday applications, such as microstructure analysis, a lean model means faster computational response and greater energy efficiency.

This efficiency advantage was demonstrated in large language models in 2024. An intelligent restructuring of architectures, incorporating small agents capable of answering specific questions in more detail, has been shown to achieve significantly higher energy efficiency than even larger general-purpose models (DeepSeek [2]). The latter often require extensive prompt engineering to generate the desired output.

2. Image pre-processing, DCNN architecture and training

The aim of this study was to investigate whether the parameter-reduced U-Net architecture (50.000 parameters) can produce a usable analyze result. The experimental dataset consisted of video footage [3], from which individual frames were extracted for analysis. A total of 400 frames were available, but only 11 images were used for training. To mitigate the influence of changing lighting conditions on the analysis results, a preprocessing step was applied to the input data (fig. 1), converting them to grayscale followed by a Sobel filter (input: 1024×1024×2). This allowed for the detection of contrast between individual pixel pairs in the image, ensuring that the absolute pixel values no longer played a role in the analysis. Since the image resolution was 1460×1088, it allowed for multiple cropping, rotation, and mirroring to synthetically increase the number of training images and create a suitable dataset. Using this approach, 2000 images were generated for training. The training was conducted within the TensorFlow framework (see fig. 1 for architecture information) using an Adam optimizer and the Jaccard index as the cost function. The process was

The project is co-financed by funds from the state budget, granted by the Minister of Science as part of the Excellent Science II Program, project no. KONF/SP/0109/2024/02, subsidy amount 67 870 PLN.

Doskonała Nauka II
Ministry of Science and Higher Education
Republic of Poland
Republic of Poland

carried out on an NVIDIA A40 GPU, with a total training duration of 4 hours and mean square error of 0.0108 in validation data set.

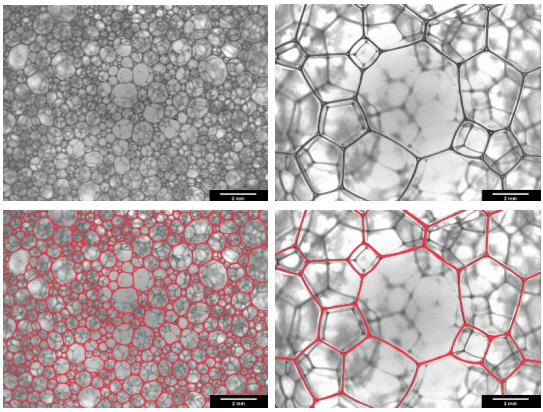

U-Net Block

- conv. 3x3
- BatchNorm.
- DropOut
- conv. 3x3
- BatchNorm.
- MaxPool. 2x2

Encoder	Decoder
Input: 1024x1024x2	Output: 1024x1024x1
512x512x9	512x512x9
256x256x16	256x256x16
128x128x23	128x128x23
64x64x30	64x64x30
32x32x36	32x32x36
16x16x43	16x16x43
8x8x50	8x8x50
4x4x57	4x4x57
2x2x64	2x2x64

Figure 1. Example of microstructure and raw mask, U-Net-Block and list of applied filter sizes

3. Results

After completing the training, the model was deployed to a cloud-based system of MiViA GmbH to enable scalable analysis. Both object detection and the measurement of individual objects were performed entirely on GPUs using TensorFlow-based image processing, which was specifically developed for this purpose. The segmented images could then be analyzed using multiple methods. In this study, results are presented using conventional planimetric measurements of individual ‚grains' and the chord length method, following the principle of the ASTM Heyn-Line Intercept method. The intercept method was significantly extended to include millions of lines, ensuring proper classification of even non-closed regions. The output results were assigned to the corresponding G-number. The data could be represented as mean values and histograms and were also compiled into a video to illustrate the dynamics of growth. The results are shown in Fig. 2, with a corresponding animation.

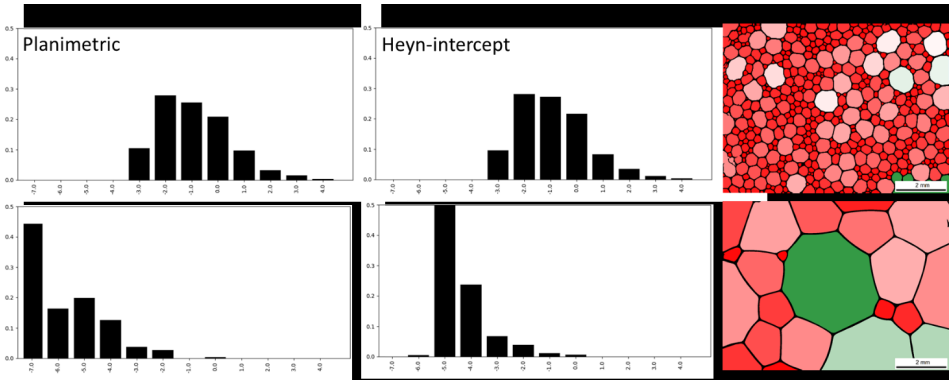

Figure 2. Postprocessed cleared segmentation with histograms

4. Summary

The presentation of measurement results as a function of time shows a typical progression of grain growth in metallic materials, despite being generated using soap bubbles. Which can be used to model the time-dependent grain growth behavior. Phenomenological and physical models can be more easily fitted in further development of evaluation systems and applied on an industrial scale for process control.

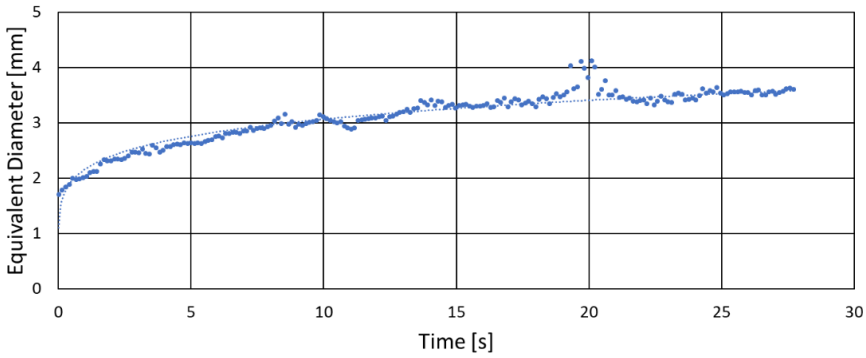

Figure 3. Average Equivalent Diameter as a Function of Time

References

1. O. Ronneberger, P. Fischer, and T. Brox, "*U-Net: Convolutional Networks for Biomedical Image Segmentation*," 2015, arXiv. doi: 10.48550/ARXIV.1505.04597.
2. DeepSeek-AI et al., "*DeepSeek-V2: A Strong, Economical, and Efficient Mixture-of-Experts Language Model*," 2024, arXiv. doi: 10.48550/ARXIV.2405.04434.
3. https://www.youtube.com/watch?v=P32ute-kyUI, acces 01.12.2024

Acknowledgements. Research project partly supported by program „Excellence initiative – research university" for the AGH University of Krakow.

The Role of Machine Learning in Metal Forming Technology: Microstructure Evolution, Heat Transfer Coefficient Determination and Flow Stress Modelling

Nikolay Biba[1], Olga Bylya[2], Denis Tretyakov[3], Artur Gartvig[3], Andrey Shitikov[3], Abhilash Puthanveettil Madathil[2], Aleksey Reshetov[2], Andrew Sherlock[2], Sergey Stebunov[3]

[1] MICAS Simulation Ltd, 107 Oxford Road, Oxford, OX4 2ER, UK
[2] National Manufacturing Research Centre, University of Strathclyde, 3 Netherton Sq, Paisley, Renfrew PA3 2EF
[3] QForm Group FZ LLC, Fujairah, UAE

nick@qform3d.com, olga.bylya@strath.ac.uk, tretyakov.denis.a@gmail.com, artur@qform3d.com, a.a.sh.ggml@gmail.com, abhilash.p-m@strath.ac.uk, aleksey.reshetov@strath.ac.uk, a.sherlock@strath.ac.uk, serg@qform3d.com

Keywords: Metals, Finite Element Modeling, Machine Learning, Microstructure Evolution, Flow Stress Curve

1. Introduction

Modern metal forming is characterised by the complexity of processes and the demand for high-quality production. Various modelling approaches are required to ensure manufacturing efficiency. However, traditional modelling has limits. Some complex phenomena are difficult to simulate accurately using methods based on simplifying assumptions and limited sets of state variables. Integrating machine learning (ML) techniques and AI-based models into metal forming FE modelling can enhance modelling accuracy, efficiency, and insight across various simulation tasks. This study investigates three examples of such ML applications in metal forming combined with QForm UK software. They include (1) the use of the recurrent neural network (RNN) models for the prediction of recrystallisation during hot forging; (2) ML techniques for estimating heat transfer coefficient (HTC) from quenching experiments; and (3) ML-based optimisation of flow stress curves for complex hot forging processes.

2. Capabilities of AI/ML techniques in microstructural modelling

Microstructure evolution during hot forging determines the quality and properties of heat-resistant parts made of Inconel 718. Traditionally, microstructure evolution during hot forging is modelled using either the JMAK model [1] or its advanced differential form. As the first step to prove the reliability of AI/ML models, an RNN-based ML model was trained on synthetic data generated in the series of QForm UK simulations using its JMAK-type model. The volume fraction of recrystallised grains and their average size were predicted for various forging conditions, including different strain, strain-rate, temperature and geometry. The ML model demonstrated

The project is co-financed by funds from the state budget, granted by the Minister of Science as part of the Excellent Science II Program, project no. KONF/SP/0109/2024/02, subsidy amount 67 870 PLN.

Doskonała Nauka II
Ministry of Science and Higher Education Republic of Poland
Republic of Poland

remarkable accuracy in reproducing the outputs of the analytical approach in all key metrics (Fig. 1).

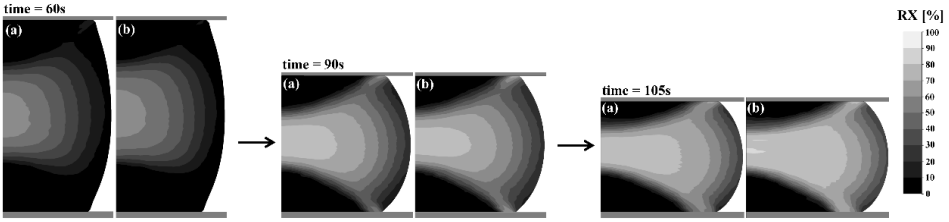

Figure 1. Comparison of recrystallisation volume fraction (RX) predictions at different time steps of the hot forged cylinder using the JMAK model (a) and the ML model trained to reproduce the JMAK model (b)

This result shows the potential of RNN-based physics-informed models to accelerate computation since a trained AI model is significantly faster while reproducing the same results. However, the shortfalls and limitations of analytical JMAK-type models are well known, and obviously, the AI model being trained on JMAK-synthesised data inherits all these problems. The further improvement of the analytical model is quite complicated because it requires introducing some extra process variables and transphenomenal mathematical relations. On the other hand, improving the AI model is relatively straightforward. Without changing the structure of the model, it can be directly trained on the actual experimental data. This was done for the hot forged of Inconel 718 parts, which has shown the ability to overcome some of the limitations of JMAK-type models [2] and demonstrated advantages over existing analytical models in predictive quality.

It is important to mention that any microstructural modelling includes the thermo-mechanical history at each point of the forged part. It is provided by FEM modelling of the process, and if it is not sufficiently accurate or wrong, all further results will be misleading. The following two examples will show how ML/AI techniques can improve the reliability of FE process modelling.

3. Estimating HTC from quenching experiments

This example investigates the problem of determining HTC curves, which are critical parameters in the thermal modelling of heat treatment processes. To acquire the temperature-time curves, an experiment in which a heated metal specimen embedded with a thermocouple is quenched in a cooling liquid can be performed. Determining HTC from such data can be challenging as it is not a single constant but a temperature-depending function. However, as this is a standardised experiment (ISO 9950 [3]), it is a perfect candidate for applying ML algorithms.

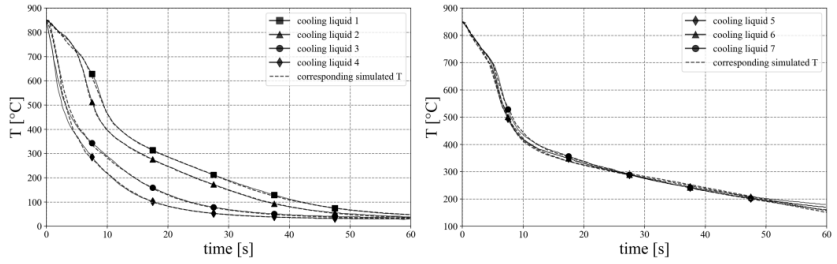

Figure 2. Temperatures acquired from experiments compared to modelling temperatures achieved with HTC curves predicted by ML model

Models of such experiments were simulated in QForm UK with random HTC curves to obtain resulting temperature-time profiles. ML algorithms were then employed, and a model was trained to solve the inverse problem. Results in Fig. 2 indicate that the ML model can achieve predictions consistent with experimental and simulated results, highlighting its effectiveness in addressing inverse thermal problems in heat treatment and metal forming.

4. ML-based optimisation of flow-stress curves

The accuracy of flow stress curves is essential for reliable metal forming simulations [4]. Traditional experimental methods for generating these curves require numerous specimens to cover wide ranges of strain-rate and temperature. This introduces issues of non-repeatability, machine dependence, and limitations in strain value as 0.7 in uniaxial compression tests and triaxiality states. Alternatively, software like JMatPro offers predictions based on chemical composition. Still, it faces notable limitations, such as a lack of validation for specific materials and inconsistencies in interpolated flow stress curves due to abrupt changes from strain rate effects and internal mechanisms influencing the material state.

There are several promising attempts to use ML for modelling flow stresses. Most of them use experimental data from uniaxial tensile or compression tests to train various artificial neural network (ANN) based regression models. This approach can overcome the limitations of analytical approximations like the Arrhenius or Hansel-Spittel equation, including softening or complex strain-rate sensitivity [5-10]. Some latest works also extend these ML constitutive models to reflect the variability of the flow stress curves depending on other conditions like fine-coarse grained, annealed, etc. [11].

However, these approaches do not resolve three main problems which are critical for FE modelling of hot forging processes, i.e. extrapolation of the stress-strain curves for large deformations, fast transitions in strain-rate and temperature and dependence of the flow curves of triaxiality. The last part of this paper presents the concept of optimisation of the basic flow stress curves using the results of industrial forgings. It is suggested that the ML/AI model can be trained using FE simulations and experimental data from actual forging trials to adjust flow stress data to reproduce the experimentally observed metal flow.

5. Conclusion

The demonstrated examples highlight the importance of integrating ML with simulation platforms like QForm UK, which combine data-driven and physics-based approaches. Robust FE modelling software not only provides a valuable data source for training ML models but also serves as a convenient tool for validating and applying these models. ML models can be seamlessly integrated into the workflow and used directly within the software alongside finite element calculations.

It is crucial to emphasize that this approach heavily depends on the accuracy of the underlying data [4]. Proper validation of FEM simulations is essential, as the accuracy of ML predictions is inherently limited by the quality of the FEM simulations.

References

1. Huang D., Wu W.T., Lambert D., Semiatin S.L., *Computer simulation of microstructure evolution during hot forging of Waspaloy and nickel alloy 718*. SFTC Paper, 368, 2001.
2. Tretyakov D., Bylya O., Shitikov A., Gartvig A., Stebunov S., Biba N., *The prospects of implementation of artificial intelligence for modelling of microstructural parameters in metal forming processes*. Materials Research Proceedings, 41, 2024, 2164-2173.
3. Totten G.E., Webster G.M., Tensi H.M., Liscic B., *Standards for cooling curve analysis*, Advanced materials & processes, 151(6), 1997, 68LL-68OO.

4. Bylya O.I., Sarangi M.K., Rohit N., Nayak A., Vasin R.A., Blackwell P.L., *Simulation of the material softening during hot metal forming*, Archives of Metallurgy and Materials, 60(3A), 2015, 1887-1893.
5. Zhu Y., Zeng W., Sun Y., Feng F. and Zhou Y., *Artificial neural network approach to predict the flow stress in the isothermal compression of as-cast TC21 titanium alloy*, Computational Materials Science, 50(5), 2011, 1785–1790.
6. Aghasafari, P., Abdi H., Salimi M., *Artificial neural network modeling of flow stress in hot rolling*, ISIJ International, 54(4), 2014, 872–879.
7. Huang W., Lei L., Fang G., *Comparison Between Four Flow Stress Models Characterizing the Constitutive Behavior of Hot Deformation of 40Mn Steel*, Journal of Materials Engineering and Performance, 30(12), 2021, 9149–9164.
8. Decke J., Engelhardt A., Rauch L., Degener,S., Sajadifar S. V., Scharifi E., Steinhoff K., Niendorf T., Sick B., *Predicting Flow Stress Behavior of an AA7075 Alloy Using Machine Learning Methods*, Crystals, 12(9), 2022.
9. Cao G. M., Gao Z. W., Gao X. Y., *Predicting flow stress of Ni steel based on machine learning algorithm,* Journal of Mechanical Engineering Science, 236(8), 2014, 4253–4266.
10. Pan T., Song C., Gao Z., Xia T., Wang T., *The Prediction of Flow Stress in the Hot Compression of a Ni-Cr-Mo Steel Using Machine Learning Algorithms*, Processes, 12(3), 2024.
11. Harikrishna K., Nithin A., Davidson M. J., *Evaluation of Machine Learning Models for Predicting the Hot Deformation Flow Stress of Sintered Al–Zn–Mg Alloy*, Journal of Engineering Materials and Technology, 147(2), 2025.
12. Reshetov A., Stefani N., Bylya O., Krishnamurthy B., Blackwell P., *Aspects of high strain rate industrial forging of Inconel 718. In Superalloys*, Proceedings of the 14th International Symposium on Superalloys, 2020, 461-470.

Multi-Aspect modeling in bainite microstructure recognition on steel products images based on supervising unsupervised learning

Tomasz Jażdżewski[1], Filip Hallo[1], Grzegorz Korpała2, Krzysztof Regulski[1]
[1] AGH University of Krakow, Mickiewicza 30, 30-059 Kraków, Poland)
[2] Institute of Metal Forming, TU Bergakademie Freiberg, 09599 Freiberg, Germany
tjazdzewski@agh.edu.pl, hallo@agh.edu.pl,
grzegorz.korpala@imf.tu-freiberg.de, regulski@agh.edu.pl

Keywords: machine learning, bainite, microstructure, image recognition, unsupervised learning

1. Introduction: Challenges in bainite recognition

The recognition of steel microstructure is a complex task requiring expertise and advanced methods to identify phases, grains, and defects within a sample [1-2]. Traditional techniques like optical microscopy and scanning electron microscopy (SEM) have been extensively used, but they come with significant limitations in terms of cost, time, and scalability. Recent advancements in machine learning (ML) offer new avenues to address these challenges, particularly for bainite microstructure recognition in steel products [3-4]. Bainite forms when austenite is supercooled and held at temperatures between 550 °C and the martensite start temperature (Ms). It consists of two phases: carbon-saturated ferrite and fine carbides. Bainite transformation combines features of both pearlitic (diffusion-controlled) and martensitic (diffusionless) transformations. Detecting bainite in optical microscopy images is particularly challenging due to:

- The subtle differences in texture and contrast compared to other microstructural constituents.
- The small number of labeled datasets available for supervised training.
- Dependence on expertise to interpret optical microscopy images, which often lack the clarity of SEM images.

While SEM provides more accurate microstructure visualization, it is time-consuming, expensive, and impractical for high-throughput industrial applications. Therefore, the use of machine learning for optical image analysis has garnered significant interest.

2. Machine learning for bainite recognition

Machine learning techniques offer promising solutions to overcome the limitations of traditional methods. This study aimed to enhance bainite recognition using a combination of unsupervised and supervised learning approaches. Supervised models achieved moderate success in identifying bainite regions, but their performance was constrained by labelled dataset size and the inherent challenges of interpreting optical microscopy images.

2.1. Unsupervised learning for segmentation

To identify regions with homogeneous microstructure, unsupervised segmentation was employed. Simple Iterative Linear Clustering (SLIC) superpixel algorithm was chosen for its low

The project is co-financed by funds from the state budget, granted by the Minister of Science as part of the Excellent Science II Program, project no. KONF/SP/0109/2024/02, subsidy amount 67 870 PLN.

Doskonała Nauka II
Ministry of Science and Higher Education
Republic of Poland
Republic of Poland

computational complexity, control over the number of segments, and accuracy in superpixel generation. The unsupervised segmentation process involved:

1) Using a dataset of 1704 unlabeled images.
2) Manually annotating several segment images to create reference masks for supervised fine--tuning.
3) Training an initial model on labeled data and using it to generate histograms for the remaining images, transitioning to a semi-supervised approach.

2.2. Supervised Classification

After segmentation, supervised learning methods such as Decision Trees (DT), Random Forests (RF), and k-Nearest Neighbors (kNN) were applied to classify the segmented regions. Statistical characteristics of the segments, such as histograms, were used as input for classification. The process included:

- Identifying optimal number of clusters and refining segmentation parameters.
- Iteratively improving model performance by integrating statistical knowledge about segment classes (histograms of grayscale pixels).

3. Results and discussion

The results (table 1) demonstrated that segmentation effectively isolated homogeneous regions within the microstructure, enabling subsequent classification. Smaller datasets yielded unstable results with limited generalizability, highlighting the need for larger datasets (results for 100 segments). Splitting images into smaller segments and analyzing their histograms proved viable for bainite detection but may overlook spatial and textural details.

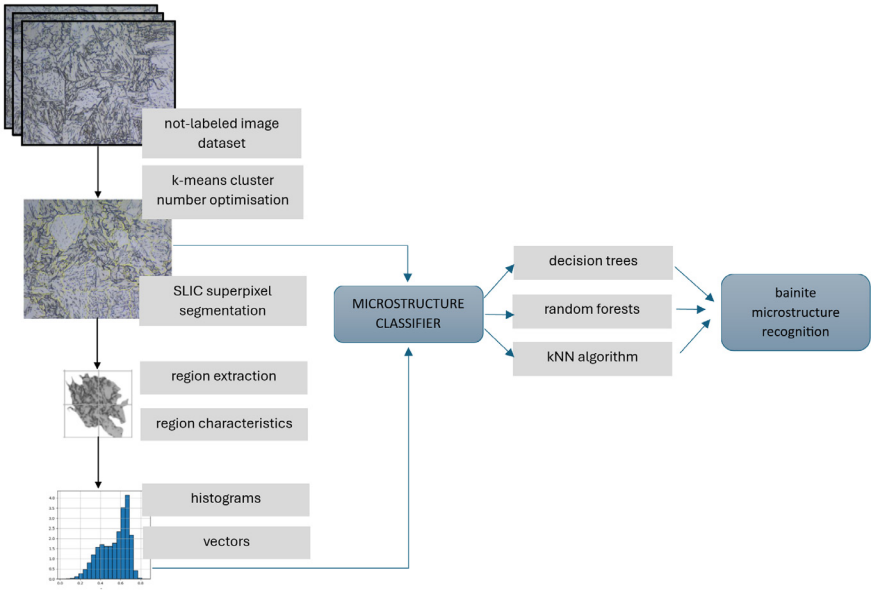

Figure 1. Pipeline diagram in multi-aspect models of bainite microstructure recognition

Table 1. Results of bainite classification

Algorithm	Segments no.	Histogram bins no.	Accuracy-test
DT	600	5	0.75
DT	400	10	0.77
DT	100	5	0.66
RF	600	100	0.83
RF	400	5	0.73
RF	100	5	1.0
kNN	600	15	0.63
kNN	400	150	0.6

This study demonstrates that bainite regions can be effectively identified from optical microscopy images using a hybrid approach combining segmentation and supervised classification (table 1). Random Forest provided accuracy at the level of 83%, which is not yet a completely satisfactory result, but it already provides a solid basis for further research and the possibility of determining optimal parameters - both the number of clusters and the resolution of histograms. It is true that for smaller resolutions it was even possible to achieve 100% accurate classification in tests, but the remaining indicators suggested that the model was unstable (f1 = 63%). The integration of statistical knowledge into the segmentation process and the use of supervised methods for classification significantly enhanced model accuracy. However, achieving robust results requires larger datasets and advanced models capable of leveraging complex spatial and textural information. Future efforts should explore neural networks to further improve bainite recognition and microstructure characterization in steel products.

References

1. Schneider J., Rostami R., Corcoran M., Korpala G., *Integration of Artificial Intelligence into Metallography: Area-wide Analysis of Microstructural Components of a Jominy Sample*, HTM Journal of Heat Treatment and Materials, 79, 2024, 3–14. https://doi.org/doi:10.1515/htm-2023-0032
2. Bhadeshia H.K.D.H., Christian J.W., *Bainite in Steels*, Metallurgical Transactions A, 21, 1990, 767–797. https://doi.org/10.1007/BF02656561.
3. Kim H., Inoue J., Kasuya T., *Unsupervised microstructure segmentation by mimicking metallurgists' approach to pattern recognition*, Scientific Reports, 10, 2020, 17835. https://doi.org/10.1038/s41598-020-74935-8
4. Müller M., Britz D., Ulrich L., Staudt T., Mücklich F., *Classification of Bainitic Structures Using Textural Parameters and Machine Learning Techniques*, Metals, 10, 2020, https://doi.org/10.3390/met10050630.

Acknowledgements. This study was carried out as part of the fundamental research financed by the Ministry of Science and Higher Education, grant no. 16.16.110.66.

Explainable Artificial Intelligence (XAI) methods and their practical use in the heavy industry sector

Wojciech Jędrysik, Piotr Hajder, Łukasz Rauch
AGH University of Krakow, al. Mickiewicza 30, 30-059 Krakow, Poland
wjedrysik@agh.edu.pl, phajder@agh.edu.pl, lrauch@agh.edu.pl

Keywords: explainable artificial intelligence, machine learning, heavy industry

1. Introduction

In recent years, there has been huge progress in the field of machine learning and artificial intelligence. With the increasing use of artificial intelligence, there is also a growing need to understand the decisions it makes, but machine learning models such as deep neural networks are difficult to interpret so they are often called „black boxes". Such a situation limits a human understanding why a given model makes specific suggestions or decisions [1]. Therefore, recently there has been an increasing interest in XAI (Explainable Artificial Intelligence) capable of explaining its decisions in a way that is understandable to humans. Explainability of Artificial Intelligence (AI) models involves the possibility of using appropriate algorithms designed to give users insight into the mechanisms that AI uses to obtain a result. Interpretability tells us to what extent the user is able to understand how the AI model works by looking at the structure of this model. Explaining AI models' decisions can bring many benefits like better results of human cooperation with AI or ensuring safety in critical areas such as medicine or automotive but also in heavy industry where advanced AI systems are used to monitor, control and optimize complex processes but in the case of malfunction it is difficult to identify the causes and understand why this happened. In this paper, we will look at different methods for explaining AI models and then, present an actual problem related to heavy industry. The data, on which it was based, will be described, and the solution to the task and the results will be presented. At the end, appropriate conclusions will be drawn.

2. XAI methods

There are many XAI methods available, and this number is dictated by the variety of problems and AI models used to solve them. XAI methods differ from each other in many aspects, so they can be divided in several ways according to type of input data, way of presenting explanations, stage of explaining, dependence on AI architecture, scope of explanation and problem type. In the next paragraphs, two selected methods are described: GradCAM and Anchors. The first one was chosen because it was used to solve the problem in heavy industry described in the next chapter, while the Anchors method was chosen because it operates in much different ways from GradCAM. GradCAM (Gradient-weighted Class Activation Mapping) is an XAI method that can be classified according to the above criteria as one that uses visualization, showing the importance of individual features in the local space, and we define it as model-specific due to the need to use an appropriate AI model for classification tasks and architecture based on convolutional layers [2]. It is used to

The project is co-financed by funds from the state budget, granted by the Minister of Science as part of the Excellent Science II Program, project no. KONF/SP/0109/2024/02, subsidy amount 67 870 PLN.

Doskonała Nauka II
Ministry of Science and Higher Education Republic of Poland
Republic of Poland

make explanations on images by generating and applying appropriate heat maps to them. To use the GradCAM method, we need a previously trained classification model. The Anchors method is classified as a method presenting explanations in text form, showing key features that influence the prediction result, it can operate locally and globally, and is model-agnostic [3]. Anchors is a method that explains the model's predictions in the form of the so-called "anchors". Anchors are rules built from conditions, so they describe what conditions must be met for the model to make a specific decision. This method can be used on data types such as text or tabular data. To use the Anchors technique, we need a previously trained AI model.

3. Problem description

A part of the case study was the problem of identifying ladles in images from CCTV cameras in the electrosteel plant. There are many such ladles in the hall, they are at various stages of production and change their location from time to time, so it is important to properly monitor them to maintain control over them and the processes with which the ladles are related. Due to the above, there was a need to introduce a system for identifying all ladles in use by using CCTV cameras installed in the hall. Additionally, having an AI model used to identify objects, we can combine it with the appropriate XAI method, which will allow us to understand what criteria the model used when making identification, by showing the image fragments that are crucial in recognizing ladles among others objects. The data used to develop the solution are image snapshots from CCTV cameras showing various places in the hall from different perspectives. Example pictures recorded by cameras and submitted for research are presented in Figure 1.

Figure 1. Pictures from CCTV cameras in the electrosteel plant

The YOLO (You Only Look Once) v3 model was used to identify ladles in the image, it uses 3 different scales to detect objects (small, medium and large objects). It can detect many classes of objects at the same time assigning them appropriate labels and frames limiting the areas of these objects in the image [4]. GradCAM was used as the XAI method to explain what fragments in the image determined that the YOLO v3 model was able to identify ladles. YOLO in its algorithm follows three paths at the same time, where each path is responsible for the detection of objects with different dimensions, so GradCAM had to be adapted to all three paths, then 3 identical images were juxtaposed, but with different heat maps superimposed on them, and the results were compared.

4. Results

The results show sample images recorded by CCTV cameras installed in the electrosteel plant hall compared to the same images after applying ladle detection using the YOLO v3 model and explaining the predictions by applying heat maps generated by the GradCAM method to the images (Table 1). The YOLO model coped well with the task of identifying appropriate objects. The GradCAM model generated heat maps for each of the three size scales considered by the YOLO model.

Table 1. Example results of the YOLO v3 model and the GradCAM method on input data in the form of camera images

Detection result (YOLO v3)	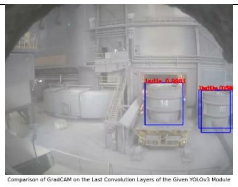	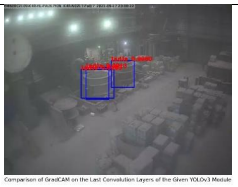
Explanation result (GradCAM)		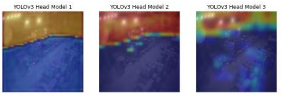

5. Conclusions

XAI is another step forward towards the further development of algorithms that make predictions related to a specific problem helping to understand how the AI models work. There are many XAI methods, they can be divided into different categories. XAI can be used in heavy industry – using GradCAM gave satisfactory results but using the improved GradCAM++ method gave more accurate marking of the areas. Further research should focus on finding other methods that would be able to extract other features crucial to understanding the performance of the YOLO model in this case.

References

1. Ciatto, G., Schumacher, M. I., Omicini, A., & Calvaresi, D. (2020). *Agent-Based Explanations in AI: Towards an Abstract Framework*. In: Calvaresi, D., Najjar, A., Winikoff, M., & Främling, K. (eds) Explainable, Transparent Autonomous Agents and Multi-Agent Systems. EXTRAAMAS 2020. Lecture Notes in Computer Science, 12175, 3–20.
2. Selvaraju, R.R., Cogswell, M., Das, A., Vedantam, R., Parikh, D., & Batra, D. (2020). *Grad-CAM: Visual Explanations from Deep Networks via Gradient-Based Localization*. International Journal of Computer Vision, 128(2), 336–359.
3. Ribeiro, M. T., Singh, S., & Guestrin, C. (2018). "*Anchors: High-Precision Model-Agnostic Explanations*". Proceedings of the AAAI Conference on Artificial Intelligence, 32(1), 1527–1535.
4. Jiang, P., Ergu, D., Liu, F., Ying, C., & Ma, B. (2022). *A Review of Yolo Algorithm Developments*. Procedia Computer Science, 199, 1066–1073.

Acknowledgements. The financial support of Polish National Centre for Research and Development project no. POIR.01.01.01-00-0996/19 is acknowledged. Research project partly supported by program „Excellence initiative – research university" for the AGH University of Krakow.

Industry 4.0 technologies in designing of monitoring systems

Jakub Michalik, Marcin Hojny, Danuta Szeliga
AGH University of Krakow, al. A. Mickiewicza 30 30-059 Kraków, Poland
jmichalik@agh.edu.pl, mhojny@agh.edu.pl, szeliga@agh.edu.pl

Keywords: industry 4.0, monitoring systems, digital twin, IIoT

1. Purpose of research

The integration of Industry 4.0 technologies, such as digital twins and Industrial Internet of Things (IIoT), has revolutionized the development of monitoring systems across various sectors [1]. These advanced technologies enable real-time data collection, analysis, and visualization, leading to enhanced process optimization and improved decision-making capabilities. By leveraging cloud-based solutions and web applications, monitoring systems can now provide remote access to critical information, facilitating more efficient and responsive management of industrial processes and medical devices. Owing to increasing requirements from customers and constantly changing standards in wide areas of industry or hospitality, it is necessary to create modern solutions in monitoring systems and develop more detailed systems to collect more data for security reasons or for collecting detailed data to optimize the processes. This paper describes selected technologies used in industry or medical device monitoring systems (especially in medical gas monitoring systems) and two cases where different monitoring process technologies were used owing to different needs. Authors describes in details prototype of medical gas monitoring system connected with cloud-based message broker with web-application and future plans for this research. Furthermore, this paper is complemented by the presentation of the characteristics of a digital twin implementation in an industrial environment for the roller leveling process. This implementation demonstrates the practical application of Industry 4.0 principles by creating a virtual replica of the physical process, enabling real-time monitoring, predictive analytics, and process optimization.

2. Medical gases monitoring system

The first case described in this article is a prototype of an innovative medical gas monitoring system based on time-series data registration in the Azure cloud instance of the InfluxDB database system. The project was designed based on three connected via RS485 physical connection medical devices: two medical gas manifolds (for Oxygen and Medical Air) and one shut-off valve box. Each device in presented case was produced by a single manufacturer. Connected devices simulate installation in hospitals, where there are two medical gases (Oxygen and Air) and one medical gas zone [1]. Physical connection of medical devices and microcontroller (Raspberry Pi 4B with Waveshare RS485 CAN HAT) created possibility for reading MODBUS registers with data from sensors in each device (using Python programming language with “minimalmodbus” library). Author created custom script dedicated for each type of device, which can combine each readings and alarm statuses from different devices in one data format – the aim is to integrate most-known devices in Poland in one “ecosystem”. Creating a physical connection was obligatory for the next step in this

The project is co-financed by funds from the state budget, granted by the Minister of Science as part of the Excellent Science II Program, project no. KONF/SP/0109/2024/02, subsidy amount 67 870 PLN.

Doskonała Nauka II
Ministry of Science and Higher Education
Republic of Poland
Republic of Poland

project: creating a cloud-based communication server and web application for customers. The cloud infrastructure was based on a Virtual Machine with Debian 11 operating system, with an MQTT broker (Mosquitto) and a Grafana instance (for visual representation of readings). Microcontroller connected to WAN network gained ability to send data for prepared cloud-based infrastructure and it was first step to create modern system to read multiple parameters and alarms live and also save them in time series NoSQL databases. Finally, the web application was prototyped using CMS "Wordpress" only for testing purposes, because it is easy to use Object-Oriented Content Management System with pre-configured solutions to create and manage access rules, roles, and users. The author connected physical infrastructure (simulating a real hospital environment), a main microcontroller, with cloud software – starting from the main broker on the Microsoft Azure platform and ending with a customer web application created on shared hosting with selected domain. Described solution is first approach for Author to create system which will be useful for medical and technical personnel in hospitals – improving the process of alarming of leakages, failures and medical devices status – regardless of manufacturer of monitored device. Future plans for this research is to strive for creating physical monitoring devices, without need for physical connection, concentrate on long-range, low-power, mesh-based connections (LoRa, NB-IoT, Zigbee) between each node (monitored medical devices), and event analytics or preventing, using artificial intelligence based on collected time series data from monitoring devices in different hospitals [3].

3. Digital twin of the roller leveling process

The general concept of the digital twin of roller leveling process was presented in Figure 1.

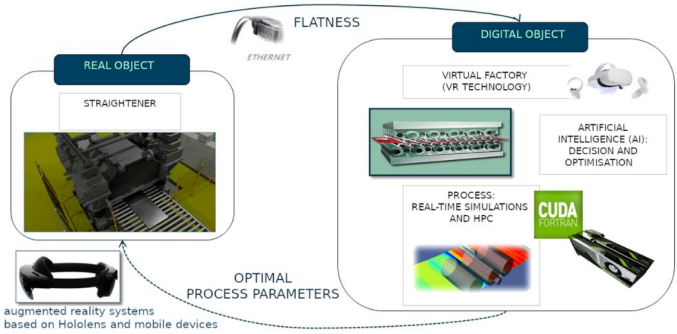

Figure 1. Concept of digital twin (roller leveling process)

The roller leveling process, coupled with a digital twin, is utilized for process optimization to achieve maximum flatness of the material in the shortest possible time. The primary objective of roller leveling is to reduce stress within the material. The digital twin represents the process in real time within a virtual environment, employing rapid GPU-based calculations to determine optimal position settings for the physical machine and material, based on measurements taken after each roller leveling step. In this project, the authors employed artificial intelligence methods to optimize the physical process. The AI-driven optimization approach significantly reduced the time required for achieving optimal flatness compared to traditional methods. By leveraging machine learning algorithms, the system could predict and adjust roller positions more accurately, resulting in improved material quality and reduced waste [4]. This innovative integration of digital twin technology and artificial intelligence not only enhanced process efficiency but also paved the way for further advancements in metal processing industries [5].

References

1. Intizar Ali, M., Patel, P., Sheth, A., G Breslin, J., & Harik., *Cognitive Digital Twins for Smart Manufacturing*, IEEE Intelligent Systems, 36(2), 2021, 96–100.
2. PN-EN ISO 7396-1:2016-07, *Systemy rurociągowe do gazów medycznych - Część 1: Systemy rurociągowe do sprężonych gazów medycznych i próżni*, 2016.
3. Owojaiye, G., & Sun, Y., *Focal design issues affecting the deployment of wireless sensor networks for pipeline monitoring.* Ad Hoc Networks, 11(3), 2021, 1237–1253.
4. Corallo, A., Morciano, P., Del Vecchio, V. D., Lezzi, M., *Shop Floor Digital Twin in Smart Manufacturing: A Systematic Literature Review.* Sustainability, 13(23), 2021, 12987.
5. Park, K.-C., Hwang, S.-M., *Development of a Finite Element Analysis Program for Roller Leveling and Application for Removing Blanking Bow Defects of Thin Steel Sheet*. ISIJ International, 42(9), 2002, 990–999.

Acknowledgements.

1) The work was realized as a part of fundamental research financed by the Ministry of Science and Higher Education, grant no. 16.16.110.663 (task 2).
2) The research work has been supported by the National Centre for Research and Development, Intelligent Development Operational Program: POIR.01.01.01-00-0031/21.

Development of a prediction model for the phases fraction in the microstructure of compacted graphite iron (CGI) using machine learning techniques

Sandra Gajoch[1], Łukasz Marcjan[1], Michał Zmarły[1],
Dorota Wilk-Kołodziejczyk[1,2], Grzegorz Gumienny[3]

[1] AGH, University of Krakow, al. Mickiewicza 30, Kraków, Poland
[2] Lukasiewicz Research Network – Kraków Institute of Technology
[3] Lodz University of Technology, 116 Zeromskiego St., 90-924 Lódź, Poland
sgajoch@agh.edu.pl, lmarcjan@agh.edu.pl,
michalzma@gmail.com, dwil@agh.edu.pl,
grzegorz.gumienny@p.lodz.pl

Keywords: machine learning, supervised learning, composition, vermicular iron, Mask R-CNN model

1. Introduction

This paper focuses on the possibility of automatically determining the percentage composition of ferrite, pearlite and graphite in analysed images of casting microstructures. For this purpose, algorithms selected from descriptions in the literature were analysed and some of them were tested. Images of casting microstructures obtained by electron microscopy were used in the study. These data were processed and analysed using unsupervised learning algorithms such as K-means and Gaussian Mixture Model (GMM). The indicated procedure allows the construction of a model based on the concept of clustering. An important aspect is the ability to efficiently assign pixels to individual phases without having to manually label the images, which significantly speeds up the analysis process and increases reproducibility. During the study, it was shown that the results obtained using the iterative segmentation method, in which each phase was progressively extracted from the image, showed higher accuracy than the classical approaches. The use of the iterative approach made it possible to distinguish more effectively between visually similar elements, which was difficult to achieve with the K-means and GMM algorithms. The results indicate that the predictive model can be a valuable tool to support the analysis of microstructures in vermicular iron, especially in the engineering industry, where precise control of material composition and mechanical properties is required. A prospect for further research is the development of phase detection and segmentation methods using supervised learning, which may further improve classification accuracy and enable the model to be used in industrial quality control systems.

2. Literature review

Traditional approaches, based on subjective operator assessment, are limited in terms of accuracy and repeatability. In the paper [1], an analysis of the effect of heat treatment on graphite morphology carried out using metallographic microscopy and image analysis systems showed that this technology enables effective investigation of the effect of structure on material properties.

The project is co-financed by funds from the state budget, granted by the Minister of Science as part of the Excellent Science II Program, project no. KONF/SP/0109/2024/02, subsidy amount 67 870 PLN.

Doskonała Nauka II
Ministry of Science and Higher Education
Republic of Poland
Republic of Poland

Further studies [2-8] discussing SEM and EBSD methods indicate their wide application in the analysis of the microstructures of various alloys, as well as the use of deep learning techniques such as U-Net to automate the phase classification process, for example in steels with complex structures. Deep modelling can effectively identify phases, such as ferrite or austenite, through image segmentation based on SEM and EBSD data.

Other approaches shown in the article [9], such as texture analysis with GLCM and classification using Random Forest and Gradient Boosting Machine models, show effectiveness in identifying steel structures after different heat treatments.

Another paper [10] describes the segmentation of microstructures without human supervision, using CNNs in combination with a superpixel algorithm. This method mimics the metallurgist's approach to pattern recognition in microscopic images and successfully distinguishes regions of similar morphology, which is comparable to the results of manual determinations.

Ultimately, the articles highlight the crucial importance of machine learning in automating the analysis of microstructures, which reduces subjective errors and speeds up the process of examining materials, enabling more precise design of their properties.

3. Methods and results

2.1. Preliminary data

The data used in this project represent images of the microstructures of test castings made from vermicular cast iron. The castings were obtained using four different variations of casting wall thickness: 3 mm, 6 mm, 12 mm, 24 mm. Three matrix phases are present in each microstructure: ferrite, pearlite and graphite. The images were taken at equal magnification of ×500 and RGB format. During data processing, images deviating from the majority in terms of colour scale were discarded. Then, due to the small data set, it was decided to use augmentation techniques (rotation, reflection) (fig1).

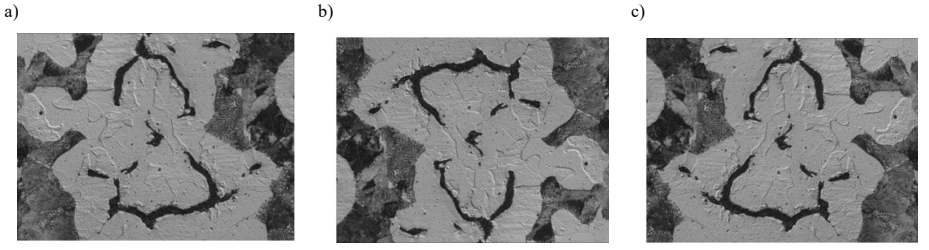

Figure 1. Augmentation techniques a) original photograph b) 180˚ rotation c) reflection with respect to the y-axis

2.2. Percentage composition prediction

After initial testing, supervised learning was rejected in the initial part of the project due to the high effort and timeconsumption during manual labelling and possible errors during phase labelling. Semi-supervised learning was rejected for similar reasons. Unsupervised learning methods using Kmeans and Gaussian Mixture Model algorithms were used in the project. The results obtained for the percentage composition of the individual phases were compared in this study. The data obtained from the tests using the Kmeans algorithm were close to the estimated values, but the

Gaussian Mixture Model algorithm did not obtain satisfactory data. The reason for the incorrect performance of the Gaussian Mixture Model algorithm was the difficulty in distinguishing between graphite and perlite. Attempts were made to improve the performance of the algorithm using an iterative approach to determine perlite based on shape detection using the findContours() method from the OpenCV library. After applying this method, the results were still unsatisfactory due to the erroneous determination of graphite when located in the vicinity of ferrite. Following this, it was decided to test supervised learning algorithms, which were initially rejected. Once the images were manually labelled, they were used to train the model in a neural network. Identifying specific areas from which features were extracted for each phase of the matrix produced satisfactory results.

References

1. Soiński, M.S.; Jakubus, A.; Borowiecki, B.; Mierzwa, P., *Initial Assessment of Graphite Precipitates in Vermicular Cast Iron in the As-Cast State and after Thermal Treatments*. Archives of Foundry Engineering. vol. 21 (No 4), 2021, 131-136.
2. Kalandyk, B.; Zapała, R.; Kasińska, J.; Madej, M., *Evaluation of Microstructure and Tribological Properties of GX120Mn13 and GX120MnCr18-2 Cast Steels*. Archives of Foundry Engineering. vol. 21 (No 4), 2021, 67-76.
3. Jezierski, J.; Dojka, M.; Stawarz, M.; Dojka, R., *Scanning Electron Microscopy as a Tool for Castings Quality Analysis*. Archives of Foundry Engineering. vol. 22 (No 1),2022, 53-61.
4. Kamińska, J.; Angrecki, M.; Dudek, P., *The Effect of Zirconium as an Alloying Additive on the Microstructure and Properties of AlSi9Mg Alloy Cast in Sand Moulds*. Archives of Foundry Engineering. vol. 22 (No 4), 2022, 5-13.
5. Trepczyńska-Łent, M.; Seyda, J., *Characteristics of Ledeburite in EDS Analyses of Directionally Solidified Eutectic White Cast Iron*. Archives of Foundry Engineering. vol. 22 (No 4), 2022, 65-71.
6. Bracka-Kęsek, K.; Szczęsny, A.; Kopyciński, D.; Guzik, E., *Evaluation of the Phases Present in the Zinc Coating Obtained on the Ductile Cast Iron Substrate in the Bath with the Addition of Ti*. Archives of Foundry Engineering. vol. 23 (No 4), 2023, 5-13.
7. Lokaj, J., Sahul, M., Sahul, M., Čaplovic, L., *Application of the EBSD method on explosively welded joins of Al – austenitic CrNi steel bimetal*. Materiały Wysokoenergetyczne, 14(S), 2022, 146–153.
8. Chunguang Shen, Chenchong Wang, Minghao Huang, Ning Xu, Sybrand van der Zwaag, Wei Xu, *A generic high-throughput microstructure classification and quantification method for regular SEM images of complex steel microstructures combining EBSD labeling and deep learning*. Journal of Materials Science & Technology, Volume 93, 2021, 191-204, ISSN 1005-0302.
9. Kazumasa Tsutsui, Hidenori Terasaki, Kyohei Uto, Tatsuya Maemura, Shogo Hiramatsu, Kotaro Hayashi, Koji Moriguchi, Shigekazu Morito, *A methodology of steel microstructure recognition using SEM images by machine learning based on textural analysis*. Materials Today Communications, Volume 25, 2020, article 101514, ISSN 2352-4928.
10. Hoheok Kim, Junya Inoue, Tadashi Kasuya, *Unsupervised microstructure segmentation by mimicking metallurgists' approach to pattern recognition*. Scientific Reports 10, 2020, 17835.

Investigating Alligator and Edge Crack Formation in High-Silicon Grain-Oriented Electrical Steel During Cold Rolling

Vipul Jain, Abhijit Ghosh, Chandan Halder
Department of Metallurgical Engineering and Materials Science,
Indian Institute of Technology Indore, Indore 453552, India
phd1701205014@iiti.ac.in, aghosh@iiti.ac.in,
chalder@iiti.ac.in

Keywords: Electrical Steel, Finite Element Method, Alligator Crack, Edge Crack, Texture

Grain-oriented electrical steel (GOES) with high silicon content is widely used in transformer cores due to its excellent magnetic properties such as low hysteresis loss. However, producing thin sheets of this material through cold rolling presents significant challenges. The inherent brittleness of high-silicon GOES often leads to the formation of defects, particularly alligator and edge cracks, which compromise both the mechanical integrity and performance of the final product [1]. This study focuses on elucidating the mechanisms driving the formation of these cracks through experimental observations and numerical simulations, providing insights for optimizing industrial rolling processes.

The brittleness of GOES is attributed to the high silicon concentration, which enhances magnetic properties but simultaneously promotes crack formation under cold rolling conditions. It has been found that Alligator cracks, parallel to the rolling plane, typically initiate in shear bands due to localized strain incompatibility and propagate along specific microstructural features, such as hot band interfaces. These interfaces, often composed of large θ-fiber (ND$\|\langle 001\rangle$) textured grains, provide a path of least resistance for crack progression due to their low cleavage fracture strength.Edge cracks, in contrast, originate from high tensile stresses along the rolling direction and propagate along the transverse direction at the strip edges during the steady stateof cold rolling.

Finite element method (FEM) simulations were conducted to analyze stress distribution within the sheet during cold rolling [2]. The results revealed that while compressive stresses along the normal direction (ND) dominate in the steady-state rolling phase, tensile stresses develop at the entry and exit stages, particularly at mid-thickness and edges. The tensile stresses are critical in initiating both alligator and edge cracks. During the steady-state zone, when the roll force peaked, the end--width region experienced high tensile stress along the rolling direction (RD), exceeding 250 MPa. This stress promoted edge crack initiation in this zone. In the exit stage, tensile stress shifted to the mid-width region, driving crack propagation along the transverse direction (TD).With anestimated cleavage fracture strength below 150 MPa of the hot rolled plate, the high tensile stress in RD likely facilitated edge crack formation during cold rolling.On the other hand, at 20% thickness reduction, tensile stress in the normal direction (ND) ranged from 20 MPa at entry to 50 MPa at exit. This stress likely promoted alligator crack propagation at the interface between the cube and gamma fiber region. Large θ-fiber (ND$\|\langle 001\rangle$) textured grains (>10 mm in RD) had a cleavage fracture stress below 50 MPa. with {001} planes parallel to the rolling plane, the tensile ND stress at mid- was sufficient to cause cleavage fracture, aligning with the alligator crack path [3].

The project is co-financed by funds from the state budget, granted by the Minister of Science as part of the Excellent Science II Program, project no. KONF/SP/0109/2024/02, subsidy amount 67 870 PLN.

The study further demonstrates that intermediate annealing between cold rolling passes significantly mitigates crack formation. This annealing step refines the microstructure, eliminates hot band interfaces, and reduces the size of θ-fiber textured grains. Consequently, the material exhibits greater uniformity and effectively prevents both alligator and edge cracks in the final product.

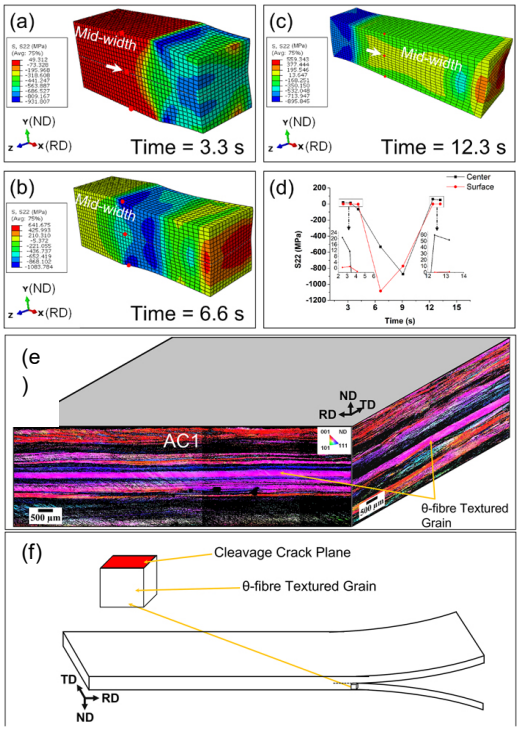

Figure 1. Normal stress distribution along y(ND)-direction (S22) along mid-width at (a) entry stage (3.3 s), (b) maximum Roll force in the steady state zone (6.6 s) and (c) exit stage (12.3 s), and (d) S22 vs Time graph for the element shown by the red dot in (a)–(c) at center and the surface during rolling simulation. (e) AC1 specimen showing IPF-ND maps after conducting large EBSD analysis on ND-RD and ND-TD cross sections through the thickness and (f) schematic representing θ-fiber textured grain and cleavage crack plane at the central region around the alligator crack formation during the cold rolling process.

2. References

1. Y. Qiao and A. S. Argon, Mech. Mater. 35, 313 (2003).
2. S. Turczyn, M. Pietrzyk, J. Mater. Process. Technol. 32, 509 (1992).
3. A. Ghosh, S. Patra, A. Chatterjee, and D. Chakrabarti, Metall. Mater. Trans. A,1, 47, 2755 (2016)

Influence of last deformations during thermo-mechanical rolling on the impact toughness of flat bars

Natalia Wolańska[1], Michał Piwowarczyk[1], Roman Kuziak[2],
Valery Pidvysots'kyy[2], Łukasz Poloczek[2], Krzysztof Radwański[2]
[1] CMC Poland, Józefa Piłsudskiego 82, 42-400 Zawiercie, Poland
[2] Łukasiewicz Research Network – Upper Silesian Institute of Technology,
Karola Miarki 12 – 14, 44-100 Gliwice, Poland
NataliaWolanska@cmc.com, Michal.Piwowarczyk@cmc.com,
roman.kuziak@git.lukasiewicz.gov.pl,
valery.pidvysotskyy@git.lukasiewicz.gov.pl,
Lukasz.poloczek@git.lukasiewicz.gov.pl,
krzysztofradwanski@git.lukasiewicz.gov.pl

Keywords: flat bar, TMCP, austenite microstructure evolution model, meso-texture, impact toughness

1. Introduction

In technical literature, many beneficial effects of TMCP are reported including increased strength and ductility, as well as good weldability of steel products [1,2]. However, as reported in publications [3,4], the unfavourable combination of deformation parameters during final rolling can cause an increase of the ductile-to-brittle transition temperature (DBTT). This was explained in term of the meso-texture development in the final product resulting in the formation of aggregates of grains having close crystallographic orientation. The low-angle grain boundaries within aggregates are weak obstacles against crack growth, and as a result, the average size of the aggregate is the crack propagation controlling parameter instead of the individual grain size.

The effect of the texture formation was observed in the flat bars rolling process at CMC Poland's rolling mill, resulting not only in DBTT increase, but also in obtaining low impact toughness values. For flat bars, a minimum Charpy V-notch fracture energy of 27 J at -20°C is required. The fracture energy is a very important quality parameter of the flat bars. Aiming at counteracting the unfavourable effect of meso-texture formation on the impact toughness, the effect of the rolling conditions in the finishing stands was investigated and deformation conditions for obtaining high impact toughness values were identified.

2. Experimental

The investigation was focussed on the rolling process of the bars of S355J2 steel having the following dimensions of cross section:150×10 mm and 140×8 mm. The billet reheating temperature during the flat bars rolling ranged from 1050 to 1080°C, whilst the finish rolling temperature was in the range of 865–805°C. The rolling process involved rough and finish rolling.

The investigation carried out included the plastometric tests aimed at the development of the austenite microstructure evolution model capable of predicting the state of the austenite microstructure during TMCP. The tests were performed using the Gleeble 3800 simulator by the deformation

The project is co-financed by funds from the state budget, granted by the Minister of Science as part of the Excellent Science II Program, project no. KONF/SP/0109/2024/02, subsidy amount 67 870 PLN.

Doskonała Nauka II
Ministry of Science and Higher Education
Republic of Poland
Republic of Poland

of Ø10 mm × 12 mm cylindrical samples at a constant nominal temperature and strain rate. The stress relaxation method was applied to provide the data for the model development [5]. To measure the austenite recrystallized grain size, the water-quenched samples were subjected to prior austenite grain boundaries etching followed by the measurement of the grain size. The following etchant was used to reveal the austenite grain boundaries: 100 ml of distilled H_2O + 2 g of picric acid, and the etching was performed at 70°C. The grain size measurements were performed with the Metilo program using pictures taken with an OLYMPUS DSX500i light microscope. The equivalent diameter was assumed as the measure of the grain size. The detailed microstructure characterisation was performed under a JSM-7200F scanning electron microscope using the SE mode and EBSD.

The tensile tests of the samples taken from the flat bars were performed using a Zwick Roell Z250 materials testing machine. The measured parameters included Yield Strength (R_e), Ultimate Tensile Strength (R_m), and Total Elongation (El). The fracture energy (AE) was measured in Charpy V-notch test using a Zwick Roell RKP 450 hammer for the impact toughness. In both cases, standard samples were machined from the bars.

3. Results of the investigation

3.1. Identification of the causes of lowering the impact toughness

The total relative reduction in the cross-section area in the last three passes of the 150×10 mm flat bar rolling was around 0.37. During rolling trials, samples after 7th, 13th and the last pass were cut and subject to mechanical properties measurement and microstructure investigation. The results of the mechanical properties measurement are presented in Table 1 whilst the microstructure of the samples is shown in Figure 1. The microstructure of the samples consists mainly of ferrite, pearlite and relatively low content of bainite (Table 2). Moreover, a substantial bending is observed with pearlite and bainite as the leading constituents in the bands. Despite the bainite occurrence, ferrite morphology has a major effect on the mechanical properties of the flat bars, including the impact toughness.

Table 1. Mechanical properties of the 150×10 mm bars after the 7th, 13th, and the last pass. Samples for the measurements were cut at distance of 10 mm from the bar edge

Stand	R_e, MPa	R_m, MPa	El, %	AE @-20°C, J
7	431±10	586±13	28.0±0.5	173±15
13	419±8	593±10	26.0±1.0	162±13
Last	442±12	662±14	24.0±1.0	60±19

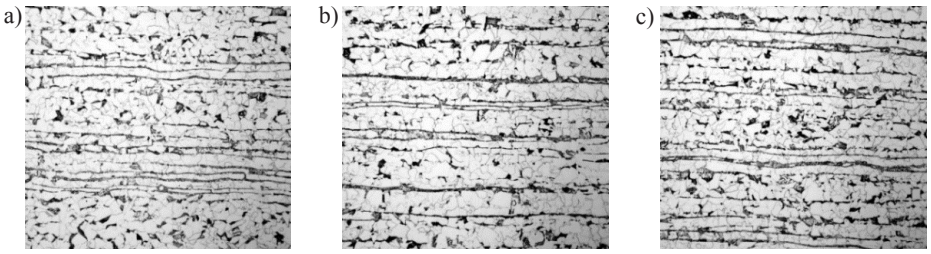

Figure 1. Microstructure of the flat bar (150×10 mm) sample after the last pass and cooling: (a) one side of the bar approximately 10 mm from the edge; (b) middle of the bar; (c) other side of the bar approximately 10 mm from the edge. LOM in the plane parallel to the rolling direction

Table 2. Microstructural parameters of the 150×10 mm flat bar. The measurements were performed on the Charpy V-notch samples taken at distance of 10 mm from the bars' edge. d_α – ferrite grain size (eq. diam.), *F*, *P* and *B*, fraction of ferrite, pearlite and bainite, respectively

Pass	d_α, µm	F	P	B
7	13.2±1.4	0.77±0.03	0.15±0.02	0.08±0.02
13	10.7±1.2	0.78±0.02	0.13±0.03	0.09±0.02
Last	10.5±0.8	0.74±0.02	0.11±0.02	0.15±0.03

The results presented above suggest that the formation of the meso-texture during TMCP affects substantially the value of fracture energy. Therefore, a subsequent step in the analysis of the microstructure of the flat bars included a more detailed investigation of the samples using the EBSD method, and the results are presented in Figure 2. The texture analysis shows that majority of ferrite grains in the sample after the last pass have orientation close to ⟨101⟩//ND, marked in green.

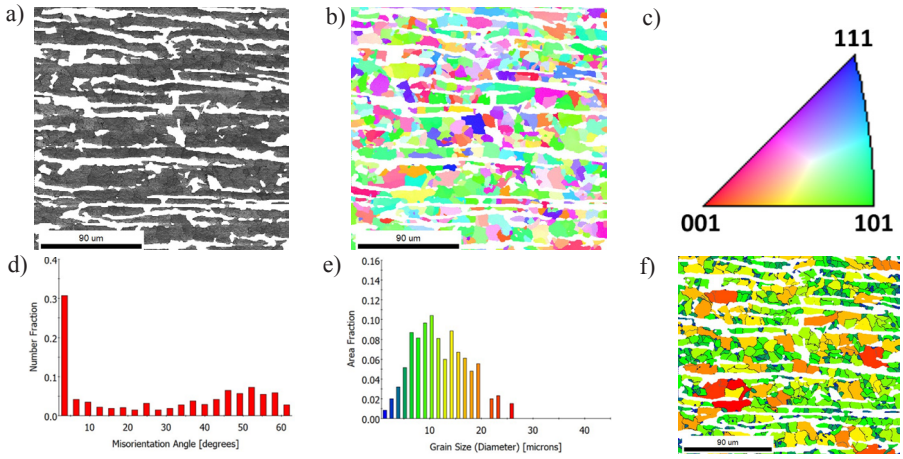

Figure 2. EBSD results of sample C of the 150×10 mm flat bar after the last pass and cooling in a cooling bed with cut-off pearlite: a) image quality (IQ), b) grain orientation map, c) standard crystallographic triangle, d) misorientation angle distribution, (e) grain size distribution, (f) coloured grain distribution map in reference to the distribution in (e)

3.2. Austenite microstructure evolution model

A conventional austenite microstructure evolution model was developed for numerical simulations of the flat bars rolling process including the dynamic, metadynamic and static recrystallization, as well as the austenite grain growth following recrystallization. The full model is presented in publication [6]. However, we found out that subjecting the S355J2 steel to low deformations, below the critical strain for the static recrystallization initiation, may contribute to the unfavorable texture development, resulting in the low values of impact toughness of flat bars. Therefore, new equations were developed and included in the process of numerical simulation, accounting for the critical strain, incubation time for the static recrystallization initiation and retain strain transmitted to the next pass:

$$\varepsilon_c^{st} = 7.9518^{-7} D_\gamma^{0.5405} \left(\dot{\varepsilon} exp\left(\frac{302522.6}{RT} \right) \right)^{0.3061} \quad (1)$$

$$\tau = 7.929 \times 10^{-12} D_{\gamma}^{0.1} \dot{\varepsilon}^{0.1} \varepsilon^{-1.559} exp\left(\frac{234660.13}{RT}\right) \quad (2)$$

$$\varepsilon_r^{i+1} = \varepsilon^i (1 - X)\left(c_{11} - c_{21} Log_{10}(t)\right) \quad (3)$$

where: $c_{11} = \frac{0.9891}{Z^{1.5052 \times 10^{-2}}}$

$$c_{21} = \varepsilon \cdot 0.1897 \cdot exp\left(-\frac{307483.34}{RT}\right) \cdot 10^{\left(2.7059 + \frac{107199.78}{RT}\right)}$$

ε, $\dot{\varepsilon}$– strain and strain rate, T – temperature in absolute scale, R – universal gas constant, D_{α} – initial grain size of austenite.

The implementation of these equations in the FEM model of the bars rolling allowed the modification of deformation parameters in the flat bars rolling process to take full advantage of TMCP. The austenite microstructure evolution model was implemented in the commercial Forge code for the sake of numerical modelling of rolling a 140×8 mm flat bar. The results of the calculations, starting from the 13th pass, are presented for the sensors marked in Figure 3, located in the plane of symmetry of the flat bar. In this case the total deformation in the last three passes was around 0.46.

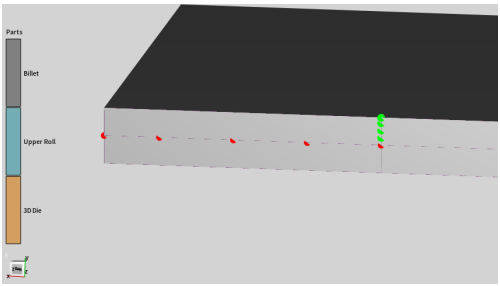

Figure 3. Sensors' location at the flat bar after the 13th stand

Figure 4 shows the variations of the calculated temperature and the mean austenite grain size as a function of the rolling time for the sensors defined in Figure 3. In the initial passes, a substantial temperature rise in the bars' centre is observed due to the heat generating during plastic deformation. At this stage of rolling, a higher temperature is observed in the bar's centre as compared to the edges. The greatest temperature increase is observed after the last pass, and as opposed to the initial deformations, the temperature rise is substantially higher at the bar's edges, as compared to the bar's centre. This is caused by high plastic resistance of experimental steel at low deformation temperatures, relatively high deformation degree and the vertical arrangement of the rolls in the next to the last pass causing the edges bulging (Figure 5). In the considered passes, static recrystallization and austenite grain growth are the main mechanisms influencing the austenite microstructure evolution. The results of the simulations presented in Figure 4 show that comparable values of mean austenite grain size are achieved in the bar's cross-section in the first passes. Substantial differences of austenite evolution occur in the last two passes due to the application of vertical rolls in the next to the last pass causing edges' bulging. In this pass, due to the largest strain, the recrystallised grain size is substantially lower at the bar's edges as compared with the centre. However, higher temperature, combined with a smaller grain size, results in the fast grain growth following the recrystallisation. As a result, a substantial difference in the mean austenite grain size is developed in this pass between the bars' centre as compared to the edges. This difference is eliminated in the last pass.

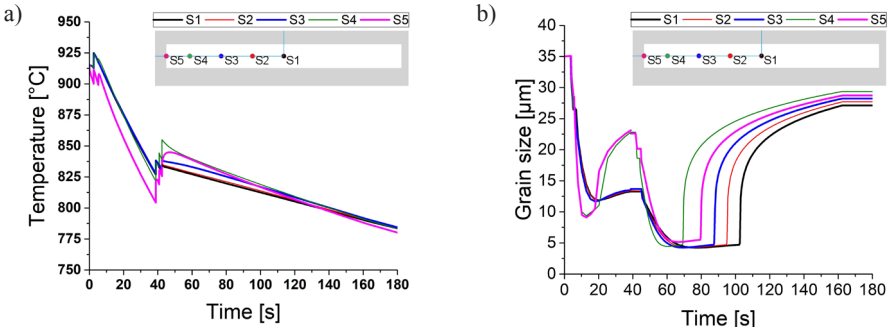

Figure 4. Variations of temperature: (a) and mean austenite grain size, (b) during the last passes of the 140×8 mm flat bar rolling

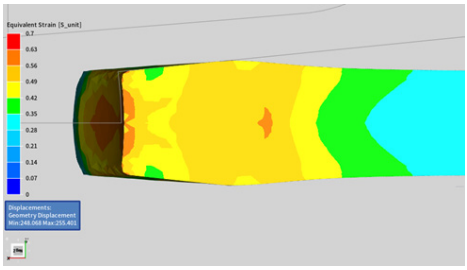

Figure 5. Equivalent strain distribution in the half of the cross-section of the bar at the end of the next to the last pass

Since the S355J2 steel does not contain the microalloying elements causing the effective retardation of the austenite recrystallization and grain growth, a significant grain growth occurred in the time interval from the last pass to the ferritic transformation start temperature. Despite this, the model predicted obtaining a small austenite grain size at the start of ferrite transformation, below 30 µm. This was caused by the low finish rolling temperature of 805°C.

3.3. Mechanical properties of 140×8 mm flat bar after rolling

The results of the mechanical properties measurement are given in Table 3, and the distribution of impact toughness values in the flat bar is shown in Figure 6. The differences in the fracture energy measured in different bar's locations are not large.

Table 3. Average mechanical properties of the 140×8 mm flat bars' microstructure after rolling and cooling in the cooling bed determined in the tensile test

Re, MPa	R_m, MPa	A, %	Z, %
406±16	536±13	17.8±1.1	72.0±1.8

Finally, for comparison with the first rolling experiment, EBSD investigation of the sample of the 140×8 mm flat bar was performed, and the results are shown in Figure 7.

It is seen that the grain size distribution is more steep and more symmetrical as compared to the results of the EBSD investigation presented in the case of the preliminary rolling trials (Figure 2). Moreover, the microstructure contains more high-angle boundaries as compared to the previous investigation, as well as is characterised by more random orientation of individual grains.

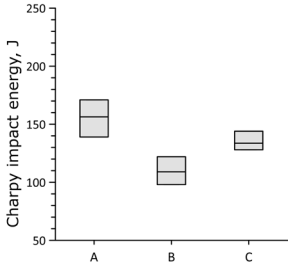

Figure 6. Distribution of fracture energy in the 140×8 mm flat bar of heat 2 after rolling and cooling in the cooling bed. The 75th and 25th percentiles are marked in the graph. A and B stands for the samples taken close to the flat bar edges, whilst B stands for the sample taken in the bars' centre

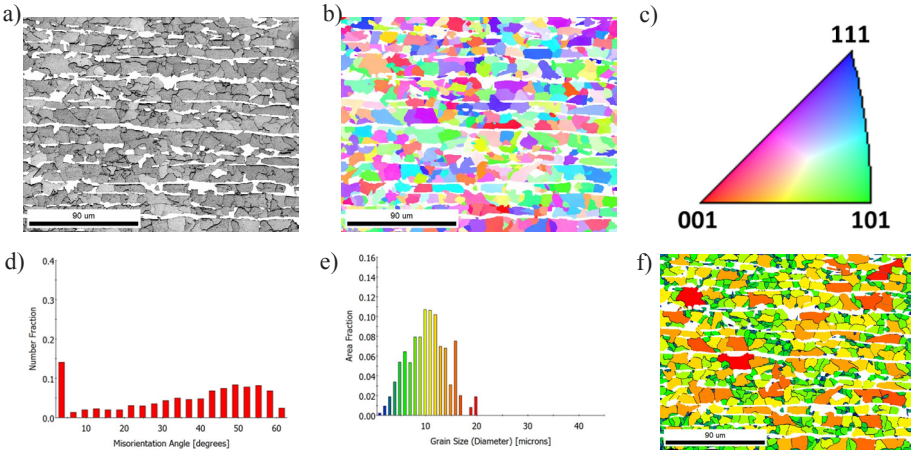

Figure 7. EBSD results of sample C of the 140×8 mm flat bar after the last pass and cooling in the cooling bed with cut-off pearlite: a) image quality (IQ), b) grain orientation map, c) standard crystallographic triangle, d) misorientation angle distribution, (e) grain size distribution, (f) coloured grain distribution map in reference to the map in (e)

4. Conclusions

1) The low fracture energies of the flat bars subjected to TMCP were explained in terms of the meso-texture formation due to the applied processing parameters, involving small deformations in the finishing passes.
2) The detailed investigation of the austenite microstructure evolution after deformation with small strains allowed the incorporation of new equations into the conventional austenite microstructure evolution model, accounting for the recovery process and critical strain for the initiation of static recrystallization.
3) The numerical simulations with the modified model allowed the modification of the deformation parameters during the rolling in the finishing stands, eliminating the disadvantageous effect of meso-texture formation, leading to a substantial increase of the fracture energy in the Charpy V-notch test.
4) The investigation has shown that the inclusion of equations for the critical strain for static recrystallization occurrence and the effective strain variation due to the recovery is critical for

obtaining accurate predictions of austenite microstructure evolution during TMCP. However, this rarely happens in the investigations presented in technical literature.

References

1. M-Ch. Zhao, K. Yang, Y. Schan; *The effects of thermo-mechanical control process on microstructures and mechanical properties of a commercial pipeline steel*, Volume 335, Issues 1–2, 25 September 2002, 14-20.
2. M.A. Suareza, O. Alvareza, M. A. Alvarez-P´ereza, R. Herrerab, C. Zorrillab, S. Valdezc, J. A. Ju´arez--Islasa; *The effect of grain refinement on the mechanical properties of a microalloyed steel*, Revista Mexicana de Fisica 2012, 58, 417–421.
3. D. Bhattacharjee, C.L. Davis, J.F. Knott; *Predictability of Charpy impact toughness in thermomechanically control rolled (TMCR) microalloyed steel*s, Iron Making and Steelmaking, 2003, 30, 3, 249-255.
4. G.J. Baczynski, J.J. Jonas, L.E. Collins; *The Influence of Rolling Practice on Notch Toughness and Texture Development in High-Strength Linepipe*, Metall. Mater. Trans. A, 1999, 30A, 3045-3054.
5. A Pohjonen, O. Seppälä, A. Jokiranta, A. Kaijalainen, M. Somani, D. Porter, J. Larkiola and J Kömi; *Determination of static recrystallization and recovery parameters for steel by fitting model to stress relaxation data*, Journal of Physics: Conf. Series 1270 (2019) 012013.
6. A. Gotti et al.; *Fast simulation tool for long product rolling*, Final Report, RFCS project No. 800746.

Acknowledgements. The authors wish to thank the Research Fund for Coal and Steel and the Polish Ministry of Education for co-financing the FastLoRoll project: Project Number: 800746/ Agreement W87/FBWiS/2018.

Thermomechanical simulations of a hot rolling process of DP600 steel

Tomasz Kaźmierski[1,2], Kamil Cichocki[2], Janusz Krawczyk[2], Łukasz Frocisz[2]
[1] ArcelorMittal Poland S.A. Unit in Krakow, ul. T. Sendzimira 1, 31-752 Krakow
[2] AGH University of Krakow, Faculty of Metals Engineering and Computer Science, al. A. Mickiewicza 30, 30-059 Krakow
tomasz.kazmierski@arcelormittal.com, cichocki@agh.edu.pl, jkrawcz@agh.edu.pl, lfrocisz@agh.edu.pl

Keywords: thermomechanical simulations, dual phase steel, hot rolling, microstructure

1. Introduction

DP600 steel is widely used in the automotive industry due to its high tensile strength and excellent cold formability. Industrial-scale production of this steel grade began in the 1990s, and production volumes have consistently increased since then [1]. DP600 is produced on an industrial scale through either annealing with controlled cooling of cold-rolled ferritic-pearlitic steel or through hot rolling. While the annealing process has been extensively studied by researchers worldwide, simulating the hot rolling process of DP steel in a laboratory setting poses significant challenges [2-4]. As a result, research on the hot rolling process is less prevalent in academic databases. This study aims to replicate the actual industrial process of DP600 production in a hot rolling mill. By varying key process parameters, we were able to achieve different microstructures influenced by total strain, strain rate, deformation temperature, and cooling rate during the experiments. The findings from this study provide a foundation for implementing changes in the hot rolling technology to enhance the mechanical properties of hot-rolled DP600 steel.

2. Results and discussion

Experiments were conducted on an ASP2 thermomechanical simulator supplied by the Servotest company. The samples were prepared as rods shaped by turning. Each rod had a middle section with a diameter of 10 mm, which served as measurement area. Total length of the rod was 200 mm. One set of samples for the simulations was obtained from a continuously cast slab, while the other was taken from transfer bar—an intermediate product of the hot rolling process, between roughing and finishing rolling. Both sets of samples had the exact same chemical composition, corresponding to that used in the production of DP600 during the hot rolling process. Figure 1a illustrates the experimental setup. The rod, secured in clamps, was heated to the required temperature using an induction heater, then cooled at a predefined rate and subjected to deformation by twisting. The thermal cycles applied during the simulations are shown in Figure 1b. Plastic deformation was induced by twisting the rod at a specified angle to replicate the strain and strain rate during the hot rolling process in each pass.

The project is co-financed by funds from the state budget, granted by the Minister of Science as part of the Excellent Science II Program, project no. KONF/SP/0109/2024/02, subsidy amount 67 870 PLN.

Doskonała Nauka II
Ministry of Science and Higher Education Republic of Poland
Republic of Poland

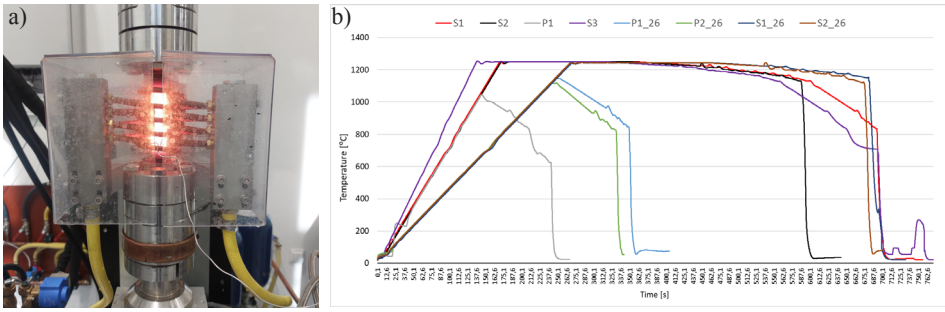

Figure 1. Thermomechanical simulations: a) experiment setting, b) thermal cycles used during simulations

During the simulations, the temperature was continuously measured using a thermocouple. The sample was cooled with air blows, and at the end of each experiment, water was used to quench the sample. As a first step, the entire hot rolling process was simulated as accurately as possible. The sample was heated to the discharging temperature and deformed in seven reversing passes at temperatures corresponding to those used in the actual process. This was followed by slow air cooling to simulate the strip transportation from the roughing mill to the finishing mill, and then deformation in six finishing stands. Finally, the controlled cooling process was simulated, including an intercritical pause during water cooling.

As a result, a dual-phase microstructure resembling the one typically achieved in the actual hot rolling process was successfully reproduced in the simulation. Figure 2a illustrates the dual-phase microstructure obtained in this experiment. The results of the initial simulation demonstrated high reproducibility of the hot rolling process in a laboratory setting. Subsequently, two additional samples were quenched immediately after deformation corresponding to the roughing mill process, with variations in the strain and temperature during the final pass. Another two simulations focused solely on finishing rolling, utilizing different strains in the last two stands and two distinct final rolling temperatures. In both cases, the samples were quenched immediately after the deformation. The quenching step was intended to produce a microstructure suitable for evaluating prior austenite grain size. Figure 2b provides an example of such a microstructure. The evaluation of prior austenite grain size revealed the influence of strain and deformation temperature on the processes of austenite recrystallization and grain growth during hot rolling.

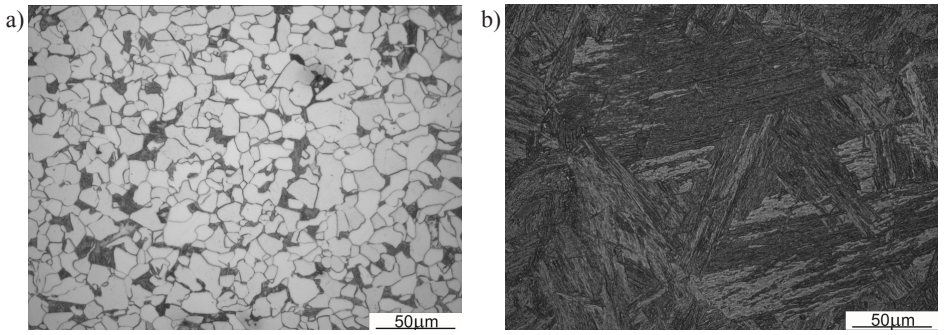

Figure 2. Microstructures obtained during simulations: a) dual phase microstructure, b) sample quenched for prior austenite grain size evaluation

The results of this experiment were used to design modifications to the hot rolling process aimed at improving the mechanical properties of hot rolled DP600 steel. Based on these findings, increasing the strain in the final passes of both the roughing mill and finishing mills is expected to achieve sufficient grain refinement to counteract any potential loss of material strength caused by other changes in the hot rolling process parameters. Moreover, austenite grain refinement is anticipated to not only result in ferrite grain refinement but also promote the formation of more equiaxed and evenly dispersed martensite islands within the dual-phase microstructure.

References

1. S. Allain, I. Pushkareva, J. Teixeira, M. Gouné, C. Scott, *Dual-Phase Steels: The First Family of Advanced High Strength Steels*, „Encyclopedia of Materials: Metals and Alloys" 2022, Z. 2, ss. 37-62.
2. V. Kumar, S. Kumar, A. Saxena, B.K. Jha, *Thermo-mechanical simulation studies for hot rolling of steel – an overview*, National Conference on "Thermo-mechanical Simulation Using Gleeble System" and 3rd Gleeble User Workshop, 2011 Vijaynagar, India.
3. F. Leysen, J. Penning, Y. Houbaert, *A view on the Strategy in the Processing of Hot Rolled Dual Phase Steels*, Materials Science Forum 2010, Vols. 638-642, pp 3343-3349.
4. A.R. Salehi, S. Serajzadeh, A. Karimi Taheri, *A study on the microstructural changes in hot rolling of dual-phase steels*, Journal of Material Science, 2006, Vol. 41, pp 1917-1925.

Acknowledgements. The Ministry of Education and Science financed this work within the 5th edition of the Implementation Doctorate programme.

Applying numerical methods to analyse the problem of rolling TRB strips

Bartosz Sułek[1,2], Janusz Krawczyk[1]
[1] AGH University of Krakow, Faculty of Metals Engineering and Computer Science,
al. A. Mickiewicza 30, 30-059 Krakow, Poland
[2] Łukasiewicz Research Network – Poznań Institute of Technology,
ul. Ewarysta Estkowskiego 6, 61-755 Poznań, Poland
bartoszsulek@agh.edu.pl, jkrawcz@agh.edu.pl

Keywords: Tailor Rolled Blanks, MES, Cold Rolling

1. Introduction

Rolled semi-finished products belonging to the Tailored Blanks (TB) product group are called Tailor Rolled Blanks (TRB) and are now widely used in the automotive and aerospace industries [1]. They have gained their popularity due to their ability to be optimized for shaping into finished parts and adapting them to working conditions. Their characteristic feature is the variable thickness of the material on the cross-section of the sheet [2]. Depending on the direction in which the thickness changes occur, different methods of manufacturing TRB products are used. The first consists of rolling with a periodically variable rolling gap and allows the production of semi-finished products with a variable cross-section in the direction longitudinal to the rolling direction. This method is used in the production of products in which the thickening or thinning of the material follows the shorter side of the sheet, such as the B-pillar (Fig. 1A). In contrast, for TRB products with transversely varying cross sections (Fig. 1B), the technology for shaping them is much more complex. Two main variations of their shaping are currently being researched and developed. In the first, variable thicknesses are obtained by repeated and gradual shaping of the material in a minimum of 30 passes [3]. The second method, on the other hand, involves simultaneous bending and thinning of the material, which reduces the number of required operations to 4 [4]. However, both methods have not found industrial application on a mass scale.

a) b)

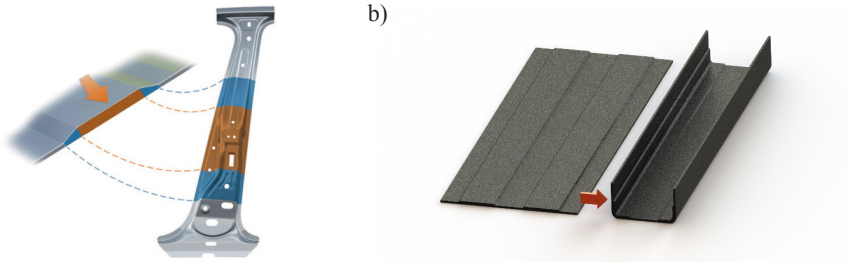

Figure 1. TRB semi-finished product varieties. a) Schematic of a TRB semi-finished product with a longitudinally variable cross-section with an example product [1], b) Schematic of a semi-finished product with a transversely variable cross-section with an example product

The project is co-financed by funds from the state budget, granted by the Minister of Science as part of the Excellent Science II Program, project no. KONF/SP/0109/2024/02, subsidy amount 67 870 PLN.

Doskonała Nauka II
Ministry of Science and Higher Education
Republic of Poland
Republic of Poland

Research conducted since 2021 at the Lukasiewicz Research Network - Poznan Institute of Technology, in cooperation with the AGH University of Science and Technology, is aimed at developing a highly efficient technology for rolling TRB strips with variable material thickness in a direction transverse to the rolling direction. For this purpose, a technology based on modified conventional rolling was developed. This modification included the use of a special set of tools, in the form of groove rolls. With these tools, variable deformations are introduced into the material during the rolling process. This leads to obtaining products in the form of strips with transversely variable cross-section. Depending on the shape and the number of rolls in the set, it is possible to produce different types of strips depending on their purpose (Fig. 2).

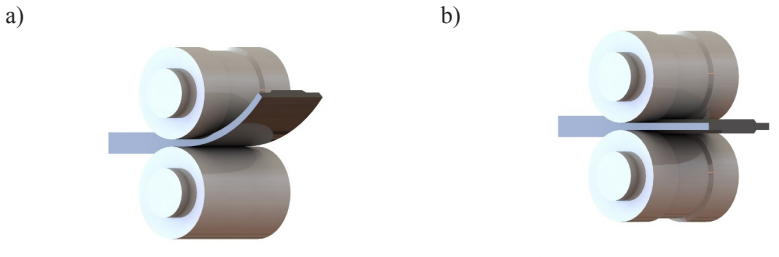

Figure 2. The investigated technology for rolling cross-section strips.
a) rolling with one groove roll, b) rolling with two groove rolls

A definite advantage of the studied technology over those currently in use is the possibility of obtaining a finished TRB strip in a single rolling pass. In addition, due to its similarity to conventional rolling, high technological velocities can be achieved. However, the technology under study has a major disadvantage, which is the non-uniform elongation of the material resulting from strain differences in the rolling pass. Excessive differences in elongation lead to product defects in the form of waviness. In addition, band curvature occurs when shaping products with a one-sided variable surface (Fig. 2A).

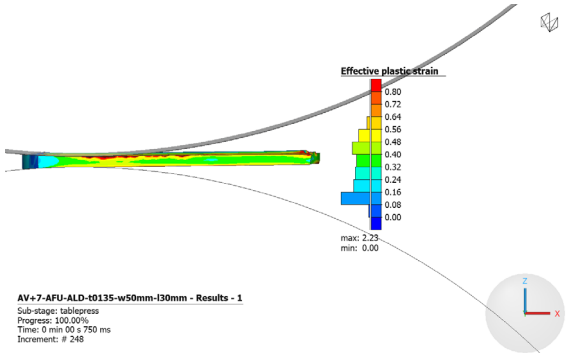

Figure 3. The result of numerical testing of rolling TRB strip free of defects

As part of the ongoing work, numerical studies were used to gain a deeper understanding of the causes of defect formation, as well as to determine the limitations of the technology under study. The research was conducted in the Simuifact Forming program and made it possible to determine the maximum elongation difference of the material at which no shape defects are formed. In

addition, the cause of curvature of the strips was determined on the basis of the conducted research, and the effect of the size of the difference in strain the size of the curvature was studied. The results from these studies made it possible to develop the shape of the tools, as well as to determine the parameters of the rolling process to obtain a TRB strip with a one-sided variable surface, with no shape defects (Fig. 3).

References

1. Merklein M., Johannes M., Lechner M., Kuppert A., *A review on tailored blanks—Production, applications and evaluation*, Journal of Materials Processing Technology 214, 2014, 151– 164.
2. Zhi Y., Wang X., Wang S., Liu X., *A review on the rolling technology of shape flat products*, Int J Adv Manuf Technol, 94, 2018, 4507–4518.
3. Koppa R., Wiednerb C., Meyerc A., *Flexibly rolled sheet metal and its use in sheet metal forming*, Advanced Materials Research, 6-8, 2005, 81-92.
4. Wang X.G., Wang S., Liu X.H., *Variable thickness rolling of plates thick in the middle and thin on the sides*, Journal of Materials Processing Tech., 277, 2020, 116432.

Acknowledgements. Research funded by Ministry of Science and Higher Education financed this work within the fifth edition of the Implementation PhD programme.

Microstructure formation during hot rolling of high-silicon steels for the manufacture of grain oriented electrical sheets

Kamila Ścibisz[1,2], Janusz Krawczyk[2], Piotr Matusiewicz[2], Karolina Wójciak[2]

[1] ArcelorMittal Poland S.A. Unit in Krakow, ul. T. Sendzimira 1, 31-752 Krakow, Poland
2 AGH University of Krakow, Faculty of Metals Engineering and Computer Science,
al. A. Mickiewicza 30, 30-059 Krakow, Poland
scibisz@agh.edu.pl, jkrawcz@agh.edu.pl,
matus@agh.edu.pl, kwojciak@agh.edu.pl

Keywords: hot rolling, microstructure, texture, high silicon steel

1. Introduction

High silicon stell with content approx. 3.2% Si are dedicated to production soft magnetic grain-oriented electrical steel. During complex production route sharp Goss texture is developed. Forming {110} ⟨001⟩ texture characterized high magnetic induction and low core loss along the rolling direction is one of the main characterizing point this kind of stell due which apply as the core material in electrical transformers [1]. Development of such a texture occurs by abnormal growth of a minority of Goss grains present at the primary recrystallised state during secondary recrystallisation. The influence of non-metallic inclusions playing the role of inhibitors of secondary recrystallization at this stage of the manufacturing process is widely reported [2-4]. This research focuses on the study of microstructure and texture evaluation in the early stages of the production process. The formation of dynamic recrystallization zone during hot-rolling process was investigated by using EBSD technique.

2. Results and discussion

Hot-rolling of GOES requires reheating slabs to 1300-1400°C to make sure inhibitors such as MnS and AlN can fully dissolve into the matrix before hot rolling.The phase volume fraction on equilibrium phases in the temperature interval from 0 to 1600°C was simulated using Thermo-calc software AB. The TCFE 10: TCS Steels/Fe-Alloys Database was used.

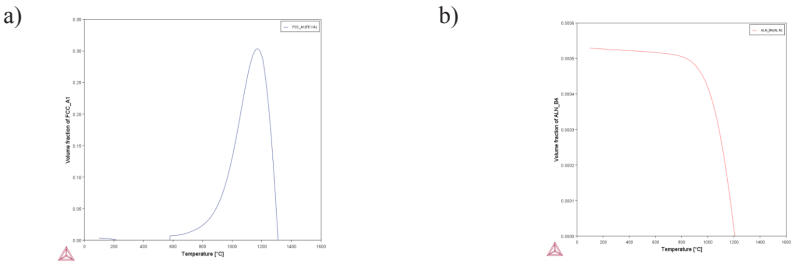

Figure 1. The predicted volume fraction of: a) fcc phase and b) AlN

The project is co-financed by funds from the state budget, granted by the Minister of Science as part of the Excellent Science II Program, project no. KONF/SP/0109/2024/02, subsidy amount 67 870 PLN.

Doskonała Nauka II
Ministry of Science and Higher Education
Republic of Poland
Republic of Poland

The results obtained show that in the temperature range of hot rolling about 30% $\alpha \rightarrow \gamma$ transformation occur (Figure 1a). It can be also concluded that high temperature reheating slabs allows for complete dissolution of AlN, according to the simulation total AlN should be dissolved in temperature about 1220°C (Figure b).

The entire hot rolling process is carried out at significantly higher temperatures than the rolling process of classic low-carbon steel, with reduced cooling at each stage [5]. Analysis of microstructure hot -rolled material including grain size was carried by Metilo 9.1 software and EBDS technique, the research of texture intensity was performed by XRD (X-ray diffraction) for hot rolled and final GOES samples. Both light microscopy microstructure analysis (Figure 2a, 2c) and EBSD results (Figure 2b, 2d) shows that deformed and dynamic recrystallized microstructures appears in the surface layers (Figure 2c, Figure 2d). The microstructure varying between thickness of hot-rolled sample, in centre zone there are incompletely recrystallised banded areas (Figure 2a, Figure 2b).

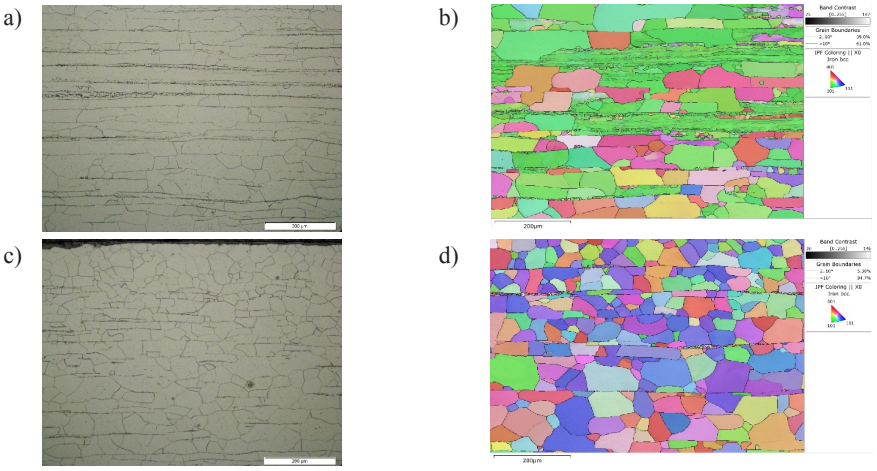

Figure 2. Microstructures of hot rolled high silicon steel: a) center zone of the sample observed by light microscopy, b) center zone of the sample investigated by EBSD characterization, c) surface zone of the sample observed by light microscopy, d) surface zone of the sample investigated by EBSD characterization

The results of the study make it possible to conclude that microstructure of the hot rolled high silicon steel is inhomogeneous through – thickness of the sheet, in the sub surface zone of hot rolled material's crystallographic texture is weak what was confirmed by texture coefficient (TC) parameter calculation.

The obtained results show that the following aspects need to be considered when modelling the microstructure of high-silicon steels, which is shaped by rolling nominally defined as hot rolling:

1) Heterogeneities in the form of band structure,
2) Simulations for the crystalline structure of BCC and AlN conglomerates in their different ranges of occurrence as a function of temperature,
3) Differences in microstructure formation in the near-surface layer and in the middle of the plate thickness, which have a basis in the microstructural and chemical inhomogeneities of the slab and the deformation and cooling conditions during rolling,
4) Consideration of only partial recrystallisation and, in part, the effects of intensive recovery for the central part of the thickness of the rolled band.

References

1. B. Zhou, C.H. Zhu, G. Li, Z. Luo, Y. Gao, S. Bao, J. Schneider, *Effect of Sulfur and acid soluble aluminum content on precipitate and microstructure of grain-oriented silicon steel*, Arch. Metall. Mater. 63 (2018), 4, 1701-1708.
2. F. Fang, Y. Zhang, X. Lu, Y. Wang, G. Cao, C. Yuan, Y. Xu, G. Wang, R.D.K. Misra, *Inhibitor induced secondary recrystallization in thin-gauge grain-oriented silicon steel with high permeability*, Materials and Design 105 (2016) 398–403.
3. A.L. Etter, T. Baudin, R. Penelle, *Influence of the Goss grain environment during secondary recrystallisation of conventional grain-oriented Fe–3%Si steels*, Scripta Materialia 47 (2002) 725–730.
4. S. Chu, B. Zhou, B. Mao, *State of the art and prospects on the metallurgical design and manufacturing process of grain-oriented electric steels*, Journal of Magnetism and Magnetic Materials 614 (2025) 172739.
5. K. Ścibisz, T. Kaźmierski, J. Krawczyk, *A roll's wear during hot rolling of high-silicon steel and it's impact on the quality of a strip's profile*, Tribologia 3/2023.

Acknowledgements. The Ministry of Education and Science financed this work within the 5th edition of the Implementation Doctorate programme.

Strengthening response to changes in the microstructure of β titanium alloy

Janusz Krawczyk, Łukasz Frocisz
AGH University of Krakow, Faculty of Metals Engineering and Computer Science,
al. A. Mickiewicza 30, 30-059 Krakow, Poland
jkrawcz@agh.edu.pl, lfrocisz@agh.edu.pl

Keywords: β titanium alloy, strengthening, microstructure, recrystallization

1. Introduction

The Titanium alloys with a body center cubic (BCC) crystallographic structure are interesting materials for the study of their plastic deformation mechanism due to the possibility of observing numerous deformation mechanisms in those materials. Dynamic recrystallization (DRX) is observed in areas of stable deformation and located mostly at the grain boundaries of the deformed phase during hot deformation processes. In metastable titanium alloys continuous DRX is realized by progressive subgrain rotation, while discontinuous recrystallisation only results in a change in the curvature of the grains boundaries. These processes is related to the dissipation of energy in the material, indicating its correlation to the strain parameters [1–4]. The softening of the material during deformation depends on the strain intensity and the process temperature. With low strain intensities and low temperatures, a stronger effect on the material softening is observed, which has to be related to the physical properties of titanium alloys and to the occurrence of continuous and discontinuous DRX [5–7]. Dynamic recrystallisation is observed in areas near the grain boundaries of the β-phase. Weakening of the texture level in the material associated with this phenomenon is observed [8–10].

The aim of the proposed research is the description of the plastic deformation mechanism of metals with a body cantered cubic crystal structure in regard of their physical properties, considering the dynamic recovery (DRV) and dynamic recrystallization (DRX) processes resulting in microstructure changes.

2. Results and discussion

The study was conducted on titanium alloy Ti3Al8V6Cr4Zr4Mo, which was prepared by homogenization annealing with supersaturation. An exemplification of the research and analysis carried out is presented in Figure 1.

A problem that makes modelling plastic forming processes difficult is the inhomogeneity of deformation during even a simple compression test (Fig. 1a). This can result in the effect of cyclic strengthening and weakening of the material when the compression test is carried out under nominal hot deformation (Fig. 1b). Even under these conditions, inhomogeneity of microstructure resulting in inhomogeneity of hardness is ultimately present (Fig. 1c). Under these deformation conditions, the largest strain strengthening should occur at the center of the thickness of the com-

The project is co-financed by funds from the state budget, granted by the Minister of Science as part of the Excellent Science II Program, project no. KONF/SP/0109/2024/02, subsidy amount 67 870 PLN.

Doskonała Nauka II
Ministry of Science and Higher Education
Republic of Poland
Republic of Poland

pressed specimen for cold deformation conditions. In the case of hot deformation, however, a clear cyclicity in the change of hardness over the thickness of the compressed specimen is apparent (Fig. 1d). In this case, the highest hardness does not occur in the middle of the specimen thickness after hot compression. This can be related to the dynamic recrystallisation process (DRX), the microstructural effect of which is shown in Figure 1. Dynamic recrystallisation reduces or even nullifies the effect of strain hardening. However, the grain grinding associated with the recrystallisation effect in areas of strain inhomogeneity can produce a strengthening effect (Fig. 1f).

In modelling the hot deformation process of a titanium alloy with a bcc crystal structure, the selective processes of strain hardening (SS) and weakening due to dynamic recrystallisation (DR) should be taken into account. It should be noted here that these processes can occur sequentially in successive layers over the thickness of the compression specimen when the strain accumulation reaches an energy effect that allows the dynamic recrystallisation process to be initiated. These processes will also be influenced by dynamic recovery processes, which will make the free energy accumulation needed to initiate the dynamic recrystallisation process. These effects will depend on the thermal conductivity, which will affect adiabatic effects in the shear band regions.

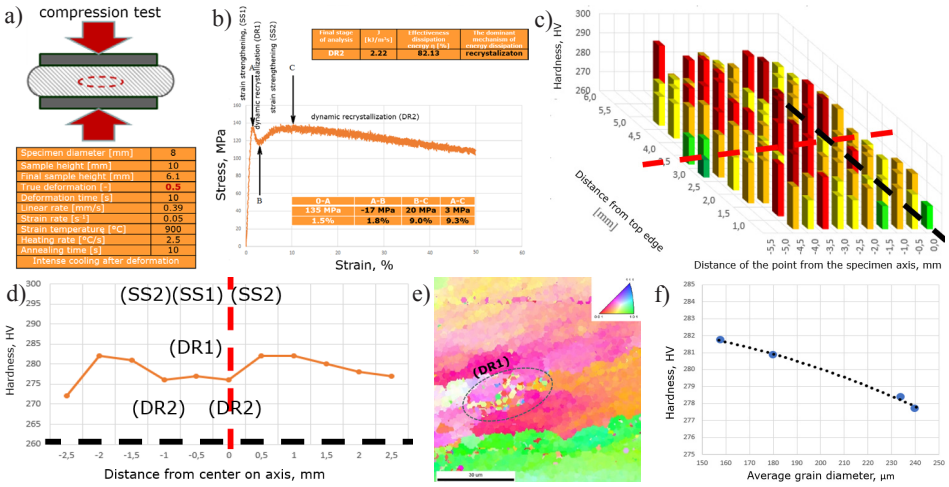

Figure 1. The exemplification of research results allowing the thesis of the effect of dynamic microstructural changes on the strengthening and weakening of β titanium alloy: a) scheme and parameters of the compression test, b) curve of consolidation during the compression test and the parameters characterizing it, c) non-uniformity of hardness for a representative quadrant of the specimen cross-section after compression, d) change of hardness on the thickness of the compressed specimen in its vertical axis, e) illustration of the effect of change in the microstructure (small grains formed as a result of recrystallisation – EBSD), f) dependence of hardness on the grain size

References

1. C. Li, L. Huang, M. Zhao, S. Guo, J. Li, *Hot deformation behavior and mechanism of a new metastable β titanium alloy Ti–6Cr–5Mo–5V–4Al in single phase region*, Mater. Sci. Eng. A. 814 (2021) 141231.
2. X.G. Fan, Y. Zhang, P.F. Gao, Z.N. Lei, M. Zhan, *Deformation behavior and microstructure evolution during hot working of a coarse-grained Ti-5Al-5Mo-5V-3Cr-1Zr titanium alloy in beta phase field*, Mater. Sci. Eng. A. 694 (2017) 24–32.
3. W. Chuan, H. Liang, *Hot deformation and dynamic recrystallization of a near-beta titanium alloy in the β single phase region*, Vacuum. 156 (2018) 384–401.

4. J.K. Fan, H.C. Kou, M.J. Lai, B. Tang, H. Chang, J.S. Li, *Hot deformation mechanism and microstructure evolution of a new near β titanium alloy*, Mater. Sci. Eng. A. 584 (2013) 121– 132.
5. T. Lu, Z. Dan, T. Li, G. Dai, Y. Sun, Y. Guo, K. Li, D. Yi, H. Chang, L. Zhou, *Flow softening and microstructural evolution of near β titanium alloy Ti-35421 during hot compression deformation in the α+β region*, J. Mater. Res. Technol. 19 (2022) 2257–2274.
6. H. Matsumoto, M. Kitamura, Y. Li, Y. Koizumi, A. Chiba, *Hot forging characteristic of Ti- 5Al-5V-5Mo-3Cr alloy with single metastable β microstructure*, Mater. Sci. Eng. A. 611 (2014) 337–344.
7. Z. Qi Chen, L. Juan Xu, S. Zhen Cao, J. Kai Yang, Y. Fei Zheng, S. Long Xiao, J. Tian, Y. Yong Chen, *Characterization of hot deformation and microstructure evolution of a new metastable β titanium alloy*, Trans. Nonferrous Met. Soc. China (English Ed. 32 (2022) 1513–1529.
8. J. Chen, J. Li, B. Tang, Y. Chen, H. Kou, *Microstructure and texture evolution of a near β titanium alloy Ti-7333 during continuous cooling hot deformation*, Prog. Nat. Sci. Mater. Int.29 (2019) 50–56.
9. Y. Chen, J. Li, B. Tang, H. Kou, X. Xue, Y. Cui, T*exture evolution and dynamic recrystallization in a beta titanium alloy during hot-rolling process*, J. Alloys Compd. 618 (2015) 146–152.
10. J. Wang, K. Wang, S. Lu, X. Li, D. OuYang, Q. Qiu, *Softening mechanism and process parameters optimization of Ti-4.2Al- 0.005B titanium alloy during hot deformation*, J. Mater. Res. Technol. 17 (2022) 1842–1851.

Acknowledgements. The research was financed by the Ministry of Education and Science (AGH—research subsidy No. 16.16.110.663).

Modeling of particles pushing and engulfment by solidification front using a cellular automaton model

Andriy Burbelko[1], Ewa Olejnik[1,2], Paweł Kurtyka[2]
[1] AGH University of Krakow, Faculty of Foundry Engineering,
al. Reymonta 23, 30-059 Krakow, Poland
[2] Innerco Sp. z o.o., Władysława Siwka 17, 31-588 Krakow, Poland
abur@agh.edu.pl, eolejnik@agh.edu.pl,
pawel.kurtyka@innerco.pl

Keywords: composite solidification, nanoparticles, entrapment, pushing, cellular automaton

1. Introduction

In recent decades, there has been a significant increase in interest in the cast metal composites reinforced with ceramic nanoparticles. This is primarily due to the unique effects produced by the entrapment of a nanometric particles of reinforcing phases in metallic matrix during solidification. These effects include improved mechanical properties such as strength, hardness and creep resistance at elevated temperatures, while maintaining satisfactory ductility of the material [1-5]. Also, these types of materials are characterised by increased abrasion resistance [6,7].

The observed improvement in properties is the result of several key mechanisms including: uniform distribution and high dispersion of the particles of reinforcing phase, the Orowan mechanism, mismatch in coefficients of thermal expansion and elastic moduli between the reinforcing particles and the metal matrix, strengthening of grain boundaries [7,8].

Due to unique properties of the reinforced cast metal composites, these composites are particularly used in areas requiring high strength performance while reducing weight, such as the aerospace and automotive industries. The continuous development of their synthesis and processing methods is systematically expanding the range of their potential applications [6,7].

2. Forces acting on particles near solid-liquid interface

Production of cast metals composites reinforced by ceramic particle is realized by the way of solidification a suspension of these particles in a liquid melt. To obtain a composite material, particles suspended in a liquid phase must be surrounded by the growing solid phase and absorbed by the metallic matrix. Under the influence of forces acting on the particles a short distance from the surface of the solid phase, they can either be trapped in the matrix or pushed back into the liquid.

The movement of a particle close to solid-liquid front is controlled by the interaction of a number of forces acting on the particle, including gravitational force, friction (drag) force resulting from the movement of a finite viscous fluid relative to the particle and interaction force with the interfacial boundary arising in a thin layer of the liquid phase (interfacial force, interface force, interatomic force). The mathematical apparatus used to calculate these and other forces is presented in the publication [9].

The project is co-financed by funds from the state budget, granted by the Minister of Science as part of the Excellent Science II Program, project no. KONF/SP/0109/2024/02, subsidy amount 67 870 PLN.

Doskonała Nauka II
Ministry of Science and Higher Education
Republic of Poland
Republic of Poland

Analyze the balance of forces acting on a particle in a liquid phase near the solid grain surface, critical velocity for the transition from particle pushing to engulfment by the interface was calculated in [9] as a function of relevant material parameters and processing variables:

A double space above and below equations must be used to separate them from the text. All new symbols must be listed and defined immediately after each equation, as follows:

$$V_c = \frac{a_0}{3\eta\alpha(n-1)} \frac{\Delta\sigma_0}{R} \left(\frac{n-1}{n}\right)^n \tag{1}$$

where: a_0 – sum of the radii of atoms in the surface layers of the particle and the solid phase;
η – the melt dynamic viscosity;
α – the ratio of the thermal conductivity of the particle material to the thermal conductivity of the liquid alloy;
R – the particle radius;
$n = 2$ through 7;
$\Delta\sigma$ – differences in the interfacial energies calculated by relation:

$$\Delta\sigma_0 = \sigma_{SP} - \sigma_{LP} - \sigma_{SL} \tag{2}$$

where σ_{SP}, σ_{LP}, and σ_{SL} are the interfacial energies between the solid phase and the liquid phase, between the liquid phase and the particle and between the solid phase and the particle, respectively.

If the linear velocity of velocity of solid-liquid interface migration is greater than critical one, the particles will be engulfed. Engulfment will normally provide to uniform distribution of particles in the metallic matrix of cast composites. On the other hand, when front migration velocity is less then critical, the particles will be pushed back in the suspension melt, resulting in particles segregation.

3. Brownian movement of the small particles

For small particles, Brownian diffusion dominates when particles are situated in the melt far from the solidification front. According to Smoluchowski [10], the density of the statistical distribu-

$$f(x) = \frac{1}{\sqrt{4\pi Dt}} \cdot \exp\left(-\frac{x^2}{4Dt}\right) \tag{3}$$

tion of displacements x with Brownian motion for time period t is given by the formula:

where: where the constant D was called by Smoluchowski the "particle diffusion coefficient"

$$D = \frac{kT}{6\pi\eta R} \tag{4}$$

related to the average displacement of a particle at time t due to Brownian motion.

where: k – Boltzman constant; T – absolute temperature, w.

Brownian motion of particles of small dimensions takes place with a random velocity u, whose density of statistical distribution for one direction follows Maxwell's statistical distribution:

$$f(u) = \sqrt{\frac{m}{2\pi kT}} \cdot \exp\left(-\frac{mu^2}{2kT}\right) \tag{5}$$

where: m – mass of the particle.

4. Cellular automaton model

The cellular automaton model described in [11] was complemented in the analysis of the Brownian motion of particles in the liquid at a greater distance from the crystallization front according to equation (3). The choice between particles pushing and engulfment by solidification front is made taking into account the direction of random motion of the particle and its kinetic energy determined according to the equation (5).

Example of the particles distribution obtained in the cases of full engulfment and full pushing is presented in Figure 1.

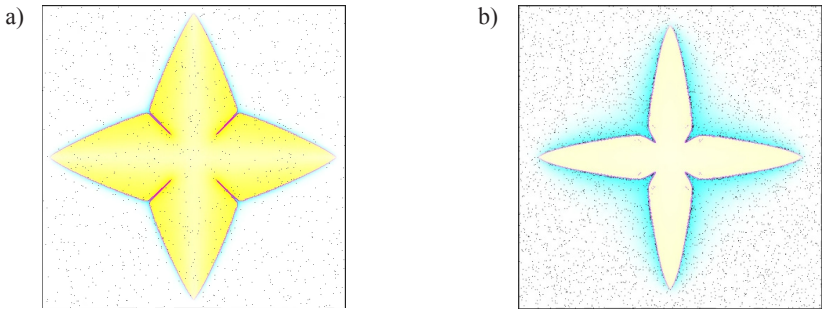

Figure 1. Examples of the full engulfment of the particles by solidification front (a) and full pushing by growing dendrite (b)

References

1. Liu W., Cao C., Xu J., Wang X., Li X., *Molten salt assisted solidification nanoprocessing of Al-TiC nanocomposites*. Mater Lett 2016, 185:392–5.
2. Cao C., Liu W., Javadi A., Ling H., Li X., *Scalable manufacturing of 10 nm TiC nanoparticles through molten salt reaction*. Proc. Manuf. 2017, 10:634–40.
3. Karbalaei Akbari M., Baharvandi H.R., Shirvanimoghaddam K., *Tensile and fracture behavior of nano/micro TiB2 particle reinforced casting A356 aluminum alloy composites*. Mater Des 2015, 66:150–61.
4. Wang M., Chen D., Chen Z., Wu Y., Wang F., Ma N., et al., *Mechanical properties of in-situ TiB2/A356 composites*. Mater Sci Eng A 2014, 590:246–54.
5. Mazahery A., Abdizadeh H., Baharvandi H.R., *Development of high-performance A356/nano-Al2O3 composites*. Mater Sci Eng A 2019, 518:61–4.
6. Surappa M.K., *Aluminium matrix composites: Challenges and opportunities*. Sadhana, 2023, 28(1), 319–334. https://dx.doi.org/10.1007/BF02717141
7. Casati, R.; Vedani, M. *Metal Matrix Composites Reinforced by Nano-Particles – A Review*. Metals, 2014, 4, 65-83. https://doi.org/10.3390/met4010065
8. Maziarz W., Wójcik A., Chulist R., Bigos A., Kurtyka P., Szymanski Ł., Jimenez Zabaleta A., García de Cortázar M., Olejnik E., *Microstructure and mechanical properties of Al/TiC and Al/(Ti,W)C nanocomposites fabricated via in situ casting method*, Journal of Materials Research and Technology, Volume 28, 2024, pp. 1852-1863, https://doi.org/10.1016/j.jmrt.2023.12.126

9. Shangguan D., Ahuja S., Stefanescu D.M., *An Analytical Model for the Interaction between an Insoluble Particle and an Advancing Solid/Liquid Interface*. Met. Trans. A. 1992, vol. 23, 669-680
10. Smołuchowski M., *O fluktuacjach termodynamicznych i ruchach Browna*. Warszawa, Wydawnictwo Redakcyi Prac Matematyczno-fizycznych. T. XXV. 1914, 263.
11. A.A. Burbelko, D. Gurgul, W. Kapturkiewicz, J. Początek, M. Wróbel: *Stochastic nature of the casting solidification displayed by micro-modelling and cellular automata method*. Solid State Phenomena. Vol. 197, 2013, pp. 101-106.

Acknowledgements. Financial support of the National Science Centre, Poland (project no. 2021/43/B/ST8/03271) is greatly acknowledged.

Investigation of Nitrogen-Doped Amorphous Carbon Nanofilms on Magnesium Alloys: A Study of Chemical Characteristics, Microstructural Analysis, Corrosion Behavior, and Biocompatibility

Adarsh Rai[1], Michal Krzyzanowski[1,2], Szymon Bajda[1]
[1] AGH University of Krakow, Al. Mickiewicza 30, 30-059 Krakow, Poland
[2] Birmingham City University, Millennium Point, Curzon Street, Birmingham, B4 7XG, UK
rai@agh.edu.pl, mkrzyzan@agh.edu.pl, sbajda@agh.edu.pl

Keywords: Magnesium alloy, corrosion, biocompatibility, adhesion

1. Introduction

Magnesium and its alloys are gaining increasing recognition in the biomedical sector due to their biodegradability, eliminating the need for a secondary surgical procedure to remove implants. Their physical properties, such as an elastic modulus ranging from 41 to 45 GPa and a density between 1.74 and 2.0 g·cm^{-3}, closely resemble those of natural bone (3–20 GPa, 1.8–2.1 g·cm^{-3}), which helps to reduce stress shielding effects often associated with conventional implants. In contrast to other biomaterials like stainless steel (200 GPa, 8.0 g·cm^{-3}) and titanium alloys (103–110 GPa, 8.3–9.2 g·cm^{-3}), magnesium alloys offer a more favorable mechanical profile [1-3].

The human body contains between 20 and 28 g of magnesium, with a recommended daily intake of 300–400 mg for healthy adults. While magnesium is essential for numerous cellular functions, its vulnerability to corrosion in moist environments presents considerable challenges. This corrosion can result in mechanical failure and inflammation due to the buildup of hydrogen gas during degradation. To improve corrosion resistance, techniques such as alloying, heat treatment, and especially surface modification have been utilized.

Nitrogen-doped amorphous carbon coatings, recognized for their exceptional wear resistance, impressive hardness, and biocompatibility, can further enhance the performance of magnesium alloys. Studies have indicated that these coatings not only improve mechanical properties but also enhance corrosion resistance, making them particularly appropriate for medical implants. The magnesium alloy (Mg-Zn-Ca), notable for its high strength and ductility, has been effectively used in clinical applications and demonstrates significant improvements in corrosion performance when extruded. Therefore, the integration of magnesium alloys and coatings offers a promising pathway for the development of efficient and safe biomedical implants [3-6].

2. Result and discussion

The alloy was polished, and after polishing and cleaning its surface, the film was transferred onto it. This study presents and examines the use of a nitrogen-doped amorphous carbon (a-C) thin layer over a magnesium alloy (Mg-0.52Zn-0.21Ca), which is ultrathin, ultrasmooth, and corrosion-resistant. A polymer composite based on branched polyethyleneimine was used to synthesize the a-C film, which was subsequently applied to the magnesium alloy surface to enhance its corrosion resistance.

The project is co-financed by funds from the state budget, granted by the Minister of Science as part of the Excellent Science II Program, project no. KONF/SP/0109/2024/02, subsidy amount 67 870 PLN.

Doskonała Nauka II
Ministry of Science and Higher Education
Republic of Poland
Republic of Poland

The amorphous nature of the synthesized film was confirmed through comprehensive characterization using multiple techniques, including XPS, Raman spectroscopy, TEM, and PXRD. Electrochemical workstation analysis, supported by AFM studies and electrochemical corrosion experiments, demonstrated that the synthesized a-C coating significantly improves corrosion resistance and reduces the corrosion rate, as shown in Figure 1a-b.

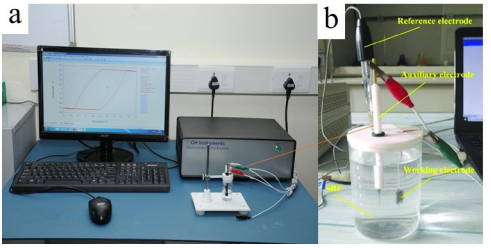

Figure 1. Utilisation of electrochemical workstation for corrosion measurement: (a) electrochemical workstation (b) demonstration of the connection setup for corrosion measurement

Additionally, cytotoxicity tests confirmed the film's non-toxicity and its suitability for orthopedic implant applications, increasing the potential clinical relevance of magnesium-based implants. As a biocompatible and inert nonmetallic element, carbon—when doped with nitrogen—serves as an excellent choice for enhancing both the corrosion resistance and biocompatibility of magnesium-based implants.

The potentiodynamic polarization tests were conducted at a scan rate of 1 mV/s, covering a potential range from −0.4 V to 0.4 V. To assess the corrosion rate, hydrogen evolution was measured through immersion tests. Five uncoated sides of the samples were sealed with silicone rubber to prevent corrosion. All samples were evaluated in modified simulated body fluid (m-SBF) at a temperature of 25 ± 1°C.

The behavior of magnesium alloys during anodic polarization is complex due to simultaneous magnesium dissolution and hydrogen evolution, rendering the anodic Tafel slope less informative. Nonetheless, the Tafel extrapolation method can effectively differentiate between samples by examining variations in corrosion current density (Icorr) and corrosion potential (Ecorr). Additionally, the polarization resistance (R_p) can be determined using the Stern-Geary equation, which shows an inverse relationship with Icorr (Table 1).

$$R_p = \frac{\beta_a \times \beta_c}{2.303 I_{corr}(\beta_a + \beta_c)} \tag{1}$$

where β_a and β_c represent the anodic and cathodic Tafel slopes, respectively.

Table 1. Potentiodynamic polarization data of the substrate and a-C coating

Sample	Ecorr	Icorr	βa ($V \cdot dec^{-1}$)	βc ($V \cdot dec^{-1}$)	RP ($\Omega \cdot cm^2$)
Alloy	-1.77	36.87	0.24	-0.17	1230
Coated Surface	-1.63	15.21	0.22	-0.20	2304

3. Conclusion

The study shows the application of a nitrogen-doped amorphous carbon (a-C) thin nano film on magnesium alloy (Mg-Zn-Ca) to enhance corrosion resistance and biocompatibility for orthopedic implants. After polishing and cleaning the alloy surface, the a-C film, synthesized by using a polymer composite based on branching polyethyleneimine, was applied, resulting in an ultrathin and ultrasmooth deposition. Characterization techniques such as XPS, Raman spectroscopy, TEM, and PXRD confirmed the amorphous nature of the coating. The electrochemical analysis reported that the synthesized a-C coating significantly reduces the corrosion rate. Additionally, cytotoxicity tests confirmed the film is non-toxic, proving its suitability for clinical applications. a-C film, being biocompatible and inert, shows to be an effective material for improving the performance of magnesium-based implants, paving the way for safer and more effective orthopedic solutions.

References

1. G. Song, *Control of biodegradation of biocompatable magnesium alloys* Corros. Sci., 49 (2007), pp. 1696-1701.
2. S. Shadanbaz, G.J. Dias, *Calcium phosphate coatings on magnesium alloys for biomedical applications: a review* Acta Biomatter., 8 (2012), pp. 20-30.
3. M. Peron, R. Bertolini, S. *Cogo on the corrosion, stress corrosion and cytocompatibility performances of ALD TiO2 and ZrO2 coated magnesium alloys* J. Mech. Behav. Biomed. Mater., 125 (2022).
4. A. Hartwig, *Role of magnesium in genomic stability* Mutat. Res Fund. Mol., 475 (2001), pp. 113-121.
5. J. Robertson, *Diamond-like amorphous carbon* Mater. Sci. Eng. R. Rep., 37 (2002), pp. 129-281.
6. J. Robertson, *Diamond-like* Carbon Pure Appl. Chem., 66 (1994), pp. 1789-1796.

Acknowledgements. Financial assistance of the NCN, project no. 2024/53/B/ST11/00799, is acknowledged.

Atomistic Simulation of Grain Boundary Segregation and its Migration in Aluminium-Magnesium Alloy

Ranesh Kumar Saha, Amlan Dutta
Department of Metallurgical and Materials Engineering,
Indian Institute of Technology Kharagpur, West Bengal, Pin: 721302, India
raneshkrsaha@kgpian.iitkgp.ac.in,
amlan.dutta@metal.iitkgp.ac.in

Keywords: Grain Boundary Segregation, Grain Boundary Migration, Al-Mg alloy, Atomistic Simulation, Hybrid Monte Carlo/Molecular Dynamics Scheme

1. Background and Motivation

Grain Boundaries are the regions in the microstructure where the atomic arrangement of two meeting crystal lattices is remarkably disturbed [1]. Compared to bulk grains, grain boundaries have higher free energy, which substantially affects the mechanical and functional properties of the material. Again, for the same ensemble of atoms, free energy is higher in polycrystalline materials compared to single crystals due to the presence of grain boundaries.

To reduce this free energy, the solute atoms of an alloy tend to segregate preferentially at the grain boundaries and other defective sites. Any changes in elemental concentration at a grain boundary in a solid solution are called grain boundary segregation. The grain boundaries can have a substantially greater solute solubility differential than the bulk [1].

Grain boundary migration denotes the movement of a grain boundary in a direction orthogonal to the tangent plane [2]. Grain boundary migration entails the translocation of atoms from one grain to another via the grain boundary. To facilitate this process, the orientation of atoms near the grain boundary must be altered, with the driving force provided in the form of thermal energy, stress, magnetic fields, and concentration gradients.

Al-Mg alloys constitute a vital category of lightweight structural materials [3], widely utilized in the automotive, marine, and defense sectors. Low-Mg aluminium alloys have been evaluated for their superior formability characteristics, rendering them an appropriate choice for the conditions of this study. Numerous studies have shown that Mg accumulates at the interfaces of aluminium grains, resulting in alterations to their thermodynamic and kinetic properties. Solute segregation in the alloys enhances their thermal and mechanical properties.

While numerous researchers have examined the phenomenon of Grain Boundary Segregation, the migration of grain boundaries influenced by solute segregation has received minimal attention. This is because contemporary technology regarding mobility and solute segregation at the grain boundary relies on certain restrictive assumptions, which constrains its capacity to measure this phenomenon.

2. Modelling and Simulation

Tubular bi-crystals have been created with the grain boundary axis parallel to different cubic axes, viz., ⟨001⟩, ⟨110⟩ and ⟨111⟩. A schematic is shown in Figure 1. Different radii of curvature

The project is co-financed by funds from the state budget, granted by the Minister of Science as part of the Excellent Science II Program, project no. KONF/SP/0109/2024/02, subsidy amount 67 870 PLN.

Doskonała Nauka II
Ministry of Science and Higher Education
Republic of Poland
Republic of Poland

of grain boundaries have also been considered. These variations help us understand the segregation of solute atoms based on atomic packing and grain boundary curvature. Semi-Grand Canonical Monte Carlo (SGMC) computations have been employed along with an isobaric-isothermal ensemble (NPT) as a hybrid Monte Carlo/Molecular Dynamics (MC/MD) scheme [4] to understand the site preference for the replacement of Al by Mg atoms. We consider two alloy compositions for the study, viz. Al-2.5at.% Mg and Al-5at.% Mg. Finnis-Sinclair semi-empirical interatomic potential created by Mendelev et al. [5] is employed to define the interatomic forces during the simulations.

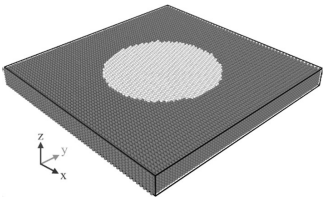

Figure 1. Schematic of the tubular bi-crystal. The grains are shown in two different colors

3. Grain Boundary Segregation

During the process of substitution of Al atoms by Mg atoms, the energy changes at intermediate steps have been computed and compared for the different structures. This is done to quantify the variation in the energetics of the structures with changes in the GB axis, grain radius, and composition. Later, we assess solute segregation at the GB region, varying with changes in the GB axis, grain radius, and composition. Multiple methods have been employed to quantify the segregation in this region. The segregation energy and excess solute content at the GB region are co-related, as shown in Figure 2.

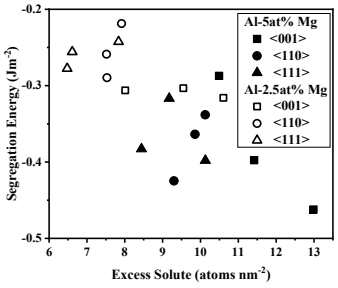

Figure 2. Co-relating segregation energy and excess solute segregation of the structures

4. Grain Boundary Migration

The migration of grain boundaries under the effect of grain boundary solute segregation has been studied. For this, the alloy structures are held at elevated temperatures until the inner grain shrinks to zero. Mobility of the grain boundary during this shrinkage is computed. Mobility is quantified based on temperature, GB's axis, the inner grain's initial radius, and alloy composition. During the heating operation, the atoms near the grain boundary tend to change their crystallographic

orientation. The convex-shaped outer grain tries to engulf the inner circular grain. However, this process is delayed due to excess solute atoms at the grain boundary region. These solute atoms seem to pin the grain boundary, restricting its migration. This grain boundary migration has been studied in detail and is co-related with the segregation of Mg atoms at the grain boundary.

5. Conclusion

The hybrid MC/MD scheme produces the best possible structure for Al-Mg alloys. Mg atoms are placed at positions that reduce the system's free energy. A considerable amount of Mg saturates the GBs, producing a segregated structure. The excess Mg saturating into the structure due to the presence of GB is quantified. Mg atoms getting into the GB region are prioritized over going to the bulk region. The pre-segregated bi-crystals have been annealed at various temperatures to understand the effect of the radius of curvature and axis of orientation of GB on its migration. The segregated Mg atoms at the GB tend to pin it and retard the GB mobility. The mobility of GB differs with the axis along which it is oriented. The concentration of solute also determines mobility. The structures containing 5 at% Mg are more mobile. Effect of grain size: larger grain has lower mobility. Mobility increases with temperature.

References

1. P. Lejcek, *Grain Boundary Segregation in Metals*, vol. 136. Berlin, Heidelberg: Springer Berlin Heidelberg, 2010. doi: 10.1007/978-3-642-12505-8.
2. H. Gleiter, "*Theory of grain boundary migration rate*," Acta Metallurgica, vol. 17, no. 7, pp. 853–862, Jul. 1969, doi: 10.1016/0001-6160(69)90105-9.
3. J.L. Murray, "*The Al–Mg (Aluminum–Magnesium) system*," Journal of Phase Equilibria, vol. 3, no. 1, p. 60, Jun. 1982, doi: 10.1007/BF02873413.
4. B.S. Daan Frenkel, *Understanding Molecular Simulation, From Algorithms to Applications*, 2nd Edition. 2001. Accessed: Feb. 24, 2023. [Online]. Available: https://www.elsevier.com/books/understanding-molecularsimulation/frenkel/978-0-12-267351-1
5. M.I. Mendelev, M. Asta, M.J. Rahman, J.J. Hoyt, "*Development of interatomic potentials appropriate for simulation of solid–liquid interface properties in Al–Mg alloys*," Philosophical Magazine, vol. 89, no. 34–36, pp. 3269–3285, Dec. 2009, doi: 10.1080/14786430903260727.

Acknowledgements. This work used the Supercomputing facility of IIT Kharagpur established under the National Supercomputing Mission (NSM), Government of India and supported by the Centre for Development of Advanced Computing (CDAC), Pune.

Electronic, Optical and Water-splitting Properties of Rare Earth Single-atom Catalysts Supported on g-C_3N_4 Monolayer: A DFT study

Tarun Kumar Kundu[1], Ranjini Sarkar[2]

[1] Department of Metallurgical and Materials Engineering,
Indian Institute of Technology Kharagpur, India, 721302
[2] Department of Engineering and System Science,
National Tsing Hua University, Hsinchu, 300044, Taiwan
tkkundu@metal.iitkgp.ac.in,
ranjinisarkar.kgp.1991@gmail.com

Keywords: Single-atom catalysts, Graphitic carbon nitride, Metal-support interaction, HER, OER

Catalytic water splitting is a highly efficient method for producing clean and sustainable hydrogen without greenhouse gas emission with easy hydrogen-storage [1]. This process comprises two half-cell reactions: i) the hydrogen evolution reaction (HER) at the cathode and ii) the more intricate oxygen evolution reaction (OER) at the anode. HER involves the reduction of protons to hydrogen, while OER entails a complex four-electron oxidation of two water molecules to produce one oxygen molecule [2]. A major challenge in this catalytic process is the substantial energy cost required to overcome the kinetic overpotential [3]. Platinum-based materials are ideal for HER due to their low overpotential, high catalytic activity, and excellent stability. However, excessive cost restricts their widespread application. As a result, palladium-based catalysts are more commonly employed in industrial settings, albeit their lower effectiveness and stability compared to platinum [4]. For OER, metal oxides such as RuO_2 and IrO_2 are typically used, but these oxides are both expensive and scarce [5]. Consequently, recent research has focused on developing cost-effective alternatives using earth-abundant transition metals (TMs) such as Fe, Co, Ni, Cu, Zn and Ti as alternatives, albeit they often compromise stability [6]. Beyond these noble and TM elements, there are growing evidences indicating that rare earth (RE) metals, which are more abundant than noble metals, are highly effective in various catalytic applications including electro-, thermo- and photocatalysis [7]. RE elements enhance catalytic activity by tuning the bandgap and controlling the bond length between reaction intermediates and metal active sites, primarily due to electron modulation from partially filled 4f orbitals.

Single-atom catalysts (SACs) consisting of metal single-atoms embedded in a support matrix offer active sites for superior catalytic performance compared to the bulk counterparts [8]. Though SACs emerge as promising candidates due to their cost-effectiveness and low metal content requirement but the primary challenge for SACs is maintaining their stability, as the weakly bound metal atoms tend to migrate and agglomerate into clusters. Effective SACs necessitate strong metal-support interactions to prevent clustering [9]. Both pristine and doped carbon-based materials serve as excellent supports for TM-SACs, with nitrogen-doped carbon systems being particularly advantageous due to the hybrid interactions between N-2p and TM-d orbitals . In the realm of N-doped carbon scaffolds for SACs, 2-D graphitic carbon nitride (g-C_3N_4) has garnered significant attention due to its inherent visible light-responsive photocatalytic properties [10]. However,

The project is co-financed by funds from the state budget, granted by the Minister of Science as part of the Excellent Science II Program, project no. KONF/SP/0109/2024/02, subsidy amount 67 870 PLN.

Doskonała Nauka II

Ministry of Science and Higher Education
Republic of Poland

Republic of Poland

pristine g-C_3N_4 faces limitations such as low visible light absorption, low mobility and kinetics of photo-generated charges, and rapid electron-hole recombination [11]. Metal and non-metal doping have been effective strategies to overcome these challenges [12]. The incorporation of RE metals reduces the bandgap of the g-C_3N_4 surface, with the partially filled 4f orbitals acting as charge-capturing centers. This leads to the delocalization of electron-donating and -accepting sites, thereby limiting electron-hole recombination. Known for its inherent photoactive properties, g-C_3N_4 monolayer turns out to be a suitable support to decorate RE single-atoms, maintaining high structural and thermal stability without forming metal clusters. Despite the recent surge in exploration of transition metal single-atom catalysts (SACs), rare earth (RE)-SACs remain relatively understudied.

In this work, two lighter RE-SACs (La and Ce) and two heavier RE-SACs (Sm, and Gd) supported on two-dimensional heptazine based graphitic carbon nitride (g-C_3N_4) monolayer are studied using spin-polarized density functional theory (DFT) to systematically explore the electronic structures, optical properties, and catalytic water-splitting performance. Both flat and buckled configurations of the g-C_3N_4 and RE single-atom-decorated g-C_3N_4 surfaces are investigated. Heavier RE-SACs (Sm and Gd) exhibit stronger metal-support interactions (showing more negative binding energies) due to substantial orbital overlap, resulting from the pronounced spin polarization of their 4f orbitals. For all the RE-SACs, more negative binding energies of RE single-atoms, relative to cohesive energies and binding energies of RE atom-dimers, confirm the structure stability of RE single-atoms on the g- C3N4 support without clustering, while electrochemical stability is assessed by positive dissolution potentials.

Charge transfer from RE atoms to the g-C_3N_4 support, as shown by Bader analysis and ELF plots, points to metallic or ionic nature of RE-C and RE-N bonds. RE single-atom decoration reduces the bandgap, shifts the Fermi level close to conduction band minimum (CBM), and delocalizes the highest-occupied and lowest-unoccupied states. Specifically, Sm- and Gd-g-C_3N_4 demonstrate intense spin polarization in 4f orbitals, enhancing orbital interaction with g-C_3N_4 support. The reduced work function and enhanced optical response across IR-Vis-UV indicate improved photoactivity for RE-g-C_3N_4 compared to g-C_3N_4.

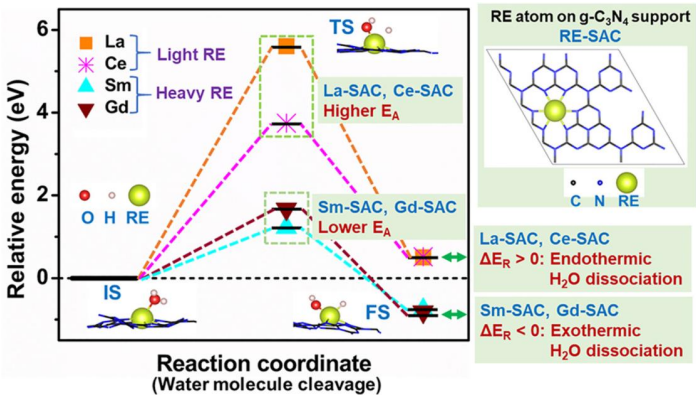

Figure 1. Relative energy profile of H2O molecule dissociation [H2O∗ → (H + OH)∗] on single rare earth element atom supported on g-C_3N_4 monolayer {IS, TS and FS indicate the initial, transition, and the final states; EA and ΔER indicate the activation energy and reaction energy}

Water molecule adsorption, activation and cleavage processes reveal that water dissociation $H_2O∗ \rightarrow (H + OH)∗$ is endothermic for La- and Ce- g-C_3N_4 but exothermic for g-C_3N_4, Sm-g--C_3N_4, and Gd- g-C_3N_4. More negative reaction energies for Sm- and Gd-g-C_3N_4 confirm the

thermodynamic favorability of water dissociation on heavier RE-SACs. Furthermore, Sm- and Gd--g-C_3N_4 systems demonstrate lower activation barriers, suggesting superior kinetic feasibility for water splitting compared to La- and Ce-g-C_3N_4.

Finally, HER and OER pathways are analyzed based on the adsorption free energies of key intermediates, namely, H∗, OH∗, O∗, and OOH∗. Regardless of flat or buckled references, systems with stronger metal-support interactions, i.e., Sm- and Gd-g-C_3N_4, show considerably lower HER overpotentials. Although OER overpotentials for RE-g-C_3N_4 systems do not exhibit significant improvements for the full OER pathway (∗+2H_2O → OH∗ → O∗ → OOH∗ → O_2), the energy differences specifically for the intermediate steps OH∗ → O∗ → OOH∗ are considerably decreased compared to pristine g-C_3N_4, suggesting better thermodynamic feasibility of OER intermediate transitions on RE-SACs. Overall, this study identifies RE- g-C_3N_4 SACs as promising candidates for catalytic water splitting, with heavier RE metals demonstrating stronger metal-support interactions and potentially superior catalytic performance [13].

References

1. Y. Yao, X. Gao, X. Meng, *Recent advances on electrocatalytic and photocatalytic seawater splitting for hydrogen evolution*, Int J Hydrogen Energy, 46, 2021, 9087-9100.
2. X. Zou, J. Su, R. Silva, A. Goswami, B.R. Sathe, T. Asefa, *Efficient oxygen evolution reaction catalyzed by low-density Ni-doped Co3O4 nanomaterials derived from metal-embedded graphitic C_3N_4*, Chem Commun, 49, 2013, 7522-7524.
3. A. Raveendran, M. Chandran, R. Dhanusuraman, *A comprehensive review on the electrochemical parameters and recent material development of electrochemical water splitting electrocatalysts*, RSC Adv, 13, 2023, 3843-3876.
4. L. Zhang, Q. Chang, H. Chen, M. Shao, *Recent advances in palladium-based electrocatalysts for fuel cell reactions and hydrogen evolution reaction*, Nano Energy, 29, 2016, 198-219.
5. C.C.L. McCrory, S. Jung, J.C. Peters, T.F. Jaramillo, *Benchmarking heterogeneous electrocatalysts for the oxygen evolution reaction*, J Am Chem Soc, 135, 2013, 16977-16987.
6. Y. Feng, H. Yang, X. Wang, C. Hu, H. Jing, J. Cheng, *Role of transition metals in catalyst designs for oxygen evolution reaction: a comprehensive review*, Int J Hydrogen Energy, 47, 2022, 17946-17970.
7. L. Li, T. Zhang, Y. Zhou, X. Wang, C tong Au, L. Jiang, *Review on catalytic roles of rare earth elements in ammonia synthesis: development and perspective*, J Rare Earths, 40, 2022, 1-10.
8. Q. Zhang, J. Guan, *Recent progress in single-atom catalysts for photocatalytic water splitting*, Sol RRL, 4, 2020.
9. J. Li, Q. Guan, H. Wu, W. Liu, Y. Lin, Z. Sun, et al., *Highly active and stable metal single-atom catalysts achieved by strong electronic metal-support interactions*, J Am Chem Soc, 141, 2019, 14515-14519.
10. X. Wang, K. Maeda, A. Thomas, K. Takanabe, G. Xin, J.M. Carlsson, et al., *A metal-free polymeric photocatalyst for hydrogen production from water under visible light*, Nat Mater, 8, 2009, 76-80.
11. R. Sarkar, S. Kumari, T.K. Kundu, *Density functional theory based studies on the adsorption of rare--earth ions from hydrated nitrate salt solutions on g-C_3N_4 monolayer surface*, J Mol Graph Model, 97, 2020.
12. M. Ismael, Y. Wu, *A mini-review on the synthesis and structural modification of g-C_3N_4 based materials, and their applications in solar energy conversion and environmental remediation*, Sustain Energy Fuels, 3, 2019, 2907-2925.
13. Ranjini Sarkar, Tarun Kumar Kundu, *Unveiling the electronic, optical, and water-splitting properties of rare earth single-atom catalysts supported on graphitic carbon nitride monolayer: A DFT study*, International Journal of Hydrogen Energy, Volume 95, 2024, 449-462.

Boron-Phosphorus Dual Doped Hard Carbon Anode for Sodium-Ion Battery

Sanchayan Mahato, Koushik Biswas
Department of Metallurgical and Materials Engineering,
IIT Kharagpur 721302, West Bengal, India
sanchayan.mahato112@gmail.com;
k_biswas@metal.iitkgp.ac.in

Keywords: Sodium-ion battery; B-P dual doped hard carbon; DFT

1. Introduction

In recent years, hard carbon has gained immense attention as the most potential anode in sodium-ion batteries. However, its relatively low capacity and rate performances limit its industrial application. Herein, experimental and theoretical studies have been done to study the effect of boron-phosphorus dual doping on hard carbon anode materials for sodium ion batteries.

2. Synthesis

Two batches were prepared with 2 wt.% boric acid and 3 wt.% ammonium dihydrogen phosphate added to low cost commercial grade hard carbon. These suspensions were dried at 110°C for 30 h and then, one batch was calcined at 950°C for 2 h under Ar atmosphere (BPHC (Ar)) while the other was calcined under N_2 (BPHC (N_2)).

3. Characterizations

The crystal structure and phase analyses of the samples were done using the powder X-ray diffraction. The morphology of samples was examined using field-emission scanning electron microscope. Raman spectroscope (λ=514 nm) was used to investigate the electronic conductivity of the samples. X-ray photoelectron spectroscopy was done to study the surface chemical states of the samples. The pore structure and surface area were measured from Brunauer-Emmett-Teller (BET) isotherm.

4. Electrochemical measurements

The electrochemical performance was tested using CR2032 coin cells with a 2-electrode configuration. The anode was prepared by mixing active material, acetylene black, and carboxymethyl cellulose in deionized water and slurry casted on Cu-foil (doctor blade method). The anode film was cut with the mass loading was 1.3±0.3 mg/cm². For full cell measurements, carbon coated $Na_3V_2(PO_4)_2F_3$ (NVPF) was used as cathode. Coin cell was assembled using glass fibre (Whatman GF/A, thickness: 0.5 mm) as separator and stainless steel (0.45 mm thick) as current collector. 1 M sodium perchlorate in ethylene carbonate and propylene carbonate (in 1:1 v/v ratio) in 5 wt. %

The project is co-financed by funds from the state budget, granted by the Minister of Science as part of the Excellent Science II Program, project no. KONF/SP/0109/2024/02, subsidy amount 67 870 PLN.

Doskonała Nauka II
Ministry of Science and Higher Education
Republic of Poland
Republic of Poland

fluoroethylene carbonate as electrolyte. Galvanostatic charge discharge measurement, cyclic voltammetry and electrochemical impedance spectroscopy were done for complete cell performance assessment.

5. Computational details: Density functional theory

An analysis of volume increase during the process of sodiation was carried out using the spin-polarized density functional theory (DFT) with the plane wave approach in the Vienna Abinitio Simulation Package (VASP) with MedeA-VASP software [1,2]. The projector augmented wave (PAW) method [3] was used for ion-electron interaction. A broad gradient approximation exchange-correlation method called GGA-PBE, created by Perdew, Burke, and Ernzerhof [4] was used together with a 520 eV limit for the plane-wave foundation in all computations. Van der Waals interactions were incorporated using DFT-D2 approach. The Monkhorst-Pack mesh approach was used for calculations throughout the Brillouin zones with a 7×7×1 k-point mesh [5].

6. Results and discussion

XRD shows [6] presence of partially amorphous carbon with a higher spaced interlayer compared to pristine hard carbon (HC). Unit cell volume change calculated from DFT and XRD suggest less expansion (2.06% for HC compared to 1.7% in dual-doped HC) due to insertion of Na-ions into the structure of dual-doped hard carbon (1.7%) as compared to pristine one (2.06%) that may enhance the cyclic performance and capacity retention of the cells. Microstructure [6] reveals particle size reduction and overall increase in BET surface area [6] due to the synergic effect of B and P contributed to the increase in the rate capability.

Figure 1(a) shows galvanostatic charge discharge characteristics of NVPF || BPHC(Ar) full cell assembly in the voltage range between 2.1 to 4.4 V. It shows that the specific capacity of the full cell to be 102.47 mAh/g at 0.1 C (1 C = 128 mAh/g considering the mass of cathode). The full--cell delivers an average voltage of 3.44 V (energy density = 352.5 Wh/k). Figure 1(b) shows an excellent rate performance of 102.47, 97.47, 91.72 and 84.47 mAh/g at 0.1, 0.2, 0.5 and 1 C. The cyclic retention of the full-cell is 92.16% at 0.5 C after 100 cycles (fig 1(c)).

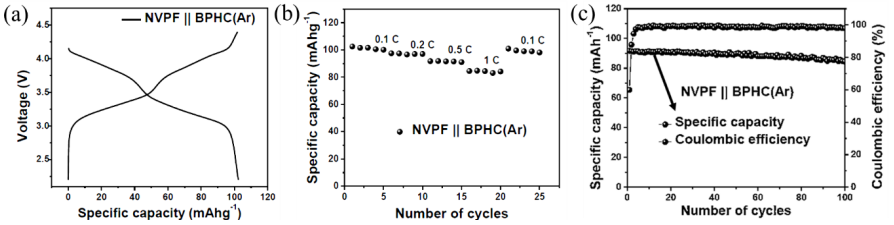

Figure 1. Galvanostatic charge discharge curve of NVPF || BPHC(Ar) full-cell at 0.1 C,
(b) rate capability of NVPF || BPHC(Ar) full-cell and
(c) cyclability and coulombic efficiency of NVPF || BPHC(Ar) full-cell [6]

Figure 2 depicts the band structure (simulated using DFT) of pure and dual-doped HC which shows reduction in band gap in the doped materials (1.874 eV) in comparison to HC (5.36 eV). Thus, electrical conductivity increases after dual-doping as the Fermi level shifts towards the conduction band following the adsorption of boron and phosphorus in HC.

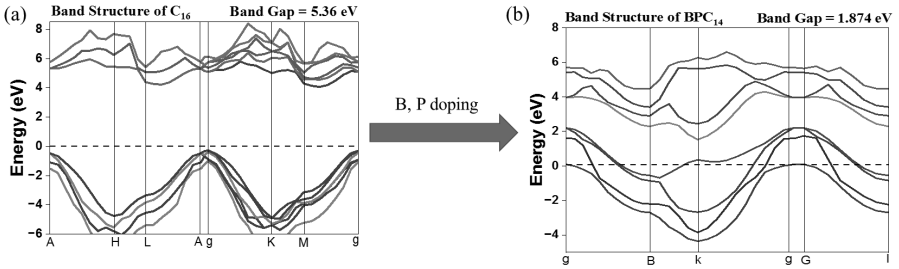

Figure 2. The band structure (simulated using DFT) of pure and boron-phosphorus dual-doped hard carbon [6]

7. Conclusions

Boron and phosphorus dual-doped hard carbons were successfully synthesized using low-cost process. These anodes showed an improved the electrochemical performances in full cell sodium ion batteries. Thus, the dual-doped hard carbon material has a great potential for next generation industry friendly SIB anode.

References

1. Kresse G. and Furthmuller J., *Efficient iterative schemes for ab-initio total energy calculations using a plane-wave basis set*, Phys. Rev. B, 54, 1996, 11169-11186.
2. Kresse G. and Furthmuller J., *Efficiency of ab-initio total energy calculations for metals and semiconductors using a plane-wave basis set*, Comput. Mat. Sci., 6, 1996, 15-50.
3. Kresse G. and Furthmuller J., *From ultrasoft pseudo-potentials to the projector augmented-wave method*, Phys. Rev. B, 59, 1999, 1758- 1775
4. Perdew. J.P., Burke K., Ernzerhof M., *Generalized Gradient Approximation Made Simple*, Phys. Rev. Lett., 77, 1996, 3865- 3868
5. Monkhorst H.J., Pack J.D., *Special points for Brillouin-zone integrations*, Phys. Rev. B, 13, 1996, 5188-5192
6. S Mahato, A Das, K Biswas, *Experimental and theoretical investigation on boron, phosphorus dual doped hard carbon as anode for sodium-ion battery*, J. Energy Storage, 104, 2024, 114422-114432

The effect of composition on local structure formation in BMGs

Debopriyo Banerjee, Amlan Dutta
Department of Metallurgical and Material Engineering,
IIT Kharagpur, 721302, West Bengal, India
debopriyo12101994@kgpian.iitkgp.ac.in1,
amlan.dutta@metal.iitkgp.ac.in

Keywords: Glass transition temperature, Molecular dynamics, Glass forming ability, Icosahedral clusters

1. Background and Motivation

Bulk metallic glass (BMG) is an intriguing category of materials that is being extensively studied due to its superior qualities, such as hardness, specific strength, and stiffness, compared to crystalline materials [1]. Their amorphous structure results in mechanisms related to mechanical, electro-chemical, and transport properties that differ from those in crystalline materials. Consequently, metallic glasses are examined not only for their potential technological uses but also to gain insight into the fundamental physics of these substances. From a thermodynamic perspective, metallic glasses constitute metastable states much removed from equilibrium. Consequently, producing sufficiently big glassy metallic samples has been a technological barrier. Earlier trials seldom yielded samples larger than 1 mm; however, current investigations have documented a ten-fold increase in sample sizes [2]. This has resulted in a renewed interest in exploring technological uses of BMGs, especially in the aerospace and defence industries. In aerospace and defence applications, the properties of materials under extreme conditions are crucial. The response of a material's atomic structure to changes in composition is a critical factor. Due to the amorphous nature of BMGs, accurately calculating the atomic arrangement is challenging as the system lacks long-order translational periodicity. Despite numerous experimental and computational investigations into the elastic, plastic, and creep deformations of bulk metallic glasses (BMGs), only a minimal subset addresses the influence of compositional variation on glass transition temperature (Tg) and atomic structure.

Atomistic simulations can offer a detailed view of a physical process at atomistic scales of length and time, thereby complementing the experimental observations by overcoming many of their limitations. A few computational investigations have studied the structure-property relationship of BMGs and reported the resulting topological changes [3]. Nonetheless, the glaring issues mentioned above are yet to be addressed. The project proposed here is aimed at taking a closer look into these aspects by means of conventional and accelerated molecular dynamics (MD) simulations. In particular, we shall examine ternary glasses of composition, $Zr_{1-x-y}Cu_xAl_y$, providing a two-dimensional composition-space unlike the one-dimensional composition of binary BMGs, which have been studied in most of the reported simulations [4,5].

2. Modeling and Simulation

Formation of Cu-Zr-Al based BMGs: Molecular Dynamics based modeling and simulation are used for the analysis of BMGs. Crystalline samples are initially formed as ternary solid solutions, $Cu_{100-x-y}Zr_xAl_y$, with Zr content ranging from 40 to 60 at.% and Al content from 5 to 10 at.%. The em-

The project is co-financed by funds from the state budget, granted by the Minister of Science as part of the Excellent Science II Program, project no. KONF/SP/0109/2024/02, subsidy amount 67 870 PLN.

Doskonała Nauka II
Ministry of Science and Higher Education
Republic of Poland
Republic of Poland

bedded atom method (EAM) potential regulates atomic interactions. The samples, once generated virtually, undergo structural relaxation and thermal equilibration at ambient temperature. The samples are subsequently melted and rapidly cooled at a rate of 10^{11} K/s to achieve the metastable glassy state.

Structural analysis: Due to the amorphous structure of glassy alloys, the radial distribution function (RDF) has been employed to characterize the atomic spatial distribution [6]. The Voronoi tessellation of the simulation cell utilizes the positions of individual particles as cell centers, thereby elucidating characteristics such as coordination numbers, atomic volumes, and cluster types. All simulations detailed in this work were conducted utilizing the LAMMPS molecular dynamics code. The OVITO software has been utilized for visualization and structural analysis.

3. Radial distribution function analysis

Analysing radial distribution function (RDF) helps to justify the formation of glassy states. It also helps in finding out the relative pairing amongst existing elements. Data obtained from the simulation shows splitting of peaks in the overall and partial RDFs that justifies the glass formation. There exists a great atomic size mismatch between the constituent elements. As a consequence of the same, certain elements finds it easier to form pairs in comparison to other. It is observed that Cu--Cu pair happens at smaller pair separation distance whereas Zr-Zr pair occurs at larger separation distance. With an increase in the Zr content in the overall composition, the probability of formation of Zr-Al pairs increases over the expense of Zr-Cu pair and Al-Al pair.

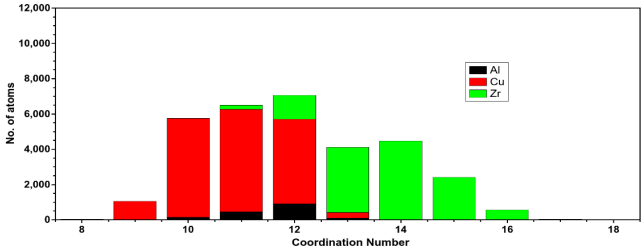

Figure 1. Coordination statistics of individual atom-type for a particular composition of Cu-Zr-Al BMG

4. Coordination number analysis:

The ideal icosahedral clusters exhibit CN = 12. The coordination number of disordered icosahedral clusters ranges in between 9-18. Hence, analysing the coordination number of individual atoms helps us to configure the number of atoms associated with the desired type of cluster. coordination number associated with individual atoms are noted and it is observed that at low CN, Cu atoms dominates whereas Zr atoms mainly attains CN more than 13. An ideal icosahedral cluster is known to show CN = 12. Therefore, out of all the atoms, the atoms and it's type which are involved with CN = 12 are expected to form icosahedral clusters that are required for the glass forming ability (GFA) of the BMG.

5. Determination of Glass transition temperature (Tg):

Tg is the most important factor during the formation of a metastable glassy state. It is a dynamic temperature and is heavily dependent on the rate of cooling. Higher the rate of cooling, higher

is the T_g. However, composition can also alter the magnitude of T_g. Hence, the exact determination of T_g is quite an arduous undertaking. In most of the literature the estimation of T_g seems to be broadly adopted owing the large curvature of the graph used to find T_g. Such a process seems to create more problem during the estimation of T_g since miscalculations can occur quickly due to large spectrum of the temperature associated with the curvature. Hence, a new method is adjusted to estimate T_g properly. The steps involve the fitting of the curve with a fourth-order polynomial and thereby derivating it to find out the exact T_g. The data obtained from the new method shows certain trends trend in between the amount of Al and T_g.

References

1. Wang W.H., *The elastic properties, elastic models and elastic perspectives of metallic glasses*, Progress in Materials Science, 57, 2012, 487-490.
2. Ponnambalam V., Poon S.J., Shiflet G.J., *Fe-based bulk metallic glasses with diameter thickness larger than one centimeter*. Journal of Materials Research,19, 2004, 1320–1323.
3. Amigo N., *Effect of the atomic construction and preparation procedure on the deformation behaviour of CuZr metallic glasses*, Molecular Simulation, 47(15), 2021, 1250–1257.
4. D. Wang, Y. Li, B.B. Sun, M.L. Sui, K. Lu, E. Ma; *Bulk metallic glass formation in the binary Cu–Zr system*, Applied Physics Letter, 84 (20),2004, 4029–4031.
5. Weeks W.P., Flores K.M., *Structural building-blocks of disordered Cu-Zr alloys*, Acta Materialia, 265, 2024, 119624.
6. Zhou Z.Y., Yang Q., Yu H.B., *Toward atomic-scale understanding of structure-dynamics-properties relations for metallic glasses*, Progress in Materials Science, 145, 2024, 101311.

Blood Flow Simulations by Lattice Boltzmann Method

Robert Straka
AGH University of Science and Technology, Faculty of Metals Engineering
and Industrial Computer Science, Department of Heat Engineering and Environment Protection,
al. Mickiewicza 30, 30-059, Krakow, Poland
strakrob@agh.edu.pl

Keywords: Computational fluid dynamics, Blood flow simulations, Lattice Boltzmann Method

1. Introduction

This study addresses the modeling of blood flow using the Lattice Boltzmann Method (LBM). Simulations are performed on three distinct geometrical representations of a selected segment of a left coronary artery. The results are then validated by comparison with those computed by SimVascular, a specialized software for the segmentation of medical image data and the simulation and analysis of patient-specific blood flow.

2. Methods

To simulate blood flow in the arteries, the in-house implementation of the 3D lattice Boltzmann method was used. The solver implements cumulant collision operator with 27 discrete velocities together with the Large Eddy Simulation model of turbulence. Boundary conditions are computed from physiological restrictions, given pressures at inlet, i.e. assumed cardiac output, and pressure at outlet, i.e. microvasculature resistance, together with steady-state flow conditions. The implementation of the solver used the CUDA C framework to speed up the computations, and all simulations were run on GeForce TITAN Z GPUs. Moreover, we used SimVascular software to perform LBM verification for all simulations [1].

3. Results

Simulations of three different geometries were performed both with LBM solver and with SimVascular, the main results are presented in the following subsections.

3.1. Blood flow simulation

The simulation of hemodynamics is conducted across three distinct geometrical configurations, utilizing both the Lattice Boltzmann Method (LBM) and SimVascular tools. The resultant velocity fields and pressure profiles derived from the LBM computations are depicted in Figures 1 and 2. The central geometric configuration is representative of a stenosed vessel, distinctly characterized by an increased blood velocity and a pronounced decrease in pressure.

The project is co-financed by funds from the state budget, granted by the Minister of Science as part of the Excellent Science II Program, project no. KONF/SP/0109/2024/02, subsidy amount 67 870 PLN.

Doskonała Nauka II
Ministry of Science and Higher Education
Republic of Poland
Republic of Poland

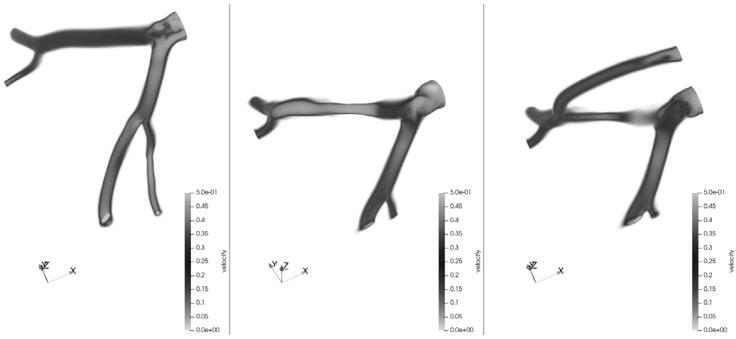

Figure 1. Velocity distribution in the left coronary artery, LBM simulation

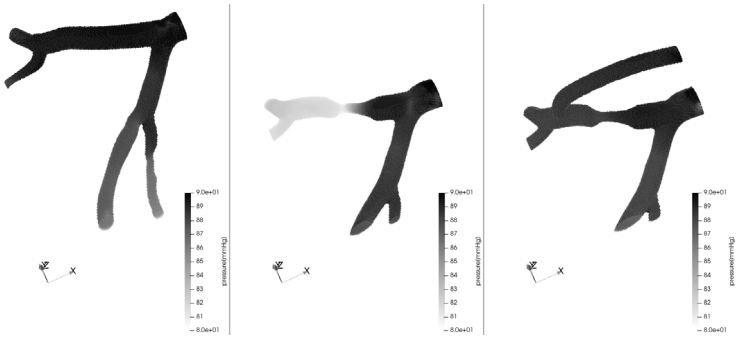

Figure 2. Pressure distribution in the left coronary artery, LBM simulation

3.2. Comparison of blood flow at outlets

A pivotal outcome of the simulations is the quantification of the blood flow through each vessel. Figure 3 illustrates the comparative analysis of volumetric blood flow at various outlets for all geometrical configurations studied.

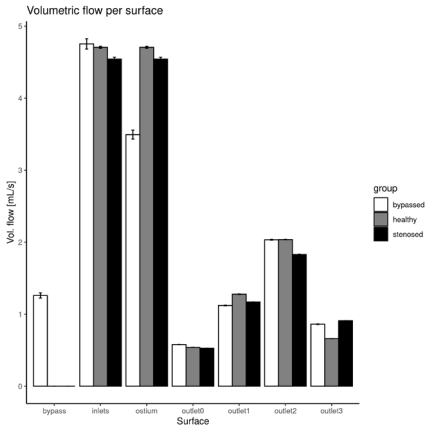

Figure 3. Pressure distribution in the left coronary artery, LBM simulation

References

1. Updegrove A., Wilson N.M., Merkow J., Lan H., Marsden A.L., Shadden S.C., *SimVascular: An Open Source Pipeline for Cardiovascular Simulation*, Annals of Biomedical Engineering, 45, 2016, 525-541 during multipass hot rolling, ISIJ Internation-al, 32, 1992, 359-367

Design of minimally invasive implatological kit for thoratic defects using advanced computational approach

Alicja Turek-Kozik[1], Bartosz Czarnecki[1], Laura Gołąbek[1], Jerzy Dybich[1], Wojciech Korlacki[2], Joanna Sulej-Chojnacka[3], Daniel Andrzejewski[3], Agata Kuliberda[3], Andrzej Milenin[4], Piotr Kustra[4], Marek Paćko[4], Konrad Perzyński[4], Mateusz Sitko[4], Marcin Kwiecień[4], Piotr Bała[4], Łukasz Madej[4], Krzysztof Muszka[4]

[1] BHH Mikromed, 11 Porozumienia Dąbrowskiego 1980 St., 42-530 Dąbrowa Górnicza, Poland
Sieć Badawcza Łukasiewicz – Poznański Instytut Technologiczny….
[4] AGH University of Krakow, Faculty of Metals Engineering and Industrial Computer Science, 30 Mickiewicza Ave., 30-059 Kraków, Poland
joanna.sulej-chojnacka@pit.lukasiewicz.gov.pl, daniel.andrzejewski@pit.lukasiewicz.gov.pl wkorlacki@gmail.com, milenin@agh.edu.pl, pkustra@agh.edu.pl, packo@agh.edu.pl, kperzyns@agh.edu.pl, msitko@agh.edu.pl, mkwiecie@agh.edu.pl, pbala@agh.edu.pl, lmadej@agh.edu.pl, muszka@agh.edu.pl

Keywords: High Entropy Alloy, Ab-initio Modelling, CALPHAD Method, Molecular Dynamics, Mechanical Response

1. Introduction

Within the project a minimally invasive, universal implantology kit for the correction of various chest deformities was developed along with the necessary surgery instruments. Chest deformities – including pectus excavatum (PE) and pectus carinatum (PC) – are the most common congenital anomalies of the chest (both symmetric and asymmetric). In patients with pectus excavatum, the front wall of the chest collapses into the chest cavity. Depending on the severity of the disease, the symptoms may be minor and may concern cosmetic aspects, while in severe cases the compression of the sternum and reduced volume of the chest may decrease vital capacity. In the case of a pectus carinatum, the defect is usually identified in the early years of adolescence. Deformation consists in the bulging of the sternum and the adjacent costal cartilage to the front. In the work a holistic approach was applied to the design of the universal implantology kit, which aim was to minimize the risk of failure at the stage of clinical trials. Approach is based on numerical models developed on the basis of data from computed tomography of skeletal system of the chest with defects. First, preliminary design of the new implant that was proposed based on the experience of medical Prof. Dzielicki. Reverse engineering methodology was then developed. This methodology follows a modified design path such as object-model-concept. The concept mimics some of the critical geometric features of existing objects and creates their accurate or enhanced virtual/physical models. Most commonly, the scanned cloud of points is used as input information to reconstruct the geometry of the investigated object. In this sense, a reverse engineering process depends on the virtual model reconstruction operations using dedicated algorithmic solutions. This process starts

The project is co-financed by funds from the state budget, granted by the Minister of Science as part of the Excellent Science II Program, project no. KONF/SP/0109/2024/02, subsidy amount 67 870 PLN.

Doskonała Nauka II
Ministry of Science and Higher Education Republic of Poland
Republic of Poland

with point cloud data acquisition and terminates as a virtual model. As an output of the first stage of the Project, based on computed tomopgraphy data, a fully 3D finite element models of rib cages with defects (funnel chest, pigeon chest both symmetric and asymmetric) for further numerical investigation, was evaluated. The second state-of-the-art methodology which whas employed is generative design of topology of new universal implantology kit. The purpose of using generative design of implant topology was: 1) guidance for reducing the weight of implants while maintaining strength characteristics and appropriate stiffness and 2) optimization of the shape of the implant in order to prevent stress concentration in the patient's bones and tissues. The third stage of the project included prototyping with 3d printing and mechanical trials using laboratory environment. A prototype set will be developed (in various series), which will be initially manufactured by FDM additive technology and then it will be subjected to mechanical analysis using computer and physical simulations on devices for testing under uniaxial loads and cyclic loads in a complex state of deformation and stress (with non-contact measurement of stiffness, displacement and deformation of the implantation set / ribs using Digital Image Corelation technique). Particular emphasis will be placed on the verification to take place under conditions reflecting the state of stress and forces in the chests with the defects (PE and PC both symmetric and asymmetric).

In parallel, the interrelation between implant material (rolled plate of 316LVM steel grade), its state of microstructure (annealed, hardened, gradient), fatigue life and wear mechanisms will be established. As-received plates will rolled using different deformation as well as asymmetrical rolling to produce different state of austenitic structure. Then, the plates will be subjected to high cycle fatigue tests using unique state-of-the-art Arbitrary Strain Path Machine. Machinability of different states of rolled plates will be established to develop the most optimal machining strategies.

To ensure that the performance of the developed implant and its interaction with ribs (during 2 years of time that is relevant to 17 mln breaths), a multi-scale computer model will also be developed that will be able to assess the impact of stresses and deformations generated by the implementation kit on the local, internal bone structure of different microarchitecture (reflecting the internal rib structure of patients at different ages using Digital Material Representation approach). This approach will assure the verification of designed product under experimental conditions. After positive verification and possible structural corrections, a trial set of 316LVM steel and instruments will be produced by Mikromed. These elements will also be verified in a manner analogous to the plastic prototype kit. Additionally, fatigue life and wear of implant kit assembly (bar, mounting plates, connectors, threads) made of 316LVM steel will be assessed using purpose-built rib cage models with selected, representative chest defects. Finally, the verified version of universal implantation kit will be machined. At that stage also set of implantation surgery tools will be designed, manufactured and tested. An additional innovative tool that will be created as part of the project will be a tool for spatial visualization of the procedure for selecting the type of implant series using the virtual reality environment (VR goggles in which surgeon will be able to see the chest in three-dimensional space with the implementation kit installed). This will significantly improve the preoperation stage.

Proposed new medical product allows for higher forces to be applied and will have much more positive effects in chest defects treatment. It will also allow a new sandwich system of chest deformities treatment for some severe chest defects by simultaneous „internal" and „external" ribs displacement, that has no equivalent in the available literature. It is expected that it will reduce the need for additional rib resections in asymmetrical distortions that require combining the Nuss procedure with the Ravich procedure while it will stabilize the correction plate with a technical solution that excludes the use of destructive wire.

It is expected that the surgical technique, standardized in this way, will allow to optimize the results of treatment of deformities, regardless of its form, and to avoid adverse events described in the literature and perceived in one's own practice. It can also be used in the treatment of sternum instability occurring as a complication after cardiac surgery in 0.2-5% of patients undergoing such surgical access.

Finally, it is expected that proposed within the Project new medical product will definitely contribute to life saving and achieving full recovery, improving health condition and the quality of life.

References

1. Beynon J.H., Sellars, C.M., *Modelling microstructure and its effects during multipass hot rolling*, ISIJ Internation-al, 32, 1992, 359-367.
2. Kobayashi S., Oh S.I., Altan T., *Metal forming and the finite element method*, Oxford University Press, New York, Oxford, 1989.
3. Mori K., Osakada K., *Finite-element simulation of three-dimensional de-formation in shape rolling*, Proc. NUMIFORM'89, eds, Thompson E.G., Wood R.D., Zienkiewicz O.C., Samuelsson A., Fort Collins, 1989, 337-342.
4. Roucoules C., "*Dynamic and metady-namic recrystallization in HSLA steels*", PhD Thesis, McGill University, Montreal, 1992.

Acknowledgements. .

Effect of a New Dieless Drawing Process on the Properties of Biodegradable Zn-Mg Alloy Surgical Wire

Marcin Kapusta[1], Piotr Kustra[1], Anna Osyczka[2], Andrij Milenin[1]
[1] AGH University of Kraków
[2] Jagiellonian University
markapusta@agh.edu.pl, pkustra@agh.edu.pl,
anna.osyczka@uj.edu.pl, milenin@agh.edu.pl

Keywords: surgical wires, biodegradability, biocompatibility, dieless drawing

1. Introduction

Surgical wire is widely used in medicine to secure bone fragments during fracture treatment. Traditionally, surgical wire has been made from stainless steel. While stainless steel offers advantages such as high strength and bioinertness, it also has significant drawbacks, including the need for a secondary operation to remove the wire and excessive compressive stress after bone healing. These limitations highlight the need for biodegradable surgical wire, which: - Eliminates the need for a secondary operation, as the wire naturally degrades after fulfilling its function. - Facilitates smooth load transfer due to the gradual degradation of the wire material as the bone heals. Magnesium- and zinc-based alloys have been identified as promising materials for biodegradable surgical wire [1]. Previous studies have explored various aspects of this problem, including material selection, production technologies, mechanical properties (including performance in surgical knots), biodegradation intensity, and biological properties [2, 3]. For example, the application of such wire in veterinary practice was detailed in [4]. These studies demonstrate that biological, corrosion, and mechanical properties depend not only on the alloy's chemical composition but also on the method of plastic deformation applied during manufacturing. For instance, materials processed through extrusion exhibited better cell survival in *in vitro* tests compared to those processed through drawing. Investigations into the crystallographic texture at various stages of deformation revealed correlations between texture and mechanical or biological properties. Particularly intriguing is the relationship between deformation methods (e.g., extrusion or drawing at varying temperatures) and the biological properties of the resulting material, including potential anticancer effects [2, 4]. However, the production processes currently used to achieve specific geometric dimensions are limited in terms of optimization for enhancing biological properties. This limitation inspired the development of a process that selectively alters the microstructure and crystallographic orientation of the wire without changing its diameter. Such a process could supplement existing manufacturing techniques, improving the biological properties of the final product. This study aims to develop and numerically model this process and analyze its effects on the biological properties of biodegradable surgical wire.

2. Materials and Methods

This study introduces an innovative laser dieless drawing process (referred to as bioLDD) for tailoring the crystallographic texture of the wire to enhance biocompatibility. BioLDD involves

The project is co-financed by funds from the state budget, granted by the Minister of Science as part of the Excellent Science II Program, project no. KONF/SP/0109/2024/02, subsidy amount 67 870 PLN.

Doskonała Nauka II
Ministry of Science and Higher Education
Republic of Poland
Republic of Poland

twisting the wire while optionally elongating it, with deformation facilitated by localized laser heating. This process achieves significant shear strain without altering the wire diameter. A photograph of the developed experimental setup is presented in Figure 1. The ZnMg0.08 alloy was selected as the study material. Initially, an ingot was extruded through a 32-channel die with each hole measuring 1.8 mm in diameter. Subsequently, the material underwent hot drawing at 250°C to produce wire with a diameter of 0.8 mm. This wire served as the precursor for the bioLDD process. To determine optimal heating and deformation parameters (laser power and twisting speed), FEM modelling of the deformation process was conducted using QForm software. Figure 2 illustrates two modelling scenarios. In the first case (Fig. 2a), a laser power of 1 W caused overheating and deformation localization, likely resulting in wire breakage in physical experiments. In the second case (Fig. 2b), a reduced laser power of 0.25 W ensured uniform deformation along the wire's length. *In vitro* cytotoxicity tests were performed on three wire variants, each with a diameter of 0.8 mm: - Wire after hot drawing (HWD). - HWD-obtained wire twisted at room temperature in the bioLDD setup (HWD+CT). - HWD-obtained wire treated with bioLDD at approximately 250°C (HWD+bioLDD). *In vitro* cytotoxicity studies, conducted according to ISO 10993-12:2021 (E), were performed at the Department of Cell Biology and Imaging, Institute of Zoology and Biomedical Research, Faculty of Biology, Jagiellonian University.

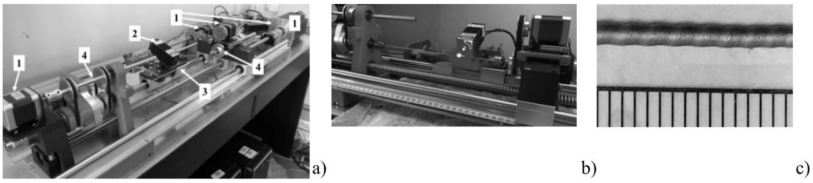

Figure 1. Device for the bioLDD process, designed by authors of proposal (a): 1 - stepper motors, 2 - laser, 3 - drawn wire, 4 - sample twisting system; (b): device during operation; (c): hot-drawn wire with diameter 0.8 mm from ZnMg0.08 alloy after twisting

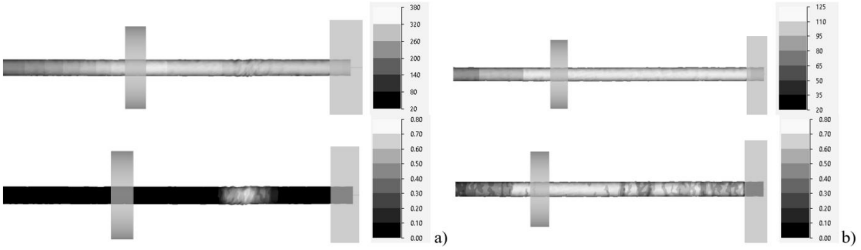

Figure 2. Results of modeling the temperature distribution (upper figures) and effective deformation (lower figures) in the wire during bioLDD at different heating powers: (a) – 1W; (b) – 0.25 W

3. Results and Discussion

In vitro cytotoxicity results for the three wire variants, compared against a perfectly bioinert plastic (TCP), are shown in Figure 3. Wire subjected to HWD exhibited the poorest cell survival. Cold twisting (HWD+CT) to a shear strain of approximately 1.6 significantly improved cell survival. However, applying the bioLDD process at 250°C (HWD+bioLDD) achieved nearly 100% cell viability. These findings suggest a dominant influence of crystallographic texture on biocorrosion behaviour and, consequently, on cell viability. Further investigations are underway to confirm this hypothesis and refine the process parameters.

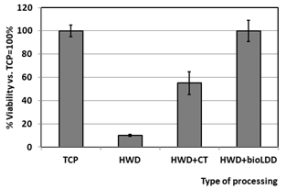

Figure 3. Cells (PDLSC) viability after 24 h exposure of cells to the extracts, extract ratio 0.75 cm^2/ml incubation medium; material - wires 0.8 mm from ZnMg0.08 alloy

4. Conclusions

This study proposes a novel deformation process – bioLDD – to enhance the biological properties of biodegradable Zn-Mg alloy surgical wire without altering its diameter. The process involves twisting the wire during laser heating to achieve large shear deformations. Results demonstrate that bioLDD significantly improves the in vitro biocompatibility of hot-drawn wire. Future research will focus on elucidating the underlying mechanisms and optimizing process conditions to further enhance the biological performance of biodegradable surgical wire.

References

1. Seitz J.-M., Durisin M., Goldman J., Drelich J.W., *Recent advances in biodegradable metals for medical sutures: a critical review*, Adv Healthc Mater., 4, 2015, 1915–1936.
2. Milenin A., et al., *Mechanical properties, crystallographic texture, and in vitro bio-corrosion of low--alloyed Zn–Mg, produced by hot and cold drawing for biodegradable surgical wires*, Archives of Civil and Mechanical Engineering, 21, 2021.
3. Milenin A., et al., *In vitro cytotoxicity of biodegradable Zn-Mg surgical wires in tumor and healthy cells*, Acta of bioengineering and biomechanics, 23, 2021.
4. Milenin A., Kustra P., Lelek-Borkowska U., et al., *In Vitro and In Vivo Degradation of the New Dissolvable Surgical Wire, Produced from Zn Based Low Alloy by Hot and Cold Drawing.*, Metallurgical and Materials Transactions A, 55, 2024, 3434–3449.

An MCDM Framework for Occupational Safety and Health Management in the Sugarcane Farming

Sumit Kumar[1], Millie Pant[1,2]
[1] Department of Applied Mathematics and Scientific Computing, Indian Institute of Technology Roorkee, Uttarakhand, India
[2] Mehta Family School for Data Science and Artificial Intelligence, Indian Institute of Technology Roorkee, Uttarakhand, India
skumar1@as.iitr.ac.in, pant.milli@as.iitr.ac.in

Keywords: Safety Management, Sugarcane Industry, Labor Disease, Health Issues

In agriculture, Sugarcane is a major cultivated crop in India after cotton. It is the lifeblood of millions of farmers and contributes to a pivotal role in the national economy. However, its cultivation process is full of occupational hazards that harm the health and safety of laborers and farmers. Occupational safety and health (OSH) have been a major concern worldwide in sugarcane cultivation. In this study, a comprehensive Multicriteria decision-making (MCDM) framework is proposed to prioritize safety concerns and to identify patterns and factors associated with injuries among farmers and workers in rural Uttar Pradesh in the cultivation of sugarcane. The study specifically addresses injuries and diseases commonly reported during sugarcane cultivation and processing. It focuses on three categories of health and safety issues: (1) Physical injuries, (2) Diseases, and (3) Environmental and occupational hazards. Fourteen specific health concerns are evaluated based on five key factors contributing to their occurrence. The study employs two well-known MCDM techniques, AHP (Analytic Hierarchy Process) and TOPSIS (Technique for Order of Preference by Similarity to Ideal Solution), to rank these concerns and provide actionable insights. The results will emphasize the importance of addressing safety issues and offer a clear framework for implementing preventive measures designed to meet the specific needs of the sugarcane industry.

1. Introduction

Sugarcane is one of the most important crops cultivated in the tropical and subtropical regions, with India being the second-largest producer after Brazil. It is a prominent cash crop and the main source of sugar globally, plays a crucial role in the agricultural economy [1]. In the 2022–2023 season, sugarcane was grown on approximately 5.9 million hectares in India, marking a 6% increase compared to 5.6 million hectares in 2021–2022 [2]. Beyond sugar production, it serves as a raw material for various industries, contributing to the production of biofuels, ethanol, molasses, and other byproducts. Because of its versatility and economic significance, it is called a “wonder cane” [3].

Sugarcane cultivation is labor-intensive and requires a long maturation period of 8 to 12 months, involving considerable effort and resources. Uttar Pradesh, the leading sugarcane-producing state in India, plants the crop in two major seasons: March and May [4]. The process of growing sugarcane, from planting to harvest, is complex and involves various risks. It requires careful management to ensure productivity, quality, and the safety of farmers. The complete process of the cultivation of sugarcane is shown in the figure 1.

The project is co-financed by funds from the state budget, granted by the Minister of Science as part of the Excellent Science II Program, project no. KONF/SP/0109/2024/02, subsidy amount 67 870 PLN.

Doskonała Nauka II
Ministry of Science and Higher Education Republic of Poland
Republic of Poland

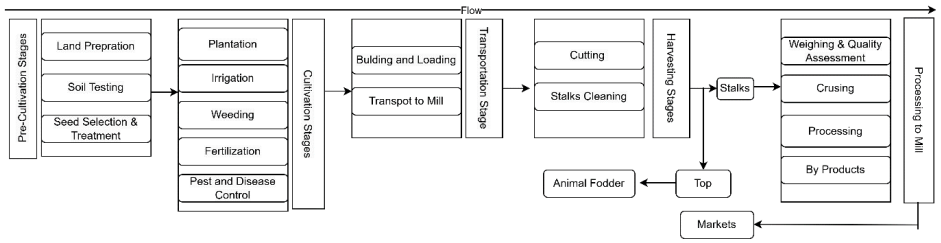

Figure 1. Sugarcane Cultivation Process from Farm to Mill

Occupational safety and health (OSH) has been a major concern worldwide in the agriculture sector. Various undesirable hazards are associated with farming. The sugarcane industry, an important part of agricultural economies, relies heavily on manual labor and exposes workers to various occupational risks [5]. Workers and farmers face a spectrum of safety issues ranging from physical injuries to long-term health effects due to environmental and chemical exposures [6]. Managing these safety concerns effectively requires a structured approach to prioritize actions based on the severity and causes of these issues [7]. However, the lack of comprehensive secondary data poses a significant challenge.

This study aims to develop a Multicriteria Decision-Making (MCDM) framework to address this challenge. Using expert knowledge and literature, the framework analyzes common injuries and health problems, identifying their main causes. The results aim to help stakeholders implement focused safety measures and improve the well-being of workers in the sugarcane industry.

2. Study Area and Methodology

Uttar Pradesh is situated in the northern part of India with an area of 243286 km^2 with coordinates 26.85° N 80.91° E. It covers 48 % of the nation's sugarcane cultivation area and contributes 50 % of India's total production, making it the leading sugarcane-producing state. It produced 2348 lakh tonnes of sugarcane with 107.29 lakh tonnes of sugar in 2022-23 [8].

Amroha district in Uttar Pradesh was chosen for this study because it has well-developed agriculture and good irrigation facilities. Farming is a major economic activity in this district, providing employment to about 60% of the population. The study involved direct one-on-one interactions with farmers in the district. A purposive and stratified multistage random sampling method was employed to collect data through direct one-on-one interactions with farmers.

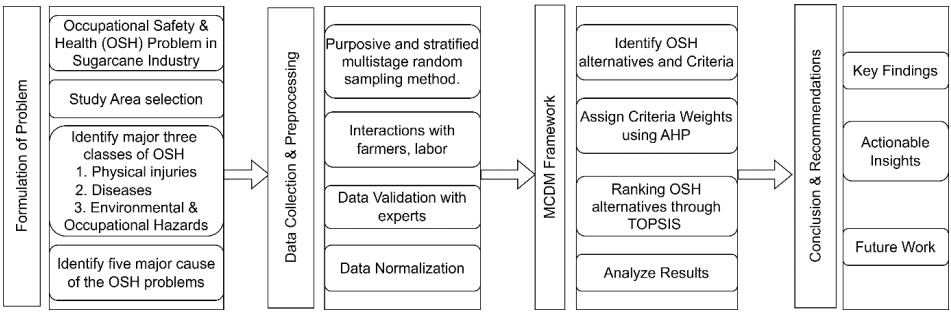

Figure 2. Proposed Framework

The study uses a comprehensive MCDM framework to analyze safety issues in sugarcane cultivation. A hierarchical structure was developed to categorize OSH concerns into three main categories: physical injuries, diseases, and environmental hazards. Fourteen specific concerns were identified and evaluated based on five key factors. The AHP was employed to determine the relative importance of these factors, and the TOPSIS was used to rank the OSH problems and derive actionable insights. The methodology of this study is shown in the figure 2.

The findings of the study will emphasize the importance of addressing occupational safety and health concerns in sugarcane farming. The MCDM framework will prioritize critical safety issues and their causes, offering actionable recommendations for stakeholders. The results will highlight the need for specific actions, such as providing more personal protective equipment, increasing awareness through training programs, and establishing safety protocols. This study will lay the foundation for developing more comprehensive safety measures and will encourage future research to validate the framework with other real-world industry datasets.

References

1. S. Kumar, M. Pant, "*A Mathematical Model to Minimize the Total Cultivation Cost of Sugarcane,*" in Soft Computing for Problem Solving, M. Thakur, S. Agnihotri, B.S. Rajpurohit, M. Pant, K. Deep, A.K. Nagar, Eds., Singapore: Springer Nature, 2023, pp. 529–542. doi: 10.1007/978-981-19-6525-8_40.
2. V. Guhan et al., "*Assessing the impact of climate change on water requirement and yield of sugarcane over different agro-climatic zones of Tamil Nadu*," Sci. Rep., vol. 14, no. 1, p. 8239, Apr. 2024, doi: 10.1038/s41598-024-58771-8.
3. S. Kumar, M. Pant, A. Nagar, "*Forecasting the Sugarcane Yields Based on Meteorological Data Through Ensemble Learning*," IEEE Access, vol. 12, pp. 176539–176553, 2024, doi: 10.1109/ACCESS.2024.3502547.
4. J. Singh, A.K. Singh, M.P. Sharma, P.R. Singh, A.C. Srivastava, "*Mechanization of Sugarcane Cultivation in India*," Sugar Tech, vol. 13, no. 4, pp. 310–314, Dec. 2011, doi: 10.1007/s12355-011-0101-5.
5. T. Mohanaselvan, S.P. Singh, A. Kumar, H.L. Kushwaha, S.K. Sarkar, P. Joshi, "*Mechanization Level and Occupational Health Hazards in Sugarcane Cultivation in India*," Sugar Tech, vol. 26, no. 2, pp. 432–445, Apr. 2024, doi: 10.1007/s12355-023-01356-y.
6. S.S. Kharb, A. Malik, "*Occupational Injuries in North Indian Agriculture: Product Development and Preventive Measures*," J. Inst. Eng. India Ser. C, vol. 105, no. 6, pp. 1603–1613, Dec. 2024, doi: 10.1007/s40032-024-01121-4.
7. S.K. Patel, M.R. Varma, A. Kumar, "*Agricultural injuries in Etawah district of Uttar Pradesh in India*," Saf. Sci., vol. 48, no. 2, pp. 222–229, Feb. 2010, doi: 10.1016/j.ssci.2009.08.003.
8. "*Sugar Industry & Cane Development Department Government of Uttar Pradesh*." Accessed: Dec. 10, 2024. [Online]. Available: https://upcane.gov.in/index.aspx

Modeling the impact of media awareness on malaria

Preeti Deolia
Department of Mathematics, IIT Bombay
preetidyolia@gmail.com

Keywords: Data-driven Epidemic model, Control intervention, Parameter estimation, Model Sensitivity

Malaria, a potentially fatal mosquito-borne disease, poses a significant public health challenge in India. This study proposes an epidemiological model to delve into the transmission dynamics of malaria, particularly considering public awareness along with limited treatment resources. The study explores the existence and stability of various equilibria within this model, shedding light on the dynamics of malaria transmission. The basic reproduction number, denoted as R_0, which plays a crucial role in determining the existence and stability of equilibria is calculated via next-generation matrix. It is shown that when R_0 is less than unity, the disease free equilibrium is locally stable, and when $R_0 > 1$, the endemic state is stable. Real data of cumulative malaria cases is collected and utilized for Odisha, a highly endemic region of India, through numerical simulations. The least square method is used to estimate the key parameters of the model. Numerical simulations are presented to vividly illustrate the analytical findings. The results emphasize the importance of providing proper treatment and public awareness to the infected population.

1. Introduction

Malaria is a life-threatening protozoan disease caused by Plasmodium parasites and transmitted through the bites of infected female Anopheles mosquitoes. The Plasmodium parasites initially multiply in the human liver and bloodstream before transforming into an infectious stage capable of being transmitted to other mosquitoes through subsequent bites [1]. Despite extensive global efforts, including interventions recommended by the World Health Organization (WHO) such as long-lasting insecticide-treated nets and indoor residual spraying, these traditional strategies face numerous implementation challenges [2,3]. Mathematical models have proven to be invaluable tools for analyzing and predicting malaria transmission dynamics [4]. For instance, the study [5] examined the role of bed nets in disease control through a mathematical model, providing insights into their impact on reducing malaria transmission. Another study by Collins and Duffy [6] investigated malaria transmission by incorporating factors such as drug resistance, treatment effectiveness, and mosquito net usage as preventive strategies.

In this context, our study focuses on the role of media-driven social awareness in shaping malaria transmission dynamics. To achieve this, we incorporate an awareness term into a mathematical model using a saturated function. This approach ensures that the density of the infected population directly influences the intensity and reach of information campaigns. As the number of infected individuals changes, the focus and scope of these campaigns adjust dynamically. To the best of our knowledge, this is the first attempt to evaluate the impact of media-driven strategies on malaria prevalence, providing a novel perspective on the role of information dissemination in controlling the disease.

The project is co-financed by funds from the state budget, granted by the Minister of Science as part of the Excellent Science II Program, project no. KONF/SP/0109/2024/02, subsidy amount 67 870 PLN.

Doskonała Nauka II
Ministry of Science and Higher Education
Republic of Poland
Republic of Poland

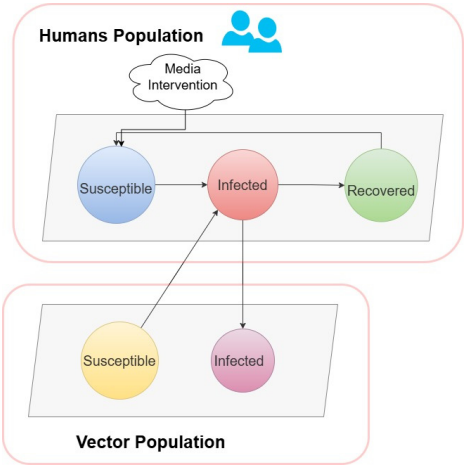

Figure 1. Mathematical model for malaria transmission

2. Results

This paper presents a mathematical model for malaria transmission that incorporates the influence of media awareness. The obtained results indicate that increased media awareness can significantly lower the peak number of infected individuals. Numerical simulations also emphasize the critical role of public awareness and effective treatment strategies in reducing malaria transmission and controlling outbreaks.

References

1. T.D. Keno, O.D. Makinde, L.L. Obsu, *Impact of temperature variability on sirs malaria model*, Journal of Biological Systems 29 (03) (2021) 773–798.
2. E.W. Kaindoa, A.S. Mmbando, R. Shirima, E.E. Hape, F.O. Okumu, *Insecticide-treated eave ribbons for malaria vector control in low-income communities*, Malaria Journal 20 (2021) 1–12.
3. S. Sougoufara, E.C. Ottih, F. Tripet, *The need for new vector control approaches targeting outdoor biting anopheline malaria vector communities*, Parasites & Vectors 13 (2020) 1–15.
4. A.K. Srivastav, M. Ghosh, *Modeling the transmission dynamics of malaria with saturated treatment: a case study of India*, Journal of Applied Mathematics and Computing 67 (1) (2021) 519–540.
5. F.B. Agusto, S.Y. Del Valle, K.W. Blayneh, C.N. Ngonghala, M.J. Goncalves, N. Li, R. Zhao, H. Gong, *The impact of bed-net use on malaria prevalence*, Journal of theoretical biology 320 (2013) 58–65.
6. O. Collins, K. Duffy, *A mathematical model for the dynamics and control of malaria in Nigeria*, Infectious disease modelling 7 (4) (2022) 728–741.

An attempt of application of Bayesian Optimization approach to modelling of materials processing

Jan Kusiak
AGH University of Krakow, al. Mickiewicza 30, 30-059 Kraków, Poland
kusiak@agh.edu.pl

Keywords: Bayesian Optimization, Gauss Process Regression, inverse calibration of models

1. Motivation

Optimization of materials processing requires two milestones: the development of reliable mathematical models of the process being analysed and an efficient optimization technique. Mathematical models in materials processing are complex and usually computationally intensive. Their use in optimization analysis, which requires numerous iterative calculations, is computationally complex and often seems useless because of the long computation time. Therefore, methods are constantly sought to reduce the optimization time by simplifying the model of the analysed process and minimizing the required iterative optimization runs.

One way to solve these problems is to use modelling methods based on machine learning techniques, which lead to a construction of a surrogate model in the form of a „black box" representing the analysed process. The surrogate model describes the analysed process with a good accuracy and requires a significantly shorter computation time. Such a surrogate model can be next successfully used in optimization analysis.

However, most „black box" modelling techniques, such as neural networks, require a large amount of training data. In the case of materials processing, the collection of numerous data is expensive and sometimes even not possible. Therefore, modelling and optimization methods are sought that minimize the number of measurement points required to develop a surrogate model and perform further optimization calculations using it. Gaussian-based modelling techniques and Bayesian optimization methods can help. They try to find the global optimum in a minimum number of steps. The main objective of the presented research is an attempt to apply the Bayesian Optimization technique to the modelling of materials processing problems. As an example, the results of applying this approach to the inverse calibration of a metal flow stress model are presented.

2. General Idea of the Bayes Optimization Technique

The idea of Bayesian Optimisation (BO) technique is based on the Bayes Theorem (Bayesian inference) [1]. This theorem allows the calculation of probabilities for future decisions (a posteriori), which are constructed from known (a priori) probabilities. This makes BO more efficient than random search methods. The basic premise of the BO method is to build a surrogate model of the objective function to be optimised. Most commonly, a surrogate model of the objective function for BO is built using Gaussian Process Regression (GPR) [...]. GPR performs an „a priori" surrogate modelling of the objective function based on an initial set of data points (x, f(x)), where x is a vector

The project is co-financed by funds from the state budget, granted by the Minister of Science as part of the Excellent Science II Program, project no. KONF/SP/0109/2024/02, subsidy amount 67 870 PLN.

Doskonała Nauka II
Ministry of Science and Higher Education
Republic of Poland
Republic of Poland

of optimisation design parameters; f(x) is the corresponding value of the objective function.

The BO algorithm consists of the following steps

1) Collect the initial data points (x, f(x)).
2) Building the surrogate model of the objective function using the GPR approach and the observed values of the objective function.
3) Next, update the surrogate model based on the value of the objective function at this additional sampling point. This additional point should improve the accuracy of the surrogate model. The so-called acquisition function is used to select this additional point.
4) If a minimum/maximum of the analysed objective function is not reached
   a. Implement this additional sampling point into the set of observed data points,
   b. Return to step 2 and continue the calculations.

There are two main elements of this algorithm which are described below: (i) a surrogate model of the objective function and (ii) an acquisition function used to select a next sampling point. The BO algorithm provides (with some accuracy) an approximation of the true objective function and its global minimum/maximum.

The main advantage of the BO algorithm is that it minimizes the number of optimization iterations resulting in a significant reduction in the time consuming computations.

2.1. Surrogate Model based on the Gauss Process Regression

The Gaussian Process is an extension of the multivariate normal distribution suitable for modelling functions of many variables. Gaussian Process inherit the properties of the multivariate normal distribution, and can model even very complex functions. For that reason, Gauss Process Regression is widely used in Bayesian optimization [1]. Its standard form is defined by:

a) the mean function $m(\mathbf{x})$,
b) the covariance function $k(\mathbf{x}, \mathbf{x}')$, which returns the similarity between two points $\mathbf{x}$ and $\mathbf{x}'$.

When the objective function is modelled using the GPR, the expected value of the function $\mathbb{E}[f(\mathbf{x})]$ is determined by the mean value function, i.e. $\mathbb{E}[f(\mathbf{x})] = m(\mathbf{x})$, and the covariance of any two points x and x' is expressed in its standard form as:

$$k(\mathbf{x}, \mathbf{x}') = \mathbb{E}\big[\big(f(\mathbf{x}) - m(\mathbf{x})\big)\big(f(\mathbf{x}') - m(\mathbf{x}')\big)\big] \tag{1}$$

Since the GPR in its main assumption is a distribution of functions, we may not be restricted to this standard form and other forms of mean and covariance functions may be applied.

2.2. Acquisition function

In the presented BO technique, a selection of the next point for a surrogate model is crucial. The question, how to select the best sampling point, appears? The answer is given by using an acquisition function, which determines the next point to be evaluated within admissible solutions. It determines the potential utility of sampling a specific point based on the current state of the optimization process. The acquisition function combines two aspects to identify sample points that should have high values of the objective function and high uncertainty, indicating potential for improvement.

One of the commonly used acquisition functions is that based on the Upper Confidence Bound. In this approach, the next sampling point is selected at the point where the UCB function reaches the maximum in the confidence interval. This function has the following form:

$$f_{acq}(\mathbf{x}) = \mu(\mathbf{x}) + \lambda\sigma(\mathbf{x}) \tag{2}$$

where: $\mu(\mathbf{x})$, $\sigma(\mathbf{x})$ – the mean and standard deviation values of the function $f(\mathbf{x})$, respectively; λ – parameter determining the upper confidence limit. As a result, the next sampling point $\mathbf{x}$' is selected at which the acquisition function takes the maximum value in a given calculation step, i.e.: $\mathbf{x}' = argmax[\mu(\mathbf{x}) + \lambda\sigma(\mathbf{x})]$.

2.3. Simple example of Bayesian Optimization

The results of the BO method can be seen from a simple example of optimizing a function $f(\mathbf{x})$, for which the initial number of data points $\mathbf{x}$ (measurements) is small. Consider the problem of finding a minimum of the following function of one variable:

with the accuracy $\varepsilon = 0.005$.

$$f(\mathbf{x}) = \sin(3x) - x^2 + 0.7; \quad x \in [0.5,1.2] \tag{3}$$

Suppose there are n = 3 initial randomly chosen points (measurements). The BO algorithm was applied to find an optimal solution. After 5 iterations (adding 5 sampling points, only) we obtain optimal solution $f(x^*) = -0.9162$ at $x^* = 0.5709$, while the real optimal values are $f(x^{opt}) = -0.9163$ at $x^{opt} = 0.5734$. The analysed function and obtained optimization results after 5 iterations are shown in the Figure 1.

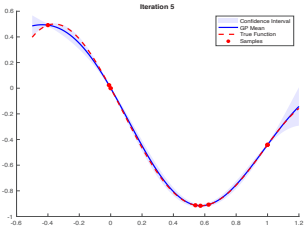

Figure 1. Optimization of function (3) using the BO algorithm

Figure 1 shows the curve of the optimization function (dashed line), the GPR surrogate of the optimization function (3) (blue line), the confidence interval of a surrogate (shaded area), as well as the sample points (red points).

3. Bayes Optimization applied to the inverse calibration of a metal stress-strain curve model

The problem of selecting the optimal parameters of the stress-strain curve of a metal by the inverse method was considered as an example of the use of the Bayesian optimisation method in materials processing. It was assumed that the model of the metal flow curve is described by a function $f(\mathbf{p}, \mathbf{x})$ with m parameters $(p_1, p_2, \ldots, p_m)$ to be evaluated and n variables $(x_1, x_2, \ldots, x_n)$. The purpose of inverse analysis is to identify optimal values of $\mathbf{p}$ parameters based on real measurements, usually subjected to disturbances [3]. In the present work, the inverse analysis was performed on the Ti6Al4V stress-strain curve presented in [2] and modelled by the Hansel-Spittel equation in the following form:

$$\sigma = p_1 \cdot e^{p_2 T} \cdot \varepsilon^{p_3} \cdot \dot{\varepsilon}^{p_4} \cdot e^{\frac{p_5}{\varepsilon}} \cdot (1+\varepsilon)^{p_6 T} \cdot e^{p_7 \varepsilon} \cdot \dot{\varepsilon}^{p_8 T} \cdot T^{p_9} \tag{2}$$

The Bayesian Optimization method described above was used to search for the optimum values of the parameters **p**. The Ti6Al4V stress-strain curve model described by the Hansel-Spittel equation (3) for optimal parameters **p** = [358.5671, -0.0088, -0.0389, -0.1776, -0.0033, 0.0034, -2.4570, 0.0004, 1.0149] is shown in Figure 2. The obtained RMSE (Root Mean Square Error) between the stress-strain curve obtained for optimum parameters and the curve presented in [2] is RMSE = 1.2826.

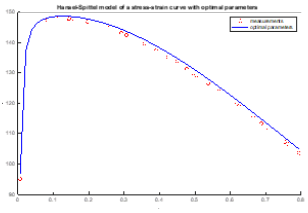

Figure 2. Stress-strain Hansel-Spittel model (3) for the optimal parameters

4. Summary

The main purpose of this article is to attempt to introduce the Bayesian optimisation technique and to encourage its use for solving complex materials engineering problems. The idea of the method is briefly outlined, and then, to illustrate its possible use, the results of the optimisation of a simple 1D function (3) and the calibration of the parameters of the Ti6Al4V stress-strain curve (4) by the inverse method using the BO are presented. The future research will focus on the application of the Bayesian Optimization technique for solving the stochastic problems of the phase transformation in steels microstructure.

References

1. Garnett R., *Bayesian Optimization*. Cambridge University Press, 2023.
2. Chen X., Zhang B., Du Y., Liu M., Bai R., Si Y., Liu B., Jung D.-W., Osaka A., *Constitutive model parameter identification based on optimization method and formability analysis for Ti6Al4V Alloy*. Materials 2022, 15, 1748, https://doi.org/10.3390/ma15051748.
3. Szeliga D., Gawąd J., Pietrzyk M., *Inverse analysis for identification of rheological and friction models in metal forming*, Computer Methods in Applied Mechanics and Engineering, 195, 2006, 6778-6798.

Acknowledgements. Financial support of the Ministry of Science and Higher Education, grant no. 16.16.110.66 is acknowledged.

Modelling of dynamic processes using Artificial Neural Networks

Łukasz Sztangret, Paweł Maczuga, Danuta Szeliga, Maciej Paszyński
AGH University of Science and Technology, al. Mickiewicza 30, 30-059 Kraków, Poland
szt@agh.edu.pl, pmaczuga@agh.edu.pl,
szeliga@agh.edu.pl, paszynsk@agh.edu.pl

Keywords: machine learning, artificial neural networks, ordinary differential equations

1. Introduction

Nowadays, we can observe an intensive expansion of artificial intelligence-based methods into practically all areas, both science and everyday life. One of the most commonly used technique for modeling static and dynamic processes is employing the Artificial Neural Network (ANN). During training, the synaptic weights in the network are changed so that the output values of the network are the same as the values from the dataset. However, recently another method of training artificial neural networks has been developed. This new method, in contrast to the classical approach, does not use a dataset but differential equation which describes the modeled process [1-3]. Therefore, this kind of network is named Physics Informed Neural Network (PINN). The DINN (Data Informed Neural Network) term is used to distinguish between these two alternative approaches to emphasize that the network training process uses dataset.

Within this paper PINN based models were compared with DINN ones. As the modelled process a ferrite transformation during cooling for steel alloy was considered.

2. Modelled process

In the work the model of the ferritic transformation for metallic materials was investigated. Kinetics of ferritic transformation is characterised by the following stages: delay due to time needed for nucleation of the new phase grains and next the maximum rate of the transformation due to growth of a new phase. To describe these phenomena the second order equation was proposed in [5] of the form:

$$B_1 X''(t) + B_2 X'(t) + X(t) = X_{eq}(T) \tag{1}$$

where: $X(t)$ is volume fraction of ferrite, $X_{eq}(T)$ is an equilibrium volume fraction of the ferrite in the temperature T, B_1 and B_2 are temperature dependent coefficients characterizing steel alloy. More information on the phase transformation model can be found in [4] and [5].

Phase transformation can occur at constant or variable temperature. In this paper, a constant temperature during the transformation or a temperature changing at a constant rate was assumed. Figure 1 presents an exemplary volume friction obtained for constant (blue) and variable (red) temperature.

The project is co-financed by funds from the state budget, granted by the Minister of Science as part of the Excellent Science II Program, project no. KONF/SP/0109/2024/02, subsidy amount 67 870 PLN.

Doskonała Nauka II
Ministry of Science and Higher Education
Republic of Poland
Republic of Poland

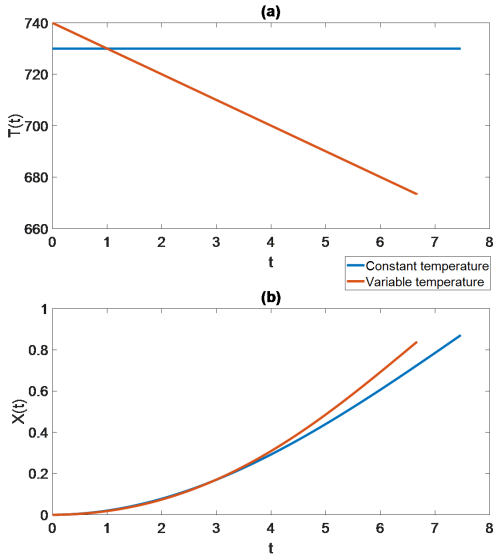

Figure 1. Temperature (a) and volume fraction of the ferrite (b) during phase transformation

3. Artificial Neural Network based modelling

The fundamental difference between PINN and DINN is the way they are trained. In the case of DINN, the training goal is to minimize the differences between the network output values and the correct values from the dataset. Thus the following loss function is minimized:

$$J(\boldsymbol{\theta}) = \frac{1}{2}\sum_{i=1}^{n}\left(DINN(t_i,T) - X(t_i)\right)^2 \tag{2}$$

where n is the number of training records, $DINN(t_i,T)$ is the network output for time t_i and temperature T, and $X(t_i)$ is the required value.

In case of PINN, the loss function is defined by the equation:

$$J(\boldsymbol{\theta}) = \left(B_1\frac{d^2PINN(t,T)}{dt^2} + B_2\frac{dPINN(t,T)}{dt} + PINN(t,T) - X_{eq}(T)\right)^2 + (PINN(0,T) - X(0))^2 \tag{3}$$

The first term in equation (3) is the differential equation to be modeled by the network, i.e. equation (1). The second component is responsible for the initial conditions.

During the training process, n points (i.e. values of t and T) are randomly selected in each epoch. The network output value, the first and second derivatives are calculated. These values are used to calculate the loss function (3). It should be emphasized that during PINN training the correct value that the network should return is not known. This is the basic difference between PINN and DINN training.

The minimization of loss functions (2) and (3) can be performed using any optimization method, however, gradient methods such as ADAM are usually used.

Within the scope of this paper four models were created:

$$X(t) = PINN(t, T) \tag{4}$$

$$X(t) = DINN(t, T) \tag{5}$$

$$X(t) = PINN(t, dT) \tag{6}$$

$$X(t) = DINN(t, dT) \tag{7}$$

Models (4) and (5) assume a constant temperature during the transformation. Therefore, the time and temperature are networks inputs. Models (6) and (7) assume that the temperature changes at a constant rate during the transformation, while the initial temperature is constant. Hence, the model input is the temperature change rate instead of temperature.

4. Conclusion

The obtained results confirm that both approaches are effective and can be used to model processes described by ordinary differential equations.

References

1. Raissi M., Perdikaris P., Karniadakis G. E., *Physics-informed neural networks: A deep learning framework for solving forward and inverse problems involving nonlinear partial differential equations*, Journal of Computational Physics, 378 (2019) 686-707
2. Rojas S., Maczuga P., Muñoz-Matute J., Pardo D., Paszyński M., *Robust variational physics-informed neural networks*, Computer Methods in Applied Mechanics and Engineering ; ISSN 0045-7825. – 2024 – vol. 425 art. no. 116904, s. 1-18.
3. Maczuga P., Paszyński M., *Physics Informed Neural Networks for wave propagation problems*, [in:] KomPlasTech 2023: XXVIII conference on computer methods in materials technology: 5–8 March 2023, Zakopane.
4. Leblond, J.B., Devaux, J., 1984, *A new kinetic model for anisothermal metallurgical transformations in steel including effect of austenite grain size*, Acta Metallurgica, 32, 137-146.
5. Milenin, I., Pernach, M., Pietrzyk, M., 2015, *Application of the control theory for modelling austenite--ferrite phase transformation in steels*, Computer Methods in Materials Science, 15, 327-335.

Acknowledgements. Research project supported by program „Excellence initiative – research university" for the AGH University of Krakow

.

Fast simulations using exponential integrators and finite difference method

Magdalena Pabisz, Askold Vilkha,
Maciej Paszyński
AGH University of Krakow, Al. Mickiewicza 30, 30-059 Krakow
mpabisz@student.agh.edu.pl,
askoldvilkha@gmail.com,
paszynsk@agh.edu.pl

Keywords: Exponential integrators, finite difference methods, MRI scan data

1. Introduction

The exponential integrators method allows for very fast and accurate simulations of time-dependent problems. The method can be applied for discretization in time, and it can be combined with a finite difference discretizations in space. It allows for ultra-fast simulations of complex phenomena. The exponential integrators method [1] has been successfully applied for material science stiff elastodynamic problems [2]. In this presentation we show a summary of the exponential integrators and the illustrative application of the brain tumor simulations [3] using exponential integrators for the Fisher-Kolmogorov diffusion-reaction equation:

$$\frac{\partial u(x,y,t)}{\partial t} = \frac{\partial D(x,y,t)}{\partial x}\left(\frac{\partial u(x,y,t)}{\partial x}\right) + \frac{\partial D(x,y,t)}{\partial y}\left(\frac{\partial u(x,y,t)}{\partial y}\right) + \rho u(x,y,t)\big(1-u(x,y,t)\big) \quad (1)$$

The scalar field $u(x,y,t)$ denotes the tumor cell density, the diffusion coefficient $D(x,y,t)$ depends on the properties of the brain, that can actually change with time when the brain tissue is damaged by the growing glioblastoma tumor, and the $\rho(x,y,t)$ denotes the brain tissue density. The application of the exponential integrators method start from the application of the finite difference discretization in space. We introduce the three-dimensional computational mesh with points $\{x_{i,j,k}\}_{i,j,k=1,\ldots,N}$. We denote by $\{u_{i,j,k}\}_{i,j,k=1,\ldots,N}$ and we rewrite the Fisher-Kolmogorov equation in a discrete form:

$$\frac{\partial u^t_{i,j,k}}{\partial t} = D_{i,j,k}\frac{u^t_{i+1,j,k} - 2u^t_{i,j,k} + u^t_{i-1,j,k}}{h^2} + D_{i,j,k}\frac{u^t_{i,j+1,k} - 2u^t_{i,j,k} + u^t_{i,j-1,k}}{h^2} + \rho u^t_{i,j,k}\big(1-u^t_{i,j,k}\big) \quad (2)$$

We create a sparse matrix based on this spatial discretization.

The project is co-financed by funds from the state budget, granted by the Minister of Science as part of the Excellent Science II Program, project no. KONF/SP/0109/2024/02, subsidy amount 67 870 PLN.

Doskonała Nauka II
Ministry of Science and Higher Education
Republic of Poland
Republic of Poland

```
for i = 2:nx-1
  for j = 2:ny-1
    for k = 2:nz-1
      l = i + (j-1)*nx + (k-1)*nx*ny;
        values(idx) = (diff(i+1,j,k)-diff(i,j,k))/hx2
              + 2.0 * diff(i,j,k)/hx2 + (diff(i,j+1,k)-diff(i,j,k))/hy2
              + 2.0 * diff(i,j,k)/hy2 + (diff(i,j,k+1)-diff(i,j,k))/hz2
              + 2.0 * diff(i,j,k)/hz2;
        row_idx(idx) = l; col_idx(idx) = l; values(idx+1) = - diff(i,j,k)/hx2;
        row_idx(idx+1) = l; col_idx(idx+1) = l-1;
          values(idx+2) = (-diff(i+1,j,k)+diff(i,j,k))/hx2 - diff(i,j,k)/hx2;
        row_idx(idx+2) = l; col_idx(idx+2) = l+1; values(idx+3) = -diff(i,j,k)/hy2;
        row_idx(idx+3) = l; col_idx(idx+3) = l-nx;
          values(idx+4) = (-diff(i,j+1,k)+diff(i,j,k))/hy2 - diff(i,j,k)/hy2;
        row_idx(idx+4) = l; col_idx(idx+4) = l+nx; values(idx+5) = diff(i,j,k)/hz2;
        row_idx(idx+5) = l; col_idx(idx+5) = l-nx*ny;
          values(idx+6) = (-diff(i,j,k+1)+diff(i,j,k))/hz2 - diff(i,j,k)/hz2;
        row_idx(idx+6) = l; col_idx(idx+6) = l+nx*ny; idx = idx + 7;
    end
  end
end
% Create the sparse matrix A
A =sparse(row_idx(1:idx-1), col_idx(1:idx-1), values(1:idx-1), nx*ny*nz, nx*ny*nz);
```

In general, we have the following system of semi-linear Ordinary Differential Equations (ODEs):

$$\frac{\partial U(t)}{\partial t} = AU(t) + F\big(U(t)\big), \;\; U(0) = U_0 \tag{3}$$

Now, the exponential integrators method comes into the picture. We introduce the time discretization:

$$0 = t_0 < t_1 < \cdots < t_{n-1} < t_n < t_{n+1} < \cdots < t_{N-1} < t_N \tag{4}$$

to rewrite the system into:

$$\frac{\partial U_n}{\partial t} = AU_n + F(U_n), \;\; U(0) = U_0 \tag{5}$$

If U_n is the numerical approximation of the solution at time moment t_n, we can compute the integral representation of U_{n+1} in the following way:

$$U_{n+1} = \exp(\tau A)\, U_n + h \int_0^1 \exp\big((1-\theta)\tau A\big) F\big(U(t_n + \tau\theta)\big) d\theta \tag{6}$$

In other words, in the exponential integrators method, the state at time moment t_{n+1} is computed by solving the integral equation, involving the exponential of the matrix A that represents the finite difference discretization of our problem. For the numerical details of the fast exponential integrators algorithm we refer to [3]. The method allows to predict the growth of the glioblastoma brain tumor 1 year forward within 30 minutes on a laptop equipped with MATLAB.

Application of the Robust Variational Physics-Informed Neural Networks augmented with the Collocation Method for stationary Stokes equations

Marcin Łoś[1], Tomasz Służalec[1], Paweł Maczuga[1],
Askold Vilkha[1], Carlos Uriarte[2], Maciej Paszyński[1]

[1] AGH University of Kraków, Poland
[2] University of the Basque Country (UPV/EHU), Leioa, Spain
los@agh.edu.pl, sluzalec@agh.edu.pl,
pmaczuga@agh.edu.pl, askoldvilkha@gmail.com,
carlos.uriarte@ehu.eus, maciej.paszynski@agh.edu.pl

Keywords: Physics-Informed Neural Networks, Collocation Methods, Robust Discrete Formulations

1. Motivation

Physics Informed Neural Networks (PINNs) have been applied to solving Partial Differential Equations (PDEs) by constructing the loss function based on the residual of either the strong (classical PINN) or the weak (Variational PINNs) formulation [1,2]. Some care must be taken in choosing the appropriate norm of the residual to minimize, otherwise the disconnect between the feedback provided by the loss function values available during the training of our neural network and the actual quality of the learned solution as measured in the norms accurately reflecting the nature of the problem being solved may make the training process unreliable. Robust VPINNs (RVPINNs) have been proposed as an alternative approach to constructing the loss function using a stable variational formulation as a foundation, allowing us to establish a concrete, strong relationship between values of the loss function and the error in the desired norm [3]. Robustness, however, comes at the expense of efficiency, since the variational formulation requires expensive integration, and the loss function involves factorization of the Gram matrix. To circumvent these issues, we propose a similar approach based on the finite difference formulation inspired by [4], which avoids integration in the construction of the residual and the Gram matrix, while maintaining the stability of RVPINNs [6].

2. Mathematical framework

In the discrete formulation we seek values of the solution on a set of collocation points, uniformly distributed inside our domain. We approximate continuous notions (L^p norms, differential operators) with their discrete counterparts (finite sums over collocation points, finite differences), inspired by [4]. We redevelop some basic concepts of the continuous theory, like integration by parts, the product rule and Poincaré inequality, in the discrete setting, which allows us to construct discrete formulations of PDEs and prove their properties using familiar techniques used for finite element formulations. The basis functions of our trial and test space are discrete functions equal to 1 at one collocation point and 0 elsewhere. The stability of the resulting variational formulation of the form

$$b(u_h, v_h) = l(v_h) \quad \forall v_h \in V_h \tag{1}$$

The project is co-financed by funds from the state budget, granted by the Minister of Science as part of the Excellent Science II Program, project no. KONF/SP/0109/2024/02, subsidy amount 67 870 PLN.

Doskonała Nauka II
Ministry of Science and Higher Education
Republic of Poland
Republic of Poland

is governed by the Babuska-Brezzi *inf-sup* condition – existence of a constant $\gamma > 0$ such that

$$|b(u_h, v_h)| \geq \gamma |u_h|_{Uh} |v_h|_{Vh} \qquad \forall u_h \in U_h, v_h \in V_h \tag{2}$$

By the Riesz representation theorem, for each $u_h \in U_h$ there exists a *residual representation* $r(u_h) \in v_h$ such that $(r(u_h), v_h)_{Vh} = b(u_h, v_h) - l(v_h)$ for all $v_h \in V_h$. In case of our discrete formulation, such r can be computed solving the equation:

$$Gr(u_h) = RES(u_h) \tag{3}$$

where G is the Gram matrix of the scalar product of V_h and $RES(u_h)$ is the standard vector of residuals used in PINNs. We define our loss function as $LOSS(u_h) = |r(u_h)|_V^2 = RES(u_h)^T G^{-1} RES(u_h)$. Assuming form b has continuity constant M, this loss function satisfies $1/M\sqrt{LOSS} \leq |u_\theta - u_{exact}| \leq 1/\gamma\sqrt{LOSS}$, where u_θ is the solution of the neural network and u_{exact} is the exact solution of the discrete formulation, which means it can serve as a robust approximation of true error, as long as the values of M and γ are not too far apart.

3. Stokes equations

We demonstrate the approach by solving the stationary Stokes equations on a 2D unit square:

$$\begin{aligned} -\Delta u + \nabla p &= f \ in \ \Omega \\ \nabla \cdot u &= 0 \ in \ \Omega \\ u &= g \ on \ \Gamma \end{aligned} \tag{4}$$

where u, p are velocity and pressure of the fluid, f is the forcing term and g is the Dirichlet boundary condition. We rewrite it into a system of first order equations and replace differential operators with their finite difference counterparts.

$$\begin{aligned} -\nabla_+ \cdot \sigma + \nabla_+ \cdot p &= f \\ \nabla_- \cdot u &= 0 \\ \sigma - \nabla_- \cdot u &= 0 \end{aligned} \tag{5}$$

where σ is a new unknown. With carefully chosen boundary conditions, this formulation is well-posed and stable with respect to the discrete version of the adjoint graph norm [6]:

$$|(\tau, v, q)|_V^2 = |\nabla_+ \cdot \tau - \nabla_+ \cdot q|^2 + |\nabla_- \cdot v|^2 + |\tau + \nabla_- \cdot v|^2 + |\tau|^2 + |v|^2 + |q|^2 \tag{6}$$

Using a mix of theoretical analysis and numerical calculations, we can demonstrate the continuity and inf-sup stability of this formulation, that is, we can show existence of constants $M = 1$, $\gamma \approx 1/8$ such that:

$$\gamma |\mathbf{v}|_V \leq \sup_{\mathbf{u} \in U} \frac{(A\mathbf{u}, \mathbf{v})}{|\mathbf{u}|_U} \leq M |\mathbf{v}|_V \tag{6}$$

Speeding up the Robust Variational Physics Informed Neural Networks with the Collocation Method

Marcin Łoś[1], Tomasz Służalec[1], Paweł Maczuga[1],
Askold Vilkha[1], Danuta Szeliga[1], Maciej Paszyński[1]
AGH University of Krakow, Al. Mickiewicza 30, 30-059 Krakow, Poland
los@agh.edu.pl, sluzalec@agh.edu.pl,
pmaczuga@agh.edu.pl, askoldvilkha@gmail.com,
szeliga@agh.edu.pl, paszynsk@agh.edu.pl,
askoldvilkha@gmail.com

Keywords: Tensorial implementation, Variational Physics Informed Neural Networks, Robust loss function

1. Introduction

The methods proposed by Prof. G.E. Karniadakis for solving partial differential equations using neural networks, the so-called Physics-Informed Neural Networks, have been very successful over the past few years. Since its inception in 2019, Prof. Karniadakis' first paper [1] has received more than 12,000 citations, and the paper summarizing Physics Informed Informed Neural Networks methods [2] published in the Nature Reviews Physics has received nearly 5,000 citations. The reason for this is that neural networks informed about physics can increasingly solve partial differential equations with accuracy approaching that proposed by traditional methods such as the finite difference method. For example, for the Partial Differential Equation (PDE), the Poisson problem with the right-hand side being a combination of the sin and exp functions,

$$\Delta u(x,y) = f(x,y) \tag{1}$$

$$f(x,y) = \exp\left(\prod(x-2y)\right)\sin\left(\prod y\right)\left(4\cos\left(2\prod x\right)-3\sin\left(2\prod x\right)\right)-\prod^{2}\exp\left(\prod(x-2y)\right)\sin\left(2\prod x\right)\left(4\cos\left(\prod y\right)-3\sin\left(\prod y\right)\right) \tag{2}$$

with zero boundary conditions, we can employ the Physics-Informed Neural Networks in the following way. We notice that the neural network is a catenation of linear functions $Ax + b$ and the non-linear activation functions,

$$u(x,t) = PINN(x,t) = A_4\sigma(A_3\sigma(A_2\sigma(A_1\{x,t\}+b_1)+b_2)+b_3)+b_4 \tag{3}$$

here $\sigma(x)$ represents the non-linear activation function, e.g. the sigmoid, A_i represent the matrices with coefficients of layers of the neural network, and b_i represent the bias vectors. This represents 5 layers with 100 neurons each, so the first layer matrix A_1 has 2 columns and 100 rows, the other matrices A_2, A_3, has each 200 rows and columns, and the last matrix A_4 has 200 columns and 1 row. The bias vectors has the same number of rows as corresponding matrices (All of them have 100 rows, except the last one which has 1 row). We denote all the parameters of matrices and vectors as $\theta = (A_1,A_2,A_3,A_4,b_1,b_2,b_3,b_4)$.

The project is co-financed by funds from the state budget, granted by the Minister of Science as part of the Excellent Science II Program, project no. KONF/SP/0109/2024/02, subsidy amount 67 870 PLN.

Doskonała Nauka II
Ministry of Science and Higher Education
Republic of Poland
Republic of Poland

The neural network is assumed to be the solution of the PDE (1-2). What does it mean? We need to find the coefficients of the matrices A_1, A_2, A_3, and A_4 and the biases b_1, b_2, b_3, and b_4 (denoted by θ) σ_{uch} that the neural network as a non-linear functions solves (1). This process is usually performed by minimizing the loss function defined as the residual of the PDE

$$RES_{PINN}(x,t) = \sum_{x,y} \left(\Delta PINN(x,y) - f(x,y) \right) \tag{4}$$

In other words, we want to minimize the loss function RES(θ) by finding minimal values of the coefficients of matrices and biases (called the weights of the neural network) such us the residual of the PDE (1-2) is as close to zero as possible. The residual (5) is evaluated at some finite selected set of points (x,y) $\in$ $[0,1]^2$. Notice that we can compute now the second derivatives of the neural network, as defined in the residual loss ΔPINN(x,y). This is because we understand our neural network as the non-linear continuous function that is infinite time differentiated.

The minimization of the residual loss (4) is usually performed by the ADAM algorithm [3]. The convergence of the PINN method and the resulting solution is presented in Figure 1.

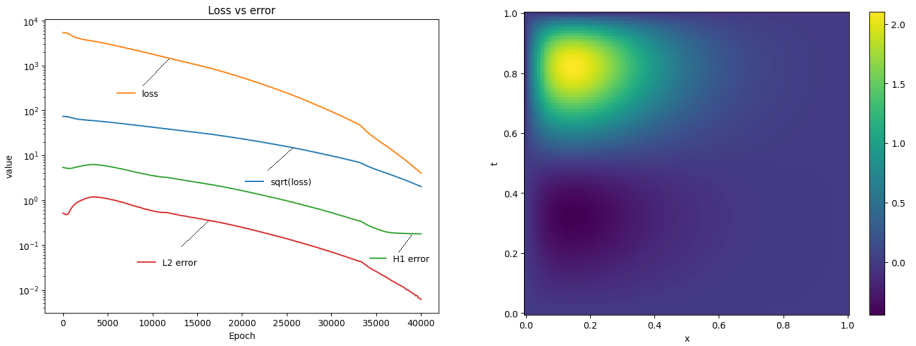

Figure 1. The convergence of the PINN method for the Poisson problem with sin-exp solution, and the resulting solution

The drawback of the PINN method is that the loss function is not robust. It is illustrated in Figure 1, where the plot of convergence of the residual loss function is not equal to the error of the solution as measured in L2 or H1 norms. This applies for the residual loss function as well as for the square root of the residual loss function.

2. Robust Variational Physics Informed Neural Network

In order to get the robust loss function, we first follow the idea of prof. Karniadakis to switch into weak residual formulation introduced in the Variational Physics Informed Neural Network [4,5]. Instead of probing the residual at the points, the loss function is averaged with test functions v(x,y) spread over the computational domain.

$$RES_{PINN}(\theta) = \left(\nabla PINN(x,y), \nabla v(x,y) \right) + \left(f(x,y), v(x,y) \right) \tag{5}$$

Here (w,v) denotes the scalar L2-product, namely (w,v) = $\int$ w(x,y) v (x,y) dxdy. This weak residual loss function can be evaluated for each test function v(x,y). The total loss is defined as the

summation of all the residual weak losses for all test functions.

$$RES_{PINN}(\theta) = \sum_{v} \left(RES_{VPINN}(\theta)\right)^2 \tag{6}$$

Unfortunatelly, VPINN suffers from the same unrobust loss function as PINN. To obtain the robust loss function, following our analysis results summarized in [6], we modify the VPINN loss function by considering the inverse of the Gram matrix G constructed with all the test functions. The robust loss function is defined in the following way

$$RES_{RVPINN}(\theta) = RES_{RVPINN}(\theta)^T inv(G) RES_{RVPINN}(\theta) \tag{7}$$

The gram matrix is computed with L2 scalar products of the test functions. Introduction of this loss function results in a better agreement between the robust loss and the true error.

3. Collocation based Robust Variational Physics Informed Neural Network

The last step of our derivation is to replace the weak residuals with the discrete weak residuals, following our detailed derivation presented in [7]. After this step, the integrals with test functions are replaced by the collocation method computed at the collocation points. We call this method Collocation based Robust Variational Physics Informed Neural Networks. The loss functions remains robust, which is illustrated in Figure 2.

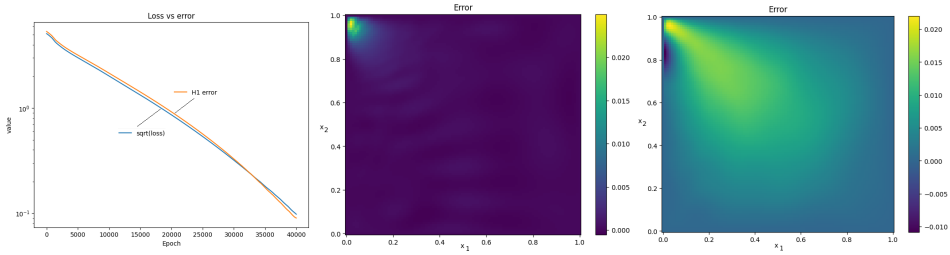

Figure 2. The convergence of the CRVPINN method for the Poisson problem with sin-exp solution. The error of the CRVPINN solution, and the error of the corresponding PINN solution from Figure 1

We perform 40,000 iterations with 100×100 collocation points of CRVPINN or 100×100 points of PINN, usng (as described before) 2 internal layers of the neural network with 200 neurons each. The execution of our Collocation based Robust Variational Physics Informed Neural Network with this setup of parameters on V100 GPGPU from Google ColabPro takes less than 5 minutes. This includes connecting and setting up the virtual environment, and generating output pictures.

The Physics Informed Neural Network implementation using 100×1000 uniformly selected points and the same setup of the neural network takes a similar execution time on V100 GPGPU from Google ColabPro.

The Variational Physics Informed Neural Networks employing 40,000 iterations with 20×20 basis functions, using the same neural network and the tensorial implementation described in [8] takes 12 minutes on A100 GPGPU card from Google Colab.

References

1. M. Raissi, P. Perdikaris, G.E. Karniadakis, *Physics-informed neural networks: A deep learning framework for solving forward and inverse problems involving nonlinear partial di erential equations*, Journal of Computational Physics, 378 (2019) 686-707.
2. G.E. Karniadakis, I.G. Kevrekidis, L. Lu, P. Perdikaris, S. Wang, L. Yang, *Physics-informed machine learning*. Nature Reviews Physics, 3(6) (2021) 422-440.
3. D.P. Kingma, J. Lei Ba, ADAM: *A method for stochastic optimization*, arXiv:1412.6980, 2014.
4. E. Kharazmi, Z. Zhang, G.E. Karniadakis, *Variational Physics-Informed Neural Networks For Solving Partial Differential Equations*, arXiv:1912.00873, 2019
5. E. Kharazmi, Z. Zhang, G.E.M. Karniadakis, *hp-VPINNs: Variational physics-informed neural networks with domain decomposition*, Computer Methods in Applied Mechanics and Engineering, Volume 374, 2021, 113547.
6. S. Rojas, P. Maczuga, J. Muñoz-Matute, D. Pardo, M. Paszyński, *Robust Variational Physics-Informed Neural Networks*, Computer Methods in Applied Mechanics and Engineering, 425, 2024, 116904.
7. M. Łoś, T. Służalec, P. Maczuga, A. Vilkha, C. Uriarte, M. Paszyński, *Collocation-based Robust Variational Physics-Informed Neural Networks (CRVPINN)* arXiv:2401.02300 (2024) submitted to Computers & Structures
8. C. Uriarte, P. Maczuga, A. Vilkha, M. Paszyński, *Tensorial Implementation for Robust Variational Physics-Informed Neural Networks*, submitted to International Conference on Computational Science ICCS 2025

Acknowledgements. This Project has received funding from the European Union's Horizon Europe research and innovation programme under the Marie Sklodowska-Curie grant agreement No 101119556. This work was partially supported by the program "Excellence initiative - research university" for the AGH University of Kraków.

CO2 sequestration problem implementation in the IGA-ADS software

Askold Vilkha, Marcin M. Łoś , Maciej Paszyński
AGH University of Krakow, Al. Mickiewicza 30, 30-059 Krakow, Poland
avilkha@agh.edu.pl, los@agh.edu.pl,
paszynsk@agh.edu.pl

Keywords: CO2 sequestration, Finite-element methods, Isogeometric analysis

1. Introduction

Given the significant influence of carbon dioxide (CO2) on global warming, the development of carbon capture strategies is of the highest importance. One of the prevalent strategies is the process called CO2 sequestration. The main idea of this process is to directly capture the CO2 from the emission sources, such as power plants and factories, and store it in the underground porous structures of both natural and human-made origin (abandoned oil wells, mines, aquifers). This strategy is more beneficial than others (ocean storage, mineralization, direct air capture) both economically and ecologically. It is expected to be the most useful in the short- and medium-term and can help mitigate the economic effects until more environmentally-friendly alternatives for energy production will come to wide usage [4, 5, 7].

In this work, we are implementing the CO2 sequestration problem in the IGA-ADS (IsoGeometric Analysis using Alternating Directions Solver) software [3]. This framework is a Finite-Element Method solver, which has been successfully applied to problems like heat transfer [3], Maxwell's equations solver [6], and tumor growth simulations [8]. In the context of the CO2 sequestration problem, four common situations are outlined: structural, capillar, dissolution, and mineralization [5]. Our solver can be applied to the first three of them, as it does not take into account the chemical reactions in the reservoir, but can effectively simulate the physical behavior of the pumped gas in the porous structure and in the case of pumping into the liquid brine solution. We believe that our method can provide a much-needed fast and reliable solver for this problem. Moreover, we also plan to experiment with the (hydrogen) H2 storage problems and implement the inverse problem solver.

2. Methods

Following [1, 2] we use multiphase Darcy's law for gas and brine phases:

$$\phi \partial_t S_w = \nabla \cdot \left(\frac{S_w}{\mu_w} K (\nabla p - \rho_w g) \right) + q_w \tag{1}$$

The project is co-financed by funds from the state budget, granted by the Minister of Science as part of the Excellent Science II Program, project no. KONF/SP/0109/2024/02, subsidy amount 67 870 PLN.

Doskonała Nauka II
Ministry of Science and Higher Education
Republic of Poland
Republic of Poland

$$\phi \partial_t S_g = \nabla \cdot \left(\frac{S_g}{\mu_g} K \left(\nabla p - \rho_g g \right) \right) + q_g \tag{2}$$

where S_g, S_w are the gas and brine saturation, p is the pressure, is ϕ porosity, K is the permeability tensor, g is the gravitational acceleration, μ_g, μ_w are gas and brine viscosity, ρ_g, ρ_w are gas and brine density, and q_g, q_w are corresponding source terms, and $S_g + S_w = 1$. Taking this constraint into consideration, we can rewrite the equation (1) as follows:

$$-\phi \partial_t S_g = \nabla \cdot \left(\frac{1 - S_g}{\mu_w} K \left(\nabla p - \rho_w g \right) \right) + q_w \tag{3}$$

Hence, we have a system of two equations with two unknown quantities: the gas saturation S_g and pressure p. Summing the equations (2) and (3) gives us:

$$\nabla \cdot \left(\left(\frac{1 - S_g}{\mu_w} + \frac{S_g}{\mu_g} \right) K \nabla p \right) = g K \nabla \cdot \left(\frac{1 - S_g}{\mu_w} \rho_w + \frac{S_g}{\mu_g} \rho_g \right) - \left(q_w + q_g \right) \tag{4}$$

We will then use this equation to compute pressure after setting some initial gas saturation S_g^0. In each following step we compute p^n based on saturation S_g^n (eq. 5):

$$\nabla \cdot \left(\left(\frac{1 - S_g^n}{\mu_w} + \frac{S_g^n}{\mu_g} \right) K \nabla p^n \right) = g K \nabla \cdot \left(\frac{1 - S_g^n}{\mu_w} \rho_w + \frac{S_g^n}{\mu_g} \rho_g \right) - \left(q_w^n + \right. \tag{5}$$

and then compute saturation S_g^{n+1} based on that pressure (eq. 6):

$$S_g^{n+1} = S_g^n + \phi^{-1} \tau \nabla \cdot \left(\frac{S_g^n}{\mu_g} K \left(\nabla p^n - \rho_g g \right) \right) + \phi^{-1} \tau q_g^n \tag{6}$$

Below, we present a table of the parameters of our simulation both in SI and CGS systems. We use that as an additional sanity check, since the simulations should remain the same in shape and behavior and differ only by the numerical values depending on the system used.

Table 1. Simulation parameters

Parameter	SI	CGS
ρ_g	479 (kg/m^3)	0.479 (g/cm^3)
ρ_w	1 045 (kg/m^3)	1.045 (g/cm^3)
g	9.81 (m/s^2)	981 (cm/s^2)
μ_g	$3.95 \cdot 10^{-5}$ (Pa·s)	$3.95 \cdot 10^{-5}$ (Pa·s)
μ_w	$25.35 \cdot 10^{-5}$ (Pa·s)	$25.35 \cdot 10^{-5}$ (Pa·s)
K	$2 \cdot 10^{-14}$ (m^2)	$2 \cdot 10^{-10}$ (cm^2)

The programming implementation is available at:
https://github.com/askoldvilkha/iga-ads-vilkha/tree/881587b8021a7a05c339ce9fde90b-3d6acb24f62/examples/co2_sequestration

3. Results and Future Work

At the time of the submission, we have completed a working direct solver version. The figures below show a few snapshots of the CO2 sequestration simulation.

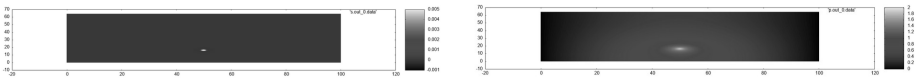

Figure 1. Saturation (left panel) and pressure (right panel) at $t = 0$ sec

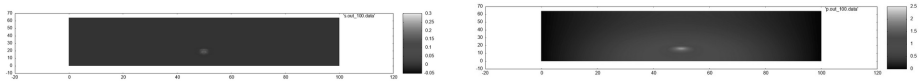

Figure 2. Saturation (left panel) and pressure (right panel) at $t = 1$ sec

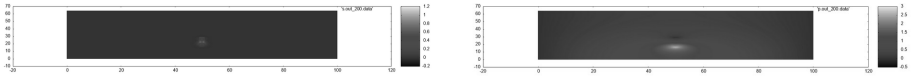

Figure 3. Saturation (left panel) and pressure (right panel) at $t = 2$ sec

The figures 1, 2, and 3 show the evolution of the model system. Please note that the simulation parameters here have been chosen for a simplistic demonstration in order to test the software rather than a profound experiment. We plan extensive testing with various parameter configurations in the short future, and expect to have preliminary results from it by the time of the conference. After completing that step we plan to move on to solving the inverse problem – the optimal location of gas pumping for a stable storage at a given reservoir. Also, the inverse problem might involve determining the best values of the adjustable parameters such as brine liquid properties. We will also experiment with a similar problem for H2 storage.

References

1. Anozie Ebigbo, Holger Class, Rainer Helmig, *CO2 leakage through an abandoned well: problem-oriented benchmarks*, Computational Geosciences, 11 (2007) 103-115.
2. Parisa Shokouhi, Vikas Kumar, Sumedha Prathipati, Seyyed A. Hosseini, Clyde Lee Giles, Daniel Kifer, *Physics-informed deep learning for prediction of CO2 storage site response*, Journal of Contaminant Hydrology, 241 (2021) 103835.
3. Marcin Łoś, Maciej Wozniak, Maciej Paszyński, Andrew Lenharth, Muhamm Amber Hassaan, Keshav Pingali, IGA-ADS: *Isogeometric Analysis FEM using ADS solver*, Computers & Physics Communications (2017).
4. Klaus S. Lackner, *A guide to CO2 sequestration*, Science, 300 (2003) 1677-1678.
5. Osama Massarweh, Ahmad S. Abushaikha, *CO2 sequestration in subsurface geological formations: A review of trapping mechanisms and monitoring techniques*, Earth-Science Reviews, Volume 253, 2024, 104793.
6. Marcin Łoś, Maciej Woźniak, Keshav Pingali, Luis Emilio Garcia Castillo, Julen Alvarez-Aramberri, David Pardo, Maciej Paszyński, *Fast parallel IGA-ADS solver for time-dependent Maxwell's equations*, Computers & Mathematics with Applications, Volume 151, 2023, 36-49.

7. Bielinski, A.: *Numerical simulation of CO2 sequestration in geological formations*. PhD thesis, Universität Stuttgart (2006).
8. Leszek Siwik, Marcin Łoś, Adrian Kłusek, Witold Dzwinel, Maciej Paszyński, *Tuning Two-Dimensional Tumor Growth Simulations*, In Proceedings of the 50th Computer Simulation Conference (pp. 1-12), July 2018.

Acknowledgements. This Project has received funding from the European Union's Horizon Europe research and innovation programme under the Marie Sklodowska-Curie grant agreement No 101119556. We gratefully acknowledge Polish high-performance computing infrastructure PLGrid (HPC Center: ACK Cyfronet AGH) for providing computer facilities and support within computational grant no. PLG/2024/017915.

Technological challenges in developing a self-forming thread design for electric car components

Tomasz Lorenc, Paweł Pańko, Łukasz Rauch,
Marek Pańko, Stanisław Węglarczyk
AGH University of Krakow, Al. Mickiewicza 30, 30-059 Krakow, Poland
pawel.packo@agh.edu.pl, lrauch@agh.edu.pl,
packo@agh.edu.pl, weglarcz@metal.agh.edu.pl

Keywords: self-forming thread, aluminum, rheological models, numerical simulations, electric cars

This article presents key challenges related to the design of a self-forming thread, which aims to reduce contamination and improve assembly stability in the context of aluminum parts. In particular, attention is drawn to the need to balance low assembly torques with strength requirements, which is becoming an important issue in the context of applications in electric cars. A central element of research and innovation was the development of rheological models that will enable accurate simulation of fastener manufacturing processes and optimization of assembly parameters, such as assembly forces and joint strength. The experimental upsetting tests performed provided the necessary data for the construction of rheological models analyzing various aluminum alloys. The cumulative relative error calculated in the field of equivalent plastic deformation φ= max 5% was achieved for the rheological models.

The aim of this research was to obtain knowledge about the relationships between material parameters and functional and strength features of joints and assembly components. As a result, the results contributed to the development of an innovative solution in the design, manufacturing technology and assembly of self-forming thread elements used in the automotive industry, especially in the context of the development of electric cars.

Acknowledgements. The work was financed within the framework of the project entitled „Development of self-forming thread and assembly system in aluminum alloys (SASAl) for use in electric car components. (Screw Assembly Systems for Aluminum) no. POIR.01.01.01-00-0917/21 (National Center for Research and Development).

The project is co-financed by funds from the state budget, granted by the Minister of Science as part of the Excellent Science II Program, project no. KONF/SP/0109/2024/02, subsidy amount 67 870 PLN.

Modelling of temperature change during dynamic deformation of TWIP steel

Zbigniew Gronostajski[1], Katarzyna Jasiak[1], Michał Kostka2,
Mateusz Wesołowski[2], Magdalena Barbara Jabłońska[3]

[1] Wroclaw University of Science and Technology, Faculty of Mechanical Engineering,
Łukasiewicza Street 5, 50-371 Wroclaw,
[2] The Silesian University of Technology, Faculty of Materials Science and Metallurgy,
Krasińskiego Street 8, 40-019 Katowice,
[3] Łukasiewicz Research Network – Institute of Non Ferrous Metals,
Sowińskiego Street 5, 44-100 Gliwice, Poland
zbigniew.gronostajski@pwr.edu.pl, katarzyna.jasiak@pwr.edu.pl,
michal.kostka@polsl.pl, mateusz.wesolowski@polsl.pl,
magdalena.jablonska@imn.lukasiewicz.gov.pl

Keywords: tensile test, TWIP steels, temperature, heat transfer

1. Introduction

The temperature due to the change of the work of deformation into heat influences TWIP steel's microstructure and mechanical properties. It could be determined by FEM or measured by a thermal camera. In the research, both methods were applied to determine the real temperature of the deformed material.

2. Research

The effort to reduce the weight of vehicles results in the use of various groups of materials such as composites, polymers, or light alloy materials [1], however, the most important and the most responsible elements of safety are made of steel [2]. Recently, it has become increasingly important to design modern steels with a wide range of changes in strength and plastic properties. [3].

The temperature of the specimens during the deformation of TWIP steel increases due to the change of the work of deformation into heat. Unfortunately, the literature in this area is very limited. Some such tests have been carried out on TRIP and DP steels. For example, Gao et al. (2015) claimed [4], that the temperature rise during adiabatic heating of TRIP and DP steel had increased with increasing strain rate. For the experiments performed under strain rates from 0.1 up to 2000 s^{-1} the temperature rise of TRIP steels was in the range of 100÷300ºC, while that of DP steel was in the range of 100÷220ºC. More detailed research was carried out by the authors, who showed that at strain rate 1000 s^{-1} temperature increases almost by100ºC and at the moment of necking, it could increase locally to over 300ºC [5]. For TWIP steels there are some studies devoted to the calculation of the amount of generated heat and the assumption that, with the strain rates over 1000 s^{-1}, the deformation process is adiabatic and the whole plastic deformation work is changed into heat [41–43]. In many cases, this seems like a significant generalization. There is very little information on the real temperatures measured through thermovision cameras, especially for high deformation rates. Information will surely be useful during the implementation of TWIP steels, especially for

The project is co-financed by funds from the state budget, granted by the Minister of Science as part of the Excellent Science II Program, project no. KONF/SP/0109/2024/02, subsidy amount 67 870 PLN.

Doskonała Nauka II
Ministry of Science and Higher Education
Republic of Poland
Republic of Poland

the elements of car bodies that ensure their strength and energy consumption. Dynamic tests were performed on a flywheel machine. Two strain rates were used: 170 s^{-1} and 750 s^{-1}.

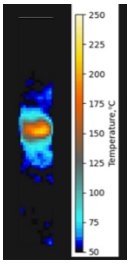

Figure 1. Thermogram at moment of specimen fracture at strain rate 750 s^{-1}

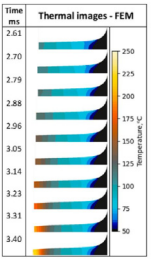

Figure 2. Temperature distribution obtained from FEM for strain rate 750 s^{-1}

2D finite element thermo-mechanical model of uniaxial tensile tests was developed using MARC software. Constitutive material model data were obtained from experimental stress-strain curves. Isotropic hardening is assumed in this study. Young's modulus of 210 GPa and Poisson ratio of 0.3 were assumed. In Figure 2, the change in the temperatures during deformation is presented.

The temperature rises almost linearly together with the deformation and at the moment of deformation localization, a significant localized temperature increase occurs with the progressing development of the necking. In the necking area for steel for the highest strain rate at the moment of rupture, the temperature reaches over 250°C. Studies [7] analyzed the temperature of the deformed sample theoretically with the assumption that the deformation process runs adiabatically. The temperature increases are determined with the use of FEM for the coefficient $\beta = 0{,}9$ describing the amount of plastic deformation work turned into heat. he authors demonstrate both an increase of the twin boundaries and the dislocation density together with the increase of strain rate. The twinning mechanism occur for all the strain rates, however, the density of deformation twins and the number of active twinning systems decreased together with the increase of strain rate. It could be the effect of the temperature. In the [9] the Authors analyzed microstructure of samples subjected to dynamic deformation at the rate of $1.5 \cdot 10^3$ s^{-1} with the Split Hopkinson Bar. Mechanical twins still dominate, however, changes have occurred in the matrix. Non-crystallographic shear bands are formed demonstrating high local deformation. The presence of large shear bands indicates greater involvement of the slip mechanism in the deformation proces.

In the present study, the microstructural changes observed for different strain rates correspond to the increase in temperature of the specimens were analyzed. Generally the density of deformation twins and the number of active twinning systems decreased together with the increase of the temperature were found, although this theory is not entirely confirmed as the nano-twin structures formed for TWIP steels during high strain rates have not been quantitatively analysed.

References

1. D. Frómeta et al., "*Fracture Resistance of Advanced High-Strength Steel Sheets for Automotive Applications*," Metallurgical and Materials Transactions A: Physical Metallurgy and Materials Science, vol. 52, no. 2, pp. 840–856, Feb. 2021, doi: 10.1007/s11661-020-06119-y.
2. R. Kuziak, R. Kawalla, and S. Waengler, "*Advanced high strength steels for automotive industry*," Archives of Civil and Mechanical Engineering, vol. 8, no. 2, pp. 103–117, 2008.

3. Z. Gronostajski, A. Niechajowicz, and S. Polak, "*Prospects for the use of new-generation steels of the ahss type for collision energy absorbing components*," Archives of Metallurgy and Materials, vol. 55, pp. 221–230, Jan. 2010.
4. Y. Gao, C. Xu, Z. He, and L. Li, "*Response characteristics and adiabatic heating during high strain rate for TRIP steel and DP steel*," J. Iron Steel Res. Int., vol. 22, no. 1, pp. 48–54, 2015.
5. Z. Gronostajski, A. Niechajowicz, R. Kuziak, J. Krawczyk, and S. Polak, "*The effect of the strain rate on the stress- strain curve and microstructure of AHSS*," Journal of Materials Processing Technology, vol. 242, pp. 246–259, Apr. 2017, doi: 10.1016/j.jmatprotec.2016.11.023.
6. K. Rahman, V. Vorontsov, D. Dye, "*The dynamic behaviour of at twinning induced plasticity steel*", Mater Sci Eng A. 2014; vol. 589, pp:252-256, doi: 10.1016/j.msea.2013.09.081.42.
7. W. Cai, C. Wang, C. Sun, L. Qian, M. Fu, "*Microstructure evolution and fracture behaviour of TWIP steel under dynamic loading*", Mater Sci Eng A, 2022, vol. 851, pp: 143657, doi: 10.1016/j.msea.2022.143657.43.
8. Park J, Kang M, Sohn S, Kim S-H, Kim H, Kim N, Lee S., „*Quasi-static and dynamic deformation mechanisms interpreted by micro-structural evolution in twinning induced plasticity (TWIP) steel*" Mater Sci Eng, A. 2017, vo. 684, pp: 54–63. https://doi.org/10.1016/j.msea.2016.12.037.
9. M. Jabłońska, K. Kowalczyk, "*Microstructural aspects of energy absorption of high manganese steels*," Proc. Manuf. 2019, vol 27, pp: 91–97, doi: 10.1016/j.promfg.2018.12.049.

Acknowledgements. Work carried out within the framework of the project UMO-2019/35/B/ST8/02184 „Effect of the heat generated during deformation at high strain rates on the structure and properties of high manganese steels with twinning as the dominant deformation mechanism" and UMO-2023/51/B/ST11/01607 "The influence of complex strain path on the microstructure, deformation mechanisms and mechanical properties of TWIP steel" both financed by The National Science Centre (NCN) Poland.

Numerical simulation of precipitates evolution during solidification and ageing of Super 304H steel

Roman Kuziak, Adam Zieliński, Hanna Purzyńska, Łukasz Poloczek
Łukasiewicz Research Network Upper Silesian Institute of technology,
Karola Miarki Street 12-14, 44-100 Gliwice
roman.kuziak@git.lukasiewicz.gov.pl,
adam.zieliński@git.lukasiewicz.gov.pl,
hanna.purzyńska@git.lukasiewicz.gov.pl,
lukasz.poloczek@git.lukasiewicz.gov.pl

Keywords: Super 304H austenitic steel, precipitation processes, Calphad metohod, numerical simulations

1. Introduction

Super 304H austenitic heat-resistant steels is widely used in ultra-supercritical boilers, mainly in superheater and reheater tubes, due to favorable combination of creep and oxidation resistance at high temperatures [1]. The chemical composition of Super 304H austenitic steel is given in Table 1. The microstructural evolution and mechanical properties of the Super304H steel during exposure to high temperatures have attracted considerable research attention. Zieliński [1] revealed that the precipitation of Cu-rich disperse particles inside grains during aging at 650°C and 700°C, effectively improved the strength of the Super 304H steel. The same effect was related to the precipitation of M23C6 carbide on grain boundaries. The addition of Nb is intended to increase the strength of the steel trough the precipitation of Nb(C,N) particles. Moreover, the presence of both Nb and N can also cause the precipitation of fine Z_Phase (NbCrN) what also could contribute to the strength of the Super 304H steel during creep [2]. Other phases that have been identified in this steel in service or during creep tests include sigma [1,3], M23C6 [1,4] and (Cr, V)2 N [5].

Table 1. Chemical composition (wt.%) of Super H304H austenitic steel

C	Si	Mn	P	S	Cu	Cr	Ni	Nb	B	N	Al
0.09	0.20	0.80	0.003	0.001	2.99	18.40	8.80	0.48	0.004	0.11	0.006

The aim of the investigation presented in this paper is to gain understanding of the precipitation processes occurring in Super 304H austenitic steel using the Calphad method [6].

2. Methodology

The investigation was performed in reference to the ageing experiments performed on Super 304H samples, described in [1]. Prior to ageing, the samples were solution treated at 1000°C for 1 hour, followed by water cooling. The ageing was performed at 700°C during 10 000, 20 000, 30 000 and 50 000 hours. Thermodynamic and kinetic modelling was performed, respectively, using ThermoCalc and TC-PRISMA software. In the TC-PRISMA software a physics-based

The project is co-financed by funds from the state budget, granted by the Minister of Science as part of the Excellent Science II Program, project no. KONF/SP/0109/2024/02, subsidy amount 67 870 PLN.

Doskonała Nauka II
Ministry of Science and Higher Education Republic of Poland
Republic of Poland

approach was implemented based upon the Langer-Schwartz theory and its development and numerical implementation in the Kampmann-Wagner (numerical) approach [7-9]. Both programs take advantage of the CALPHAD method. The calculations presented in this paper were performed using ThermoCalc software (v. 2023a) and database TCFE11.

The microstructure investigation was carried out using Joel JSM 6610LV scanning electron microscope (SEM). The precipitations were identified using TITAN 80-300 transmission electron microscope (TEM). The Metilo program was used for the assessment of the precipitates size which was defined as mean equivalent diameter.

3. Results

3.1. Results of the equilibrium calculations

The calculated volume fractions of phases that can form under equilibrium conditions, as function of temperature, are shown in Figure 1. The detailed description of the phases is given in Table 2.

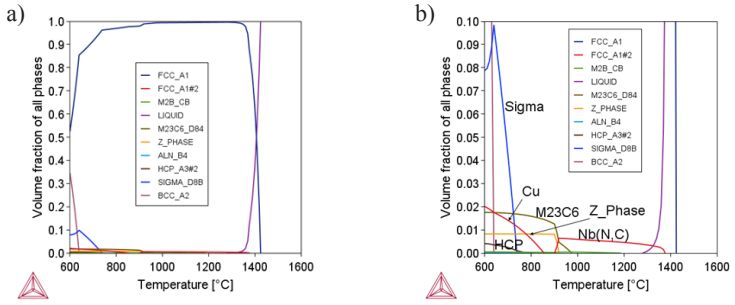

Figure 1. The fraction of equilibrium phases as function of temperature

Table 2. Temperature range of the equilibrium secondary phases occurrence

Predicted phase	Temperature range [°C]
FCC A1/Austenite	1 424.4
FCC_A1#2/Nb(N,C)	1 373.3
$M_{23}C_6$_D84	973.3
Z_Phase	919.5
ε Cu	847.5
Sigma_D8B	736.7
HCP_A3#2/Cr_2N	763.4
M_2B_CB	1 163.1
AlN_B4	814.4
BCC_A2	638.7

One can see that the first formed element during the steel solidification is carbonitride Nb(C,N). The phases that can form under service conditions include: $M_{23}C_6$ carbide, Z_Phase, ε_Cu, Sigma phase and Cr_2N nitride. The results of the thermodynamic calculations are in a good agreement with the experimental observations [1].

3.2. Simulation of the solidification process with Scheil module

The results of the calculations presented in section 3.1 relate to the thermodynamic equilibrium. Therefore in the next stage, the simulation of the solidification process was performed using non-equilibrium Scheil [10] model that is incorporated in the ThermoCalc program. The simulation was performed assuming back diffusion phenomenon for C and N. The assumed cooling rate during the solidification was 1°C/s. The results of the simulation are presented in Figure 2 and Figure 3. The following phase transformations sequence was predicted during cooling from the liquid phase:

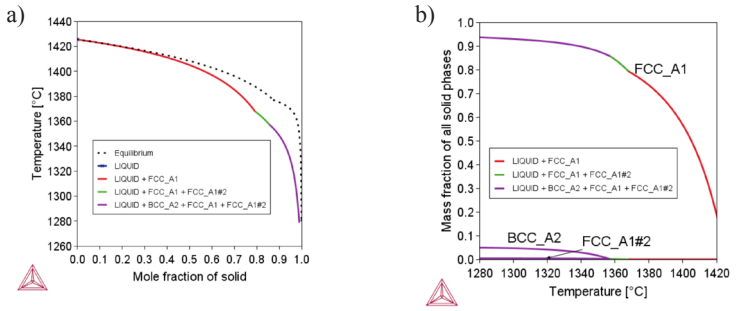

Figure 2. Scheil simulation of the solidification process: (a) mole fraction of solid phase; (b) volume fraction of phases formed during the solidification

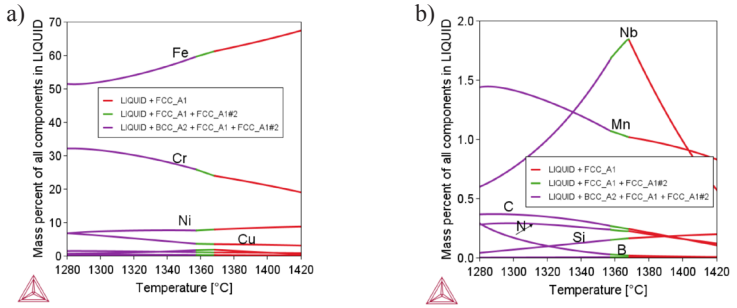

Figure 3. Segregation of elements into inter-dendritic liquid phase during the solidification process

From Figure 3, one can see that non-equilibrium solidification leads to a substantial increase of Cr in the liquid phase, resulting in the δ ferrite formation although the content of this phase is low. The formation of δ ferrite was observed in welds of Super 304H steel [11].

3.3. Simulation of the kinetics of the precipitation proces

The simulation of the kinetics of the precipitation reaction is a very advanced process, since it requires adjustment of many model coefficients. For the sake of illustration, here the precipitation process of sigma phase is considered. The precipitation of this phase has a substantial impact on the mechanical properties of Super 304H steel [1]. Figure 4 presents the sigma phase particles in the sample of Super 304H steel.

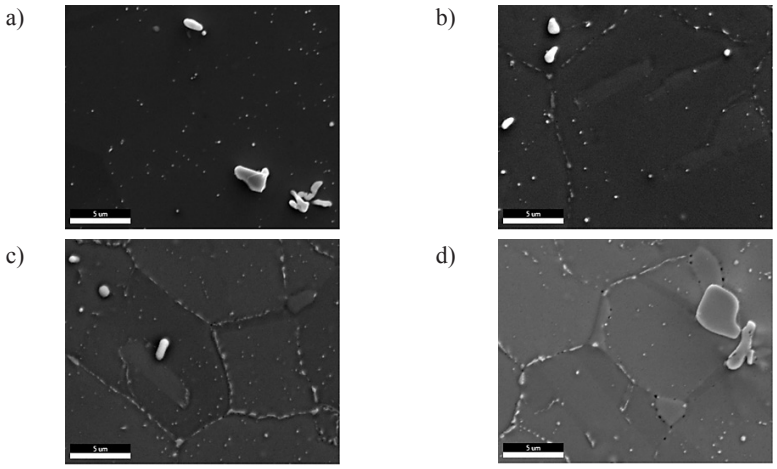

Figure 4. Precipitates of sigma phase in Super 304H steel: a) initial state, b) 10 000 h, c) 30 000 h, d) 50 000 h

Interfacial energy (precipitate/matrix) is the most important parameter used in the precipitation kinetics simulations. For the sake of illustration, precipitation of Following [12] the value of this parameter 0.032 J/m^2 was assumed.

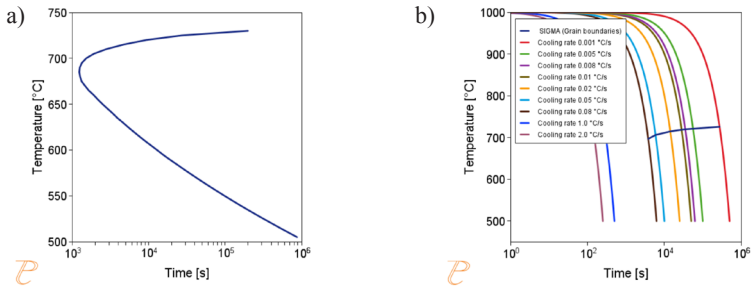

Figure 5. TTT – (a) and CCT – (b) diagrams for the precipitation of sigma phase

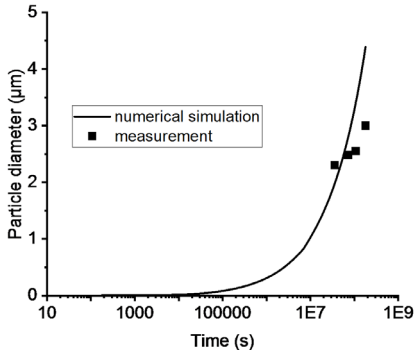

Figure 6. Comparison of the measured values of the mean value of sigma phase equivalent diameter with the results of the numerical simulations

Figure 5 presents the results of the TTT and CCT diagrams calculations. The TTT diagram (Figure 5a) shows that the sigma phase precipitation starts at the lowest time (incubation period) at approximately 690°C. Since the reaction is diffusion controlled, lowering temperature causes extension of the time for the start of precipitation process. This also causes the suppression of the process as the cooling rates following solution treatment are greater than 0.1°C/s (Figure 5b).

Figure 6 presents the results of the calculations of the variation of mean particle diameter changes as function of time. The results of the mean particle diameter are also included in this figure.

The results of the calculation presented in Figure 6 suggest that the precipitation reaction did not reached equilibrium even at the longest ageing time. It should be noted that the results of the simulation compare fairly well with result of the measurement.

4. Conclusions

1) The application of CALPHAD method enabled obtaining a concise and accurate description of the precipitation processes occurring in Super 304H steel. The obtained results are in a very good agreement with the results of the investigations presented in technical literature.
2) The adjusted precipitation kinetics model, implemented in PRISMA program, can be used for the prediction of the evolution of precipitates at times beyond these applied in the laboratory experiments.
3) The thermodynamic calculations also can be used to modify the chemical composition of Super 304H steel to obtain new functional capabilities.

References

1. Zieliński A., *Trwałość eksploatacyjna żarowytrzymałych stali o osnowie austenityczej*, Monografia, GIT, 2021.
2. Golański G, Zieliński A, Purzyńska H, *Precipitation Processes in Creep-Resistant Austenitic Steels*, http://dx.doi.org/10.5772/intechopen.70941.
3. M. Jesenský, *Structure stability and weldability of stainless steels*, Ph.D. Thesis, MTF STU, Trnava, Slovakia; 2006.
4. Padilha AF, Escriba DM, Materna-Morris E, Rieth M, Klimenkov M, Precipitation in AISI 316L(N) during creep tests at 550 and 600 °C up to 10 years, J Nucl Mater 2007;362:132–8.
5. Cheng-yu Chia,n, Hong-yaoYub, Jian-xinDongb, Wen-qingLiuc, Shi-changChengd, Zheng-dong Liud, Xi-shanXieb, *The precipitation strengthening behavior of Cu-rich phase in Nb contained advanced Fe–Cr–Ni type austenitic heat resistant steel for USC power plant application*, Progress in Natural Science: Materials International 2012;22(3):175–185.
6. Lukas HL, Fries SG, Bo Sundman, *Computational thermodynamics – The CALPHAD method*, 2007.
7. Langer J, Schwartz K, *Kinetics of nucleation in near-critical fluids*, Physical Review A 21 (1980).
8. Kampmann R, Wagner R, *Decomposition of alloys: the early stages*, [in:] Proc. 2nd Acta-Scripta Metall. Conf., Pergamon, Oxford, 1984, pp. 91–103.
9. Wagner R, Kampmann, Voorhees PW, *Homogeneous second-phase precipitation, Materials science and technology*, [in:] Phase Transformations in Materials, ed. by Gernot Kostorz, p. 948 Wiley-VCH (2001).
10. Siedlecki J, Szopa R, Wojciechowska W, *Numerical simulation of solidification process using the Scheil model*, Scientific Research of the Institute of Mathematics and Computer Science, 2007, Volume 6, Issue 1, pages 253-260.
11. Kumar MV, Balasubramanian V, Rao AG, *Effect of filler addition on solidification behaviour and hot tensile properties ofGTA-welded tube joints of Super 304H austenitic stainless steel*, International Journal of Mechanical and Materials Engineering (2015), DOI 10.1186/s40712-015-0051-x
12. Shunyi L. *Precipitation behaviour of the super austenitic stainless steel SANICRO® 35 and the effect on impact toughness and pitting corrosion resistance*, Degree Project in Materials Science and Engineering, Stockholm, Sweden, 2022.

Numerical modelling of thin-layer PLD sputtering using the COMSOL Multiphysics numerical package

Bartłomiej Kopecki, Konrad Perzyński, Łukasz Madej
AGH University of Krakow, Mickiewicza 30 av., Krakow, 30-059, Poland
kopecki@agh.edu.pl, kperzyns@agh.edu.pl,
lmadej@agh.edu.pl

Keywords: simulation, pulsed laser deposition, ablation, COMSOL, sputtering

1. Introduction

Metal and ceramic coatings applied by laser ablation are becoming increasingly widely used in industry materials. Their use allows for a significant improvement in the functional properties of standard materials by, e.g., increasing abrasion resistance (ceramic coatings), reducing thermal conductivity (thermal barriers), or improving the level of biocompatibility (biocompatible coatings). Laser ablation phenomena have been intensively studied since the 1960s when initially used in LIBS (Laser-Induced Breakdown Spectroscopy) or LIF (Laser-Induced Fluorescence). Since then, the physicochemical phenomena occurring during laser-target interaction have been thoroughly researched [1]. The prime example of a currently used laser ablation technique is the Pulsed Laser Deposition (PLD) method. However, due to the short duration of the laser pulse in this process (nanoseconds, femtoseconds), some process parameters are difficult to measure using laboratory techniques, e.g. the temperature reached during the interaction of the laser beam with the sputtered material [1]. Additionally, the process itself requires taking into account many variables such as laser energy, refractive index, etc. At the same time, the analysis of the results obtained in the process requires the use of specialized laboratory equipment such as a transmission electron microscope. All that makes the research time-consuming and costly. Therefore, there is a need to support such investigations with computer-aided technology design techniques.

That is why the current work aims to develop a complex numerical model based on the finite element (FE) method to simulate the material's behaviour during PLD with high accuracy. As a result, such an approach allows for replacing time-consuming experimental studies with simulations, leading to a deeper understanding of the process and faster determination of the required sputtering parameters, eventually reducing production costs.

2. Pulsed Laser Deposition modelling

As mentioned, the aim of this work is to create a numerical model of the thin-film PLD deposition method within the commercial numerical package COMSOL Multiphysics. The developed model simulates the process of heating the material intended for evaporation using a laser beam and the deposition of the material layer on the substrate. The model includes information such as laser energy, laser-material interaction on the surface, pulse time, frequency, light wavelength and the total duration of the process. The model allows for the assessment of the increase in the thickness

The project is co-financed by funds from the state budget, granted by the Minister of Science as part of the Excellent Science II Program, project no. KONF/SP/0109/2024/02, subsidy amount 67 870 PLN.

Doskonała Nauka II
Ministry of Science and Higher Education
Republic of Poland
Republic of Poland

of the deposited film depending on the given parameters and time. At the same time, data entry is maximally simplified so that the user running the simulations does not need to have extensive knowledge of the FE method or the mathematical equations capturing the underlying physics. The developed model allows for the simulation of thin film deposition from pure metals, alloys and ceramic materials. However, at this stage, it does not take into account chemical reactions occurring between the components of the deposited material, the substrate or the atmosphere of the PLD chamber. The developed deposition model consists of two cylinders representing the sputtered material and the PLD chamber, respectively, presented in Figure 1.

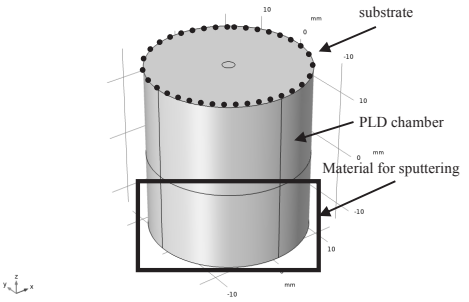

Figure 1. Model assembly for simulation

Heating of the deposited material with a laser was conducted according to the approach presented by Cocean, et al. and based on the Heat Transfer in Solids module[2]. The second approach will be tested in the future based on the Radiative Beam in Absorbing Media and Radiation in Absorbing-Scattering Media modules [3]. This method of heating with a laser beam was used in the deposition model, which additionally uses the Free Molecular Flow module. The model was tested for laser energy of 50, 100 and 150 mJ, and a pulse time of 10 ns and temperature results are gathered in Figure 2. The simulation results were also compared with the experimental data available in the literature [4], as presented in Figure 3.

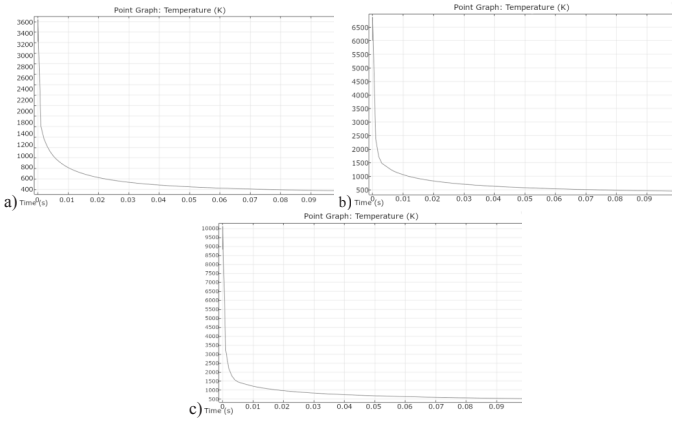

Figure 2. Temperature evoluition during the entire simulation for a) 50 mJ, b) 100 mJ, c) 150 mJ

As presented, after a single laser beam pulse, the maximum thickness of the deposited film was obtained at the level of 0.01 nm for 50 mJ, 0.29 nm for 100 mJ, and 0.59 nm for 150 mJ. The

thickness of the deposited film depends on the temperature reached in the hotspot during the process, for 50 mJ a temperature of 3600 K was reached, for 100 mJ 6500 K, and for 150 mJ 10,000 K.

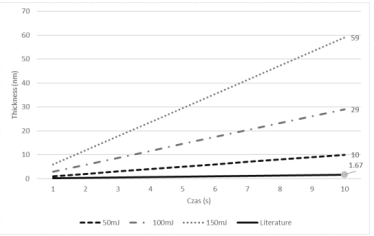

Figure 3. Comparison of extrapolated data from simulations and literature [4]

Comparing data obtained from simulation and literature and taking into account higher laser influence in simulated cases, it can be concluded that the simulation gives results in a realistic range.

3. Conclusions

Creating a user-friendly model of PLD sputtering facilitates the selection of parameters for the process and creates a basis for further work on this topic. The use of numerical modeling allows to speed up the selection of the PLD process parameters to several hours and reduces the requirements for a large number of laboratory experiments. The developed model at the current stage allows for determining what parameters can work in reality and, with some approximation, what thickness of the deposited film will be obtained.

References

1. Cocean, A.; Cocean, G.; Postolachi, C.; Garofalide, S.; Pricop, D.A.; Munteanu, B.S.; Bulai, G.; *Cimpoesu, N.; Motrescu, I.; Pelin, V.; et al. High Energy Pulsed Laser Beam to Produce a Thin Layer of Crystalline Silver without Heating the Deposition Substrate and Its Catalytic Effects*. Quantum Beam Sci. 2024, 8, 16. https://doi.org/10.3390/qubs8020016.
2. Cocean, A.; Cocean, I.; Gurlui, S.; & Iacomi, F. *Study of the pulsed laser deposition phenomena by means of Comsol Multiphysics*. Univ. Politeh. Buchar. Sci. Bull. Ser. A Appl. Math. Phys. 2017, 79, 263-274.
3. Frei, W. *Modeling Absorption and Scattering of Collimated Light*. https://www.comsol.com/blogs/modeling-absorption-and-scattering-of-collimated-light [07.01.2025].
4. Kadri, L.; Abderrahmane, A.; Bulai, G.; Carlescu, A.; Doroftei, C.; Motrescu, I.; Gurlui, S.; Leontie, L.; Adnane, M. *Optical and Structural Analysis of TiO2–SiO2 Nanocomposite Thin Films Fabricated via Pulsed Laser Deposition Technique*. Nanomaterials 2023, 13, 1632. https://doi.org/10.3390/nano13101632.

Acknowledgements. Research project supported by program „Excellence initiative – research university" for the AGH University of Krakow.

Defect-Influenced Plasticity and Deformation Mechanisms in Ni-Based High Entropy Alloys under Nanoindentation

Francisco Javier Dominguez-Gutierrez[1], Edyta Wyszkowska[1], Gordana Markovic[2], Marie Landeiro Dos Reis[3], Amil Aligayev[1], Damian Kalita[1], Iwona Jozwik[1], Krzysztof Muszka[4], Lukasz Kurpaska[1]

[1] NOMATEN Centre of Excellence, National Center for Nuclear Research, 05-400 Swierk/Otwock, Poland

[2] Institute for Technology of Nuclear and Other Mineral Raw Materials, 11000 Belgrade, Serbia

[3] LaSIE UMR CNRS 7356, La Rochelle Université, Av. Michel Crépeau, 17042 La Rochelle Cedex 1, France

[4] AGH University of Krakow, al. Mickiewicza 30, 30–059 Kraków, Poland

javier.dominguez@ncbj.gov.pl, edyta.wyszkowska@ncbj.gov.pl, markovicg1997@gmail.com, marie.landeiro_dos_reis@univ-lr.fr, amil.aligayev@ncbj.gov.pl, damian.kalita@ncbj.gov.pl, iwona.jozwik@ncbj.gov.pl, muszka@agh.edu.pl, lukasz.kurpaska@ncbj.gov.pl

Keywords: Nanoindentation, Plastic deformation, MD simulations, Microstructural Characterization

1. Introduction

High entropy alloys (HEA) have emerged as a promising class of materials owing to their exceptional mechanical properties, such as high strength and excellent ductility. These attributes have spurred considerable interest in their potential application as advanced structural materials. In particular, Ni-based HEAs have attracted attention due to their distinctive combination of mechanical performance and chemical stability. To elucidate the fundamental plasticity mechanisms governing their behavior, nanoindentation tests were performed at room temperature on samples characterized by large grain sizes. The use of large-grained samples is a deliberate strategy aimed at minimizing grain boundary effects, thereby providing a more intrinsic evaluation of the material's deformation behavior. Complementing the experimental investigations, atomistic simulations have been employed to explore plastic deformation processes at the nanoscale, with a specific focus on dislocation nucleation and propagation. This computational approach allows for a detailed examination of the influence of microstructural defects-such as stacking fault tetrahedra (SFTs) and voids-on the mechanical response of the alloy. By comparing pristine materials with defected counterparts, this study aims to delineate the defect-mediated plastic deformation mechanisms that dictate hardening behavior. Stress–strain analyses, dislocation density evaluations, and atomic shear strain mappings collectively provide comprehensive insights into the dynamic evolution of deformation, surface morphology, and slip behavior.

The integrated experimental and computational framework presented herein not only deepens our understanding of the interplay between microstructural defects and mechanical properties in Ni-based HEAs but also offers valuable guidance for optimizing these materials for advanced structural applications.

The project is co-financed by funds from the state budget, granted by the Minister of Science as part of the Excellent Science II Program, project no. KONF/SP/0109/2024/02, subsidy amount 67 870 PLN.

Doskonała Nauka II

Ministry of Science and Higher Education
Republic of Poland

Republic of Poland

2. Methods

Experimental Methods – We investigate two different [001] HEAs: NiFeCrCo and NiFe23. Nanoindentation tests were performed using a NanoTest Vantage system with a 3 nN force sensitivity and 0.002 nm depth sensitivity. A Synton-MDP diamond Berkovich-shaped indenter with a tip radius of 50–100 nm was used for all measurements, ideal for comparison with atomistic simulations. The tests applied a 150 mN load with 100 indentations spaced 100 μm apart. The microstructural evolution of the homogenized sample was analyzed using a ThermoFisher Helios 5 UX SEM, equipped with an EDAX Velocity Pro EBSD camera for precise crystal orientation mapping. EBSD was conducted with a 0.25 μm step size, and data analysis was performed using EDAX OIM Analysis 8 software, excluding points with a confidence index (CI) below 0.1. TEM analysis was carried out on a JEOL JEM-F200 at 200 kV. Thin foils for TEM were prepared using the FIB lift-out technique with a ThermoFisher Helios 5 UX dual beam SEM, with final thinning done at 2 keV to minimize Ga ion effects on the microstructure.

Computational Methods – The initial sample was a pristine FCC [001] Nickel crystal oriented with 18.7 million Ni atoms, measuring (71,69,42) nm^3. NiFe23 and NiFeCrCo alloys were created by substituting Ni atoms with Fe, Cr, and Co atoms respectively. Energy optimization was achieved using the FIRE 2.0 protocol, with an energy tolerance of 10^{-6} eV. The sample was then thermalized at 300 K for 100 ps using an NPT thermostat, followed by a 10 ps relaxation to dissipate artificial heat, ensuring a homogeneous temperature and pressure profile. For nanoindentation, the sample was divided into three sections along the z-direction to set boundary conditions. The two lowest layers were frozen to maintain atomic stability during indentation, with a thermostatic region above to dissipate heat. The remaining layers were dynamic, where atom interactions occurred as the indenter tip deformed the surface. A 5 nm vacuum region was added above the sample. The indenter was modeled as a non-atomic repulsive rigid sphere with a radius of 12 nm. The tip's position moved at a speed of 20 m/s during loading and unloading, with an initial gap of 0.5 nm. MD simulations were conducted using LAMMPS with corrected EAM interatomic potentials with periodic boundary conditions along the x and y axes, simulating an infinite surface. The process lasted 225 ps with a time step of 1 fs with a maximum depth of 3nm, and the defects were introduced in agreement with the Silcox and Hirsch mechanism, SFTs can be formed from an equilateral triangular vacancy plate situated on the (111) planes and spherical voids were obtained by removing atoms.

3. Results

Figure 1 presents the MD simulation setup for defected NiFeCrCo HEA alongside an SEM image showing pile-up formation after nanoindentation. The characteristic 4-folded rosette pattern aligns with MD results, where slip traces propagate along [110] and its symmetrical planes. The HR-TEM image reveals SFT in the indented sample, consistent with atomistic modeling. SFT

formation obstructs half-loop propagation from the indenter tip, limiting the evolution of prismatic dislocation loops (PDL). This behavior is strongly influenced by surface characteristics, SFs, and dislocation glide energies during nanoindentation loading.

Figure 2 shows the pile-up formation in defect-free NiFe23, with the characteristic fourfold rosette pattern observed in SEM experiments, demonstrating good agreement with simulations. Additionally, we examine the effect of voids by considering different radii located close to the surface, revealing two key mechanisms: (i) voids can obstruct SF planes propagation and dislocation half-loops, and (ii) if a void is smaller than the stacking plane, it is absorbed, facilitating the formation of a PDL. Our study demonstrates that nanoindentation-induced plasticity in Ni-based CSAs is strongly influenced by microstructural defects, with SFTs and voids playing a critical role in dislocation propagation and pile-up formation. The combined experimental and atomistic

modeling approach provides fundamental insights into defect-mediated deformation mechanisms, offering guidance for optimizing the mechanical properties of these alloys for advanced structural applications.

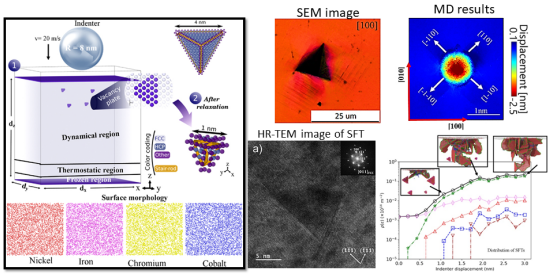

Figure 1. Schematic of the nanoindentation simulation (left) and structural characterization of the NiFeCrCo HEA, with SEM and HR-TEM images revealing pile-up formation and SFTs, consistent with MD simulations (right)

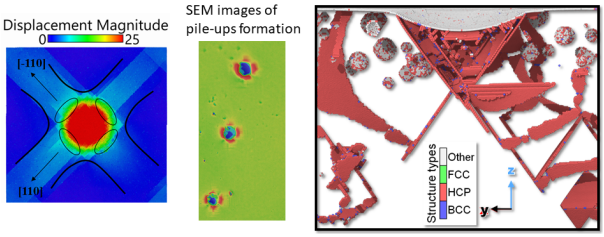

Figure 2. Comparison between MD and SEM image for pile-up formation of NiFe23 (left) and visualization of stacking planes evolution and their interaction with voids (right).

Our study demonstrates that nanoindentation-induced plasticity in Ni-based HEAs is strongly influenced by microstructural defects, with SFTs and voids playing a critical role in dislocation propagation and pile-up formation. The combined experimental and atomistic modeling approach provides fundamental insights into defect-mediated deformation mechanisms, offering guidance for optimizing the mechanical properties of these alloys for advanced structural applications.

References

1. L. Kurpaska, F. Javier Dominguez-Gutierrez, Y. Zhang, K. Mulewska, H. Bei, W.J. Weber, A. Kosińska, W. Chrominski, I. Jozwik, R. Alvarez-Donado, S. Papanikolaou, J. Jagielski, M. Alava a h *Effects of Fe atoms on hardening of a nickel matrix: Nanoindentation experiments and atom-scale numerical modeling*, Materials & Design 217, 110639 (2022).
2. F.J. Dominguez-Gutierrez, A. Olejarz et al. *Atomistic-level analysis of nanoindentation-induced plasticity in arc-melted NiFeCrCo alloys: The role of stacking faults*, J. Appl. Phys. 135, 185101 (2024).
3. A. Naghdi, F.J. Domínguez-Gutiérrez et al. *Dynamic Nanoindentation and Short-Range Order in Equiatomic NiCoCr Medium-Entropy Alloy Lead to Novel Density Wave Ordering*, Phys. Rev. Lett. 132, 116101 (2024).
4. A. Ustrzycka, F.J. Dominguez-Gutierrez et al. *Atomistic analysis of the mechanisms underlying irradiation-hardening in Fe–Ni–Cr alloys*, Int. J. of Plasticity 182, 104118 (2024).
5. F.J. Dominguez-Gutierrez et al. *Plastic deformation mechanisms in BCC single crystals and equiatomic alloys: Insights from nanoindentation*, Computer methods in materials science 24, 37 (2024).

6. Wenyi Huo, Shiqi Wang, F.J. Dominguez-Gutierrez et al. *High-entropy materials for electrocatalytic applications: a review of first principles modeling and simulations,* Mat. Res. Lett. 11, 713 (2023).
7. M. Landeiro Dos-Reis et al. *On the stability of nanovoids in fcc metals and the influence of hydrogen*, Acta Materialia 281, 120400 (2024).
8. M. Landeiro Dos-Reis et al. *Atomic scale simulations for the diffusion-assisted crossing of dislocation anchored by vacancy clusters*, Phys. Rev. Materials 4, 103603 (2020).

Acknowledgements. Research was funded through the European Union Horizon 2020 under Grant Agreement No. 857470, the Foundation for Polish Science International Research Agenda PLUS, grant No. MAB PLUS/2018/8, the initiative of the Ministry of Science and Higher Education under agreement No. MEiN/2023/DIR/3795, and the Ministry of Science, Technological Development, and Innovation of the Republic of Serbia, grant No. 451-03-136/2025-03/200023. We gratefully acknowledge Polish high-performance computing infrastructure PLGrid (HPC Center: ACK Cyfronet AGH) for providing computer facilities and support within computational, grant No. PLG/2024/017084.

Digital Twin for temperature prediction in the laser hardening process of NC10 steel

Piotr Lacki, Anna Derlatka, Michał Lacki, Kuba Lachs
Czestochowa University of Technology, J.H. Dabrowskiego 69, 42-201 Czestochowa, Poland
piotr.lacki@pcz.pl, anna.derlatka@pcz.pl,
michal.lacki3210@gmail.com, kublac24@gmail.com

Keywords: digital twin, neural networks (ANN), FEM, laser hardening

1. Introduction

Laser hardening, which is increasingly used in industry, is performed to achieve a hard and wear-resistant surface layer. This technology is suitable for all materials that can undergo flame and induction hardening. Today, laser hardening is fully automated and allows for the treatment of components with nearly any level of geometric complexity. Its application enables the processing of parts that, due to their design or function, could not be hardened using other methods. In the laser hardening process, only about 20% of the heat is introduced into the material compared to induction hardening. This significantly reduces the need for subsequent mechanical processing. Additionally, laser hardening allows the operation to be completed in a relatively short time. During the process, the surface layer of the workpiece is heated to the austenitizing temperature, just below the material's melting point. Approximately 40% of the laser's emitted power is absorbed; however, in practice, the absorption rate depends on specific process conditions and the material's properties. To ensure effective laser hardening, tests are conducted to select optimal laser parameters and to properly prepare the surface.

Currently, the engineering focuses on developing methods for simulations and optimization of different processes. From years the finite element method [2] and method of fundamental solutions [3] are known. Methods of analysis of variance (ANOVA) [1], artificial neural networks (ANNs) [4], genetic algorithms (GA) [5] and statistically equivalent representative volume elements (SERVE) for microstructural characterisation [6] are becoming more and more popular.

This study presents a Digital Twin (DT) for temperature prediction during the laser hardening process of NC10 steel. This steel is a traditional tool material commonly used for manufacturing tools designed for cold plastic forming. It is characterized by a high carbon and chromium content, as well as a significant amount of retained austenite after quenching from high temperatures [7]. A parametric numerical model based on the Finite Element Method (FEM) was developed to simulate the laser hardening process. This numerical model was then used to generate results for various process parameters. These data sets were subsequently applied to train an Artificial Neural Network (ANN).

2. Numerical model

To analyse temperature variations in the material during the laser hardening process, a parametric FEM model was developed. Creating a parametric numerical model for the laser

The project is co-financed by funds from the state budget, granted by the Minister of Science as part of the Excellent Science II Program, project no. KONF/SP/0109/2024/02, subsidy amount 67 870 PLN.

Doskonała Nauka II
Ministry of Science and Higher Education
Republic of Poland
Republic of Poland

hardening process requires incorporating key components to accurately reflect the physical phenomena occurring during material treatment. This study considers laser beam modelling (using a Gaussian heat source), laser power, beam scanning speed, spot shape, and exposure time. The model also accounts interactions with the external environment. The thermal model for NC10 steel includes the following properties: thermal conductivity λ = 24.2 W/mK (at 700°C), specific heat capacity c = 460 J/kgK, and the laser absorption coefficient on the sample surface. The model also incorporates the variable geometry of the sample. Three-dimensional solid finite elements (3D Solid) were used, with the mesh element size not exceeding 1.6 mm. An example of the temperature distribution along with the sample dimensions is shown in Figure 1.

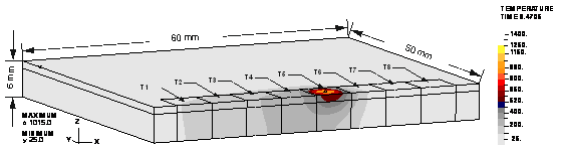

Figure 1. The example of the temperature distribution, °C on the surface of the analyzed sample

The selection of parameters in the laser hardening process primarily depends on the type of material being treated, the thickness of the components, the performance requirements of the hardened element, and the type of laser used. Precise control of all process parameters is crucial for achieving optimal results. Modern control systems enable dynamic adjustment of parameters in real-time, allowing more efficient and effective hardening. However, accurately predicting the hardening temperature is not always possible. This temperature depends on the amount of energy delivered, the thermal conductivity of the material, and the changing thermal conditions within the hardened component. For NC10 steel, it is essential to precisely reach the target temperature range of 960–1000°C. Figure 2 presents temperature variation graphs over time for measurement points T1–T8 in the analysed case study. The analysis shows that the lowest temperature was recorded at the first point T1, with a value of TT1 = 940°C. At each subsequent point, the peak temperature slightly increased. The highest temperature was recorded at the final point, T8, reaching TT8 = 1015°C.

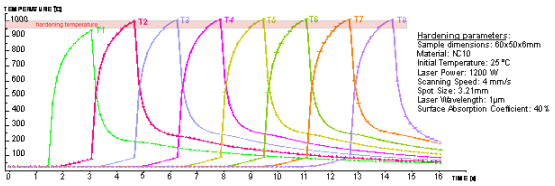

Figure 2. The temperature variation, °C over time, s for the points T1–T8

In the hardening process, the cooling rate also plays a crucial role. Cooling typically occurs through natural heat dissipation into the surrounding cooler material (air cooling). In the analysed case, the cooling rate did not fall below vc=700°C/s. Due to the rapid cooling, the material's structure does not revert to its original state, resulting in the formation of a very hard martensitic structure.

3. Digital Twin

The concept of the Digital Twin (DT) was introduced over a decade ago as an innovative and versatile tool, offering significant advantages such as real-time monitoring, simulation, optimization, and precise forecasting [8]. In this study, the development of the DT was achieved through the integration of Finite Element Method (FEM) simulations and Artificial Neural Networks (ANN).

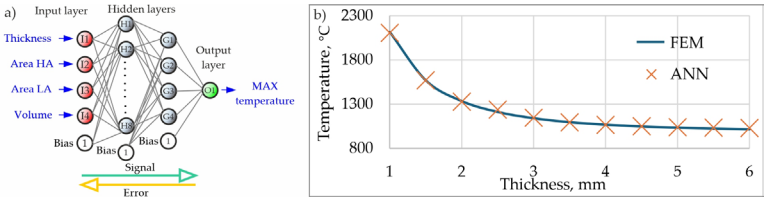

Figure 3. Digital Twin Prediction: (a) ANN Topology, (b) Comparison of FEM and ANN Predictions

4. Conclusions

The Digital Twin presented in this work for laser hardening is the methodology with immense potential, combining real-time modeling, simulation, autonomy, machine learning, prototyping, optimization, and big data. One of the key advantages of the Digital Twin is its speed of action, while a limitation lies in the generation and processing of large volumes of data.

References

1. Lesyk D.A., Martinez S., Mordyuk B.N., Dzhemelinskyi V.V., Lamikiz A., Prokopenko G.I., *Effects of laser heat treatment combined with ultrasonic impact treatment on the surface topography and hardness of carbon steel AISI 1045*, Optics & Laser Technology, 2019, 111, 424-438. https://doi.org/10.1016/j.optlastec.2018.09.030.
2. Derlatka A., Lacki P., *Experimental study and numerical simulation of cellular I-beam manufactured using refill friction stir spot welding technology*, Thin-Walled Structures, 2024, 200, 111890. https://doi.org/10.1016/j.tws.2024.111890.
3. Szczucka-Lasota B., Uściłowska A., Węgrzyn T., Węgrzyn-Wolska K., *Aluminum busducts welding with micro-jet cooling-process parameters estimation by numerical simulations with MFS*, Continuum Mechanics and Thermodynamics, 2024, 37, 1, 14. https://doi.org/10.1007/s00161-024-01351-y.
4. Lacki P., Derlatka A., Więckowski W., Adamus L., *Development of FSW Process Parameters for Lap Joints Made of Thin 7075 Aluminum Alloy Sheets*, Materials, 2024, 17, 3, 672. https://doi.org/10.3390/ma17030672.
5. Lacki P., Derlatka A., Lacki M., *Digital Twin of the Refill Friction Stir Spot Welding Process*. [in:] XV Konferencja Naukowa Odkształcalność Metali i Stopów – OMIS' 2024, 65-66.
6. Rauch Ł., Bzowski K., Szeliga D., Pietrzyk M. *Development and Application of the Statistically Similar Representative Volume Element for Numerical Modelling of Multiphase Materials*. [in:] Krzhizhanovskaya, V., et al. Computational Science – ICCS 2020. ICCS 2020. Lecture Notes in Computer Science, 12142. https://doi.org/10.1007/978-3-030-50433-5_30.
7. Berkowski L., Borowski J., *The influence of structure on the results of the nitriding of ledeburitic chromium steels Part II. Heat treatment conditions of NC10 steel*. Obróbka Plastyczna Metali t. XVIII nr 1 (2007).
8. Sharma A., Kosasih E., Zhang J., Brintrup A., Calinescu A. Digital Twins: *State of the art theory and practice, challenges, and open research questions*, Journal of Industrial Information Integration 2022, 30, 100383. https://doi.org/10.1016/j.jii.2022.100383

Challenges in Processing of High Integrity Aerospace Alloys

Brad Wynne, Salah Rahimi
Advanced Forming Research Centre, University of Strathclyde, Glasgow, UK

The thermomechanical performance of high-integrity aerospace alloys, particularly in forged components, presents significant challenges due to the complex interplay of temperature, strain, and microstructure evolution during processing. At the Advanced Forming Research Centre (AFRC) in Glasgow, extensive expertise in precision forging enables the development of robust forming strategies to enhance alloy performance. Key challenges include managing residual stresses, optimizing grain refinement for superior mechanical properties, and mitigating phase transformations that affect long-term stability, in particular for titanium and nickel alloys. In the presentation a number of case studies are given that highlight the key challenges in emerging techniques for maximising the opportunity of titanium and nickel alloys, with an emphasis on using the minimal amount of material to maximise properties and production rate.

The project is co-financed by funds from the state budget, granted by the Minister of Science as part of the Excellent Science II Program, project no. KONF/SP/0109/2024/02, subsidy amount 67 870 PLN.

Doskonała Nauka II
Ministry of Science and Higher Education
Republic of Poland
Republic of Poland

Cyber Physical System in welding industry – data management and analysis challenges

Krzysztof Bzowski[1], Krzysztof Regulski[1], Monika Pernach[1], Lukasz Rauch[1]

[1]AGH University of Krakow, al. Mickiewicza 30, 30-059 Krakow, Poland
kbzowski@agh.edu.pl, regulski@agh.edu.pl, pernach@agh.edu.pl, lrauch@agh.edu.pl

Keywords: cyber-physical systems, welding, artificial intelligence, heavy industry

1. Introduction

Cyber-Physical Systems (CPS) are revolutionizing heavy industry by integrating computing, networking, and physical processes to enhance efficiency and innovation. However, the implementation of CPS in sectors such as manufacturing, energy, and transportation is hindered by a range of challenges spanning technical, economic, and social dimensions. From a technical standpoint, CPS involve the integration of diverse subsystems from different suppliers, making design and verification complex. The interoperability of various components, such as sensors and actuators, remains a challenge due to evolving standards and protocols [1-4]. Additionally, CPS must process large volumes of real-time data, necessitating robust storage and communication infrastructures that meet stringent reliability requirements [5]. The interconnected nature of these systems also exposes them to cybersecurity threats, necessitating the implementation of strong security measures to prevent operational disruptions [6,7]. Economically, the high development costs associated with specialized hardware, software, and integration efforts present a significant barrier. Moreover, maintaining and upgrading CPS further escalates expenses [1]. Another major concern is the shortage of skilled professionals who possess expertise in both cyber and physical domains, limiting the pace of development and deployment. Social and organizational challenges also play a crucial role in the adoption of CPS. The growing complexity of these systems calls for new educational and training approaches that equip employees with both technical expertise and awareness of the ethical and social implications of CPS. Furthermore, as CPS become increasingly integrated into critical infrastructure, ensuring accountability in their design, development, and operation is paramount. While CPS hold immense potential to drive industrial innovation, addressing these multifaceted challenges requires a multidisciplinary approach. Overcoming technical, economic, and social barriers will enable industries to fully leverage CPS for improved efficiency and safety in heavy industry applications. In the case of this work, the CPS was implemented in practice in company manufacturing welded steel profiles. The main challenge is related to obtain fast and reliable models for big data analysis and prediction of welds quality in non-destructive way.

2. Data acquisition and analysis

The aim of the work was to develop filters of measurement data from the welding machine, implement procedures to validate data consistency and work interpolation procedures for inconsistent data. The filtering module has been implemented using Python and its dependency manager pipenv. The main task of the module is to export data from the measurement database, based on timescaledb, to a file format. The exporter produces data in CSV format. The application consists of three parts: selecting data from the database, filtering and exporting to file format. A Python client was used to query the database. The client is configurable and allows to enter input parameters to customize the exported data to your needs. The built-in timescaledb functionality was used, allowing to fill in the data from missing timestamps. On the basis of the collected learning sets concerning only the process parameters, not yet supplemented with the results of material tests, the development of temperature forecasting models was undertaken, which were aimed at determining whether the temperature reading is correct, i.e. whether it is possible to forecast the temperature measured with a pyrometer using parameters determining current data. Models made on relatively small data sets (20000-48000 records) proved that the parameters allow such a prediction – the coefficient of determination for the models reached $R^2 = 0.97$. The parameters of measurement data depending on the manufactured product ranges were also determined. Then, the results of measurements collected during the first material tests were subjected to cluster analysis to verify whether the samples that did not pass the tests stood out from others in terms of measurement values. An important element of the work was also to perform an analysis allowing for discretization of variables (power, temperature), thus enabling the implementation of classification models. The analysis of measurement data in the context of testing the relationship with material testing is also a classification problem – the product meets or does not meet the quality condition. With discretized values of both power, temperature and endurance, a relationship model was built at a more abstract level. For classes prepared in this way, models of classification trees were developed. The number of models were developed as part of the work. They worked on two different data sets. The fuzzy logic models (Figure 1) based on first dataset used measurements from a pyrometer placed on a measuring device. These were data from work in progress – cleared of downtime and changeovers, start-ups and shutdowns. The data included 12575 records for which optimal network architectures were determined. The quality of validation was obtained at the level of $R^2 = 0.945$. The second dataset included production results (including downtime, start-up and shutdown), data were sampled every half second, and a temperature delay was added to mimic the actual weld heating delay. The data included 50,400 records. The developed models had a coefficient of determination $R^2 = 0.984$. In the next steps, even more accurate models were implemented.

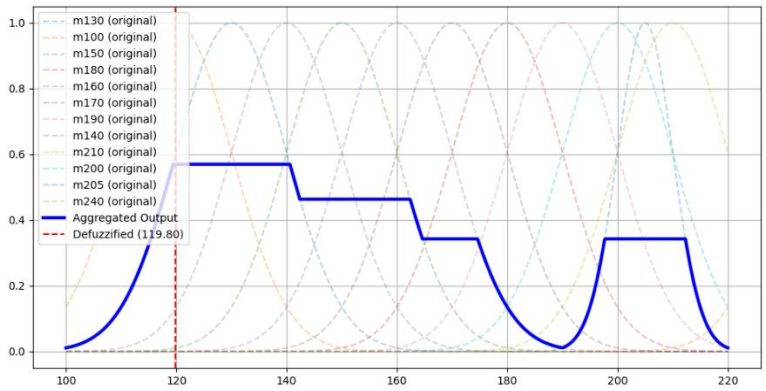

Figure 1. Defuzzification of models – example for specific material, thickness and diameter.

3. Conclusions and future work

The key tasks were the selection of software architecture and the development of a communication project for individual components. An analysis of various software architectures was performed in terms of the possibility of applying the selected solution to design problems. Two architectures were taken into account, i.e. monolithic and microservice. A microservices architecture was chosen, which is a set of rules and characteristics, and is based on the creation of applications as a set of small services. Each service has its own process and communicates using a lightweight mechanism, e.g. RESTful API. Websites are created based on business functions. Each is an independent entity that can be developed, tested, and deployed separately. As a result, services that require the use of other implementation technologies have been implemented differently, e.g. modules for handling drivers of selected devices. Often these are also different kinds of libraries for a given language that have been linked at the compilation level and used as if they were part of the application. In addition to the measurement infrastructure being built, which enables the collection of process data, profiling tests of selected sections were carried out, and samples were taken in order to carry out metallographic tests and strength tests of the linear weld, enabling the comparison of the properties of the weld with the prediction of the model based on artificial neural networks. As part of the work, a series of samples of sections of various shapes were taken from different types of steel and produced with different process parameters. Control materials taken from product samples for different parameter settings and configurations and for different product groups and sections were tested. Models were developed for different phases of the process. Validation of the reliability of the models in production conditions allowed the models to be verified in real production conditions, experimental and control interventions. In order to perform a comparative analysis of the results and validate the models, the industrial environment was designed and installed. In this environment, predictive models for temperature were implemented both in the regression approach and after discretization, in the classification approach. As shown in Figure 1, the models give a prediction of power, but not of weld quality. However, based on these predictions and comparing them to the measured power values, it is possible to estimate whether the power is too low or high. Values between the limiting thresholds therefore make it possible to estimate the probability of weld quality, so that it will be possible to develop a model to map the relationship between the input process parameter values and the estimated quality. The challenge continues to be the size of the database, which is growing at a rate of tens of measurements per second. The current size of the database is several terabytes. Also a limitation is the ability to analyze the data at such fast rates, in particular the Vee angle images, which are crucial for the estimation of weld quality. Parallelised welding angle detection procedures are currently being developed.

References:

1. Dhir S., Kumar Y., Study of machine and deep learning classifications in cyber physical system, Proceedings of the 3rd International Conference on Smart Systems and Inventive Technology, ICSSIT 2020, art. no. 9214237, pp. 333 - 338
2. Seyam A.R.M., Nassif A.B., Nasir Q., AlShabi M., Denial of Service Detection on Industrial Control System using BLSTM, Proceedings of SPIE - The International Society for Optical Engineering, 12538, art. no. 125381X
3. Prasat K., Sanjay S., Ananya V., Kannadasan R., Rajkumar S., Raut R., Selvanambi R., Analysis of Cross-Domain Security and Privacy Aspects of Cyber-Physical Systems, International Journal of Wireless Information Networks, 29 (4), pp. 454 - 479
4. Leitão P., Colombo A.W., Karnouskos S., Industrial automation based on cyber-physical systems technologies: Prototype implementations and challenges, Computers in Industry, 81, pp. 11 - 25
5. O'Donovan P., Gallagher C., Leahy K., O'Sullivan D.T.J. A comparison of fog and cloud computing cyber-physical interfaces for Industry 4.0 real-time embedded machine learning engineering applications, Computers in Industry, 110, pp. 12 – 35
6. Rajasekar V., Sathya K., Dhanaraj R.K. Fault diagnosis in digital twin manufacturing, Digital Twin for Smart Manufacturing, pp. 203 - 220
7. Frontoni E., Loncarski J., Pierdicca R., Bernardini M., Sasso M., Cyber Physical Systems for Industry 4.0: Towards Real Time Virtual Reality in Smart Manufacturing, Lecture Notes in Computer Science (including subseries Lecture Notes in Artificial Intelligence and Lecture Notes in Bioinformatics), 10851 LNCS, pp. 422 - 434

Acknowledgment. The financial support of Polish National Centre for Research and Development project no. POIR.01.02.00-00-0091/19 is acknowledged.

The Kalman Filter as a state estimation method based on measurement data from hardware sensors

Andrzej Opaliński, Maciej Urbański, Kacper Bielak
AGH University of Krakow, Al.A.Mickiewicza 30, 30-059 Krakow, Poland
andrzej.opalinski@agh.edu.pl, urbanskimac@gmail.com,
kbielak@student.agh.edu.pl

Keywords: Kalman Filter, measurement data filtration, sensors, process state estimation

1. The challenge of measurement data quality in process state estimation

Data acquisition is a fundamental step in conducting research across various scientific disciplines. The collected data, reflecting both the system and its environment, serve as the foundation for constructing models that represent the actual state of the observed process. However, a key challenge in many research areas is ensuring the quality of the acquired data. Measurements may be affected by noise, distortions, or redundancy due to sensor inaccuracies, signal interference, or environmental disturbances such as mechanical vibrations or electromagnetic interference.In many cases, sensor fusion techniques are employed to integrate data from multiple sources, further complicating the task of ensuring data accuracy. To enhance the quality of acquired information, it is essential to apply appropriate data filtering and state estimation techniques.

Various methods have been developed for filtering and state estimation in dynamic systems, including the Particle Filter, Smoothing Filters, Bayesian optimization techniques (such as Markov Chain Monte Carlo), Adaptive Filters (LMS and RLS), and wavelet transform-based filtering [1]. Among these, the Kalman Filter and its extensions—Extended Kalman Filter (EKF) and Unscented Kalman Filter (UKF)—are widely used. This paper presents the application of the Kalman Filter for estimating position, azimuth angle, and motion trajectory in scenarios involving sensor data fusion. Additionally, this method can be effectively applied to other types of data and industrial processes.

2. Application of the Kalman Filter in position and course estimation

The Kalman Filter is a recursive algorithm for estimating the state of a dynamic system based on a series of noisy measurement observations [2]. Its primary objective is to obtain an optimal estimate of the system's state while accounting for the uncertainties associated with both the measurements and the mathematical model of the system. State estimation is performed in iterative filtering cycles that occur at a predefined frequency. In each cycle, the filtering algorithm performs a series of matrix operations, ultimately yielding an updated estimate of the system's state [3,4].

2.1. Vectors and matrices used in the filtering process

State vector (X): Contains the set of state variables to be estimated.
State covariance matrix (P): Represents the precision of the estimated state.

The project is co-financed by funds from the state budget, granted by the Minister of Science as part of the Excellent Science II Program, project no. KONF/SP/0109/2024/02, subsidy amount 67 870 PLN.

Doskonała Nauka II
Ministry of Science and Higher Education
Republic of Poland
Republic of Poland

State transition matrix (A): Describes how the components of the state vector X evolve over consecutive filtering cycles.

Measurement vector (Z): Contains the actual observed values obtained from sensors at a given time step.

Observation matrix (H): Defines the relationship between the measured values in Z and the elements of the state vector X.

Process noise covariance matrix (Q): Represents the uncertainty associated with the evolution of the system's state over time.

Measurement noise covariance matrix (R): Quantifies the uncertainty related to measurement accuracy

2.2. Stages of the filtering process

The Kalman Filter algorithm consists of three main stages: initialization (executed at the start of the process), prediction, and correction (performed iteratively at a predefined frequency). Due to space limitations, the detailed mathematical equations governing each step can be found in references [3,4].

Initialization: This stage involves defining the structure of the state transition matrix A (which remains constant throughout the process) and setting the initial values for the state vector X and the covariance matrices P, Q, and R.

Prediction: In this step, the filter estimates the next system state based on its previous state and the mathematical model describing the system's evolution over time (matrix A). The output of this step is the predicted values of the state vector X and the state covariance matrix (P_{pred}).

Correction: The predicted state (X_{pred}) is updated using actual measurement data (Z_{real}). The observation matrix H is defined, and a predicted measurement is calculated for the next time step based on the estimated state vector X. At this stage, actual sensor measurements are incorporated, and the difference between the real and predicted measurements is computed. A key component of the correction step is the Kalman Gain, which determines the degree to which new sensor measurements influence the estimated system state. Based on the computed matrices, the system state is updated for the current time step

2.3. Example filter parameters

Example matrices used for position estimation in pedestrian motion are presented in Figure 1. Depending on the type of motion (walking, driving, or maritime navigation), the available sensors in the environment, and the data they provide, the values within the matrices may be adjusted or adapted accordingly.

$$X = \begin{bmatrix} a_x \\ a_y \\ v_x \\ v_y \\ x \\ y \end{bmatrix} \quad A = \begin{bmatrix} 1 & 0 & dt & 0 & 0{,}5 * dt^2 & 0 \\ 0 & 1 & 0 & dt & 0 & 0{,}5 * dt^2 \\ 0 & 0 & 1 & 0 & dt & 0 \\ 0 & 0 & 0 & 1 & 0 & dt \\ 0 & 0 & 0 & 0 & 1 & 0 \\ 0 & 0 & 0 & 0 & 0 & 1 \end{bmatrix} \quad Z = \begin{bmatrix} 0 \\ 0 \\ 0 \\ 0 \\ x_{pos\ measured} \\ y_{pos\ measured} \end{bmatrix} \quad H = \begin{bmatrix} 0 & 0 & 0 & 0 & 0 & 0 \\ 0 & 0 & 0 & 0 & 0 & 0 \\ 0 & 0 & 0 & 0 & 0 & 0 \\ 0 & 0 & 0 & 0 & 0 & 0 \\ 0 & 0 & 0 & 0 & 1 & 0 \\ 0 & 0 & 0 & 0 & 0 & 1 \end{bmatrix}$$

$$Q = \begin{bmatrix} 0{,}0004 & 0 & 0 & 0 & 0 & 0 \\ 0 & 0{,}0004 & 0 & 0 & 0 & 0 \\ 0 & 0 & 0{,}0004 & 0 & 0 & 0 \\ 0 & 0 & 0 & 0{,}0004 & 0 & 0 \\ 0 & 0 & 0 & 0 & 0{,}003 & 0 \\ 0 & 0 & 0 & 0 & 0 & 0{,}003 \end{bmatrix} \quad R = \begin{bmatrix} 0{,}1 & 0 & 0 & 0 & 0 & 0 \\ 0 & 0{,}1 & 0 & 0 & 0 & 0 \\ 0 & 0 & 0{,}03 & 0 & 0 & 0 \\ 0 & 0 & 0 & 0{,}03 & 0 & 0 \\ 0 & 0 & 0 & 0 & 0{,}009 & 0 \\ 0 & 0 & 0 & 0 & 0 & 0{,}009 \end{bmatrix}$$

Figure 1. Example values of matrices used in calculations for pedestrian motion
where: a_x, a_y – acceleration values, v_x, v_y – velocity values,
x, y – position coordinates, dt – time interval between filtering cycles

2.4. Obtained results

As part of the study, the standard Kalman filter was tested for estimating position, azimuth angle, and trajectory across different motion models. The left section of Figure 2 demonstrates the improved (compared to GPS coordinates) accuracy of position estimation for pedestrian movement. The middle graphic represents the trajectory estimation for a passenger car, while the rightmost graphic in Figure 2 illustrates the position tracking for a remotely controlled boat model.

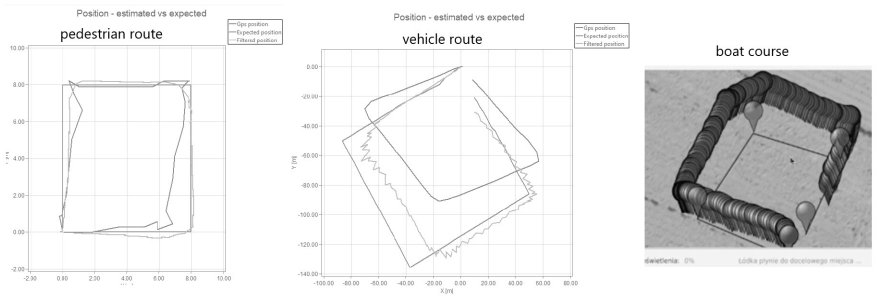

Figure 2. Force vs. displacement obtained from the measurements

Each of the developed models required a unique set of filter configuration parameters, including matrix dimensions and values. In every case, these parameters were adjusted to optimize the accuracy of the estimated results. The final parameter values were determined based on an evaluation of the outcomes obtained for each configuration. The results presented in the figures represent only a subset of the conducted tests. Additionally, estimations of azimuth and trajectory were performed for various path shapes, considering different motion types, including pedestrian, vehicle, and boat movement.

3. Summary

The results presented in this abstract demonstrate that probabilistic state estimation methods, such as the Kalman filter, can effectively enhance the quality of process data. In the conducted experiments, the filter was applied to estimate the position, azimuth, and trajectory of various moving objects. However, in principle, it can be used for state estimation in a wide range of processes across different fields. The key challenge in implementing such solutions lies in the appropriate selection of models that characterize a given system or process, including the definition of relevant parameters and the quality and significance of the measurements used for estimation.

References

1. Simon D., *Optimal State Estimation: Kalman, H Infinity, and Nonlinear Approaches*, John Wiley & Sons, 2006
2. Kalman R.E., *A new approach to linear filtering and prediction problems*, 1960, 35-45.
3. Gibbs B.P., *Advanced Kalman filtering, least-squares and modeling: a practical handbook*, John Wiley & Sons, 2011.
4. Brown R.G., Hwang P.Y.C., *Introduction to random signals and applied Kalman filtering: with MATLAB exercises and solutions*, 1997.

Acknowledgements. This study was carried out as part of the fundamental research financed by the Ministry of Science and Higher Education, grant no. 16.16.110.66.

The Impact of FPV Drone Frame Materials on Motor Thermal Conditions: Experimental and Numerical Analysis

Andrij Milenin
AGH University of Krakow, Al.A.Mickiewicza 30, 30-059 Krakow, Poland
milenin@agh.edu.pl

Keywords: FPV drone, carbon fiber, drone thermal management

1. Introduction

Effective thermal management of FPV (First Person View) drone motors is critical for enhancing their performance and durability, particularly under high-load conditions characteristic of competitive applications. This problem has become even more pressing now that FPV drones originally intended for amateur and sports purposes have begun to be used over longer distances (and therefore with a heavier battery) and with a large additional load. This significantly increases the load on the motors and can bring their thermal state to a critical point. Recent studies highlight the role of frame materials in dissipating heat generated by motors in UAV (Unmanned Aerial Vehicle) systems. Research such as [1,2] emphasizes the need to incorporate thermal properties into frame design, underlining the relevance of this study. The aim of this work was an experimental and theoretical study of the thermal conditions of the frame of an FPV drone flying with an additional load and a heavy battery. As an option for improving the thermal conditions of the drone, replacing the frame material from carbon fiber to aluminum alloy was considered.

2. Materials and methods

This study combines experimental and numerical approaches to assess the thermal behavior of a 7-inch FPV drone (Figure 1a) with carbon fiber and aluminum alloy frames (Figure 1b). In the experimental setup (Figure 2a), the drone was mounted on a force sensor to control thrust while motor and frame temperatures were monitored using an infrared camera BOSH GTC 600 C.

a) b)

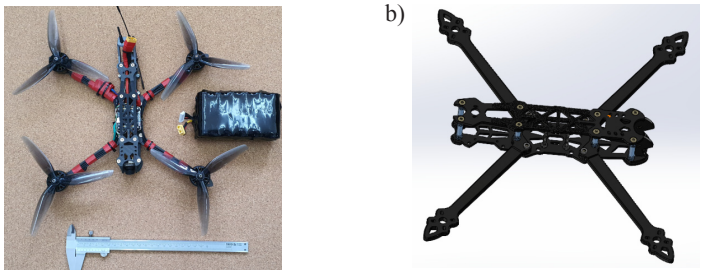

Figure 1. Illustration of a 7-inch FPV drone (a) and the CAD model of its frame (b)

The project is co-financed by funds from the state budget, granted by the Minister of Science as part of the Excellent Science II Program, project no. KONF/SP/0109/2024/02, subsidy amount 67 870 PLN.

Doskonała Nauka II
Ministry of Science and Higher Education Republic of Poland
Republic of Poland

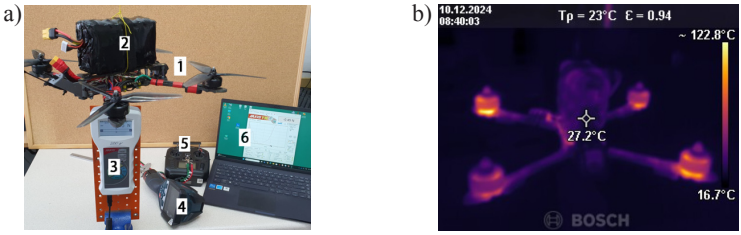

Figure 2. Experimental setup for steady-state drone flight testing: (a) 1 – FPV drone; 2 – battery 6s2p; 3 – force sensor (AXIS FM); 4 – infrared camera; 5 – remote drone control device (Radiomaster TX12); 6 – computer for recording force measurements; (b) example of a drone image captured by the infrared camera

During the experiment, the drone is connected to the force sensor, and, using the control equipment (Radiomaster TX12), the thrust is brought to the value of the payload (in our experiments it was 20N). The drone weighed 5.4 N, and the 6s2p battery weighed 8.8 N. After 10 minutes of physical simulation of the flight under load, the temperature of the motors and frame fragments in contact with the motors was measured. Subsequently, a numerical simulation of the steady-state thermal distribution in the arm was performed, leveraging inverse analysis to estimate the heat flux transferred from the motor to the frame. For thermal simulation, the SolidWorks 2022 program was used. The following thermal conductivity coefficients were adopted for the simulation: K_{carbon} = 10 W/mK; $K_{aluminium}$ = 170 W/mK.

3. Results and discussion

The experimental tests showed, that for the carbon fiber frame, the motor and arm beneath it reached a temperature of 120°C (Figure 2b). Replacing the carbon fiber frame with an aluminum alloy frame in the FEM simulation demonstrated a significant reduction in maximum temperatures, with values dropping to 50°C due to aluminum's superior thermal conductivity (Figure 3). These results were validated experimentally by integrating an aluminum arm into the drone, confirming the superior heat dissipation properties of aluminum compared to carbon fiber.

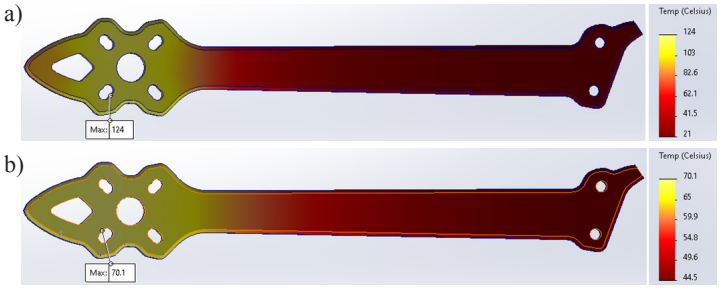

Figure 3. Calculated temperature distribution in the frame arm: (a) made of carbon fiber; (b) made of aluminum alloy

4. Conclusions

The findings indicate that aluminum alloy frames can substantially improve the thermal conditions of FPV drone motors by functioning as effective radiators. This dual functionality of aluminum - structural support and heat dissipation - positions it as a promising material for applications

requiring enhanced thermal management. These insights underscore the potential for optimizing drone frame materials to improve both thermal performance and component longevity.

References

1. A.S.J. van Heerden, D.M. Judt, S. Jafari, C.P. Lawson, T. Nikolaidis, D. Bosak, *Aircraft thermal management: Practices, technology, system architectures, future challenges, and opportunities*, Progress in Aerospace Sciences, V. 128, 2022, https://doi.org/10.1016/j.paerosci.2021.100767.
2. A. Balayan, R. Mallick, S. Dwivedi, S. Saxena, B. Haorongbam, A. Sharma, *Optimal Design of Quadcopter Chassis Using Generative Design and Lightweight Materials to Advance Precision Agriculture*. Machines, V. 12, 2024 https://doi.org/10.3390/machines12030187

Efficient Aerodynamic Wing Load Discretization for Static Structural Testing Using Optimization and Machine Learning

Javed Arshad Butt, Florian Dexl, Johannes Markmiller
Institute of Aerospace Engineering, TUD Dresden University of Technology,
01062 Dresden, Germany
Javed.butt@tu-dresden.de, Florian.dexl@tu-dresden.de,
Johannes.markmiller@tu-dresden.de

Keywords: optimization, load discretization, structural testing, beam modelling, surrogate modelling

Experimental static structural validation tests are mandatory to get small and large aircraft approved by certification authorities and thus be made available for commercial application. When designing such a validation test, engineers need to approximate the continuous aerodynamic load that the aircraft faces during flight through discrete loads. This requires addressing several key questions about the load introducing elements (LIEs): their type, dimensions, placement, spacing, quantity, and the applied forces. Answering these questions through experimental tests, systematically or through a random approach, is inefficient, since experimental tests, especially on the scale of large aircraft, are expensive. This work presents a numerical global optimization framework to address these challenges. The framework leverages well-established, open-source tools, offering both accessibility and reliability. Its modular design enables straightforward adaptation to diverse real-world requirements. Notably, the framework achieves efficient performance on standard consumer hardware. Basic optimizations for 4 to 8 LIEs are solved within one hour. Even with additional constraints beyond those presented here, making the optimization problem substantially more complex, solutions are obtained within 24 hours, eliminating the need for high-performance computing resources.

The optimization aims to determine discrete force magnitudes and their positions that best approximate the structural behavior under continuous aerodynamic loading. Using bending moment as the primary measure of structural response, the objective function represents the deviation between the continuous aerodynamic load and discrete force bending moment distributions. Aerodynamic forces can be obtained through numerical methods or experimental wind tunnel testing. Among various numerical approaches offering different trade-offs between computational speed and accuracy, this work employs APAME [2], a 3D panel method. While APAME provides 3D load distributions, the optimization process utilizes 1D data for computational efficiency and result interpretability. The 3D load distribution is transformed into 1D by averaging across two axes, yielding loads that vary along the span direction. This simplified load distribution serves as input for beam modelling using the open-source tool IndeterminateBeam [1]. The output yields the reference or true shear force and bending moment distribution. To prepare the data for clustering, the aerodynamic load distribution is discretized into uniformly spaced point forces along the span. This preprocessing step is crucial since the kmeans++ algorithm's clustering performance is sensitive to point density variations, which could otherwise bias the LIE placement toward regions of naturally higher point force concentration. A free, open-source, and performant implementation of kmeans++

The project is co-financed by funds from the state budget, granted by the Minister of Science as part of the Excellent Science II Program, project no. KONF/SP/0109/2024/02, subsidy amount 67 870 PLN.

Doskonała Nauka II
Ministry of Science and Higher Education
Republic of Poland
Republic of Poland

can be accessed through scikit-learn [3]. The cluster centers (centroids) have the physically relevant interpretation of representing the centers of the LIEs. The accumulated force values of each cluster's members determine the desired resulting force on the respective LIE. However, with kmeans++ alone, the design freedom for the dimensioning of the LIEs is significantly constrained. While this might be acceptable for some testing requirements, generally having more precise control over the LIE dimensions is required.

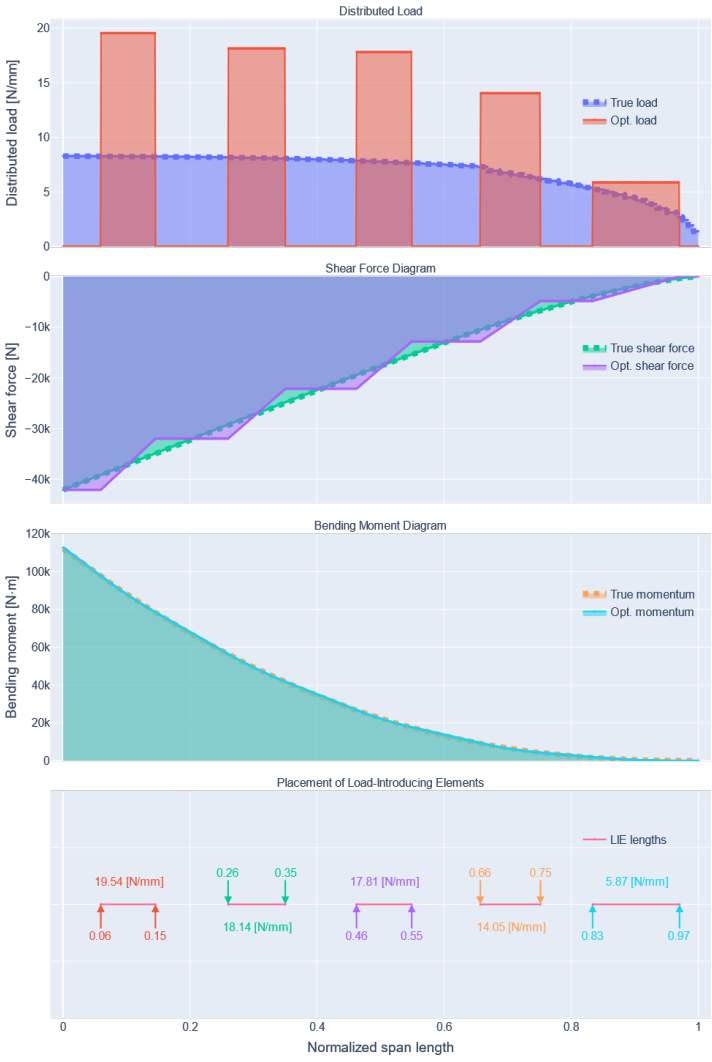

Figure 1. Illustrative output of one optimization comparing the true and optimized load, shear force and bending moment distribution as well as the placement of the five LIEs

To address these limitations, this clustering-based approach is transformed into an optimization problem, where the LIE lengths are defined as the design variables and the clusters act as the centers of the LIEs. The problem formulation includes geometric constraints ensuring that the

sum of all LIE lengths does not exceed the total span length. Additionally, each LIE must be positioned within the defined span boundaries, ranging from the starting to the ending position of the span. The dimensions of individual LIEs can be further controlled through user-defined bounds on their lengths. This optimization definition includes the basic requirements for aerodynamic load discretization using optimization. Depending on real-world requirements that could be based on measurement technology, LIE specifications, or project-specific demands, the presented constraints and bounds can be adapted, removed, or new ones added to fulfill these application-specific needs. The optimization problem is solved using SciPy's differential evolution optimizer [4]. While SciPy was chosen for its performance and open-source availability, the evolution optimizer eliminates the need for gradient determination and offers a higher chance of finding the global optimum. This approach allows less experienced users to adapt the framework to their specific use cases without requiring deep mathematical and engineering expertise. Figure 1 demonstrates a representative solution obtained using this optimization framework. The developed framework was applied to design an experimental testing in collaboration with IMA Materialforschung und Anwendungstechnik GmbH, a company with expertise in structural validation tests. Finally, the proposed optimization framework extends beyond conventional aircraft configurations and can be adapted for novel designs. For example, it could be applied to configurations incorporating new elements such as hydrogen tanks, regardless of whether these serve as load-bearing structural components or additional mounted elements.

References

1. Bonanno, J. (08. 01 2025). Github. Von https://github.com/JesseBonanno/IndeterminateBeam.
2. Ing, D.F.D. *Apame-Aircraft 3D Panel Method*.
3. Fabian, P. (2011). *Scikit-learn: Machine learning in Python*. Journal of Machine Learning Research 12, 2825.
4. Virtanen, P., Gommers, R., Oliphant, T.E., Haberland, M., Reddy, T., Cournapeau, D., ... & van Mulbregt, P. (2020). *Fundamental algorithms for scientific computing in python and SciPy 1.0 contributors*. SciPy 1.0. Nat. Methods, 17, 261-272.

Acknowledgements. We thank Dr. Silvio Nebel from IMA Materialforschung und Anwendungstechnik GmbH in Dresden for fruitful discussions.
This research was funded by the German Federal Ministry for Economic Affairs and Climate Action under grant number 20M2117B. The responsibility for the content of this abstract is with its authors. The financial support is gratefully acknowledged.

Discrete element model for coupled thermal and electrical phenomena in spark plasma sintering

Fatima Nisar[1], Jerzy Rojek[1], Szymon Nosewicz[1],
Marcin Chmielewski[2], Kamil Kaszyca[2]

[1] Institute of Fundamental Technological Research, Polish Academy of Sciences,
Pawińskiego 5B, 02-106 Warsaw, Poland
[2] Lukasiewicz Institute of Microelectronics and Photonics,
al. Lotników 32/46, 02-668 Warsaw, Poland
fnisar@ippt.pan.pl, jrojek@ippt.pan.pl,
snosew@ippt.pan.pl,
marcin.chmielewski@imif.lukasiewicz.gov.pl,
kamil.kaszyca@imif.lukasiewicz.gov.pl

Keywords: Spark Plasma Sintering, Discrete Element Model, microscopic modelling, thermo-electric coupling

1. Introduction

The increasing interest in Spark Plasma Sintering (SPS) stems from its potential as a sustainable and ecological powder consolidation process. In this process, the powder is simultaneously subjected to mechanical pressure and heated by Joule heating, generated as an electrical current flows through the powder and tools. Initially, the powder consists of loosely bonded particles. As the process progresses, the particles become connected through necks, which grow over time due to diffusion and mass transport. SPS process involves complex interdependence of electrical, thermal, and mechanical phenomena. Therefore, to develop a comprehensive model for the SPS process, a coupling approach is required where all these phenomena are integrated together. Discrete Element Method (DEM) is a suitable choice as it allows microscopic modelling of the sintering process. In DEM based approach, each particle in the powder is treated as a discrete element, allowing precise representation of microscopic structures and interactions. In this work effective thermal and electrical conductivity of metallic powders undergoing densification is studied and a coupled thermo-electric DEM model is developed. The simulation results are validated using our own experimental measurements.

2. Experimental work

NiAl powder with spherical morphology (as shown in Figure 1a) was sintered under different pressures and temperatures to obtain four samples with varying density levels. Heating rate of 100K/min was used during all the processes. Microstructural analysis using SEM showed the sintering mechanism, beginning with neck formation in the low-density samples, followed by neck growth as the density increased, and ultimately resulting in a fully densified microstructure at higher densities. Figure 1b illustrates SEM image of the fractured surface showing necks and texture in the grain boundaries. This observation is important for incorporating grain boundary resistance in the

The project is co-financed by funds from the state budget, granted by the Minister of Science as part of the Excellent Science II Program, project no. KONF/SP/0109/2024/02, subsidy amount 67 870 PLN.

Doskonała Nauka II
Ministry of Science and Higher Education
Republic of Poland
Republic of Poland

model. Thermal and electrical conductivities was measured for all the samples, showing increase in conductivities with densification. These results were used to validate the DEM model [2,3].

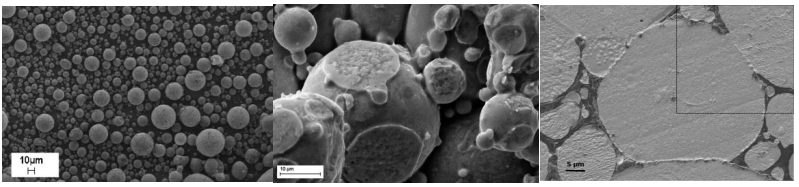

Figure 1. SEM images a) powder morphology, b) fractured surface showing necks and c) grain boundary texture

3. DEM model

An original DEM model, based on sintering geometry where two particles are connected via neck, was presented in [1]. This model was revised by including grain boundary resistance. Additionally, neck-size correction was introduced to compensate for non-physical overlaps at higher densities. The revised DEM model was used to simulate thermal [2] and electrical [3] conduction and evaluate the effective properties of partially sintered porous material with heterogeneous microstructure. The coupled thermoelectric model takes into account the heat generated as result of Joule heating. From the electrical simulation, potential distribution and resulting electric current flow is evaluated by time integrating the following equation:

$$C_i^{el}\dot{V}_i = \sum_{j=1}^{N_i^j} I_{ij} + I_i^{ext} \tag{1}$$

where: C_i^{el} – electrical capacitance of the i^{th} particle, V_i – particle voltage and I_i^{ext} – external current source and I_{ij} – current flow. The temperature evolution in particles is evaluated by time integrating the following heat balance equation:

$$C_i^{th}\,\dot{T}_i = \sum_{j=1}^{N_i^j} Q_{ij} + Q_i^{ext} + \sum_{j=1}^{N_i^j} Q_{ij}^{Joule} \tag{2}$$

where: C_i^{th} – particle heat capacitance, T_i – particle temperature, Q_i^{ext} – external heat source, Q_{ij} – interparticle heat flux and Q_{ij}^{Joule} is Joule heating rate given as follows:

$$Q_{ij}^{Joule} = I_{ij}^2 R_{ij} \tag{3}$$

where R_{ij} is interparticle resistance.

4. Simulation results

The model was validated on the whole sample comprising of 17515 particles. Four geometries with different densities were obtained from hot-press simulation. Similar boundary conditions were assigned to all the geometries. Axial current flow was obtained by prescribing voltage to the top and bottom particles, and the sample was radially insulated to imitate adiabatic conditions as shown in Figure 2. Resulting steady state potential distribution in one of the sample is shown in Figure

3a. Heat generated as a result of current flow resulted in increase in temperature. Homogenous temperature distribution was achieved in the whole sample as represented in Figure 3b. Heating in geometries with different densities is illustrated in Figure 3c. It can be observed that the heating rate increases with increasing density.

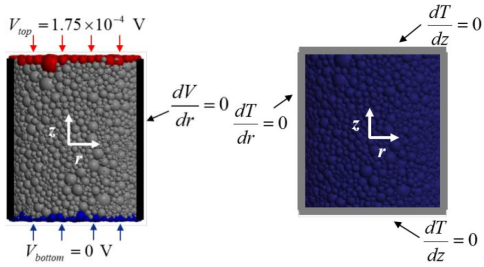

Figure 2. Boundary conditions for the thermo-electric problem

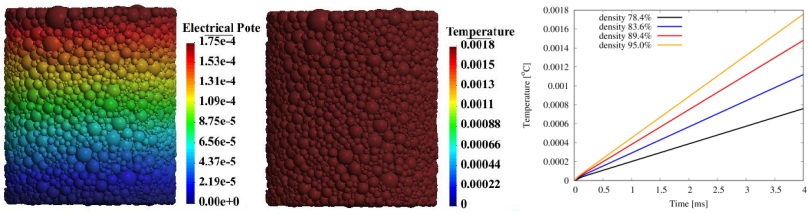

Figure 3. Simulation results a) potential distribution, b) temperature distribution and c) heating in DEM samples with different densitites

5. Conclusion

The coupled thermo-electric model allows to establish a relation between applied current and heating rate for the sintering process. The proposed DEM model can be used for microscopic analysis and can be integrated with sintering models to have a fully coupled thermo-electric-mechanical model for the SPS process.

References

1. Rojek J., Kasztelan R., Tharmaraj R., *Discrete element thermal conductance model for sintered particles*, Powder Technology, 405(117521), 2022.
2. Nisar F., Rojek J., Nosewicz S., Kaszyca K., Chmielewski M., *Evaluation of effective thermal conductivity of sintered porous materials using an improved discrete element model*, Powder Technology, 437(119546), 2024.
3. Nisar F., Rojek J., Nosewicz S., Szczepański J., Kaszyca K., Chmielewski M., *Discrete element model for effective electrical conductivity of spark plasma sintered porous materials*, Computational Particle Mechanics, 1-11, 2024.

Acknowledgements. Research funded by National Science Centre, Poland, project no. 2019/35/B/ST8/03158.

A DEM model to analyse granular material compaction process

Hanna Sadłowska[1], Andrzej Kochański[1], Joanna Wiącek[2],
Rafał Kobyłka[2], Robert Biernacki[1], Artur Soroczyński[1]
[1] Warsaw University of Technology, Faculty of Mechanical and Industrial Engineering,
Narbutta 85, 02-524 Warsaw, Poland
2 Institute of Agrophysics (IA PAS), Doświadczalna 4, 20-290 Lublin, Poland
hanna.sadlowska@pw.edu.pl, andrzej.kochanski@pw.edu.pl,
j.wiacek@ipan.lublin.pl, r.kobylka@ipan.lublin.pl,
robert.biernacki@pw.edu.pl,
artur.soroczynski@pw.edu.pl

Keywords: DEM, Rapid Tube Hydroforming, granular material

1. Introduction

The aim of this paper is to present and evaluate a Discrete Element Method (DEM) model for a sand compaction test in a cylindrical sleeve. The motivation for this research is the exploration of the Rapid Tube Hydroforming (RTH) method, which involves metal tube hydroforming in deformable dies, and the attempt to model the material of the die composed of granular material [1, 2].

As an introduction, the RTH method (see Figure 1) will be briefly discussed, particularly in comparison to classical hydroforming processes. Recent advancements in scientific research related to this method and numerical models used for analyzing the RTH process, including the interaction of continuous and granular materials, will also be reviewed.

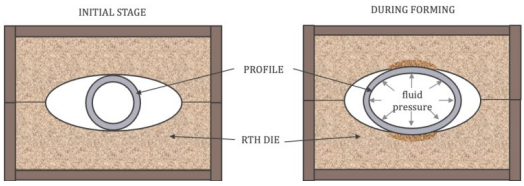

Figure 1. Rapid Tube Hydroforming scheme

Since RTH dies undergo significant deformation during tube shaping, controlling this deformation necessitates advanced numerical tools dedicated to analyzing granular material deformations. The Discrete Element Method (DEM) is a promising approach for this purpose.

This paper presents preliminary results of sand compaction tests performed in a cylindrical sleeve, followed by modeling these tests using the DEM method. The bench experiments were designed by compacting sand with a fraction size of 0.8 mm in a 50×140 mm sleeve (standard green sand test equipment).

The project is co-financed by funds from the state budget, granted by the Minister of Science as part of the Excellent Science II Program, project no. KONF/SP/0109/2024/02, subsidy amount 67 870 PLN.

Doskonała Nauka II
Ministry of Science and Higher Education
Republic of Poland
Republic of Poland

2. Discrete Element Method in granular material compaction

For realistic simulation of granular material deformation, special attention was paid to the geometry of individual grains. Fractionated sand with a nominal grain size of 0.8 mm was used in the experiments, representing a mixture of grains ranging from 0.63 to 0.80 mm (see Figure 2a and c). However, a crucial factor in interpreting the results is the irregular geometry of the grains, which can only approximately be described as spherical. In reality, the grains exhibit significant angularity and concavity (Figure 2b), affecting their interactions and the results of both experimental and numerical analyses.

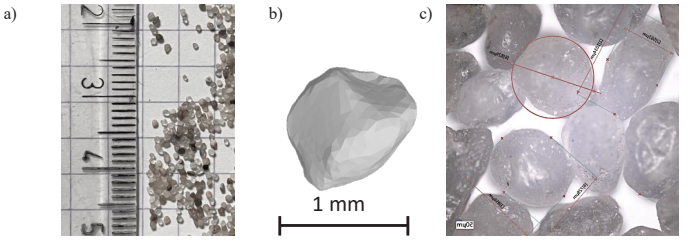

Figure 2. Granular material used in experiments: a) sand granules in macro view, b) 3D scan of a single sand grain c) sand particles in a microscopic view with size measurements

The Discrete Element Method (DEM), first developed by Cundall and Strack [3], is a numerical technique for predicting the behaviour of granular materials under various conditions. It involves solving equations of motion for each particle, characterized by its shape, size, material properties, and initial velocity. Despite its potential, DEM has limitations. The accuracy of the method is highly sensitive to input data, such as material properties and interaction models between particles [4]. Oversimplified models can lead to unrealistic results, particularly in scenarios involving complex forces or material properties, such as high-impact collisions or fine particles.

DEM does not inherently account for continuous behaviours, such as macroscopic material deformation, making it less suitable for materials that do not exhibit purely granular behaviour. Additionally, large-scale systems or long-duration simulations are computationally expensive, necessitating the use of scaling procedures to balance accuracy and efficiency. This can involve reducing the sample size to a Representative Elementary Volume (REV) or increasing particle size. For processes like those modelled here, these methods can yield reliable results within reasonable computation times.

The experiment's accuracy in representing the loading behavior of granular materials depends on both material and contact properties (e.g., elasticity, internal friction, or cohesion) and the geometry of the grains. In most DEM analyses, grains are assumed to be spherical, a significant approximation that overlooks behaviors such as interlocking or blocking caused by irregularly shaped grains. This discrepancy often leads to differences between experimental and numerical results, especially in terms of displacement and load characteristics.

Numerical simulations were performed using an assembly of spherical particles with diameters uniformly distributed between 0.63 and 0.8 mm. The material properties corresponded to quartz sand. The numerical setup replicated the experimental conditions, and the simulations were conducted using GPU-based DEM software (Blaze-DEM) [5] with a nonlinear Hertz-Mindlin contact model.

The calculations were divided into two stages: backfilling the 50×140 mm sleeve and compacting the sample to mimic the real experiment. Figure 3a illustrates the grain distribution after the backfilling stage. The sample was then compacted by a vertically moving punch. The distribution of grain displacements was non-uniform due to the arrangement of sand grains, mechanical properties,

and contact conditions. The largest displacements occurred near the moving punch, while the lower section of the sample showed minimal movement (see Figure 3b).

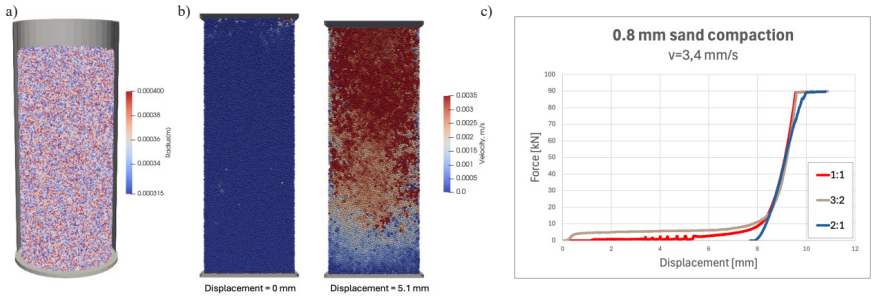

Figure 3. DEM calculation results: a) sand grain distribution after filling stage, b) sand displacement distribution during compaction stage, c) compaction results for different calculation scales

Numerical calculations using DEM are time-consuming. To address this, initial tests evaluated the impact of scaling grain sizes to reduce computation time. Particle sizes were scaled by factors of 1.5 (3:2) and 2.0 (2:1) relative to the original size. At a velocity of 3.4 mm/s, the scaling had minimal impact on displacement-force characteristics, except in the final phase, where 2:1 scaling deviated from real-scale results. The simulation time for the real scale (1:1, 861222 grains) was 76 hours. Scaling reduced computation times by over three and four times for 3:2 and 2:1 scale, respectively, making the 3:2 scale the most efficient compromise.

The study demonstrated that the DEM method is an effective tool for modeling granular material compaction processes, although its results are sensitive to input parameters such as grain geometry and physical properties. The simulation outcomes aligned well with experimental results, and the use of geometric scaling significantly reduced computation time while maintaining high result accuracy.

Further research will focus on developing a DEM model that better accounts for the irregular shape of granular materials. This includes refining contact conditions between grains and exploring new models for irregular geometries to improve the accuracy of simulations.

References

1. A. Kochański, H. Sadłowska, *Method for hydromechanical shaping of thin-walled sections and the die for hydromechanical shaping of thin-walled sections*, Patent no. PL 235400, 2018.
2. H. Sadłowska, A. Kochanski, P. Grzegorzewski, *Multi-Phase Fuzzy Modeling in the Innovative RTH Hydroforming Technology*, IEEE International Conference on Fuzzy Systems, Luxembourg, 2021, pp. 1-6.
3. P.A. Cundall, O.D. Strack, *A discrete element model for granular assemblies*, Géotechnique, 1979, 29, pp. 47-65.
4. C.J. Coetzee, D.N.J. Els, *Calibration of discrete element parameters and the modelling of silo discharge and bucket filling*. Comput. Electron. Agric., 65, 2009, pp. 198–212.
5. N. Govender, D.N. Wilke, S. Kok, *Blaze-DEMGPU: modular high performance DEM framework for the GPU architecture*, SoftwareX 5, 2016, pp. 62–66.

Acknowledgements. The work was founded by Warsaw University of Technology R5.1/IDUB D5 “Grant for a Prototype” 2025.

Influence of the pseudo-random number generators on the determination of grain growth driving force in full-field discrete modelling approach

Mateusz Sitko, Łukasz Madej
AGH University of Krakow, Al. A. Mickiewicza 30, 30-059 Krakow, Poland
msitko@agh.edu.pl, lmadej@agh.edu.pl

Keywords: cellular automata, pseudo-random number generation, recrystallization

1. Abstract

Discrete simulation methods such as cellular automata (CA) and Monte Carlo (MC) frequently incorporate probabilistic components to capture the stochastic nature of material behavior. These elements often represent physical factors like heterogeneous energy distributions or random crystallographic orientations. This study investigates the impact of such stochastic components within a CA-based recrystallization model for predicting material microstructure morphology evolution under thermo-mechanical processing. Firstly, available pseudo-random number generation tools and their working time will be evaluated. Various input data preparation approaches will be shown next, including deformation energy distribution strategies. Next, the role of different pseudo-random number generators (rand, lcg, mt, ranlux) will be assessed on the simulation outcomes. Finally, simulation results will be presented to demonstrate the influence of the generator type on recrystallization kinetics and the morphology of recrystallized grains.

2. Introduction

The dynamic growth of the automotive and aerospace industries drives the development of advanced materials with enhanced performance properties. Traditional laboratory and industrial testing methods remain essential but are often time-consuming, costly, and resource-intensive. They require a significant amount of raw materials, specialized equipment, and skilled technicians. To overcome these challenges, numerical simulations have become helpful tools for predicting material behavior and supporting research efforts while reducing costs and time constraints. Various numerical methods exist for modeling material behavior during manufacturing. These methods range from simplified phenomenological approaches, such as the Johnson-Mehl-Avrami-Kolmogorov (JMAK) model, through mean-field to complex full-field methods, including vertex, level-set (LS), phase-field (PF), Monte Carlo (MC), or cellular automata (CA) simulations [1]. While phenomenological and mean-field models simplify computations and reduce simulation times, they often lack the precision needed to capture complex microstructural morphologies, especially for heterogeneous materials. In contrast, full-field approaches explicitly represent the material microstructure, offering greater predictive accuracy but at the cost of increased computational demands. The mentioned CA method is well-suited for simulating phenomena such as grain evolution under thermo-mechanical processing. It naturally captures changes in microstructure, making it practical for

The project is co-financed by funds from the state budget, granted by the Minister of Science as part of the Excellent Science II Program, project no. KONF/SP/0109/2024/02, subsidy amount 67 870 PLN.

Doskonała Nauka II
Ministry of Science and Higher Education
Republic of Poland
Republic of Poland

modelling static recrystallization (SRX), dynamic recrystallization (DRX), or grain growth (GG) phenomena.

CA-based recrystallization simulations require carefully prepared input data, including initial microstructure morphology and stored deformation energy. These inputs can be derived from detailed multi-scale models or extensive metallographic studies. However, due to time and resource constraints, such approaches are often impractical for industrial use. To address this issue, a hybrid numerical method for the generation of input data based on digital material representation and phenomenological models can be used. These approaches utilize pseudo-random number generators (PRNGs) to distribute stored deformation energy across the computational domain, enabling efficient simulations of heterogeneous energy distributions even for large-scale 3D computations. However, the reliance on random elements can significantly influence simulation time and its outcomes, making the choice of PRNG critical to accurate modelling. As numerous PRNG implementations and data distribution methods are available, evaluation of the optimal generators for CA-based microstructure evolution models becomes critical. Therefore, this paper investigates the impact of different generator types on recrystallization kinetics and the morphology of recrystallized grains. Additionally, various generation methods (homogeneous, heterogeneous, gradient) are evaluated to assess their influence on the accuracy and predictive capabilities of CA recrystallization models.

3. Methodology

The energy stored during the plastic deformation of metallic materials is the main driving force for the recrystallization phenomenon. As mentioned, the veracity of this energy can be obtained during experimental analysis, but it is also possible to map it in a statistically representative way. For this, it is necessary to specify the locations in the material that are more likely to store more energy during deformation, for example, grain boundaries, interfacial interfaces, or areas near precipitations or inclusions.

During the analysis of deformation energy generation in cellular automata simulations, the energy value in a particular CA cell was achieved by adding an artificial package of energy to each cell using a pseudo-random number generator. The paper explored several factors, including data dispersion, repetitiveness over numerous simulations, the influence of energy package sizes, and the effectiveness of using different types of distributions to achieve heterogeneous energy allocation. The current article is a continuation of the work presented in [2], extending the analysis of data preparation time using different approaches to pseudo-random number generation. To achieve this goal, three primary approaches were proposed for generating the input in the form of stored energy data for CA simulation.

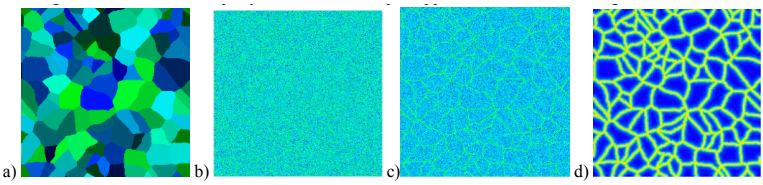

Figure 1. Visualization of a) initial microstructure and corresponding different energy distribution variants: b) homogenous, c) heterogenous, d) gradient (blue – minimal energy, green – middle energy, red – maximal energy)

The first is homogeneous energy distribution, where each CA cell in the space has exactly the same probability of criteria of acceptance of the energy package. This approach aimed to establish

a baseline energy distribution independent of microstructural characteristics. The second one is heterogeneous, where before simulation, different probabilities were assigned to locations based on their relation to grain boundaries: highest probability with tiple-junctions, middle probability with interfaces between two grains, and low probability with non-boundary regions. Lastly, to enhance the accuracy of the CA simulation, a gradient implementation was developed, where probability increased for cells located closer to the grain boundaries. Exemplary results for developed approaches are shown in Figure 1.

4. Summary

Different methods for artificial deformation energy distribution in CA-based recrystallization simulation were investigated in this paper. Generation was based on the addition of artificial energy packages to CA cells using pseudo-random number generators. Three distribution versions were tested: homogeneous distribution with uniform energy, heterogeneous distribution with location--based probabilities favoring grain boundaries, and gradient-based distribution where probabilities increased near boundaries. Simulations with homogeneous nucleation demonstrated that distribution choice slightly affected energy dispersion results. Additionally, switching from Ranlux48 to Mersenne Twister improved data generation speed fourfold without compromising simulation quality, optimizing computational efficiency for recrystallization modelling.

References

1. Serajzadeh P., *Microstructural Changes During Static Recrystallization of Austenitic Stainless Steel 304L: Cellular Automata Simulation*, Metallography, Microstructure, and Analysis (2020). https://doi.org/10.1007/s13632-020-00623-8.
2. Baran K., Sitko M., Madej L., *Analysis of the influence of a pseudo-random number generator type on the kinetics of the cellular automata recrystallization model*, J Comput Sci 75 (2024). https://doi.org/10.1016/j.jocs.2023.102193.

Acknowledgements. The financial assistance of the National Science Centre project No. 2019/35/B/ST8/00046 is acknowledged.

Evaluation of deformation inhomogeneity in multilayered steel-titanium systems

Bartłomiej Pabich, Bartłomiej Żurowski, Łukasz Madej, Janusz Majta
AGH University of Krakow, Al. A. Mickiewicza 30, 30-059 Krakow, Poland
bpabich@agh.edu.pl, bzurowski@student.agh.edu.pl,
janusz.majta@gmail.com, lmadej@agh.edu.pl

Keywords: heterostructured materials, multilayered composite, multi-stage wire drawing, numerical simulation

1. Introduction

It is known that the combination of two metallic materials that differ significantly in their plasticity in a multilayer system due to their crystal lattice - the number of possible slip systems, stacking fault energy (SFE), chemical composition, phase composition, morphology and the degree of microstructure refinement of the microstructural components - make it possible to obtain an attractive combination of mechanical properties [1]. In the presented research, investigated material consisted of: microalloyed steel matrix, characterized by high strength and good ductility during the plastic deformation process [2] and titanium layers with limited plasticity. The main advantage of a material with such a structure is the synergistic effect of the coexistence of the hcp phase in the form of thin layers within the ductile bcc phase matrix, i.e., microalloyed steel strengthened by precipitation and ferrite grain refinement.

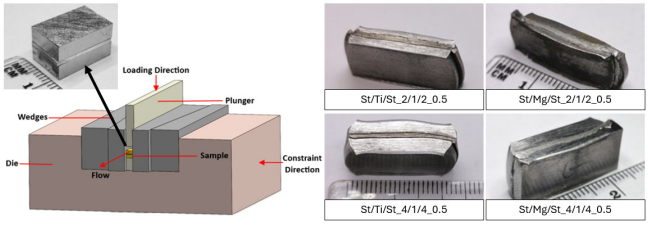

Figure 1. Schematic and example of deformed multilayered systems produced through channel die compression test

In the study, channel compression tests were conducted on heterogeneous systems with different configurations of component layers, such as steel and titanium or magnesium (Figure 1). Various configurations, conditions, and deformation schemes were applied, which were then replicated in numerical simulations. Rheological models were used in the studies, which, through computer simulations, allowed modeling of the interactions between the incoherent components of the microstructure. The primary outcome of the experiments and numerical simulations is the ability to

The project is co-financed by funds from the state budget, granted by the Minister of Science as part of the Excellent Science II Program, project no. KONF/SP/0109/2024/02, subsidy amount 67 870 PLN.

Doskonała Nauka II
Ministry of Science and Higher Education
Republic of Poland
Republic of Poland

evaluate the heterogeneity of the studied multilayer systems. This heterogeneity arises from the diverse microstructural and rheological characteristics of the investigated materials, with particular emphasis on the strengthening effect associated with the presence of low-plasticity hcp phases and their degree of fragmentation. The obtained results were subsequently applied to the design of metal forming processes, such as multi-stage drawing (Figure 3), enabling the production of wires from heterostructured materials with attractive mechanical and performance properties.

2. Numerical simulations

In the first part of the numerical simulations, a channel die compression test was reproduced using the Forge NxT software (Figure 2). The simulations were conducted under conditions consistent with experimental tests, which involved three-layer systems: two outer layers made of steel (St) with thicknesses of 2 mm or 4 mm and an inner layer made of titanium (Ti) or magnesium (Mg) with a thickness of 1 mm. These sample setups were subjected to a deformation value of 0.5. To better understand the interaction between the layers, the simulations were modified by introducing different friction conditions, an additional layer of St and Ti or Mg, and by swapping the positions of the St layers with the Ti or Mg layers (Figure 3a). As a result, 12 variants with different layer configurations were obtained, from which data on temperature, stress, strain, and material distributions were extracted. Selected results of these analyses are presented in Figure 3b.

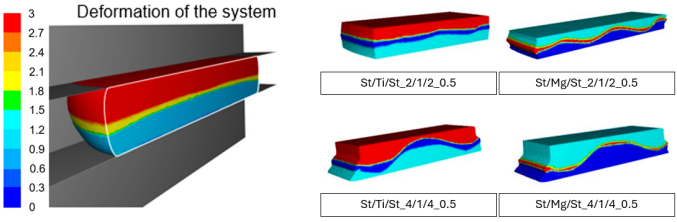

Figure 2. Numerical simulation of channel compression test with example of deformed systems

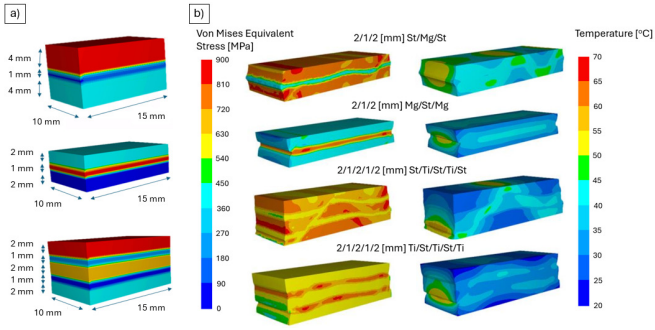

Figure 3. a) Dimensions of defined samples for numerical calculations; b) Stress and temperature distribution for selected St/Mg and St/Ti systemss

Further numerical simulations were conducted to analyze the processes of deformation and work hardening during the multi-stage wire drawing process of two configurations of heterogeneous systems: Pipe/Rod (St/Ti) and Pipe/Pipe/Rod (St/Ti/St) (Figure 4). These simulations served as a valuable tool for understanding the processes of plastic deformation in the studied inhomogeneous

Industrial Partners

Gold

Silver

Bronze

The project is co-financed by funds from the state budget,
granted by the Minister of Science and Higher Education as part of the Excellent Science II Program,
project no. KONF/SP/0109/2024/02, subsidy amount 67 870 PLN

Doskonała Nauka II

Ministry of Science and Higher Education
Republic of Poland

Republic of Poland